UNSW SYDNEY

Finite element modelling and analysis of composite flywheel disk including effects of filament-winding mosaic pattern

Author:
Uddin, Md. Sayem

Publication Date:
2013

DOI:
https://doi.org/10.26190/unsworks/16550

License:
https://creativecommons.org/licenses/by-nc-nd/3.0/au/
Link to license to see what you are allowed to do with this resource.

Downloaded from http://hdl.handle.net/1959.4/53117 in https://unsworks.unsw.edu.au on 2024-05-04

Finite element modelling and analysis of composite flywheel disk including effects of filament-winding mosaic pattern

Md. Sayem Uddin

A thesis submitted in fulfilment
of the requirements for the degree of
Doctor of Philosophy

School of Engineering and Information Technology
The University of New South Wales
Canberra

August 2013

THE UNIVERSITY OF NEW SOUTH WALES

Thesis/Dissertation Sheet

Surname or Family name: UDDIN
First name: Md Sayem | Other name/s:
Abbreviation for degree as given in the University calendar: PhD
School: School of Engineering and Information Technology | Faculty: UNSW Canberra
Title: Finite Element Modelling and Analysis of Composite Flywheel Disk including Effects of Filament-winding Mosaic Pattern

Abstract

A filament-wound composite flywheel disk is characterised by the mosaic-patterned configuration of the layers produced during a filament-winding process. In this structure, each helically wound layer consists of curved triangular-shaped units alternating in the radial and circumferential directions. The mosaic-patterned configuration is not normally considered in general stress analysis procedures based on the conventional modelling of laminated composite structures, including those available in finite element analysis (FEA) packages. However, the filament-winding mosaic pattern could significantly affect the stress fields developed due to rotational loading. Hence, a methodology for finite element modelling of the filament-wound disk taking into account different types of mosaic-patterned configurations is developed and structural analyses are performed.

The modelling which is governed by the first order shear deformation theory is performed using the SHELL281 element from ANSYS. First, using a conventional approach, the filament-wound composite disk is modelled as a laminated circular plate composed of different number of plies in which interlacing of plies due to filament-winding is not considered. Alternatively, three designs composed of 4, 8 and 14 plies are chosen to model the mosaic-patterned structure and to demonstrate the change in stress levels in different layers and the extent of the influence of ply interlacing. Each design is associated with 4, 6 and 8 mosaic units around the circumference of the disk. As observed, the stress levels in the thin filament-wound composite flywheel disk could be underestimated in case of using a conventional technique.

Radially varying fibre trajectories of the filament-wound disk generate stiffness variations due to continuous changes in fibre orientation angles. Thus, varying fibre paths should be modelled accurately to incorporate the actual stiffness variations for FEA of variable-stiffness laminates. Therefore, a modelling approach is developed that would incorporate the continuously varying fibre angles of the predefined changing fibre trajectories.

Based on the results obtained from the numerical analyses of the flywheel disk, various design aspects are assessed in terms of the dimensions and energy storage capacity of the disk. Parametric and comparative analyses of various disks are performed using different performance-controlling factors.

Declaration relating to disposition of project thesis/dissertation

I hereby grant to the University of New South Wales or its agents the right to archive and to make available my thesis or dissertation in whole or in part in the University libraries in all forms of media, now or here after known, subject to the provisions of the Copyright Act 1968. I retain all property rights, such as patent rights. I also retain the right to use in future works (such as articles or books) all or part of this thesis or dissertation.

I also authorise University Microfilms to use the 350 word abstract of my thesis in Dissertation Abstracts International (this is applicable to doctoral theses only).

…… …… ……..……...…
Signature Witness Date

The University recognises that there may be exceptional circumstances requiring restrictions on copying or conditions on use. Requests for restriction for a period of up to 2 years must be made in writing. Requests for a longer period of restriction may be considered in exceptional circumstances and require the approval of the Dean of Graduate Research.

FOR OFFICE USE ONLY Date of completion of requirements for Award:

Copyright Statement

I hereby grant The University of New South Wales or its agents the right to archive and to make available my thesis or dissertation in whole or part in the University libraries in all forms of media, now or hereafter known, subject to the provisions of the Copyright Act 1968. I retain all proprietary rights, such as patent rights. I also retain the right to use in future works (such as articles or books) all or part of this thesis or dissertation.

I also authorise University Microfilms to use the abstract of my thesis in Dissertation Abstract International (this is applicable to doctoral thesis only).

I have either used no substantial portions of copyright material in my thesis or I have obtained permission to use copyright material; where permission has not been granted I have applied/will apply for a partial restriction of the digital copy of my thesis or dissertation.

Signed .....

Date .....

Authenticity Statement

I certify that the Library deposit digital copy is a direct equivalent of the final officially approved version of my thesis. No emendation of content has occurred and if there are any minor variations in formatting, they are the result of the conversion to digital format.

Signed .....

Date .....

Statement of Originality

I hereby declare that this submission I hereby declare that this submission is my own work and to the best of my knowledge it contains no materials previously published or written by another person, or substantial proportions of material which have been accepted for the award of any other degree or diploma at UNSW or any other educational institution, except where due acknowledgement is made in the thesis. Any contribution made to the research by others, with whom I have worked at UNSW or elsewhere, is explicitly acknowledged in the thesis.

I also declare that the intellectual content of this thesis is the product of my own work, except to the extent that assistance from others in the project's design and conception or in style, presentation and linguistic expression is acknowledged.

Signed ….…….

Date …….

Dedicated to ***my parents***

Abstract

A filament-wound spinning composite disk is characterised by the mosaic-patterned configuration of the layers produced during a filament-winding process. In this structure, each helically wound layer consists of curved triangular-shaped units alternating in the radial and circumferential directions. The mosaic-patterned configuration is not normally considered in the general stress analysis procedures based on the conventional modelling of laminated composite structures, including those available in FEA packages. However, the filament-winding mosaic pattern of the composite layer could significantly affect the stress fields developed due to rotational loading. Therefore, a methodology for the FE modelling and analysis of the filament-wound disk taking into account this effect is developed and structural analyses are performed using ANSYS, with different types of filament-winding mosaic patterns incorporated. Also, the disk is modelled and analysed using a conventional method and the differences in predicted stress values from both techniques are demonstrated through distributions of various stresses.

The modelling governed by the first order shear deformation theory is performed using the SHELL 281 element. Firstly, using a conventional approach, the filament-wound composite disk is modelled as a laminated circular plate composed of different numbers of plies in which interlacing of plies due to filament-winding is not considered. Alternatively, three designs composed of 4, 8 and 14 plies are chosen to model the mosaic-patterned structure and to demonstrate changes in the stress levels in different layers and the extent of the influence of ply interlacing. Each design is associated with three types of mosaic-patterned configurations, namely 4, 6 and 8 mosaic units around the circumference of the disk. The disk is rotated at a constant angular velocity with the boundary conditions to

prevent in-plane rigid body motions in both the radial and circumferential directions and also out-of-plane rigid body motion in the axial direction. As observed, the stress levels in the thin filament-wound composite flywheel disk could be underestimated in case of a structural analysis using the conventional mechanics of laminated structures.

The layers of the filament-wound composite flywheel disk are reinforced with radially varying fibre trajectories that result in continuous changes in fibre orientation angles which generate stiffness variations and composite laminates with such stiffness variations are called variable-stiffness laminates. Thus, varying fibre trajectories should be modelled accurately to incorporate the actual stiffness variations for FEA of variable-stiffness composite structures. Therefore, a modelling approach is developed that would take into account the continuously varying fibre orientation angles derived from the predefined changing fibre trajectories. FE modelling of variable-stiffness laminates is performed using the proposed method and corresponding results obtained from various analyses are reported.

Based on the results obtained from the numerical analyses of the filament-wound flywheel disk, various design aspects are assessed in terms of the dimensions and energy storage capacity of the disk. Parametric and comparative analyses of various disks are performed using different performance-controlling factors.

List of publications from this thesis

Journal Article

M. S. Uddin, E. V. Morozov, and K. Shankar, "The effect of filament winding mosaic pattern on the stress state of filament wound composite flywheel disk," *Composite Structures,* 2013, DOI: http://dx.doi.org/10.1016/j.compstruct.2013.07.004.

Conference Papers (peer reviewed)

M. S. Uddin, E. V. Morozov, and K. Shankar, "Stress analysis of a filament wound composite flywheel disk," in the proceedings of *19th International Conference on Composite Materials (ICCM 19)*, Montreal, Canada, 2013, pp. 3053-3063.

M. S. Uddin, E. V. Morozov, and K. Shankar, "Finite element modelling and analysis of a filament wound spinning composite disk," in the proceedings of *7th Australasian Congress on Applied Mechanics (ACAM 7)*, The University of Adelaide, Australia, 2012, pp. 1121-1129.

Acknowledgements

First, I would like to express my deep gratitude to my supervisor Professor Evgeny V. Morozov for his appropriate guidance and valuable ideas and continuous support throughout the course of my research. His insights into research thinking are truly remarkable and his enthusiasm and constant encouragement have kept me motivated to work with him. Regular brainstorming sessions with him have convincingly provided me with the necessary direction for my research. I am indebted to him for his timely help for accomplishing my research work. Without his support, my research would not have been possible. Additionally, his meticulous proof-reading has been a tremendous help in improving my writing skills.

Secondly, I would like to thank my co-supervisor, Dr. Krishna Shankar for the valuable comments and suggestions for the past years.

I sincerely acknowledge the PhD scholarship from UNSW Canberra to support my research in varied possible ways.

Many thanks to all my friends and colleagues at ADFA who made my stay in Canberra and work at ADFA a memorable experience. This group includes, but not certainly limited to Dr. Mustafizur Rahman, Dr. Md. Ariful Islam, Dr. Anup Kumar Chakrabortty, Dr. S. M Shahidul Islam, Karthik Ram Ramakrishnan, Zhi Fang Zhang, Xiao Shan Lin, Dr. Rajibul Karim, S. M. Mahfuzur Rahman, Vishal Naidu, Md. Younus Ali, Md Asafuddoula Asaf, Mohammad Sharif Khan, Khairul Alam, Mohammad Shakhaout Hossain Khan, Dr. Md. Abdul Lahil Baki and Rakib Zaman.

Finally, I would also like to express my gratefulness to my parents and all my family members for their consistent love and support during the time I studied abroad.

Contents

List of Figures

List of Tables

List of Symbols

ω	Rotational speed of the disk
r_o	Inner radius of the disk
R	Outer radius of the disk
I	Moment of inertia of the disk
M	Mass of the disk
V	Volume of the disk
ϕ	Fibre orientation angle
h	Thickness of the filament-wound disk
w_o	Tape width
δ	Tape thickness
ρ	Material density
n	Number of plies
k	Number of fibrous tapes
T_o	Angle of the reference fibre path at geometrical centre
T_1	Angle of the reference fibre path at a specified distance
a	Length of the laminated composite panel
b	Width of the laminated composite panel

Abbreviations

2D	Two Dimensional
3D	Three Dimensional
AMB	Active Magnetic Bearing
CA	Conventional Approach
CEACS	Combined Energy and Attitude Control System
DOF	Degree of Freedom
EPM	Energy per Unit Mass
EPV	Energy per Unit Volume
FE	Finite Element
FEA	Finite Element Analysis
FES	Flywheel Energy Storage
FSDT	First Order Shear Deformation Theory
GP	Gaussian Point
HEV	Hybrid Electric Vehicle
ISS	International Space Station
MP	Mosaic Pattern
PMC	Polymeric Matrix Composite
TMC	Titanium Matrix Composite
UPS	Uninterruptible Power Supply
VS	Variable-stiffness
VSE	Variable-stiffness Element

Chapter 1

Introduction

From the early age of human civilisation, the increasing need for energy storage in different applications has taken different forms, with various types of techniques introduced for use in different sectors. Of the available methods, a flywheel-based energy storage system is the most promising as it offers several advantages over others, such as having a large number of charging/discharging cycles and a prolonged service life without any need for frequent servicing. A flywheel is a device designed to store energy in the form of kinetic energy for release when required. Currently emerging flywheel technology encompasses a variety of applications in different fields. Although a flywheel can be made of metals or composite materials, a composite flywheel is considered to be more effective than others as it offers higher energy storage capability per unit mass. High power and energy densities without reduction in capacity under repetitive charging/discharging cycles can be obtained from a composite flywheel-based energy storage system because design flexibility of composite laminates can be achieved through modifying their fibre angles to produce varying degree of anisotropy in a structure. Therefore, improved performances under various types of loadings can be realised; for example, if the fibre paths in a fabricated structure are varied as a function of location, a gradient in the structure's material properties is created which greatly improves its strength. Similarly, the performance of a composite flywheel can be significantly enhanced through changing its material stiffness with respect to the radius. For these reasons, composite flywheels are increasingly being used in different energy storage applications.

1.1 Composite flywheels

As advanced composite materials are characterised by high strength-to-density and stiffness-to-density ratios, they have gained momentum as high-performance structural materials. Blending their directional properties with design optimisation provides ample opportunities to improve the performances of composite structures over their metallic counterparts. Moreover, modern computer-controlled automatic filament-winding machines have simplified the fabrication of composite structures, providing greater accuracy and, thus, broadening the range of applications of composite materials in different products.

The performance of a flywheel can be attributed to three major factors, i.e., the strength of the material used to fabricate its rotor, the geometry of its rotor and its rotational speed [1]. Although flywheels can be made of either metals or composite materials, a composite flywheel is promising as it can attain a higher rotational speed than metallic ones and, consequently, a comparatively higher specific energy storage capacity. The low densities of composite materials used in a flywheel do not affect the kinetic energy storage capacity of the rotor since the increased rotational speed compensates for the lower mass. In general, a structure's mass can be reduced by 20 to 30% through replacing metal alloys with composite materials [2].

Composite flywheels are gaining increased use in different energy storage applications in which a flywheel acts as a capacitor by storing kinetic energy [3]. Compared with traditional chemical battery-based energy storage systems, flywheel energy storage (FES) systems offer various advantages. Firstly, particularly flywheels fabricated using composite materials have higher energy densities than most batteries. Secondly, a FES system has a longer charging/discharging life cycle than a battery and, furthermore, is more environmentally safe due to it not containing the toxic elements present in batteries. However, there are some major challenges associated with the proper design of a FES

system, one of which is to design a flywheel that provides a higher energy storage capacity and does not fail during operation. Considering this, composite materials are the most promising and suitable options for fabricating a flywheel due to their directional properties that can be exploited to improve the flywheel's strength without modifying its convenient shape. In this thesis, a filament-wound flywheel disk is chosen for study because it is an example of an optimal composite structure reinforced with the fibre patterns necessary to produce uniform fibre tension and operates at half the stress of a simple hoop for a given tip speed and fibre mass per unit length [4]. The first purpose of this research work is to investigate the manufacturing effects of the filament-winding process on mechanical strength using a finite element (FE) technique to gain a better idea of the performance of such a flywheel and to demonstrate the necessity of incorporating manufacturing characteristics for a performance analysis under various loadings. The second aim is to illustrate the performance of such a filament-wound disk through parametric analyses and, finally, stiffness variations in composite laminates due to varying fibre paths and the FE modelling and analysis of such variable-stiffness (VS) laminates are investigated and discussed.

1.2 Filament-wound composite flywheels

A filament-wound composite flywheel disk with optimal fibre trajectories [2, 4] is an example of the increasing number of optimal composite structures. The concept of a uniform-stress filament-wound spinning composite flywheel disk composed of structural filaments of uniform cross-sections is illustrated by Kyser [4]. It has symmetric spiral net-type filament winding, with the clockwise outward-directed fibres attached point-by-point to the counter-clockwise outward fibres. These fibres are arranged as a fine-mesh circular net forming curved load-carrying paths that spiral outward from the centre of the disk and maintain constant tension through cancelling the decreasing fibre tension towards the centre

due to radially directed loading and increasing fibre tension towards the centre caused by inertia forces due to rotation. This constant tension condition can be achieved by arranging the fibres in such a way that allows the two tension gradient effects to cancel each other out. The intersection between the fibres is shown in Figure 1.1 in which each branch has a local radius of curvature μ and meets the radius vector at angle (β).

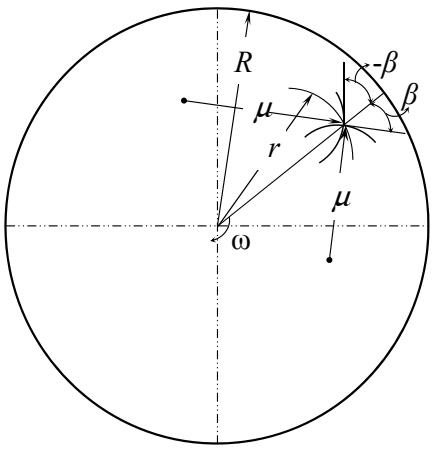

Figure 1.1: Local geometry of fibre pattern - intersection of opposite fibres

The fibre paths of a Kyser spinning disk can be defined using the following equations.

$$\frac{\mu^2}{R^2} = \frac{1}{2\Omega}\left[1 + \left(\frac{2-\Omega}{\Omega}\right)\frac{1}{G^4}\right] \tag{1.1}$$

and

$$\Omega = \frac{m'\omega^2 R^2}{T}, \quad G = \frac{r}{R} \tag{1.2}$$

where m' is the mass per unit length of fibre, ω the rotational speed of the disk, R the outer radius of the disk and T the tension in the structural fibre. The uniform stress condition can be imposed by choosing Ω to be constant. Eqn. (1.1) can also be written as

$$\sin^2\beta = \frac{\Omega G^2}{2}\left[1 + \left(\frac{2-\Omega}{\Omega}\right)\frac{1}{G^4}\right] \tag{1.3}$$

Two distinct types of curves bounded by $\Omega = 2$ can be obtained using Eqns. (1.1) and (1.3) for the condition $\Omega \geq 1$ whereby, for $\Omega < 2$, μ must increase with decreasing G and, for $\Omega > 2$, μ must decrease. The condition $\Omega < 2$ produces an annular band of fibre paths,

as shown in Figure 1.2(a). These smooth, continuously turning curves are tangent alternatively to the outer periphery and some to the inner periphery. The radius of the inner periphery is defined by

$$G_{min}^2 = \frac{2}{\Omega} - 1 \quad \text{for} \quad \Omega < 2 \tag{1.4}$$

For $\Omega = 1$, the fibre path is only a circular hoop while $\Omega = 2$ generates fibre paths that are circles tangent to the periphery and passing through the origin (Figure 1.2 (b)), with a constant radius of curvature ($\mu = R/2$).

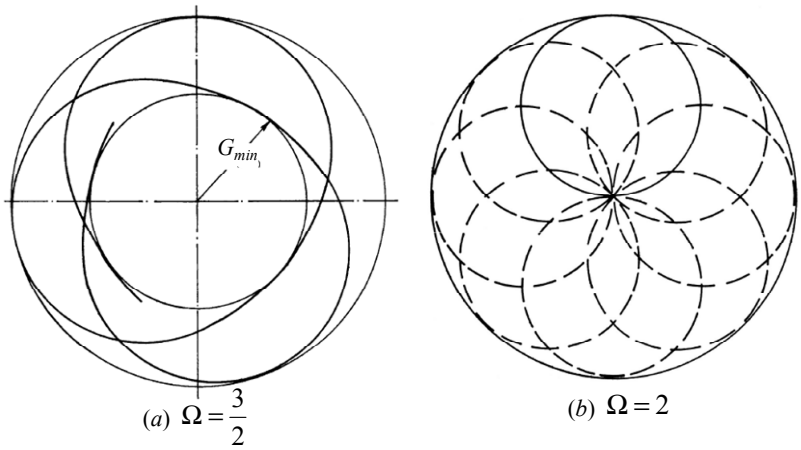

Figure 1.2: Fibre pattern for isotensoid disk [4].

1.3 Manufacturing effects on filament-wound composite flywheel

As previously indicated, the fibres are arranged as a fine-mesh circular net forming curved load-carrying paths that spiral outward from the centre of the disk, as presented by Kyser [4]. The optimal design of a filament-wound composite spinning flywheel disk of uniform strength based on the monotropic model of unidirectional filaments has been discussed by Vasiliev and Morozov [2]. The resultant structure of the filament-wound layer of the spinning flywheel disk shown in Figure 1.3 is composed of two plies with $+\phi$ and $-\phi$ orientations of the fibres interlaced in the process of continuous filament winding. As a result, the structure of the layer has a distinctive mosaic pattern (MP). The mosaic-

patterned configuration which might have a noticeable effect on the strength of a filament-wound composite structure with certain level of thickness is investigated in this work.

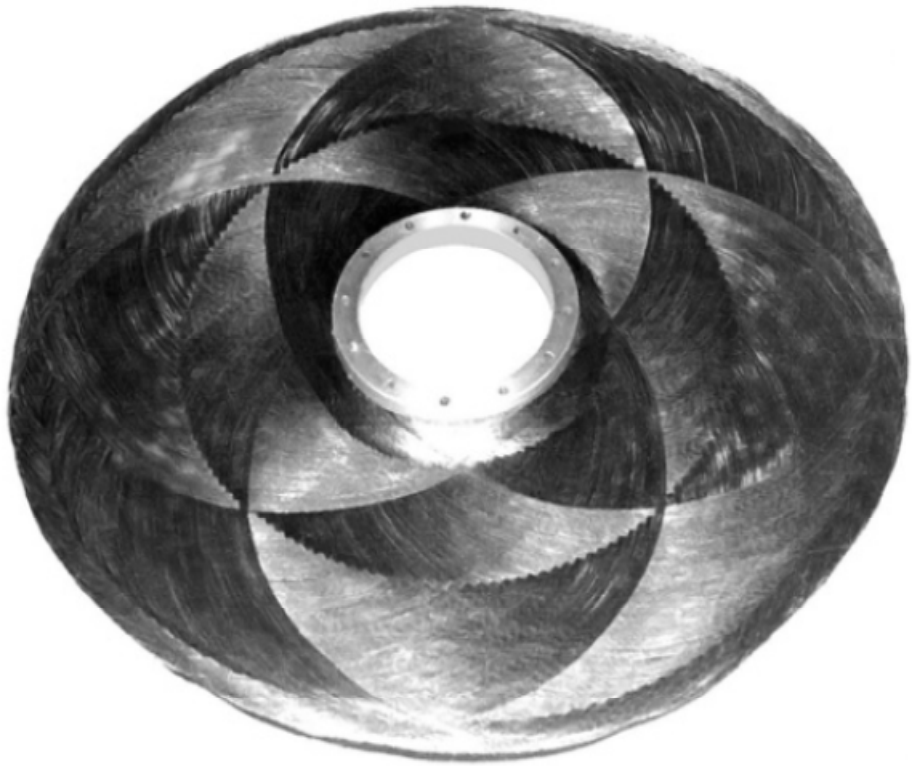

Figure 1.3: Carbon-epoxy flywheel [2]

1.3.1 Filament-winding mosaic pattern

The filament-wound spinning composite disk considered (Figure 1.3), which is fabricated by a filament-winding process and composed of antisymmetric $\pm\phi$ angle-plies, has an annular band of smooth, continuously turning fibre paths tangent to both its outer and inner peripheries [2, 4] as shown in Figure 1.4. It consists of an even number of angle-ply antisymmetric layers [2, 5], each of which is composed of two plies with $+\phi(r)$ and $-\phi(r)$ angles of fibre orientation to the radius of the disk as shown in Figure 1.4. These plies are interlaced in the process of helical filament winding. As a result, each angle-ply layer has a particular type of repeating filament-winding pattern around the circumference and along the radius (Figure 1.3). These patterns consist of curved triangular-shaped two-

ply units with alternating $\pm\phi$ and $\mp\phi$ fibre orientations repeated in a chess-board fashion [5-6]. The plies are not interlaced within a unit but combined into the angle-ply antisymmetric laminates. The units are arranged in a regular geometric pattern around the circumference and along the radius. Therefore, the spinning composite disk comprises multiple numbers of mosaic units of varying sizes depending on the filament-winding parameters. The texture of each angle-ply layer depends on the process parameters for the filament winding for the same fibre orientation ($\phi(r)$) [5].

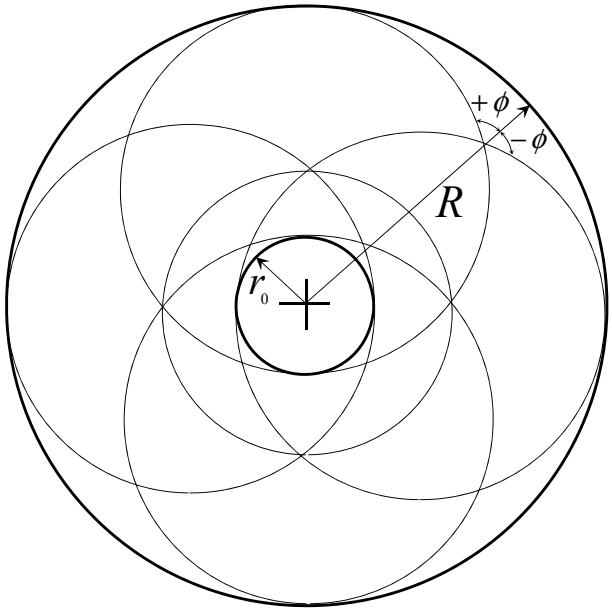

Figure 1.4: Schematic representation of filament-wound composite disk with winding angle trajectories

1.3.2 Analysis of effect of stiffness variations in laminates

The layers of the filament-wound composite flywheel disk are reinforced with radially varying fibre trajectories that results in continuous changes in the fibre orientation angles which generate stiffness variations and composite laminates with such variations are called VS laminates. Therefore, for a finite element analysis (FEA) of VS composite structures, varying fibre trajectories should be modelled accurately to incorporate actual stiffness variations. Hence, a modelling approach should be developed to take into account the

continuously varying fibre orientation angles obtained from predefined fibre paths. Different techniques for analysing such VS laminates have been reported in the literature [7-28].

Traditionally, a composite laminate is tailored by exploiting its design variables, namely the fibre volume fraction, fibre orientation in each individual lamina, number of laminas, thickness of each ply and stacking sequence of all the plies bonded together. The fibre orientation angle within each ply is generally assumed to be constant at all points in the plane of the laminate. These design variables can be configured in different ways to obtain laminates suitable for particular applications under different loadings. However, the most usual designs of laminates limit the potential of composite materials because any combination of these design variables with constant values produces unvarying laminate properties. Laminates tailored in this way cannot show the maximum possible strength required to withstand non-uniformly distributed in-plane stress; for example, holes and notches create non-uniform stresses in laminates. Therefore, in order to enable a laminate to withstand the highest loads, its fibres should be steered along load paths. Of the different techniques for tailoring a composite laminate, the most flexible is to vary the fibre orientations at different locations throughout each lamina which, for some composite structures, occurs automatically through manufacturing processes; for example, during the manufacturing of a filament-wound pressure vessel, as its fibre-path trajectories automatically change, VS is inherently produced. VS is also produced by design as some composite structures need to be designed with varying fibre paths; for instance, designing a composite plate with a hole could be performed through steering fibres along the load-path trajectories in order to handle stress concentrations. Directing fibre paths according to load-path trajectories for stress variations under given loads facilitates the strengthening of laminates by diverting loads from the most sensitive regions in composite structures.

Therefore, as VS laminates need to be manufactured with a high degree of precision, correct fibre orientation angles should be maintained during both the laying of the fibres and curing. As, with the help of a computer-controlled automatic advanced fibre-placement machine, VS laminates are produced according to required configurations, composite materials offer the design flexibility to tune a specific stiffness and, thereby, a specific strength through controlling various design variables. As simplified constant values of design variables are often utilised, the potential of laminates to improve stiffness in accordance with the requirements of a specific application is ignored.

Fibre-reinforced laminated composites have been used in structural design for many years. Designers have ample options for designing laminates according to particular needs by changing various design variables to achieve high stiffness and strength but low weight. Also, the structural responses of laminated composites depend greatly on what types of laminates (symmetric, balanced, etc.) are used. Although the stiffness of a laminate with straight fibres and a particular stacking sequence is fixed, VS laminates are required for applications such as the composite shell design for an aircraft fuselage, redistribution of an applied loading to deal with stress concentrations, provision of various degrees of bend-twist coupling by asymmetric VS laminates[28] and improvement in buckling performance [17].

The fabrication of a VS laminated composite necessitates varying either the laminate's fibre volume fraction or the orientations of its fibres at each point while VS of a laminated composite panel can be attained also by varying the laminate's thickness [10]. Tailoring the elastic stiffness of a laminated composite panel by allowing the fibres to curve within the plane of the laminate is a relatively novel design concept [29]. In the past, the limitation of fabrication techniques and analysis procedures was that they precluded the use of a curvilinear fibre orientation for the design of laminated composites [7-8]. Recent

manufacturing techniques, such as computer-controlled 3-axes filament winding, tape-laying machines and fibre-and-tow placement technology, have facilitated the fabrication of composite structures with varying fibre orientations [17]. Wu and Gurdal [30] discussed different issues regarding the fabrication of VS panels.

Leissa and Martin [31] modelled a VS composite panel using the Ritz method for varying fibre volume fraction and proved that the VS concept improves the buckling performance of a laminated composite panel. After the analysis of a simply-supported square plate with a centrally located hole loaded in compression, Hyer and Lee [7] showed how curvilinear fibres not only improve its buckling capacity by moving the load away from its unsupported hole region to its supported edges but also improve its tensile capacity. The calculated tensile strength of the laminated plate with varying fibre orientations was 1.26 times greater than that of one with traditional straight-line orientations. They used FE discretisation for the analysis assuming the fibre orientation within each element to be constant. However, this element-to-element variations of fibre angles doesn't accurately exhibit continuously varying fibre orientation angles for any layer of the laminate while fabricating such discontinuous orientations from element to element is impossible even using the most advanced manufacturing methods.

A convention for the definition of tow paths for a rectangular VS panel was first introduced by Gurdal and Olmedo [17] who also analysed VS panels in cases of in-plane loads [17, 32]. Their results demonstrate that, because of its changing fibre orientation, a panel with VS has higher buckling resistance than a conventional straight-fibre laminate. For a VS panel, its buckling load and in-plane stiffness as a function of its fibre orientation angle are generally opposite to one another. According to their findings, a VS panel with a particular value of the overall stiffness has a specific configuration for which the panel will have a critical load greater than the corresponding straight-fibre configuration. Therefore,

the flexibility of the VS concept lies in the fact that, for a given critical load, a straight-fibre format has only one corresponding value of overall stiffness whereas many VS configurations with various values of the overall stiffness can have the same critical load values [32].

Gurdal and Olmedo [17, 33] also analysed the stiffness variation and its effect on the elastic response of a panel. Wu et al. [11] performed both analytical and experimental studies to determine the structural responses of two compression-loaded VS panels and evaluated them using FEA. Wu and Gurdal [10] used a nonlinear material model for predicting the structural response of a laminated composite panel without overlaps under uniform end-shortening and then compared the obtained results with those found by Wu et al. [11]. The analysis of VS panels [11] showed a 4 percent improvement in the normalised extensional stiffness for a panel without overlapping and, according to the results obtained, its weight-normalised failure load is 8 percent greater than that of a conventional panel. The results [11] also suggest that the buckling load of a panel without overlaps should be 40 percent greater than that of a conventional straight-line fibre-orientated panel.

From their analysis, Hyer and Charette [8] concluded that curvilinear designs show improved performances in both tension and compression. Setoodeh et al. [34] investigated the optimal in-plane design of VS composites using lamination parameters and solved the minimum compliance design problems with the aid of bilinear finite elements.

To study the responses of VS laminated plates, Gurdal and Olmedo [17, 32] considered the variations of fibre orientation angles along one direction. Muc and Ulatowska [35] demonstrated how a substantial improvement in bending stiffness can be achieved by spatially varying fibre angles and concluded that this is strongly dependent on the plate's geometry.

The improved buckling performance due to varying fibre orientation can be attributed to two phenomena [36]: the local increase in stiffness at the edges of the plate; and the increased flexural stiffness at the buckle locations corresponding to the buckling mode.

Alhajahmad et al. [20] meshed a VS panel using S4R Abaqus element and considered the local fibre orientation at the centroid of each element to define the curvilinear fibre path, that is, an approximation of the continuous paths of fibres. Hyer and Lee [7] and Tatting and Gurdal [9, 29] considered the straight-fibre orientation within each element for FEA while the FE model of a panel chosen by Wu et al. [11] had discontinuous fibre orientation angles.

1.4 Design and manufacture of composite flywheels

The varying stiffness of composite laminates with continuously changing fibre orientations complicates the design of a composite flywheel. Moreover, under different loading conditions, the anisotropic behaviour of composite materials makes the modelling and analysis of a flywheel intricate.

Modifying the fibre direction offers design flexibility that cannot be obtained through homogeneous materials. Varying degrees of anisotropy can be utilised for improving the performances of composite parts under various types of loadings. In a filament-wound composite flywheel disk, this is achieved by maintaining the fibre paths that follow specified trajectories.

As a flywheel constructed with fibre reinforcement in only the tangential direction is prone to failure in the radial direction due to the weakness of its matrix materials, Thielman and Fabien [37] presented a stacked-ply approach for designing composite flywheel disks that consist of plies of unidirectional fibres in which the flywheel is fabricated using alternating plies of circumferential and radial reinforcements, as shown in Figure 1.5. Although it was expected that this design would provide improved performance with more

reinforcement in the tangential direction, manufacturing a flywheel with such fibre trajectories is a most challenging issue, and assembling different plies is also very complicated and may result in degradation of the actual strength of the laminates.

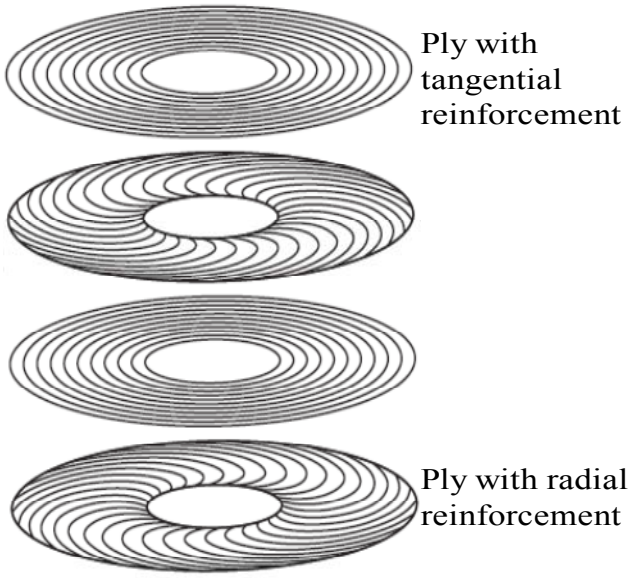

Figure 1.5: Flywheel with stacked-ply arrangement [37]

Bokov et al. [38] examined the optimum design of a flywheel in the form of a moment-free shell of revolution formed by winding or placing of orthotropic reinforced strips and explored the reinforcing paths for ensuring maximum bearing capacity while assessing the energy storage capacity of these shells. Seleznev and Portnov [39] demonstrated the chord winding process of a composite-tape disk and showed that variations in elastic properties along the radius must be taken into account in a stress analysis.

The tailoring of elastic moduli in the radial direction has been studied by Nie et al. [40] for the design of a fibre-reinforced orthotropic linear elastic rotating disk, with the constant radial or hoop stress or constant in-plane shear stress, considering two types of fibre arrangements, in concentric circles and along the helices, as shown in Figure 1.6. For the former, the axes of material symmetry coincide with the radial and circumferential directions while, on the other hand, for the latter, the orientations of the material principal axes vary with the radial coordinate of a point. For a structure with fixed geometry, the

interest is in finding the gradation of its material properties so as to achieve the desired stress state in its body, a problem usually called material tailoring.

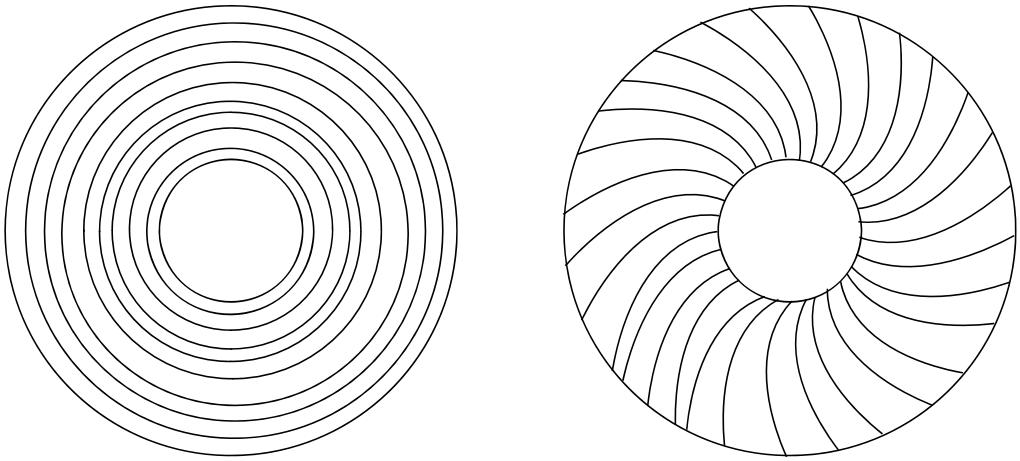

(i) Fibres forming concentric circles (ii) Fibres aligned along helices

Figure 1.6: Different alignments of fibres in fibre-reinforced composite rotating disk

Abdul-Aziz et al. [41] analysed two configurations of composite flywheel rotors. The first was called a pancake rotor assembly which was basically a single thick ring assembled on a solid aluminium hub. The rim's inside and outside diameters were 6.9 and 11.5 inches, respectively, its height 1 inch, its radial interference fit 0.014 inch, and it was made of M30G carbon fibre and an epoxy resin system. The second was a non-axisymmetric cylindrical rotor mass-loaded by the aluminium hub, with inside and outside diameters of 6.9 and 10.5 inches, respectively, a height of 8.5 inches and a radial interference fit of 0.013 inch introduced between its rim and hub to reduce the peak radial tensile stresses. The rim was made of Hexel's IM7 carbon and AS4D carbon fibre and a shell epoxy resin mixture, with the IM7 fibre wound at the inner and outer diameters and the AS4D fibre in the central portion.

The dominating stresses in a flywheel are generally circumferential and radial. As, if the fibre reinforcement is aligned in the circumferential direction, the radial tensile stress is more crucial due to the low strength in the radial direction [42], the concept of a hybrid composite flywheel rotor has gradually emerged. For a hybrid composite rotor assembled

using rims of different materials, the material sequence is chosen as per an increasing stiffness per density value for an increasing radius [43]. A composite flywheel manufactured using a number of concentric rings press-fitted together with a specified misfit between each ring [44], which results in the compressive radial stress at the interface of each ring, is illustrated in Figure 1.7.

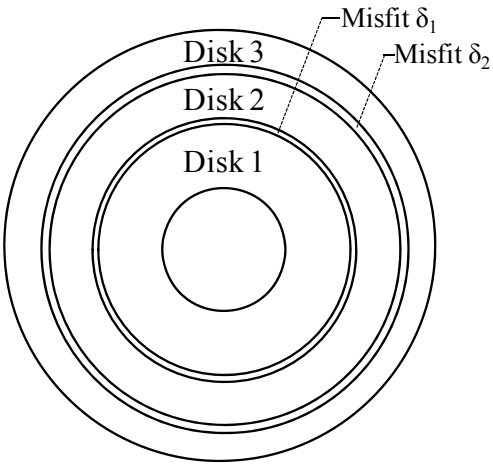

Figure 1.7: Schematic representation of three concentric disks with misfit

Each flywheel shown in Figure 1.8 consists of a rotating mass ('rotor' A) and its mechanical connection to a shaft ('hub' B) [45]. As a very rigid hub transmits all inertial forces (F_i), the path between the rotor's opposite rim portions is radial with stress . A relatively flexible hub results in a radial displacement of the rotor whereby the circumferential stress ( ) develops.

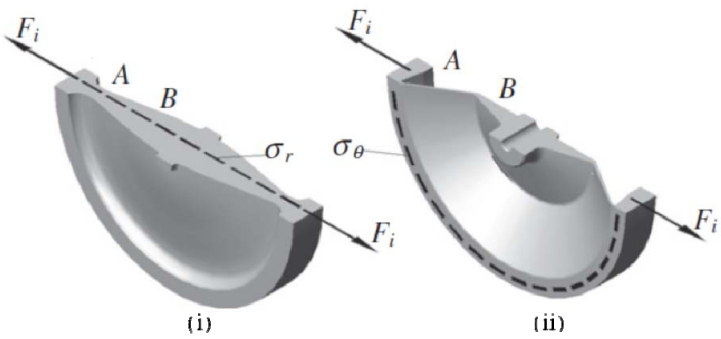

Figure 1.8: Flywheel rotors with: (i) rigid hub with radial stress transmission; and (ii) flexible hub with circumferential stress transmission [45]

Abdel-Hady et al. [46] manufactured a multi-directional composite flywheel composed of multiple radial rings consisting of fibres in the radial direction and multiple hoop rings with fibres in the hoop direction and these are assembled using an adhesive film. The University of Texas at Austin Centre for Electromechanics (UT-CEM) designed the composite flywheel rotor shown in Figure 1.9 which was composed of a series of concentric cylindrical rings press-fitted together. The motivation for fabricating this flywheel was to use in a flywheel battery system for power averaging on a hybrid electric transit bus [47].

Ha et al. [48] discussed three different rim designs of a hybrid composite flywheel rotor composed of four hybrid composite rims fabricated from carbon-glass/epoxy with varying volume fractions of hoop-wound reinforcements.

Figure 1.9: UT-CEM composite flywheel [47]

1.4.1 Modelling and analysis of composite flywheels

Although composite flywheels hold great promise, as a number of challenges need to be overcome for their better service and long-term performance, implementation of advanced design and analysis approaches is required. Most research work performed to date on

flywheels has aimed to maximise their energy storage capabilities while keeping their masses at the minimum possible level.

In most research, two-dimensional (2D) axisymmetric models have been considered for stress analyses of flywheel rotors, with the plane stress assumption for composite flywheels which have significantly larger diameters than heights [49-50]. Also, some analytical methods have been reported by a number of researchers, with analytical solutions available for the stress state analysis of axisymmetric rotors limited to certain considerations. Although these methods are demonstrated to be sufficiently accurate, as they are largely dependent on relatively simple one-dimensional models that involve assumptions regarding stress and strain in some directions which are not captured directly, they introduce a degree of inaccuracy [51]. Alexandrova and Real [52] presented a mathematical model of an annular elastically isotropic and plastically orthotropic rotating disk comprising a numerically convenient set of equations governing the stress balance in its elastic and elastic-plastic regions. The role of plastic material anisotropy on its performance was assessed by considering stress-free boundary conditions. Ha et al. [53] performed the structural analysis of a composite flywheel rotor consisting of multiple rings with radially varying interferences and ply angles assuming the rotor to be an axisymmetric, thick laminated shell with a plane strain state. Zheng-yi et al. [54] used a FE method to determine the stresses and strains of a composite flywheel induced by the rotation of the two-layer pre-stressed rotor and its interference fit. Three 2D FE models of hybrid composite flywheel rotors with two layers, considering the properties of plane stress, axisymmetric and plane strain conditions, were built.

A flywheel experiences various types of stresses during its service life. As inertial stresses in it during operation are dominant in the circumferential direction, a composite flywheel rotor is manufactured through filament winding with the fibres orientated in the

circumferential direction [55]. Generally, a filament-wound composite rotor fails by radial delamination prior to fibre breakage in the circumferential direction as it lacks reinforcement through radial thickness [55] while the radial stresses of relatively lower values act in the materials' weakest direction. For a thin-walled rotor configuration, failure occurs due to circumferential stress but, for a thick one, radial stress [45]. As, during rotation, a composite flywheel allows its rotor to expand radially as much as possible, radial stress is minimised. As a flywheel rotor experiences non-uniform stress distribution in the circumferential direction, stress concentration induced in the rotor limits its capability to properly bear the stress. Therefore, proper modelling and analysis techniques should be employed to accurately determine stress distributions under different loadings which would help to better understand the performances of flywheel disks and how to design them appropriately for particular applications in different sectors.

Different loadings, such as centrifugal, interference, thermal and residual stresses, can be considered for analysing flywheels. Abdul-Aziz et al. [41] performed 2D and 3D stress analyses of flywheels utilising both a FE method and non-destructive evaluation techniques under combined centrifugal and interference-fit loadings. Pérez-Aparicio and Ripoll [45] developed a formulation that includes the effects of mechanical loads as well as residual stresses for accurately estimating stresses in rotors, with two cases used for the analysis of flywheels based on their rotor geometry: for a short rotor (disk), the plane stress assumption was considered and, for a long rotor (cylinder), the plane strain case. Mechanical loads are those produced by rotational speed and temporal variation in rotational speed (acceleration) while residual stresses are developed by thermal variation for cooling after the curing process and by resin moisturisation throughout a rotor's life. Although hygrothermal stresses are not present in flat unidirectional composites, the closed circumferential geometry of a flywheel encounters significant levels of residual stresses (up to 20% of

mechanical stresses) in the transverse direction of its composites. Arnold et al. [44] considered three major factors for the assessment of composite flywheel disk systems subjected to pressure surface tractions, body forces (temperature change and rotation) and interfacial misfits. These three factors are related to additional loading beyond the rotational speed (e.g., temperature, interference fit), material behaviour (e.g., isotropic/anisotropic, elastic/inelastic) and geometry (e.g., uniform/variable thickness). Assembling a rotor using a press-fit or shrink-fit induces compressive radial stress that helps to mitigate the radial tensile stress developed during operation of the flywheel [55] and avoid premature failure by radial delamination. However, significant banding and shear stresses along the axial direction may develop during fabrication due to the press-fit process. Although, for the study of composite flywheels involving material orthotropy, centrifugal forces have always been considered, for systems in which energy is released suddenly, acceleration has only recently been taken into account [56]. To minimise radial stress in flywheel rotors, optimal rotors with layers of different materials that result in increasing stiffness with increasing radius have been proposed.

Of the three factors for controlling the performance of a flywheel, i.e., material strength, geometry and rotational speed, Arslan [1] focused only on the effects of geometry on a flywheel's energy storage/delivery capability per unit mass (specific energy), and so chose the six most common different geometries (i.e., straight/concave or convex shaped 2D cross-sections). Although, for a simple flywheel geometry, its maximum energy density is presented [57] in the form of shape factor that depends on its moment of inertia, for a complicated geometry, assessment of the shape factor remains elusive. Therefore, a FE-based analysis of flywheels could help to determine a maximum achievable energy density [1].

For the maximisation of stored energy per unit mass (EPM) of a flywheel, firstly, the maximum rotational speed a given disk configuration can withstand before its induced stresses exceed the allowable limit should be determined [44]. To set the limit speed of a rotating disk, the ultimate tensile strength of the material, or endurance limit in the case of fatigue, can be considered an allowable design stress and, for an anisotropic material, this allowable limit will vary significantly depending on its fibre orientation and volume fraction [44].

Although several publications can be found in the literature concerning analytical solutions for simple circumferentially-wound composite flywheels, no such solution has been reported for a filament-wound flywheel disk.

1.4.2 Tests and energy output

A detailed analysis of the maximum power with regard to the energy supply and pick-up of a filament-wound disk-type composite flywheel has been presented [58] in which it is shown that flywheels made of advanced composite materials are capable of generating short-term impulses of very high power.

Herbst et al. [59] presented spin tests of two 10 MJ composite flywheel rotors designed to achieve an energy density of greater than 310 kJ/kg in a volume of less than 0.05 m^3. Flexible composite arbours were utilised to connect a composite rim to a metallic shaft, with the flywheel rim constructed of two concentric rings assembled with a radial interference. The spin test speeds selected to demonstrate strains equivalent to those present at selected energy storage levels in a full-scale machine reached 45,000 rpm.

Thielman [3] reported a spin test of optimal flywheels and predicted their failure speed to be 47,000 rpm. Abdel-Hady et al. [46] employed a non-destructive evaluation method

using X-ray and thermal imaging techniques to evaluate hoop and radial rings in terms of fibre architecture, fibre volume fraction and lay-ups.

Thesken et al. [60] investigated the time-temperature behaviour of a composite rotor manufactured using carbon fibres wound in the hoop direction and found that that of the epoxy matrix that controls the uniaxial properties transverse to the fibres and shear properties may limit the long-term durability of a filament-wound flywheel rotor.

Hayes et al. [47] reported the test results for a FES system conventionally referred to as a flywheel battery designed for power averaging on a hybrid electric transit bus. The system comprised a high-speed 150 kW permanent magnet motor generator with magnetic bearings for levitating a 2 kWh composite flywheel. Based on anticipated duty cycles, it was recognised that the flywheel could be required to complete 10,000 start-up and shut-down cycles (0 to 40,000 rpm) and 5.5 million charging/discharging cycles (30,000 to 40,000 rpm) over a service life of 15 years.

1.4.3 Design optimisation

To obtain an optimum design for flywheels, Ebrahimi [61] devised a continuous function of thickness variation and formulated the flywheel design problem as a numerical optimisation problem with the coefficients of the thickness function as design variables, and the results obtained from an optimised flywheel show remarkable advantages over a constant-thickness flywheel. Adali et al. [62] optimised multi-layered composite disks rotating at a constant speed with the objective of maximising the rotational speed by optimally determining fibre angles as well as lamination. The disks were modelled as symmetric, balanced laminates with angle-ply and/or cross-ply layers.

Three different rim designs of a hybrid composite flywheel rotor composed of four hybrid rims have been presented by Ha et al. [48] using strength ratio optimisation to

reduce the maximum strength ratio for two rotor states, stationary and maximum allowable rotational speed, with the strength ratio varying depending on the rims' fabrication process.

Wen and Jiang [63] obtained an optimum design of a hybrid composite multi-ring flywheel rotor for maximising its energy storage capacity considering the preload stress generated by the interference fit, fibre failure and delamination between two adjacent rings under a high rotational speed. In order to satisfy the requirements of various applications, four types of optimal schemes for the energy storage capacity of a flywheel rotor, namely EPM, energy per unit volume (EPV), energy per unit cost and energy per unit mass and cost together, have been proposed. The results show that the maximum allowable rotational speed and energy storage capacity are closely related to the optimal schemes chosen.

Thielman and Fabien [37] formulated the design of the fibre angle distribution in a stacked-ply composite flywheel disk arrangement as an optimal control problem incorporating classical lamination theory to describe the constitutive behaviour and the Tsai-Wu failure criterion to predict the failure of the flywheel laminate. Both radial and tangential reinforcements were used with a view to distributing the loads from the fibres at the outer radius to those at the inner radius to prevent failure in the transverse fibre direction. On the other hand, Fabien [50] presented the influence of the failure criteria on the design optimisation of stacked-ply composite flywheels. The results indicate that estimation of the energy density of this design is greatly dependent on the selection of the proper failure criterion to be employed for the optimisation problem.

1.5 Motivation

Despite the numerous promises offered by composite flywheels, the quest for their better service and long-term performance necessitates the implementation of advanced design and analysis approaches. To date, different studies of composite flywheels have been performed to achieve maximum performances under certain conditions but maximising the energy

storage capability of a flywheel while maintaining its mass at the minimum possible level is the most sought-after performance improving factor in terms of the design of a composite flywheel.

Different studies of filament-wound composite flywheels have been limited to certain considerations that cannot fully encompass the actual structure of composite materials. The filament-winding mosaic pattern (MP) of a filament-wound composite structure is one special feature that is not generally considered in the modelling and stress analysis of such a structure as laminated shells using analytical and/or FE solutions and exploiting the mechanics of composite laminates taking into consideration their numbers of plies, stacking sequences and fibre orientations [2, 5-6]. The filament-wound composite flywheel disk under consideration has this special in-built mosaic pattern produced by the filament-winding process. Each of the disk's layers is composed of two plies with $+\phi$ and $-\phi$ fibre orientations and these are interlaced during the process of continuous helical filament winding. As a result, the structure of the layer has the distinctive mosaic pattern.

The effect of the filament-winding mosaic pattern on the strength of thin-walled composite cylindrical shells has been investigated by Morozov et al. [5-6], its sensitivity on the compressive stability of filament-wound composite cylinders demonstrated by Jensen and Pai [64], and its effect on a filament-wound composite pressure vessel demonstrated by Mian and Rahman [65]. As has been shown in these analyses, assessments of the mechanical responses of filament-wound composite structures are considerably influenced by the incorporation of mosaic-patterned units. However, the effect of thickness variation in filament-wound structures on the stress state has not been considered in these studies. Therefore, this is an important motivation for performing a stress analysis of the filament-wound composite flywheel disk with a variety of filament-winding pattern around its circumference and an actual varying thickness. This would demonstrate the effect of the

mosaic pattern created during a filament-winding process on stress distributions and effectively on the strength characteristics of the filament-wound spinning composite flywheel disk with varying stiffness properties.

Similar to radially varying fibre trajectories in the filament-wound composite flywheel disk, a composite laminate can be fabricated with spatially varying fibre paths, which results in changes in the fibre orientation angles, to achieve desired stiffness variation. Composite laminates with predefined varying fibre paths are called VS laminates and, in order to obtain their accurate responses under different loadings, employing a proper analysis technique capable of incorporating actual stiffness variations is essential. Therefore, a modelling approach that takes into account the continuously varying fibre angles derived from predefined fibre trajectories needs to be developed.

1.6 Objectives

The main focus of this research is to model and analyse a filament-wound spinning composite disk using a FEA technique incorporating various types of mosaic-patterned configurations as well as different thickness levels. The specific objectives aimed at achieving this goal are as follows.

- To conduct FE modelling and analysis of the filament-wound composite flywheel disk with the representation of an actual mosaic-patterned configuration. Three designs, composed of 4, 8 and 14 plies, are chosen to model the mosaic-patterned structure and each design will be associated with three types of mosaic-patterned configurations, namely, of 4, 6 and 8 mosaic units around the circumference of the disk.
- To model and analyse the filament-wound flywheel disk using the conventional mechanics of laminated structures and compare the predicted stress values with

those obtained from mosaic-patterned models in order to demonstrate the sensitivity of a mosaic-patterned configuration on stress levels in a structural analysis.

- To develop a modelling approach that considers the continuously varying fibre orientation angles obtained from predefined fibre paths and, consequently, incorporates actual stiffness variations more accurately for a FEA of VS composite laminates. FE modelling and analysis of VS composite panels are performed using the proposed method for different varying fibre paths.
- To assess various design aspects in terms of the dimensions and energy storage capacity of the filament-wound composite flywheel disk based on the results obtained from numerical analyses. Also, parametric and comparative analyses of various disks are conducted using different performance-controlling factors.

1.7 Thesis outline

According to the objectives outlined above, this thesis is organised in six chapters. In this chapter, different types of composite flywheels, along with their design and manufacturing techniques, are presented. Then, methods for modelling and analysing composite flywheels are demonstrated, based on which the aim of, and motivation for, this research are established.

Details of the mosaic-patterned architecture generated during the filament-winding process for fabricating the flywheel disk and corresponding fibre paths as well as thickness are presented in Chapter 2. FE modelling of the disk considering mosaic units of varying sizes is performed using a special technique developed to represent the actual characteristics of filament-wound structures.

The results obtained from stress analyses of the filament-wound composite flywheel disk considering the mosaic-patterned configuration with 4, 6 and 8 mosaic units around its

circumference and variable thickness are presented in Chapter 3 and compared with those obtained using a conventional approach (CA).

A special FE modelling approach for VS composite laminates is proposed in Chapter 4. Continuously varying fibre orientation angles of changing fibre paths are taken into consideration in order to accurately model stiffness variations, with the proposed technique applied to model and analyse composite panels with different fibre paths, and the corresponding results are discussed.

In Chapter 5, the findings from the assessment of various design aspects in terms of the dimensions and energy storage capacity of the flywheel disk are highlighted based on the results obtained from the numerical analysis of the disk. Also, parametric and comparative analyses of various disks are conducted on the basis of different performance-controlling parameters.

A summary of the research outcomes and contributions are highlighted in the final chapter, and suggested areas for future research based on the proposed methodologies identified.

Chapter 2

Modelling of Filament-wound Composite Flywheel Disk

2.1 Overview

A filament-wound spinning composite disk characterised by the mosaic-patterned configuration produced during the filament-winding process consists of curved triangular-shaped repeating units around the circumference of the disk. However, a conventional approach (CA) for structural analyses of composite shells using the mechanics of composite laminates does not consider the manufacturing effects specific to the filament-winding process which could significantly affect the stress and strain fields in thin filament-wound structures. One such effect is the mosaic-patterned configuration of the filament-wound layers which is not usually considered in general stress analysis procedures, including existing FEA packages. Also, a mosaic pattern present in a filament-wound composite flywheel disk could significantly affect the stress fields developed due to rotational loading which cannot be predicted by a conventional modelling technique. Therefore, incorporating a mosaic-patterned configuration in modelling is a significant step towards analysing the mechanical responses of filament-wound structures under different loading conditions. Firstly, conventional FE modelling approaches are discussed and then the modelling of a filament-wound spinning composite disk with different types of filament-winding mosaic-patterned configurations incorporating the actual thickness variations in the disk is demonstrated.

2.2 FE modelling of filament-wound flywheel disk

In comparison with an analytical solution technique, as a FE modelling approach offers several benefits in terms of modelling accuracy, complicated composite lay-ups other than a simple unidirectional laminate can be modelled. Also, as the simplified assumptions required to obtain a closed-form solution in an analytical model are not necessary, a FE approach facilitates in-depth modelling with greater flexibility.

2.2.1 Mosaic-patterned architecture of filament-wound disk

The finished filament-wound composite flywheel disk shown in Figure 1.3 consists of an even number of $\pm\phi$ angle-ply antisymmetric layers [2, 5] composed of two plies with $+\phi(r)$ and $-\phi(r)$ fibre orientation angles to the radius of the disk with an annular band of smooth, continuously turning fibre paths tangent to both its outer and inner peripheries [2, 4] (Figure 1.4).

As the plies are interlaced in the process of helical filament winding, each angle-ply layer has a particular type of repeating filament-winding pattern, as can be seen in Figure 1.3, which consists of curved triangular-shaped two-ply units with alternating $\pm\phi$ and $\mp\phi$ fibre orientations repeated in a chess-board fashion [5-6], with the plies in each not interlaced, and combined into angle-ply antisymmetric laminates. As the units are arranged in a regular geometric pattern around the circumference and along the radius of the filament-wound disk, it comprises multiple numbers of mosaic units of varying sizes depending on the filament-winding parameters. The arrangement of these mosaic units with four units around the circumference and corresponding fibre orientations are shown in Figure 2.1 in which it can be seen that the curved triangular area with $\mp\phi$ fibre orientations (ABD) is surrounded by other areas, such as ABC and DEB that have $\pm\phi$ fibre

orientations. The texture of an angle-ply layer depends on the parameters used in the filament-winding process for the same fibre orientation $\phi(r)$ [5].

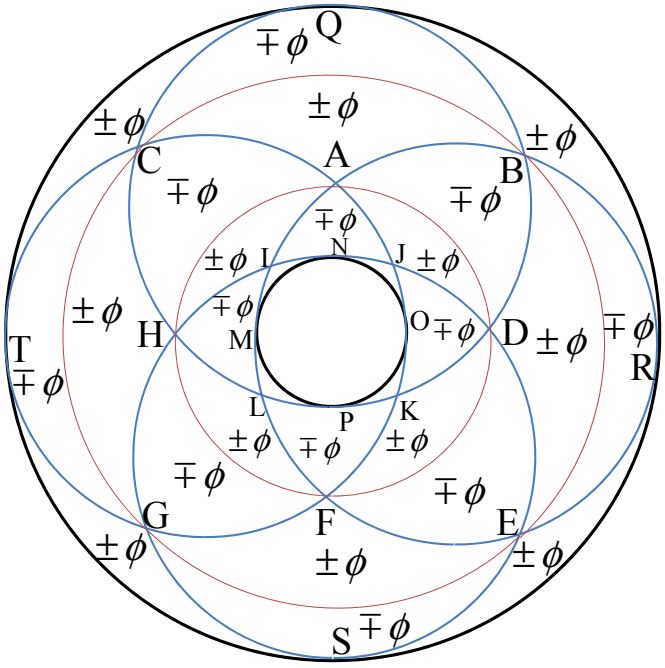

Figure 2.1: Curved triangular mosaic pattern with alternating fibre orientations

2.2.2 Varying fibre trajectories and thickness

Letting a filament-wound composite flywheel disk reinforced with fibres which make angles of $+\phi(r)$ and $-\phi(r)$ with the radius, as shown in Figure 1.4, rotate around its axis with an angular velocity (ω), optimal trajectories of the fibres can be determined using the following process [2, 66]. The radial (N_r) and circumferential (N_β) stress resultants acting on the flywheel disk follow from the corresponding free-body diagram of a disk element shown in Figure 2.2 and can be written in terms of the stresses acting along and across the fibres (σ_1 and σ_2, respectively) and shear stress (τ_{12}) as

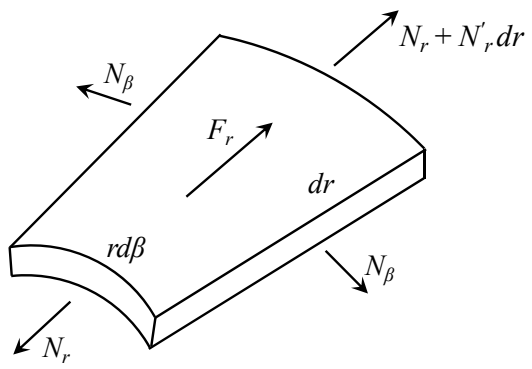

Figure 2.2: Forces acting on disk element

$$N_r = h(\sigma_1 \cos^2 \phi + \sigma_2 \sin^2 \phi - \tau_{12} \sin 2\phi)$$
$$N_\beta = h(\sigma_1 \sin^2 \phi + \sigma_2 \cos^2 \phi + \tau_{12} \sin 2\phi) \tag{2.1}$$

Using the monotropic material model and assuming that transverse (σ_2) and shear (τ_{12}) stresses in the unidirectional ply are zero ($\sigma_2 = \tau_{12} = 0$), we obtain

$$N_r = h\sigma_1 \cos^2 \phi, \qquad N_\beta = h\sigma_1 \sin^2 \phi \tag{2.2}$$

The force (F_r) acting on the disk element shown in Figure 2.2 can be expressed as

$$F_r = \rho h \omega^2 r^2 \tag{2.3}$$

where ρ is the material density.

The equilibrium condition of the forces shown in the disk element in Figure 2.2 yields

$$\frac{d(rN_r)}{dr} - N_\beta + F_r = 0 \tag{2.4}$$

and the disk thickness is specified by

$$h(r) = \frac{kw_o\delta}{2\pi r \cos \phi} \tag{2.5}$$

where k is the number of fibrous tapes passing through the circumference (r = constant), and w_o and δ the tape width and thickness, respectively. The disk thickness varies depending on the values of the radial location (r) and fibre orientation angle (ϕ), as can be observed from Eq. (2.5).

For a disk of uniform strength, $\sigma_1 = (\sigma_1)_{ult}$, where $(\sigma_1)_{ult}$ is the ultimate stress for a unidirectional composite laminate under tension along the fibres, and $\omega = \bar{\omega}$, where $\bar{\omega}$ is the ultimate angular velocity of the disk, are considered.

Substituting Eq. (2.5) in Eq. (2.2) and the obtained stress resultants (N_r and N_β) in Eq. (2.4), the following equation is obtained for the fibres' orientation angles.

$$r\frac{d\phi}{dr}\sin(\phi)\cos(\phi) + \sin^2(\phi) = \frac{1}{(\sigma_1)_{ult}}\rho\bar{\omega}^2 r^2 \tag{2.6}$$

The first order differential in Eq. (2.6) needs to satisfy only one boundary condition to obtain a solution.

For a disk with a radius (R) and central opening with a radius (r_o), as in Figure 1.4, the boundary conditions are $N_r = 0$ at $r = r_o$ and $r = R$. Therefore, taking into account the first expression in Eq. (2.2), we arrive at the boundary conditions

$$\phi(r = r_o) = \frac{\pi}{2},\ \ \phi(r = R) = \frac{\pi}{2} \tag{2.7}$$

Using the 2nd condition from Eq. (2.7), fibre orientation angle (ϕ) in the spinning composite disk [2] can be obtained from the solution to the first-order differential in Eq. (2.6). Solving this equation in MAPLE [67], we obtain

$$\sin\phi = \frac{1}{2}\frac{\sqrt{-2(\sigma_1)_{ult}(-\rho\bar{\omega}^2 r^4 + 4(\sigma_1)_{ult}C_1)}}{(\sigma_1)_{ult}r} \tag{2.8}$$

here C_1 is a constant that needs to be determined using one boundary condition.

Using the second boundary condition from Eq. (2.7), the value of the constant term (C_1) is obtained as

$$C_1 = \frac{1}{4}\left(\frac{\rho\bar{\omega}^2 R^4}{(\sigma_1)_{ult}} - 2R^2\right) \tag{2.9}$$

Using the value of C_1 in Eq. (2.8) we obtain

$$\sin\phi = \frac{1}{2}\sqrt{4\frac{R^2}{r^2}\left(\frac{\rho\bar{\omega}^2R^2}{(\sigma_1)_{ult}}\frac{r^4}{2R^4} - \frac{\rho\bar{\omega}^2R^2}{(\sigma_1)_{ult}}\frac{1}{2} + 1\right)} \tag{2.10}$$

$$\lambda = \frac{\rho\bar{\omega}^2R^2}{(\sigma_1)_{ult}} \tag{2.11}$$

Introducing the constant term in Eq. (2.11) (λ), the final equation for the fibre orientation angle in the filament-wound composite disk with a radius (R) and central opening of a radius (r_o) becomes

$$\sin\phi = \frac{R}{r}\sqrt{1 - \frac{\lambda}{2}\left(1 - \frac{r^4}{R^4}\right)} \tag{2.12}$$

Applying the 1st condition from Eq. (2.7), we arrive at the following equation for specifying the parameter (λ).

$$\lambda = \frac{2}{1 + \left(\frac{r_0}{R}\right)^2} \tag{2.13}$$

Combining Eqs. (2.11) and (2.13) gives the maximum value of the disk's angular velocity as

$$\bar{\omega}^2 = \frac{2(\sigma_1)_{ult}}{\rho R^2\left[1 + \left(\frac{r_0}{R}\right)^2\right]} \tag{2.14}$$

2.3 Modelling of filament-wound $\pm\phi$ angle-ply layers

A filament-wound composite shell usually consists of a number of $\pm\phi$ angle-ply layers wound in a helical pattern onto a mandrel [6], with each layer a combination of two alternating plies with fibre orientation angles of $+\phi$ and $-\phi$ to the shell meridian. These plies are interlaced in the filament-winding process and the resulting angle-ply layer comprises a filament-wound mosaic-patterned configuration.

2.3.1 Conventional approaches

A filament-wound $\pm\phi$ angle-ply layer is usually modelled as a laminated shell utilising the mechanics of composites that takes into consideration the number of plies, stacking sequence and fibre orientation. Two main approaches for modelling angle-ply layers are generally used in a mechanical analysis of filament-wound composite shells [6] and both are widely employed for stress analyses of composite plates and shells using analytical and/or FE solutions.

2.3.1.1 Homogeneous orthotropic $\pm\phi$ angle-ply layer

The first technique assumes that a filament-wound shell is usually composed of a large number of $\pm\phi$ angle-ply layers, with each treated as orthotropic and homogeneous and described by the following set of constitutive equations [2].

$$\begin{aligned} &\sigma_x = A_{11}\varepsilon_x + A_{12}\varepsilon_y, \quad \sigma_y = A_{21}\varepsilon_x + A_{22}\varepsilon_y \\ &\tau_{xy} = A_{44}\gamma_{xy}, \quad \tau_{xz} = A_{55}\gamma_{xz}, \quad \tau_{yz} = A_{66}\gamma_{yz} \end{aligned} \tag{2.15}$$

The stiffness coefficients (A_{mn}) are

$$\begin{aligned} A_{11} &= \bar{E}_1 c^4 + \bar{E}_2 s^4 + 2E_{12}c^2s^2 \\ A_{12} &= A_{21} = \bar{E}_1\nu_{12} + (\bar{E}_1 + \bar{E}_2 - 2E_{12})c^2s^2 \\ A_{22} &= \bar{E}_1 s^4 + \bar{E}_2 c^4 + 2E_{12}c^2s^2 \\ A_{44} &= (\bar{E}_1 + \bar{E}_2 - 2\bar{E}_1\nu_{12})c^2s^2 + G_{12}(c^2 - s^2)^2 \\ A_{55} &= G_{13}c^2 + G_{23}s^2 \\ A_{66} &= G_{13}s^2 + G_{23}c^2 \end{aligned} \tag{2.16}$$

where

$$\bar{E}_{1,2} = \frac{E_{1,2}}{1 - \nu_{12}\nu_{21}}, \quad E_{12} = \bar{E}_1\nu_{12} + 2G_{12}, \qquad c = \cos\phi\,, s = \sin\phi$$

E_1 and E_2 are longitudinal and transverse moduli, ν_{12} and ν_{21} Poisson's ratios ($E_1\nu_{12} = E_2\nu_{21}$), and G_{12}, G_{13} and G_{23} shear moduli of a unidirectional ply.

The thickness of a homogeneous orthotropic layer (h) is double that of a unidirectional ply. The constitutive equations that link the stress resultants and couple them with the

corresponding strains of the reference middle surface of a homogeneous orthotropic laminate are [2, 6]:

$$\begin{aligned} &N_x = B_{11}\varepsilon_x^0 + B_{12}\varepsilon_y^0, \quad N_y = B_{21}\varepsilon_x^0 + B_{22}\varepsilon_y^0, \\ &N_{xy} = B_{44}\gamma_{xy}^0, \quad M_x = D_{11}\kappa_x + D_{12}\kappa_y, \\ &M_y = D_{21}\kappa_x + D_{22}\kappa_y, \quad M_{xy} = D_{44}\kappa_{xy}, \\ &V_x = S_{55}\gamma_x, \quad V_y = S_{66}\gamma_y \end{aligned} \tag{2.17}$$

where the stress resultants and couples are

$$N_x = \int_{-h/2}^{h/2} \sigma_x \, dz, \quad N_y = \int_{-h/2}^{h/2} \sigma_y \, dz, \quad N_{xy} = \int_{-h/2}^{h/2} \tau_{xy} \, dz,$$

$$M_x = \int_{-h/2}^{h/2} \sigma_x z \, dz, \quad M_y = \int_{-h/2}^{h/2} \sigma_y z \, dz, \quad M_{xy} = \int_{-h/2}^{h/2} \tau_{xy} z \, dz,$$

$$V_x = \int_{-h/2}^{h/2} \tau_{xz} \, dz, \quad V_y = \int_{-h/2}^{h/2} \tau_{yz} \, dz$$

and the stiffness coefficients calculated as

$$B_{mn} = A_{mn}h, \quad D_{mn} = A_{mn}\frac{h^3}{12}, \quad S_{mn} = A_{mn}h$$

The strains of the reference surface of a homogeneous orthotropic laminate are in-plane tension or compression (ε_x^0, ε_y^0), in-plane shear (γ_{xy}^0), bending in the xz and yz planes (κ_x, κ_y), twisting (κ_{xy}), and transverse shear (γ_x,γ_y).

2.3.1.2 Antisymmetric balanced $\pm\phi$ angle-ply layer

The second approach deals with the angle-ply layer as an antisymmetric balanced laminate consisting of two $+\phi$ and $-\phi$ unidirectional plies with the same thickness and fibre orientation angles ($+\phi$ and $-\phi$). The constitutive equations for this layer are (considering the mid-plane as the reference surface) [6]

$$
\begin{aligned}
N_x &= B_{11}\varepsilon_x^o + B_{12}\varepsilon_y^o + C_{14}\kappa_{xy} \\
N_y &= B_{21}\varepsilon_x^o + B_{22}\varepsilon_y^o + C_{24}\kappa_{xy} \\
N_{xy} &= B_{44}\gamma_{xy}^0 + C_{41}\kappa_x + C_{42}\kappa_y \\
M_x &= C_{14}\gamma_{xy}^0 + D_{11}\kappa_x + D_{12}\kappa_y \\
M_y &= C_{24}\gamma_{xy}^0 + D_{21}\kappa_x + D_{22}\kappa_y \\
M_{xy} &= C_{41}\varepsilon_x^0 + C_{42}\varepsilon_y^0 + D_{44}\kappa_{xy} \\
V_x &= S_{55}\gamma_x + S_{56}\gamma_y, \quad V_y = S_{65}\gamma_x + S_{66}\gamma_y
\end{aligned}
\tag{2.18}
$$

where the stiffness coefficients are calculated as

$$B_{mn} = A_{mn}h, \;\; C_{mn} = -\frac{h^2}{4}A_{mn}, \;\; D_{mn} = \frac{h^3}{12}A_{mn} \;\; (h = 2\delta)$$

The coefficients characterising the transverse shear (S_{55}, S_{66}, and $S_{56} = S_{65}$) are calculated in terms of A_{55}, A_{66} and $A_{56} = A_{65} = (G_{13} - G_{23})cs$ [2]. The set of stiffness coefficients from Eq. (2.16) should include the following coefficients.

$$
\begin{aligned}
A_{14} = A_{41} &= [\bar{E}_1 c^2 - \bar{E}_2 s^2 - E_{12}(c^2 - s^2)]cs \\
A_{24} = A_{42} &= [\bar{E}_1 s^2 - \bar{E}_2 c^2 + E_{12}(c^2 - s^2)]cs
\end{aligned}
\tag{2.19}
$$

In this approach, the layer is treated as anisotropic because the $+\phi$ and $-\phi$ plies are located in different planes with regard to the reference surface.

2.3.2 Actual structure of $\pm\phi$ angle-ply layer

Both techniques mentioned above overlook some effects of a filament-winding manufacturing process on the formation of laminated composite structures. The filament-winding pattern configuration described previously is one such inherited characteristic specific to a composite structure made by filament winding [2, 5-6, 65]. The first technique (Section 2.3.1.1) neglects both the filament-winding mosaic pattern and the anisotropy of the layer as an angle-ply layer is treated as homogeneous orthotropic. Although the anisotropy of an angle-ply layer is reflected in the second approach (Section 2.3.1.2), the real texture of a filament-wound layer is not taken into account, that is, the interlacing of

filaments in the winding process is neglected. Furthermore, an angle-ply layer is considered to be composed of two plies in which the $+\phi$ ply is placed on top of the $-\phi$ ply or vice versa. Although this model works well for a laminated composite plate, it overlooks the actual construction which contains alternating triangular-shaped areas as a result of the interlacing of unidirectional plies [6].

As previously discussed, the real angle-ply layers of a filament-wound composite flywheel disk are composed of triangular-shaped repeating mosaic-patterned units placed around its circumference and along its radius. Each unit consists of two plies with either a $[+\phi/-\phi]$ or $[-\phi/+\phi]$ structure which are not interlaced within a unit area. The difference between alternating units of two different layer structures are in the stiffness coefficients (A_{14}, A_{24} and A_{56}) responsible for the anisotropic behaviour of an angle-ply layer [6]. Consequently, two alternating mosaic-patterned units exhibit antisymmetric stretching-twisting and bending-shear coupling effects. For an antisymmetric angle-ply laminate, the stretching stiffnesses (B_{11}, B_{12}, B_{22}, B_{44}) and bending stiffnesses (D_{11}, D_{12}, D_{22}, D_{44}) are independent of the number of layers and there is coupling neither between the tension and shear ($B_{14} = B_{24} = 0$) nor the bending and twisting ($D_{14} = D_{24} = 0$). However, an antisymmetric angle-ply laminate shows coupling between the tension and twisting (C_{14}, C_{24}) and shear and twisting. These couplings decrease progressively as the number of layers increases (C_{14} and C_{24} are inversely proportional to the number of layers) [68]. As this coupling between the stretching and bending does not exist in symmetric laminates, nonsymmetric laminates need to be employed for certain applications; for example, the stretching-bending coupling may be necessary in the design of a turbine blade with a warped profile that twists under centrifugal forces. Also, in some other cases, such as robotic parts undergoing complicated deformation under simple loading and airplane wings twisting under bending, it is necessary for the layers to possess different orientations [2,

68]. An antisymmetric angle-ply laminate is formed from an even number of layers the thickness distribution of which is symmetric and the distribution of the orientations of the axes is antisymmetric with respect to the middle plane. The existence of a stretching-twisting coupling in an antisymmetric angle-ply laminate results from the coefficients C_{14} and C_{24}.

2.3.3 Coordinate systems used for FE modelling

In different steps of the FE modelling and analysis of a filament-wound spinning composite disk, different types of coordinate systems need to be utilised to obtain accurate results in a proper coordinate system. Primarily, a cylindrical coordinate system is required for modelling a composite disk using ANSYS [69], with the following coordinate systems used to model and analyse a filament-wound spinning composite disk, as illustrated in Figure 2.3.

- **Local coordinate system** – user-defined coordinate system with a certain rotation of the working plane with respect to the *x*, *y* or *z* axis of the global coordinate system or with movement of its origin.
- **Element coordinate system** – local coordinate system for each element which helps in orienting elements along the axes while maintaining a certain angle with respect to the global coordinate system.
- **Layer coordinate system** – local coordinate system for each lamina in which the *x* axis is along the fibre and the *y* axis perpendicular to the fibre direction. The fibre orientation angle given in the 'section data' when modelling a composite is actually the angle between the *x* axes of the element coordinate and layer coordinate systems.

- **Result coordinate system** – helps to list the results based on the radial/angular or axial location. For a composite laminate, the results in this system represent the stresses along and across the fibres, and the shear stress.

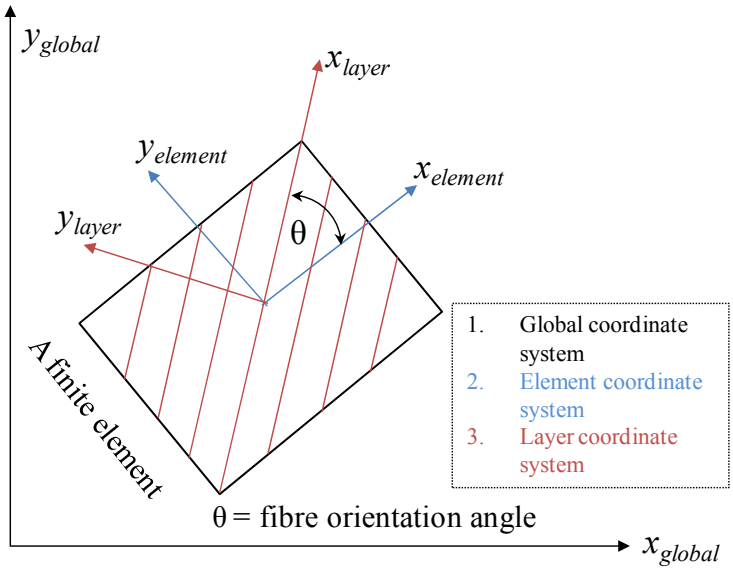

Figure 2.3: Different coordinate systems in ANSYS for modelling composites

Firstly, a filament-wound flywheel disk is modelled using the cylindrical coordinate system. Then, a defined cylindrical local coordinate system is assigned as the element coordinate system for the subsequently defined elements which allows the fibre orientation angles of the disk to be calculated using the radial distance of the centroid of each element from the disk's centre (Figure 1.4).

2.4 Development of FE models of filament-wound disk

2.4.1 Modelling varying fibre paths

In order to investigate the effect of a filament-winding mosaic pattern, stress analyses of a filament-wound composite flywheel disk with different numbers of mosaic-patterned units around its circumference are performed. Each layer of the disk with a radius R and central opening with a radius r_o is reinforced along radially varying fibre orientation trajectories ($\phi(r)$) defined in accordance with Eqs. (2.12) and (2.13), with the thickness of

the disk calculated using Eq. (2.5). In the FE modelling of the disk using ANSYS, the fibre angles as well as thickness of each FE are determined from corresponding equations with the help of the radial location of the element's centroid from the centre of the disk model. Based on these properties provided during the modelling phase, ANSYS automatically maps thickness variations.

2.4.2 Modelling thickness variation

The FE modelling of a filament-wound composite flywheel disk with different numbers of mosaic-patterned units around its circumference is performed taking into account actual thickness variations. Three designs composed of 4, 8 and 14 plies are considered to demonstrate the changes in stress levels in different layers and the extent of the influence of ply-interlacing. Although the overall thickness of the disk is determined in accordance with Eq. (2.5), the total thickness values at both its inner (h_{r_o}) and outer (h_R) radii cannot be determined using this equation as the fibre orientation angles at these locations are obtained as 90^0 from Eq. (2.12). Therefore, for the three designs chosen for the FE modelling of the disk, constant values are assumed up to the distance w_o from its inner and outer edges (i.e., $h(r = r_o) = h(r = r_o + w_o) = h_{r_o}$ and $h(r = R) = h(r = R - w_o) = h_R$). The approximate variations of the thickness according to Eq. (2.5) along a radial cross-section of the disk for chosen values of w_o, δ and k from Tables 2.1 and 2.2 are presented in Figure 2.4 for the three designs. The total thickness values at the inner (h_{r_o}) and outer (h_R) radii and corresponding numbers of plies are given in Table 2.1, with the corresponding FE models of the disk shown in Figure 2.5.

Table 2.1: Different thickness values and corresponding numbers of plies

Number of plies (n)	k	h_{r_o} (m)	h_R (m)
4	484	1.0×10^{-2}	0.4×10^{-2}
8	968	2.0×10^{-2}	0.8×10^{-2}
14	1694	2.6×10^{-2}	1.5×10^{-2}

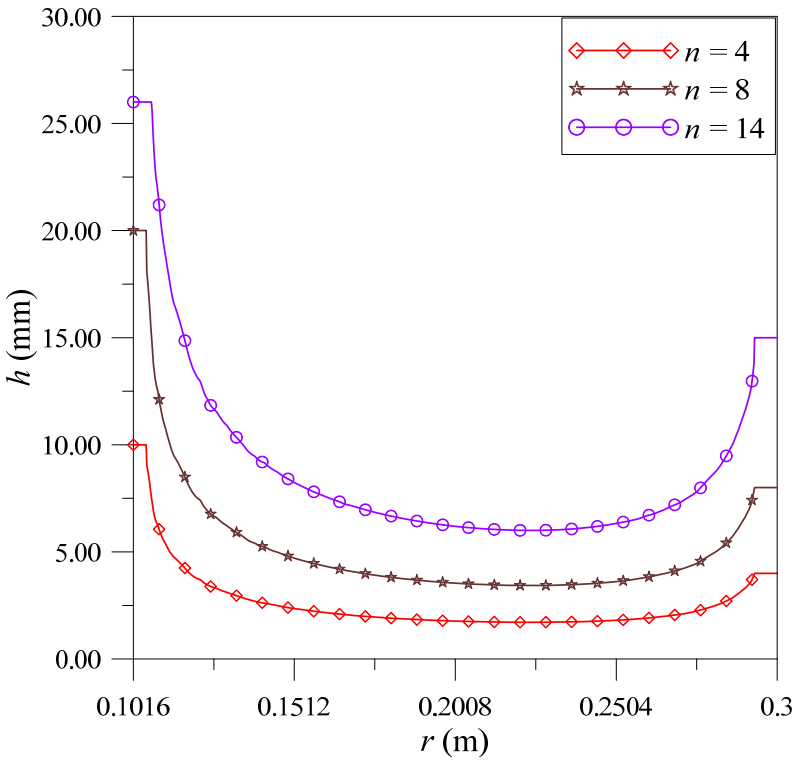

Figure 2.4: Variations of thickness in three models of filament-wound flywheel disk

Table 2.2: Dimensions and material properties of filament-wound disk

Dimensions	Material	Properties
Outer radius (R) = 0.30 m Inner radius (r_o) = 0.1016 m	IM6 – Epoxy (Carbon–Epoxy)	E_1 = 203.00 GPa E_2 = 11.20 GPa G_{12} = 8.40 GPa
$w_o = 4.00\times10^{-3}$ m $\delta = 0.70\times10^{-3}$ m	Density – 1600 kg/m^3	$\nu_{12} = 0.32$

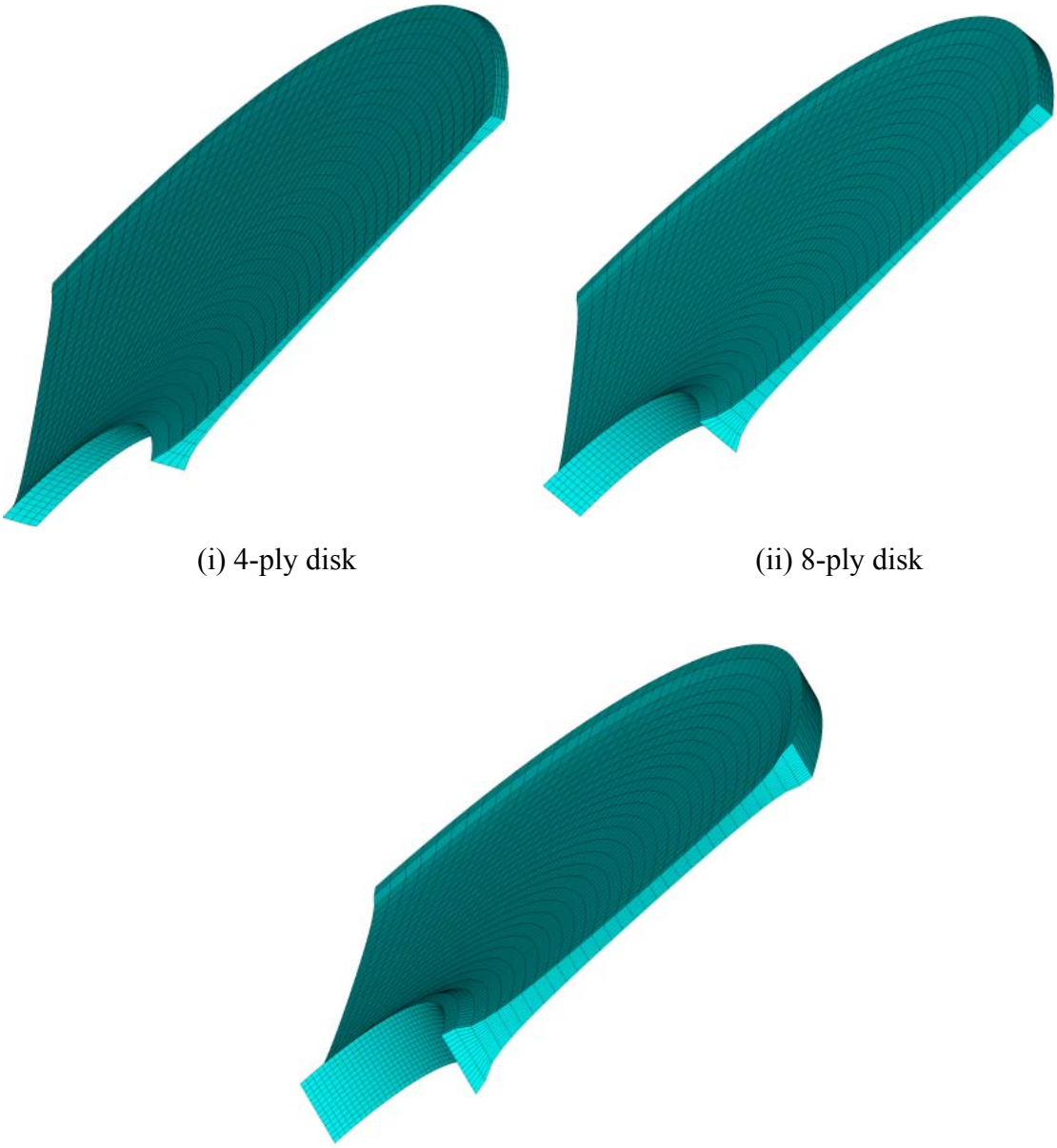

(i) 4-ply disk (ii) 8-ply disk

(iii) 14-ply disk

Figure 2.5: Three thicknesses chosen for modelling filament-wound disk

2.4.3 Modelling mosaic-patterned architecture

2.4.3.1 Elements for modelling laminated composites

Both the development of the FE model and analyses of the filament-wound composite flywheel disk are performed using ANSYS which has SHELL181, SHELL281, SOLSH190, SOLID185 and SOLID186 elements in its element library for modelling

layered composite materials. The disk is modelled using both SHELL181 and SHELL281 elements with the process governed by the first-order shear deformation theory.

SHELL181 is suitable for analysing thin to moderately-thick shell structures. It is a four-nodal element with six degrees of freedom at each node, translations in the x, y and z directions, and rotations about the x, y and z axes, with a full integration scheme used in the FE modelling. On the other hand, SHELL281 has eight nodes each with six degrees of freedom.

Then, the layered configuration of the filament-wound composite flywheel disk is defined after selecting these elements.

2.4.3.2 Conventional approach (CA) for modelling filament-wound disk

Firstly, using a CA, the filament-wound flywheel disk is modelled as a laminated circular plate composed of different numbers of plies (Figure 2.6(i)). The 4-ply disk (Figure 2.5(i)) comprises four plies $[+\phi(r)/-\phi(r)]_s$ and the 8-ply (Figure 2.5(ii)) and 14-ply (Figure 2.5(iii)) disks are composed of eight plies $[+\phi(r)/-\phi(r)/+\phi(r)/-\phi(r)]_s$ and fourteen plies $[+\phi(r)/-\phi(r)/+\phi(r)/-\phi(r)/+\phi(r)/-\phi(r)/+\phi(r)]_s$, respectively, with the middle plane taken as the reference plane. As, in the conventional model, the interlacing of plies due to the filament-winding process is not considered, each ply has a fibre orientation angle of either $+\phi(r)$ or $-\phi(r)$ all over the disk.

2.4.3.3 Modified approach for modelling mosaic-patterned architecture

A CA clearly does not correctly reflect the real structure of a filament-wound composite flywheel disk since a filament-winding mosaic-patterned architecture realised due to the interlacing of plies, and, subsequently, the anisotropy of the antisymmetric angle-ply structures of the units are neglected. In order to model the mosaic-patterned structure, the disk is partitioned into mosaic units and, corresponding FEs are combined into respective

alternating groups. The composite material for the FEs of each group is defined as either $[+\phi(r)/-\phi(r)/+\phi(r)/-\phi(r)]$ or $[-\phi(r)/+\phi(r)/-\phi(r)/+\phi(r)]$ laminate for the 4-ply disk (Figure 2.5(i)), either $[(+\phi(r)/-\phi(r))_4]$ or $[(-\phi(r)/+\phi(r))_4]$ for the 8-ply disk (Figure 2.5(ii)) and either $[(+\phi(r)/-\phi(r))_7]$ or $[(-\phi(r)/+\phi(r))_7]$ for the 14-ply disk (Figure 2.5(iii)).

2.4.3.4 Models of filament-wound flywheel disk

Four, six and eight mosaic units around the circumferences of three designs (4, 8 and 14 plies) of a filament-wound flywheel disk are considered for modelling the mosaic-patterned configuration and the corresponding FE models are shown in Figure 2.6(ii-iv), respectively. As previously mentioned, the number of mosaic units in a filament-wound ply is determined by the selection of appropriate manufacturing parameters for the filament-winding process.

For modelling the different numbers of mosaic-patterned units around the circumferences of the flywheel disk's models, various element sizes are specified for the corresponding areas to represent the mosaic units all over the disk. The element sizes and corresponding total numbers of elements chosen for the different models are listed in Table 2.3. It should be noted that a large number of elements is obtained from meshing in order to more accurately approximate the varying fibre trajectories and, thereby, attain the closest possible fibre orientation angles which are assigned to different elements. Although the ANSYS mesher cannot produce a mapped mesh for mosaic-patterned models, all elements are maintained as quadrilateral rather than triangular. However, for the conventional modelling of the disk, a mapped mesh is ensured by defining a fixed number of elements along its circumference.

For each unit, the layer configuration through the thickness of the disk is defined as a layer-by-layer assembly from the bottom (layer 1) to the top of the reference plane in the positive direction of the coordinate normal to the reference plane.

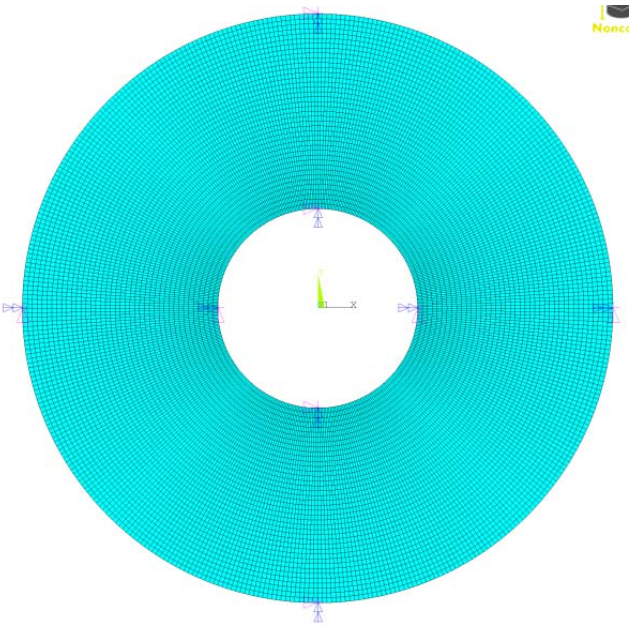

(i) Conventional model

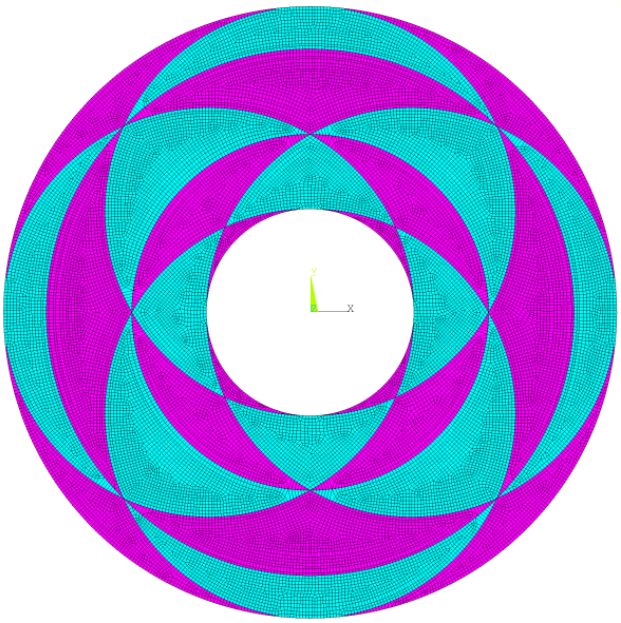

(ii) 4–unit model

Figure 2.6: (i) Conventional, (ii) 4-unit, (iii) 6-unit and (iv) 8-unit FE models

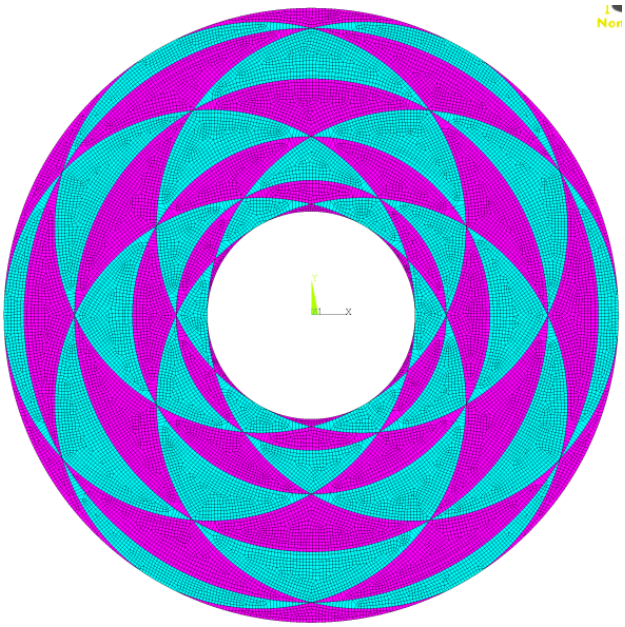

(iii) 6–unit model

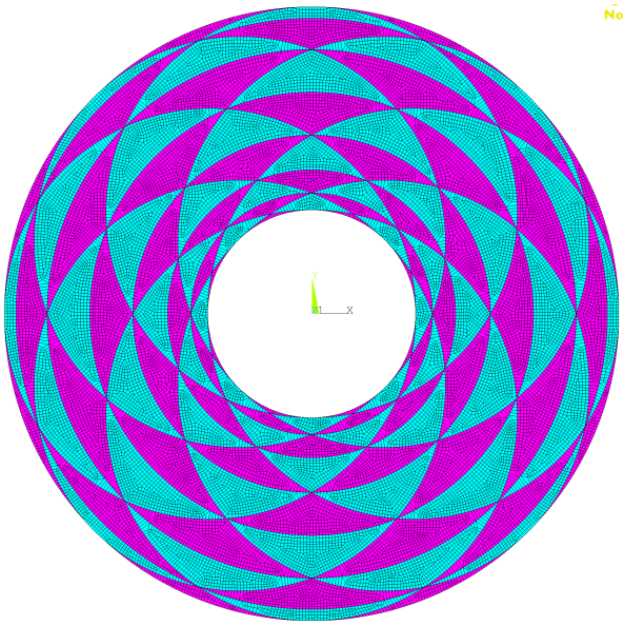

(iv) 8–unit model

Figure 2.6: (i) Conventional, (ii) 4-unit, (iii) 6-unit and (iv) 8-unit FE models

(*continued*)

Table 2.3: Total numbers of elements for various element sizes used in meshing models of filament-wound flywheel disk

Disk model	Element sizes (m)		Total numbers of elements
	Minimum	Maximum	
4-unit	0.0025	0.0031	26964
6-unit	0.0030	0.0031	27009
8-unit	0.0028	0.0030	28541
Conventional	-	-	28800

2.5 Chapter summary

A methodology for the FE modelling of a filament-wound composite flywheel disk performed using ANSYS and governed by the first-order shear deformation theory is presented. Different types of filament-winding mosaic patterns are incorporated in the disk's models. Also, the disk is modelled using a CA in order to show the difference in stress values predicted by both FE techniques through distributions of various stresses. Modelling the filament-wound disk as a laminated circular plate composed of different numbers of plies using a CA does not capture the interlacing of the plies developed during the filament-winding process. Alternatively, three designs composed of 4, 8 and 14 plies are chosen to model the mosaic-patterned structure, each of which is associated with three types of mosaic-patterned configurations, namely 4, 6 and 8 mosaic units around the circumference of the disk, with the actual thickness variations of the disk taken into consideration. As the methodology outlined in this chapter will be advantageous for building FE models of other filament-wound structures, incorporating a mosaic-patterned architecture produces more realistic responses of filament-wound structures under various types of loadings.

Chapter 3

Stress Analyses of Filament-wound Composite Flywheel Disk

3.1 Overview

Due to spinning filament-wound composite flywheel disks being used in a wide range of practical engineering applications, accurately determining the stresses that develop in them is very important for an efficient design. Therefore, using the methodology discussed in Chapter 2, structural analyses of such a disk, taking into account the effect of its mosaic-patterned architecture on its stress states are presented in this chapter.

The results obtained from stress analyses of a filament-wound flywheel disk are compared with those calculated using a conventional method and the differences between them demonstrated through the distributions of various stresses. As observed, because the stress levels in a thin filament-wound composite flywheel disk could be underestimated in a structural analysis using the conventional mechanics of laminated structures, manufacturing effects, such as the mosaic-patterned units located around the disk's circumference, should be incorporated in FE modelling and analysis.

3.2 Model validation

A flywheel comprising a rotor and hub, assembled by maintaining an interference fit between them, acts as a kinetic energy storage and retrieval device designed to deliver high output power at high rotational speeds. A model of an annular solid flywheel rotor is shown

in Figure 3.1. A flywheel energy storage (FES) system is an emerging energy storage technology being utilised in various advanced engineering applications.

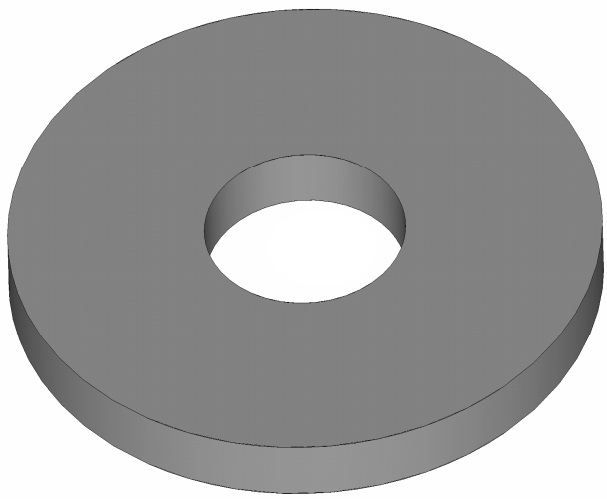

Figure 3.1: Model of annular rotating disk

For the development of a flywheel fabricated using advanced composite materials, the main focus is on improving its performance (energy storage capability) while ensuring safety during its operation. As a flywheel undergoes high rotational speeds during its service life, to ensure safety, the stress levels developed under different loading conditions need to be accurately determined on the basis of the strengths of the fabricating materials as a crucial step in the design of a flywheel system. In this chapter, firstly, the processes involved in a stress analysis of the filament-wound flywheel disk using a FEA technique are checked and verified for an isotropic flywheel using available analytical solutions for the stresses developed in it.

3.2.1 Analytical solutions for stresses in spinning annular isotropic disk

Considering the annular disk shown in Figure 3.2 that undergoes rotation at a constant angular velocity (ω) with no internal or external pressure applied, equations for the stresses developed in it can be derived using some conditions [70-71].

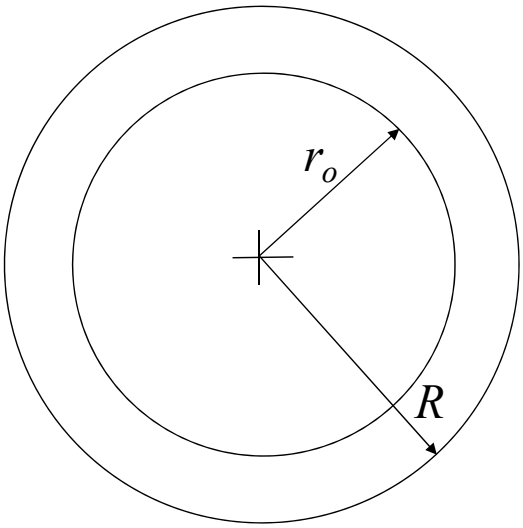

Figure 3.2: Dimensions of annular disk

Applying the condition that the radial stress (σ_r) would be zero because of the absence of any pressure load at either the inner or outer radius yields

$$\sigma_r = \frac{3+\nu}{8}\rho\omega^2\left[r_o^2 + R^2 - \left(\frac{Rr_o}{r}\right)^2 - r^2\right] \tag{3.1}$$

where r_o and R are the inner and outer radii, respectively.

The tangential stress (σ_θ) developed due to rotation is

$$\sigma_\theta = \frac{3+\nu}{8}\rho\omega^2\left[r_o^2 + R^2 + \left(\frac{Rr_o}{r}\right)^2 - \frac{1+3\nu}{3+\nu}r^2\right] \tag{3.2}$$

The maximum radial stress occurs at $r = \sqrt{Rr_o}$, where its value is

$$(\sigma_r)_{max} = \frac{3+\nu}{8}\rho\omega^2(R^2 - r_o^2) \tag{3.3}$$

The maximum tangential (hoop) stress occurs at the inner surface, where $r = r_o$ and is expressed as

$$(\sigma_\theta)_{max} = \frac{\rho\omega^2}{4}[(3+\nu)R^2 + (1+\nu)r_o^2] \tag{3.4}$$

3.2.2 FE modelling and analysis of isotropic disk

To demonstrate the FE modelling of a spinning flywheel disk, firstly, an annular isotropic disk is modelled and analysed. Due to its symmetry, only a quarter of its geometry

is modelled using the commercial FEA package ANSYS under the plane stress condition. The dimensions of the disk and the material properties used for this analysis are given in Table 3.1 in which E is Young's modulus, G shear modulus and ν Poisson's ratio.

Table 3.1: Dimensions and material properties of annular isotropic flywheel disk

Dimensions	Material	Properties
Outer radius (R) = 0.30 m Inner radius (r_o) = 0.1016 m	AISI 1006 steel (cold drawn)	E = 205 GPa G = 80 GPa
Thickness = 0.0508 m	Density = 7872 kg/m^3	ν = 0.29

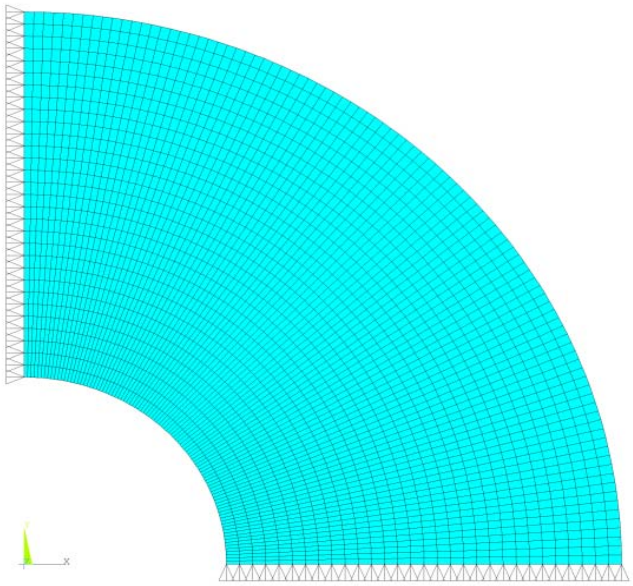

Figure 3.3: FE model of quarter of annular isotropic disk

The annular disk is modelled using a 2D four-nodal structural solid element, PLANE182, with the symmetry boundary condition applied at both edges of the quarter model (Figure 3.3) and the disk rotated about its central axis at a constant speed of 5,000 rpm.

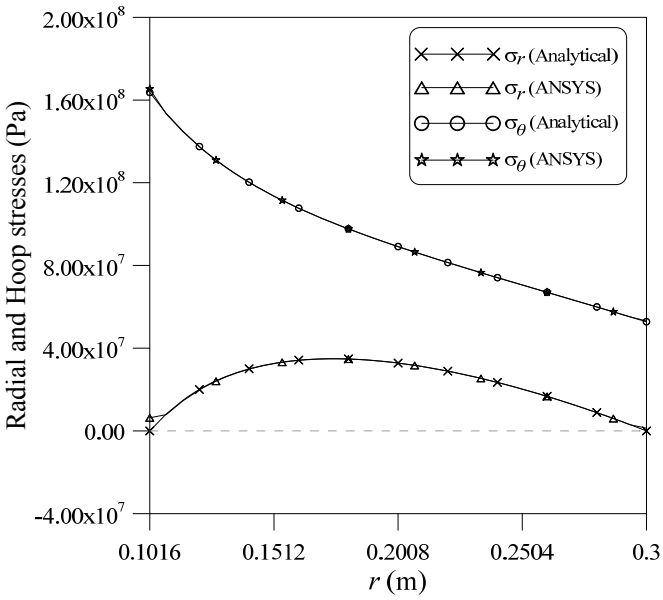

Figure 3.4: Distributions of σ_r and σ_θ in rotating annular isotropic disk

Distributions of the radial and tangential (or hoop) stresses along the radius of the isotropic annular disk are determined using a FEA technique, with its results and those obtained from an analytical solution illustrated in Figure 3.4 which shows that they closely match. However, the FE technique predicts comparatively smaller rather than zero radial stress values at both the inner and outer radii of the rotor due to the selected element's failure to capture zero stress values at these locations under given mesh conditions, with the maximum radial stress occurring at a position between the inner and outer surfaces of the rotor. The analytical solution predicts the location of the maximum radial stress developed at a radial distance of 0.174 m which is also confirmed by the result predicted by the FEA. Similarly, the maximum hoop stress occurs at the inner radius and gradually decreases towards the outer radius of the rotor, with the hoop stress developed due to rotation of the annular disk higher than the radial stress. Based on a comparison of the stresses predicted by both methods, as it can be concluded that the procedures followed for the FEA of the spinning annular isotropic disk are correct, they can be extended further for the analysis of a filament-wound composite flywheel disk.

The radial and tangential stress distributions calculated using ANSYS for the spinning annular isotropic disk are illustrated by contour plots shown in Figures 3.5 and 3.6, respectively, which clearly show the locations of both the maximum and minimum values of the calculated stresses.

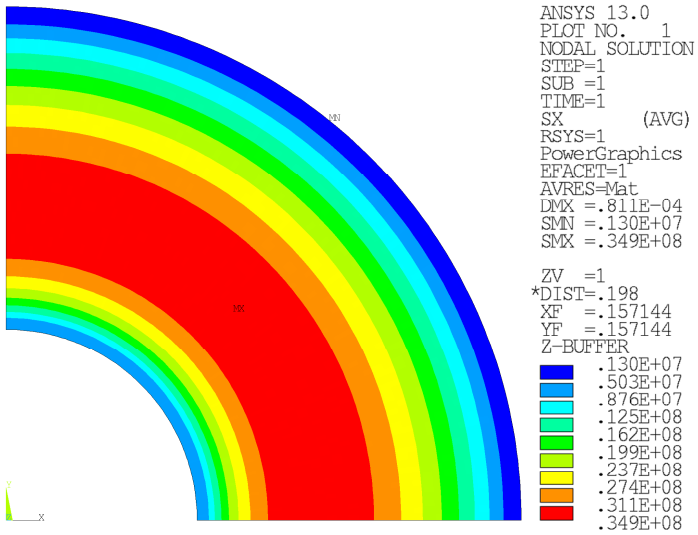

Figure 3.5: Contour plot of σ_r in annular isotropic disk

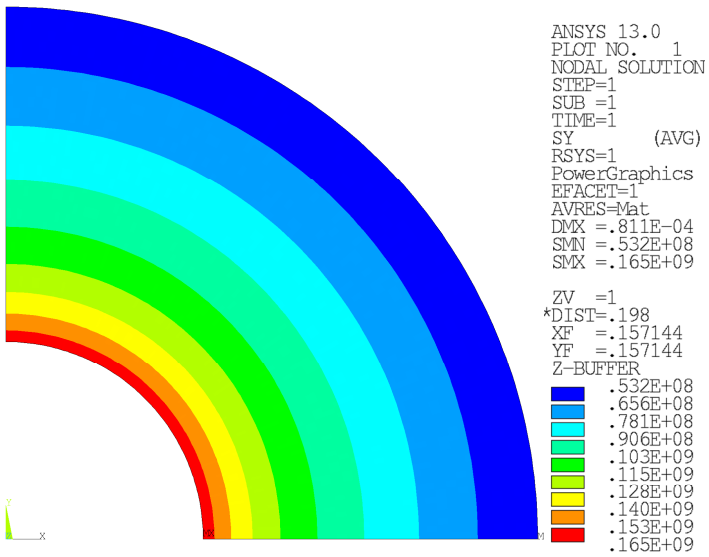

Figure 3.6: Contour plot of σ_θ in annular isotropic disk

3.3 Stress analyses of filament-wound flywheel disk

As discussed in Chapter 2, using a conventional approach for modelling and analysing a filament-wound structure not only overlooks its mosaic-patterned configuration but also assumes its thickness to be constant by ignoring the actual variations generated during the filament-winding process. Therefore, stress analyses of a filament-wound flywheel disk are performed by, firstly, taking into account a constant thickness and then incorporating actual varying thicknesses in FE models of the disk.

3.3.1 Mosaic-patterned models with constant thickness

In order to investigate the effect of the filament-winding mosaic pattern, a 2D FEA of a filament-wound composite flywheel disk with 4 and 6 mosaic units around its circumference is performed using the plane stress condition to determine its stresses. The resultant 4- and 6-unit FE models shown in Figure 2.6 (ii-iii) are composed of 4 plies which are reinforced along the radially varying fibre trajectories defined in Eqs. (2.12) and (2.13) for a disk of a radius (R) with central opening of a radius (r_o), and the composite spinning disk modelled using the SHELL181 element and governed by the first-order shear deformation theory. The 4-unit model consists of 25,129 elements and the 6-unit 25,181.

3.3.1.1 Stress analysis of disk with constant thickness

In order to investigate the effect of the filament-winding mosaic pattern, FE stress analyses of a conventional and the 4- and 6-unit mosaic-patterned models of a filament-wound composite disk, with the disk rotated about its central axis at a constant angular velocity, are performed.

The dimensions of the filament-wound composite disk considered and material properties used in FE analyses are listed in Table 2.2 (Chapter 2). It should be noted that the constant thickness of the disk which consists of 4 plies is 2.8×10^{-3} m. Displacement and

rotational boundary conditions are applied at the nodes on its inner and outer radii along the *x* and *y* axes (Figure 2.6(i)) of the working plane to prevent in-plane rigid body motions in the radial and circumferential directions and out-of-plane rigid body motion in the axial direction.

The radial (σ_r), tangential (σ_θ) and shear ($\tau_{r\theta}$) stress distributions calculated for the top layer (layer 4) of the models are shown in Figures 3.7-3.9, respectively. As can be seen, those in the models with mosaic patterns differ substantially from those calculated by conventional modelling of a laminated shell. It follows that, in the structure of a real filament-wound disk, the stress levels vary considerably from one mosaic unit to the adjacent ones in both the radial and circumferential directions, as illustrated in Figures 3.10-3.13.

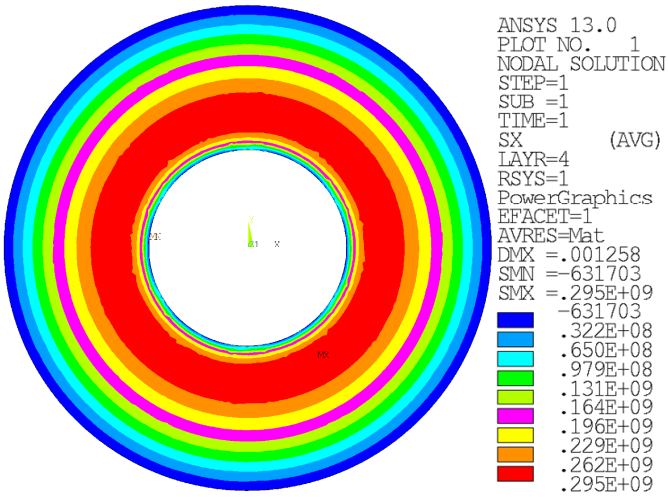

(i) σ_r (conventional model)

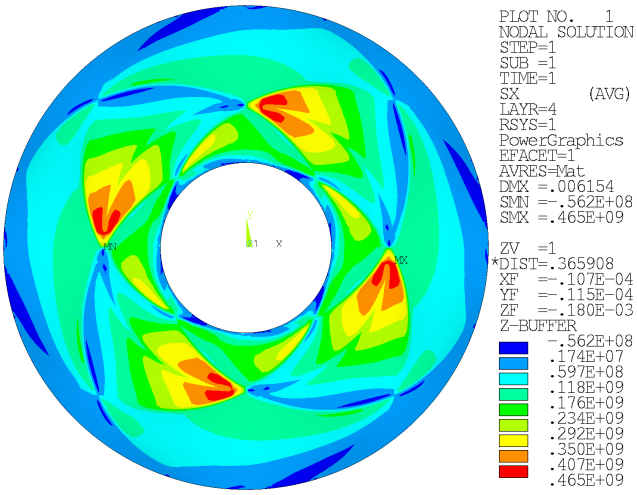

(ii) σ_r (4-unit model)

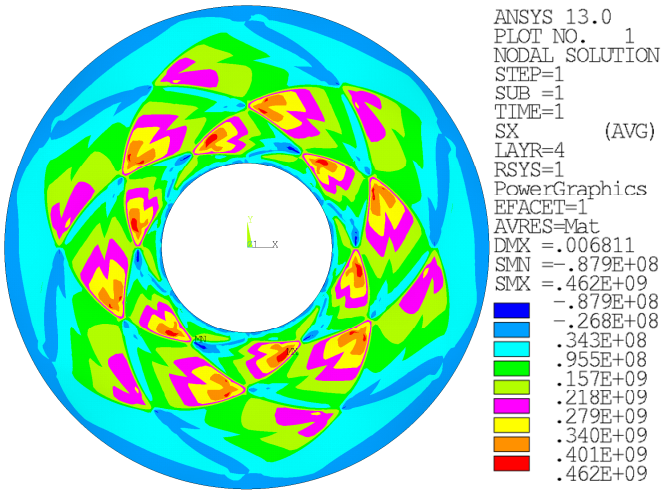

(iii) σ_r (6-unit model)

Figure 3.7: Contour plots of σ_r in spinning filament-wound composite disk models

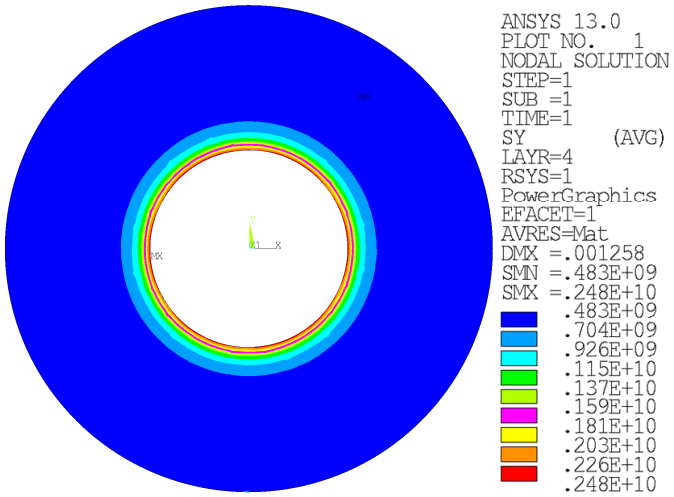

(i) σ_θ (conventional model)

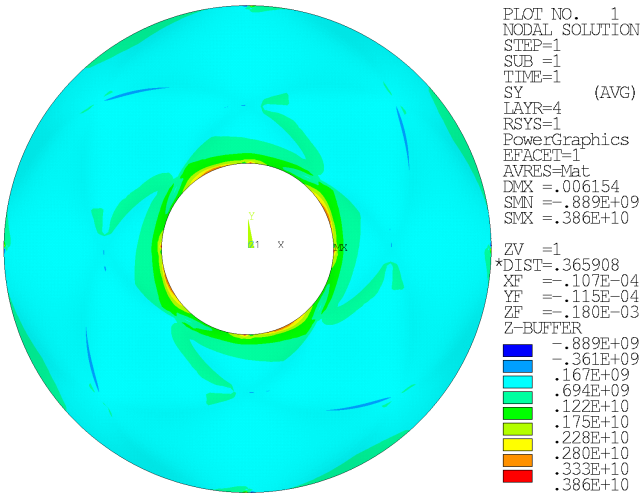

(ii) σ_θ (4-unit model)

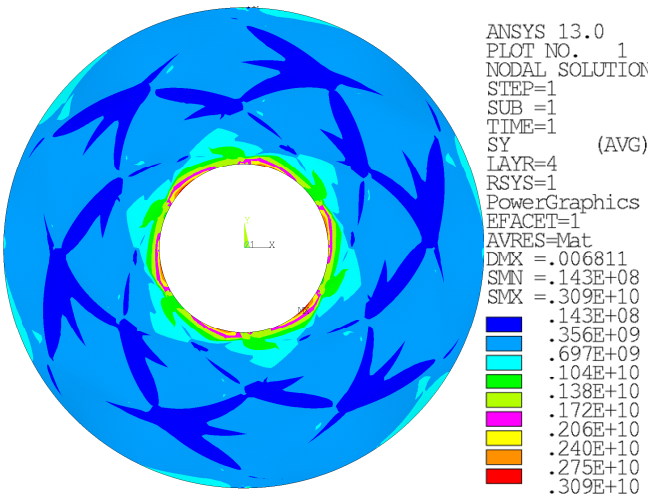

(iii) σ_θ (6-unit model)

Figure 3.8: Contour plots of σ_θ in spinning filament-wound composite disk models

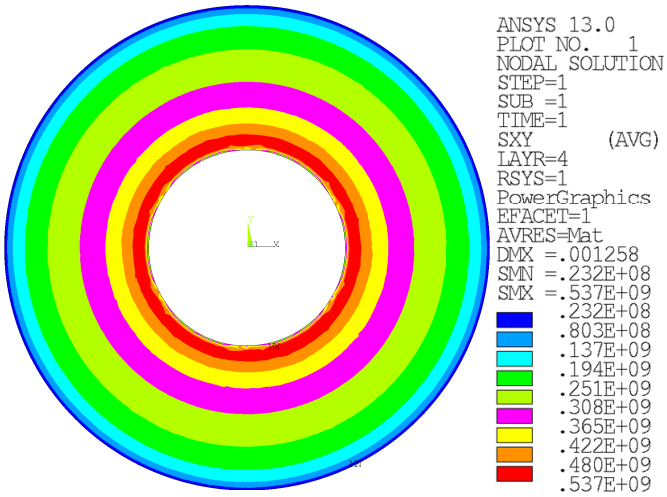

(i) $\tau_{r\theta}$ (conventional model)

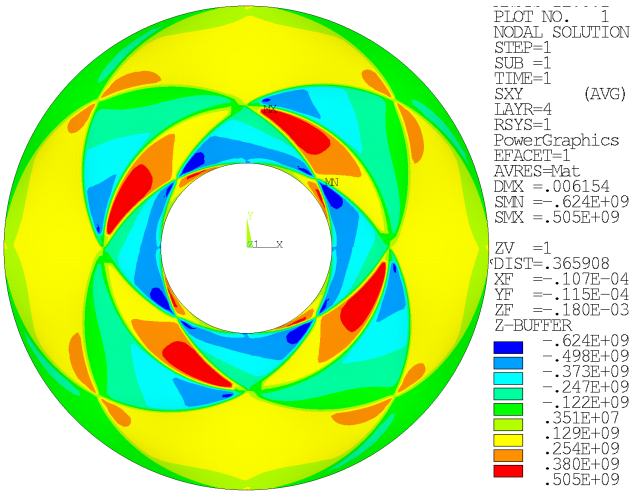

(ii) $\tau_{r\theta}$ (4-unit model)

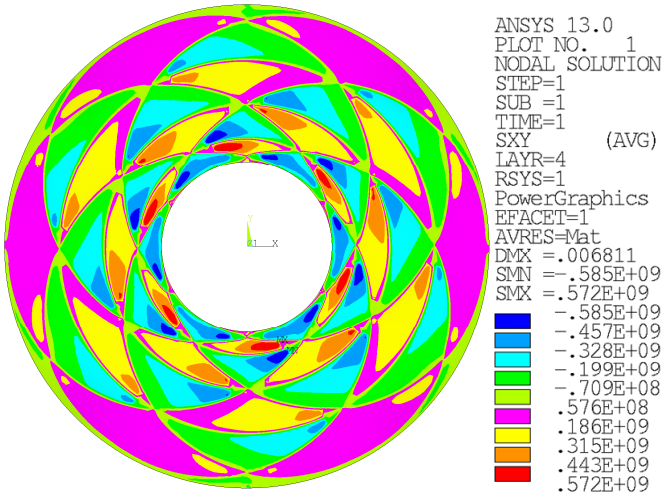

(iii) $\tau_{r\theta}$ (6-unit model)

Figure 3.9**:** Contour plots of $\tau_{r\theta}$ in spinning filament-wound composite disk models

The stress distributions around the circumference of the disk ($0^0 \leq \theta \leq 360^0$) calculated at a radial distance of 0.21644 m are shown for both the 4- (Figure 3.10) and 6-unit (Figure 3.11) models. The two different mosaic units arranged circumferentially in alternating fashion at this radial location are denoted 'Zone A' and 'Zone B' in the stress plots. As can be seen in Figure 2.1 (Chapter 2), if the mosaic unit EBD and other units of the same size are denoted 'Zone A', the unit DBA and other similar units will be denoted 'Zone B'.

The distributions of both the radial (σ_r) and tangential (σ_θ) stresses (Figure 3.10) around the circumference of the disk in the 4-unit model show that their values are substantially different from those determined using the conventional FEA. As an actual mosaic-patterned configuration is not incorporated in conventional modelling, this approach does not predict real variations in the stress values developed in the disk which clearly indicates its limitations for analysing a spinning filament-wound composite disk.

Also, the distributions of both σ_r and σ_θ (Figure 3.11) around the circumference of the 6-unit model demonstrate differences in the calculated stress values from one mosaic unit to the adjacent ones. The circumferential distributions of the stresses along the fibres (σ_1) and across the fibres (σ_2) obtained from analyses using the mosaic-patterned models also reflect the effect of specific mosaic-patterned configurations of a filament-wound structure.

The stress distributions along the radius of the disk in the 4-unit (Figure 3.12) and 6-unit (Figure 3.13) models are plotted for radial cross-sections orientated at 45^0 counter-clockwise from their $+x$ axes. The first mosaic-patterned unit located in this cross-section and connected to the inner radius is denoted 'Zone 1' and the consecutive units numbered sequentially.

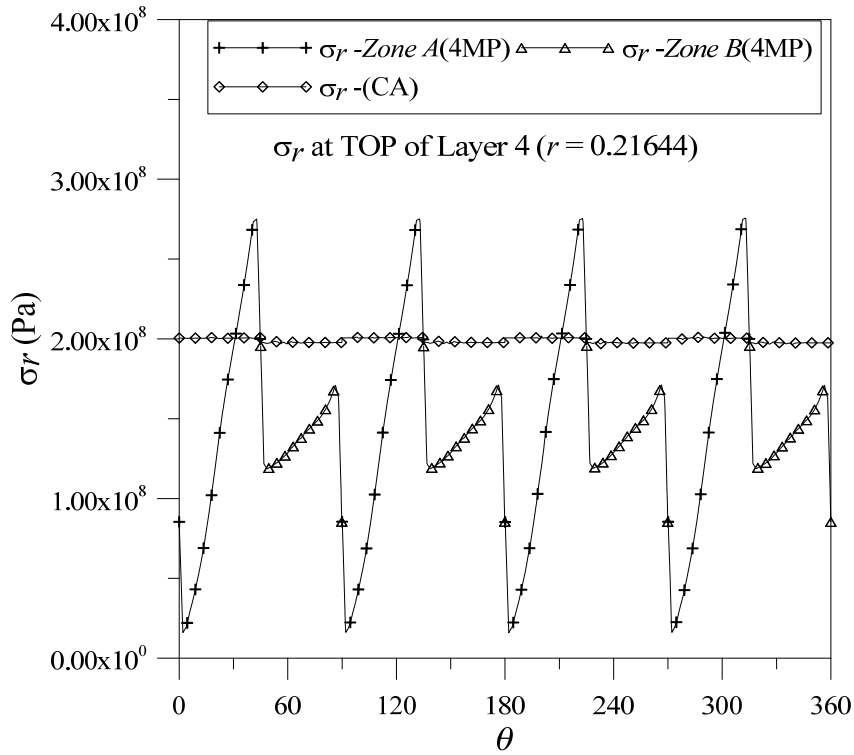

(i)

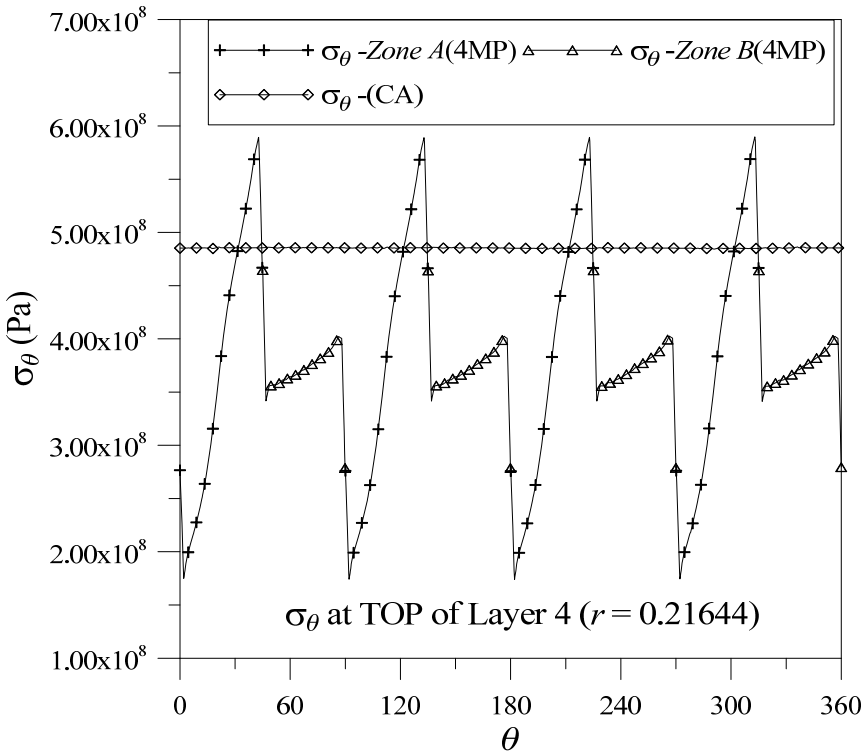

(ii)

Figure 3.10: Distributions of (i) σ_r and (ii) σ_θ around circumference for 4-unit model

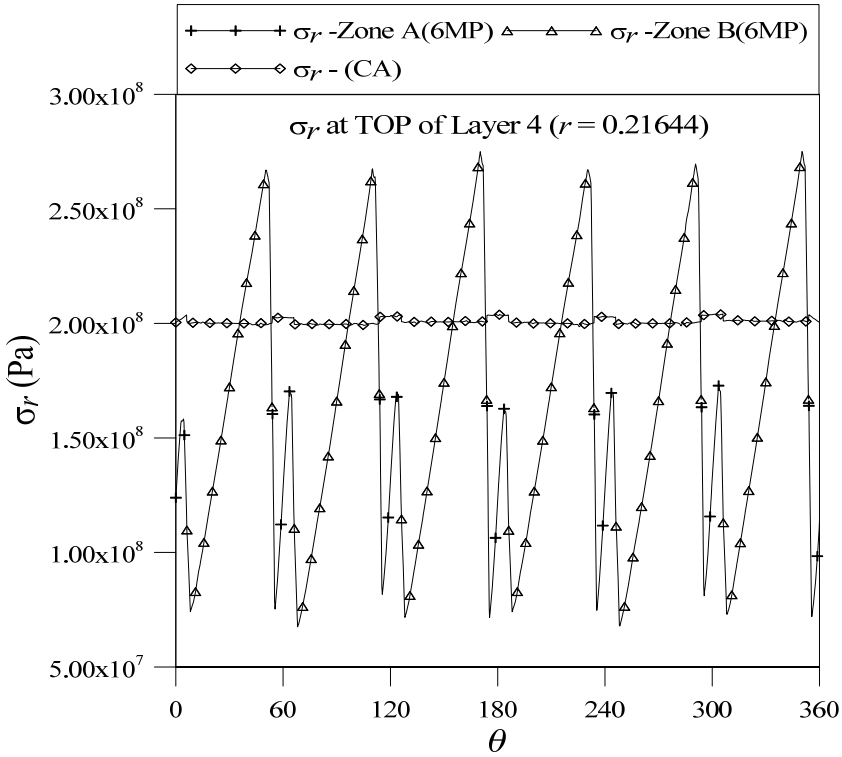

(i)

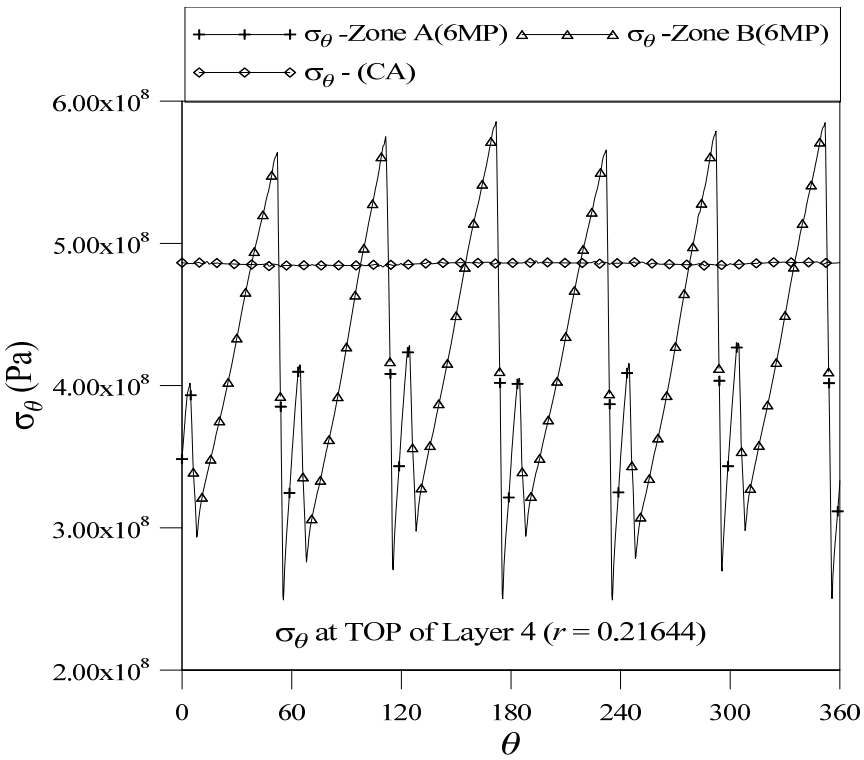

(ii)

Figure 3.11: Distributions of (i) σ_r and (ii) σ_θ around circumference for 6-unit model

Comparisons of the stress distributions in different zones clearly show variations in the stress values obtained from the two different FEA approaches, with the results from the conventional approach not reflecting variations in the values of σ_θ and σ_2 in different mosaic units, as shown in Figure 3.12. The conventional approach predicts higher values of σ_θ and lower values of σ_2 at the selected radial cross-section than those predicted by a model with an actual mosaic-patterned configuration.

Similarly, the distributions of σ_r and σ_1 along the radius of the disk in the conventional and 6-unit models demonstrate differences in the calculated stress values (Figure 3.13). As can be seen, at the chosen radial cross-section, the conventional approach predicts considerably different values of both σ_r and σ_1 than a mosaic-patterned model. It should be noted that, even for other radial sections of the disk, the stresses calculated using a mosaic-patterned model would be substantially different from those predicted by a conventional modelling technique.

The influence of the filament-winding mosaic pattern on the stress states of a spinning filament-wound composite disk with a constant thickness is observed from various stress distributions determined for different locations. The maximum values of the stresses obtained from FE analyses of the disk are presented in Table 3.2 for two numbers of plies (3 and 4) in which it can be seen that the overall maximum stress values (for the whole disk) calculated using the mosaic-patterned models are higher than those obtained using the conventional FEA approach.

Table 3.2: Maximum stresses from FEA in conventional and mosaic-patterned models

Model	σ_r (MPa)		σ_θ (MPa)		$\tau_{r\theta}$ (MPa)		σ_1 (MPa)		σ_2 (MPa)		τ_{12} (MPa)	
Layer	3	4	3	4	3	4	3	4	3	4	3	4
Conv.	293	295	2483	2477	536	547	2487	2486	42	42	100	98
4-unit	587	467	3012	3274	957	633	3096	3348	58	108	115	200
6-unit	628	461	3076	3069	998	601	3166	3066	60	126	108	196

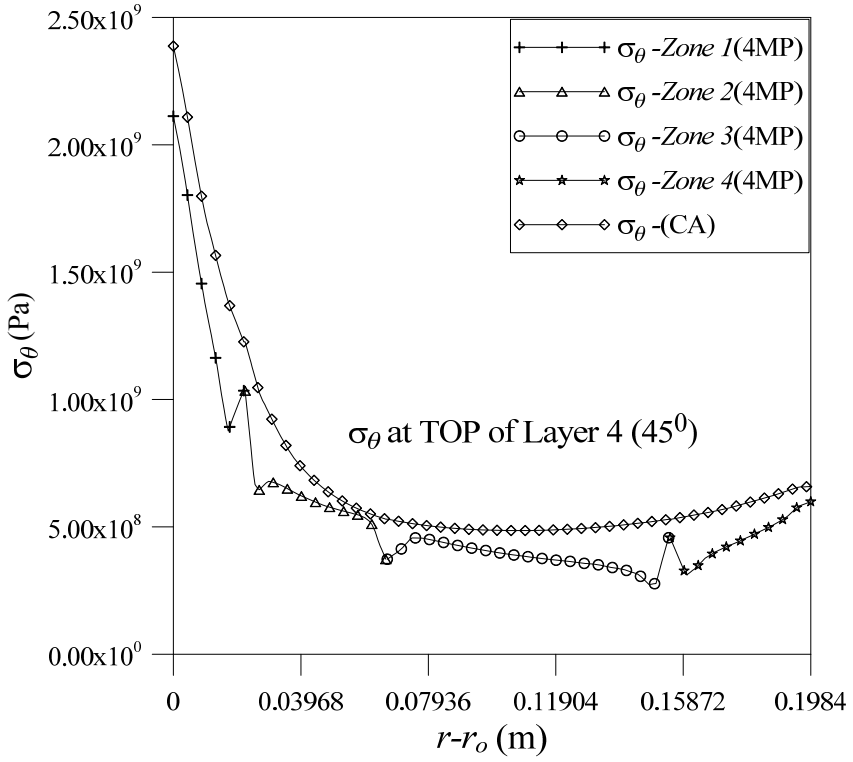

(i)

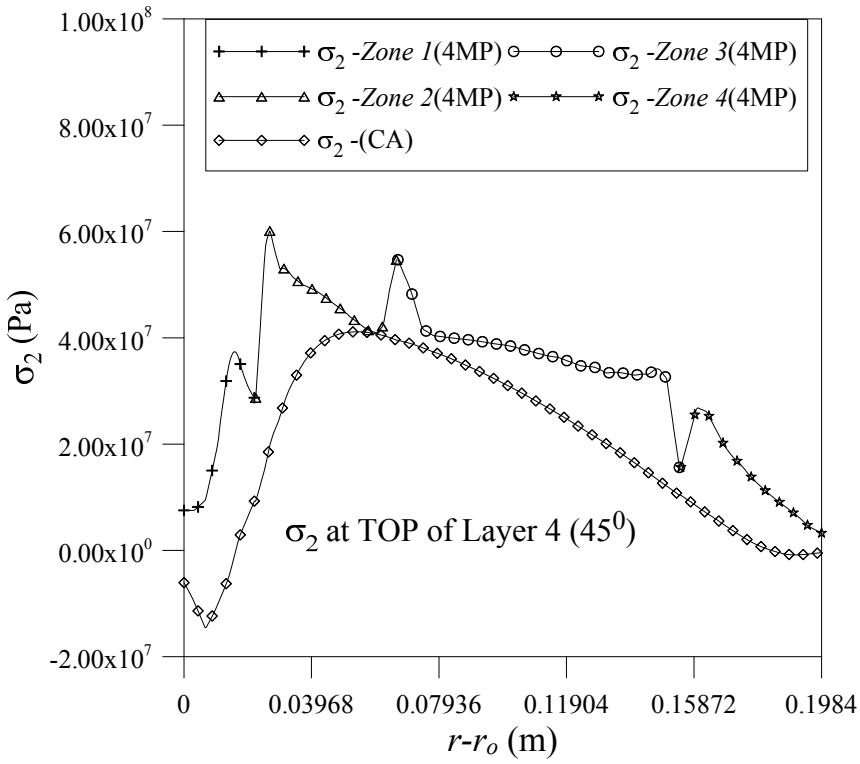

(ii)

Figure 3.12: Distributions of (i) σ_θ and (ii) σ_2 along radius for 4-unit model

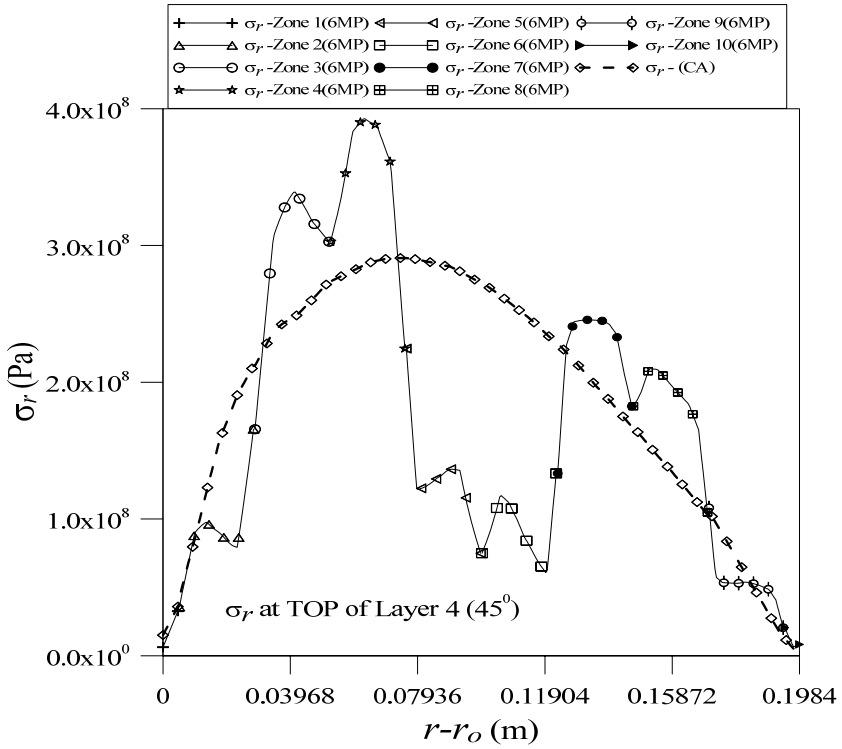

(i)

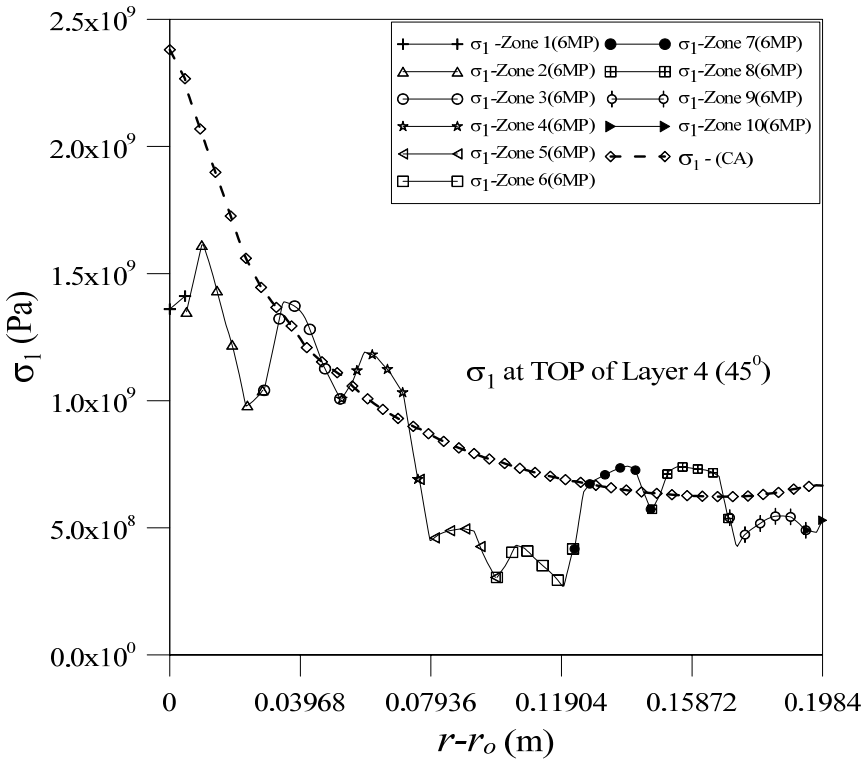

(ii)

Figure 3.13: Distributions of (i) σ_r and (ii) σ_1 along radius for 6-unit model

3.3.2 Mosaic-patterned models with actual thickness variations

The stress analysis of a filament-wound composite flywheel disk with actual thickness variations is performed considering different numbers of mosaic-patterned units around its circumference to explore the effect of the filament-winding mosaic pattern on the stress states developed due to rotational loading. The fibre orientation angle in the disk of a radius (R) with central opening of a radius (r_o) is defined by Eqs. (2.12) and (2.13) and the disk's thickness defined by Eq. (2.5) varies depending on the values of its radial location (r) and fibre orientation angle (ϕ).

3.3.2.1 Stress analysis of disk with thickness variations

Considering the plane stress condition, FE stress analyses are performed to investigate the effect of the filament-winding mosaic pattern in the filament-wound 4-, 6- and 8-unit composite disk models (Figure 2.6, Chapter 2) composed of 4, 8 and 14 plies, respectively. The modelling of variable thickness and development of FE models for analysing a filament-wound flywheel disk with actual thickness variations are discussed in Chapter 2, Sections 2.4.2 and 2.4.3, respectively. The disk is rotated about its central axis at a constant angular velocity, with its dimensions and material properties used in the FE analyses listed in Table 2.2 (Chapter 2) in which E_1 and E_2 are Young's moduli, G_{12} shear moduli and ν_{12} Poisson's ratio. Displacement and rotational boundary conditions are applied at the nodes on the inner and outer radii along the *x* and *y* axes of the reference plane (Figure 2.6(i)) to prevent in-plane rigid body motions in the radial and circumferential directions and out-of-plane rigid body motion in the axial direction.

The radial (σ_r), tangential (σ_θ) and shear ($\tau_{r\theta}$) stress distributions are determined for the top layer (layers 4, 8 and 14 of the 4-, 8- and 14-ply disks, respectively) of each of the conventional and mosaic-patterned models. Variations in the stresses observed at different

locations and their dependency on the arrangement of the mosaic units are demonstrated through the results obtained from the FE stress analyses. The radial stress distributions calculated using ANSYS for the conventional and mosaic-patterned models of the spinning 4-ply disk are illustrated by contour plots in Figure 3.14. As can be seen, those in the model incorporating a mosaic-patterned configuration differ substantially from those calculated on the basis of a conventional modelling technique for laminated shells. It follows from the contour plots of σ_r that, in a real filament-wound disk, the radial stress varies considerably from one mosaic unit to the adjacent ones in both the radial and circumferential directions. Not only are the levels of σ_r experienced by the flywheel disk due to rotation significantly affected by considering actual structural characteristics but also by the location of the maximum σ_r. Also, the numbers of mosaic units around the disk's circumference substantially influence the distribution and level of magnitude of σ_r. The maximum radial stress in the 4-ply disk obtained from a conventional model is found to be uniform over a wide range of radial distances, as can be seen in Figure 3.14(i) whereas, in models with other numbers of mosaic units, it is located at different positions.

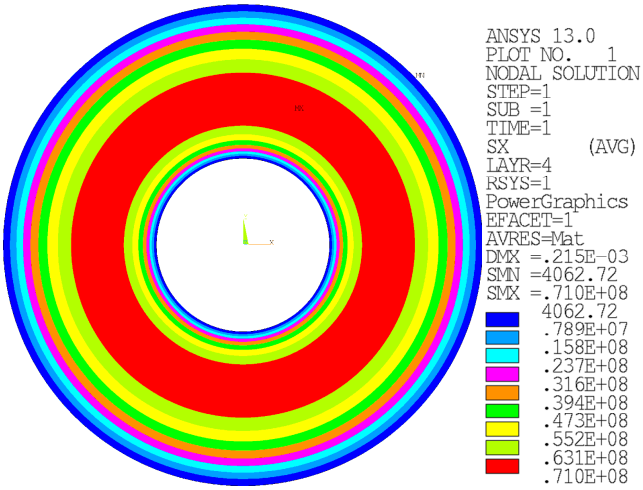

(i) σ_r (conventional model)

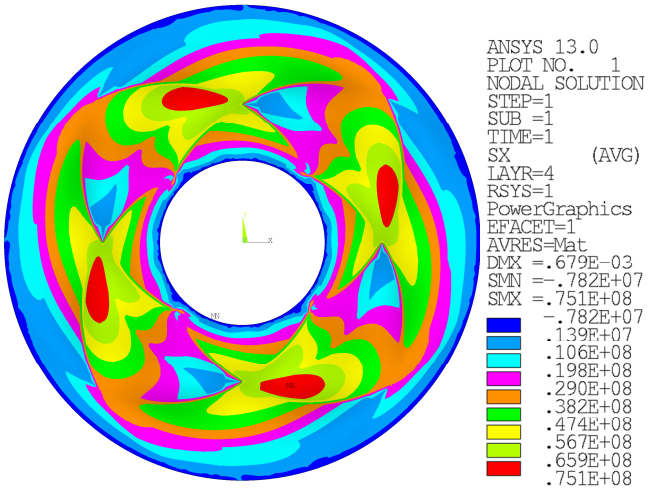

(ii) σ_r (4-unit model)

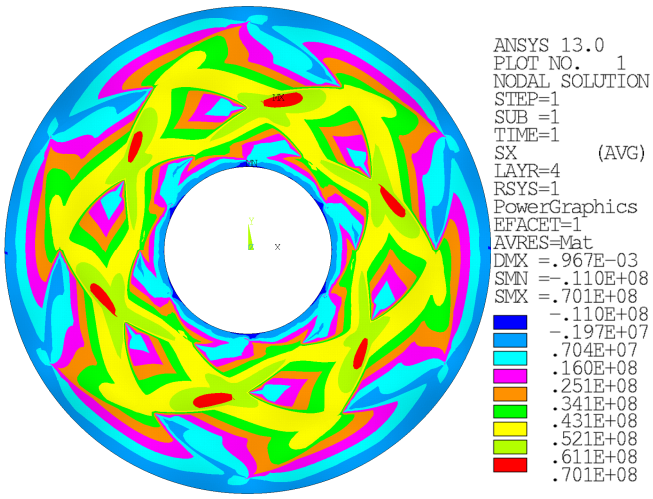

(iii) σ_r (6-unit model)

Figure 3.14: Contour plots of σ_r in models of 4-ply disk

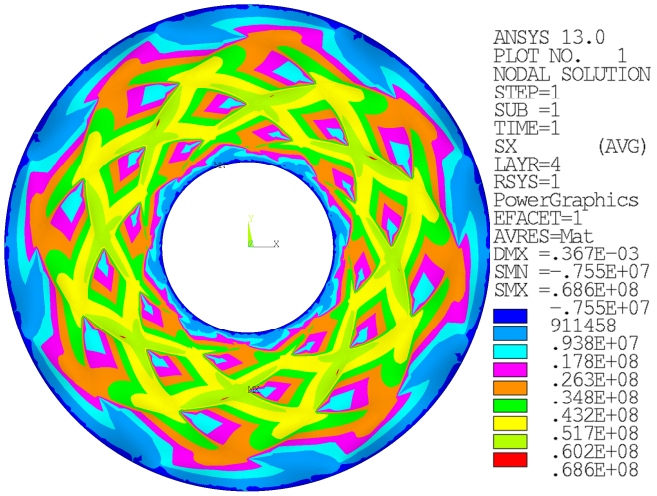

(iv) σ_r (8-unit disk)

Figure 3.14: Contour plots of σ_r in models of 4-ply disk (*continued*)

Similarly, the contour plots of the hoop stress (σ_θ) predicted for different models of the 4-ply disk (Figure 3.15) reflect the significant effect of the mosaic pattern on its distributions, with those obtained from a conventional model differing markedly from those determined using models with various numbers of mosaic units. Also, the magnitude of the maximum σ_θ calculated using a conventional model of the 4-ply disk, which reaches 238 MPa, varies considerably from that obtained from the 4-unit mosaic-patterned model of 352 MPa. This maximum stress value changes with increasing numbers of mosaic units and is predicted to be 350 MPa for the 6-unit model and 336 MPa for the 8-unit model of the 4-ply disk. Therefore, the effect of the mosaic pattern on stress distributions is also substantiated by the hoop stress predicted for the 4-ply disk.

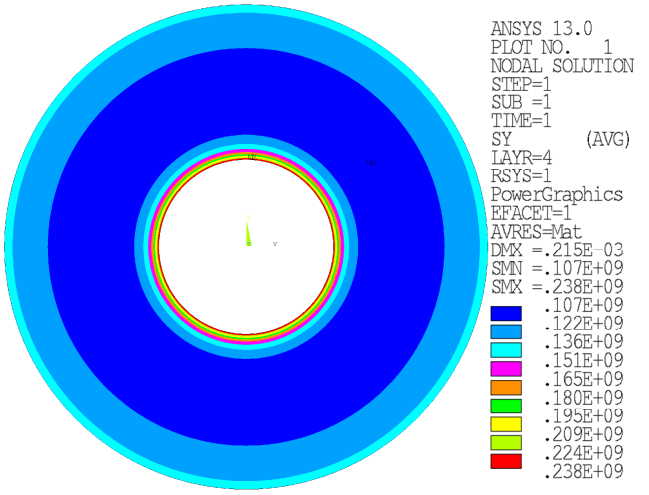

(i) σ_θ (conventional model)

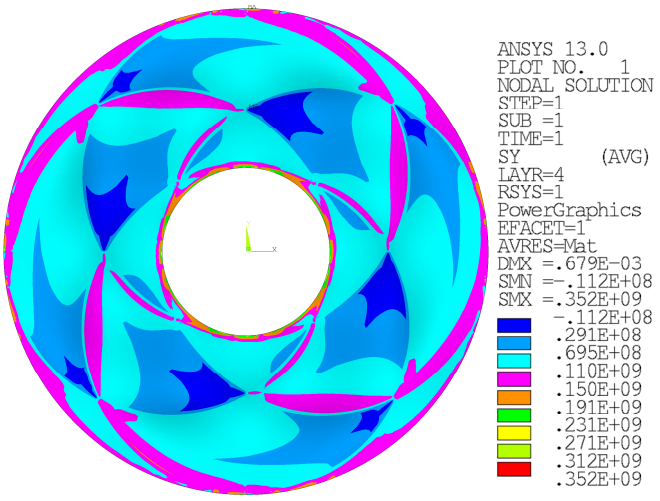

(ii) σ_θ (4-unit model)

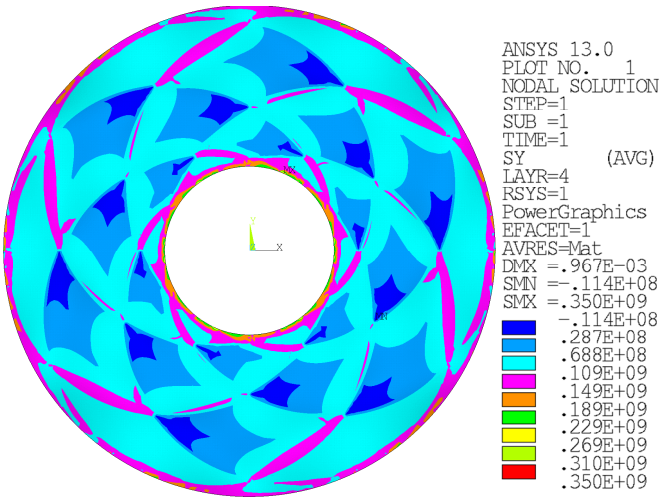

(iii) σ_θ (6-unit model)

Figure 3.15: Contour plots of σ_θ in models of 4-ply disk

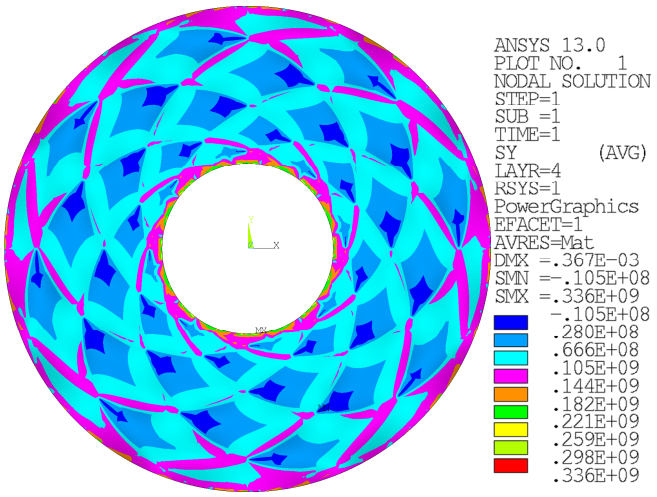

(iv) σ_θ (8-unit model)

Figure 3.15: Contour plots of σ_θ in models of 4-ply disk (*continued*)

Distributions of the shear stress ($\tau_{r\theta}$) are also influenced by the incorporation of a mosaic pattern in FE models of the filament-wound composite flywheel disk. As can be seen in Figure 3.16, the shear stress distribution in the top layer of the 4-ply disk's conventional model does not reflect the distinctive variations in magnitude in different mosaic units due to this model's failure to capture the effect of the mosaic-patterned configuration. However, the values of $\tau_{r\theta}$ predicted for the mosaic-patterned models with various numbers of mosaic units fluctuate over a wide range of magnitudes; for instance, its maximum and minimum values for the 8-unit model of the 4-ply disk (Figure 3.16(iv)) are -70.9 MPa and 70.7 MPa, respectively, whereas the conventional FEA predicts the corresponding values to be 10.2 MPa and 75.5 MPa (Figure 3.16(i)) which clearly indicates the susceptibility of a filament-wound disk to the influence of a mosaic-patterned configuration.

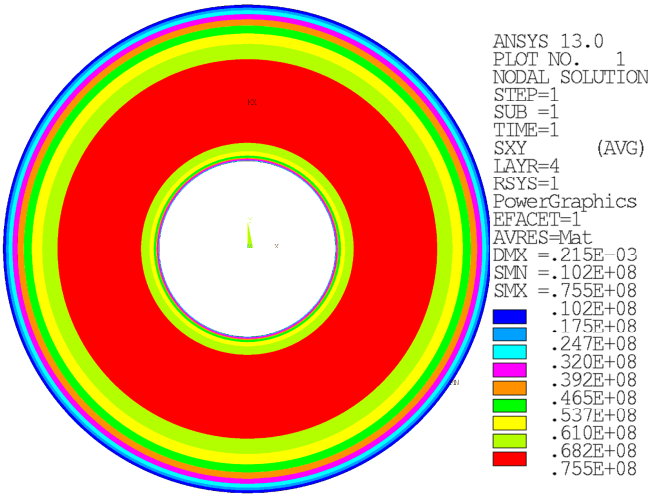

(i) $\tau_{r\theta}$ (conventional model)

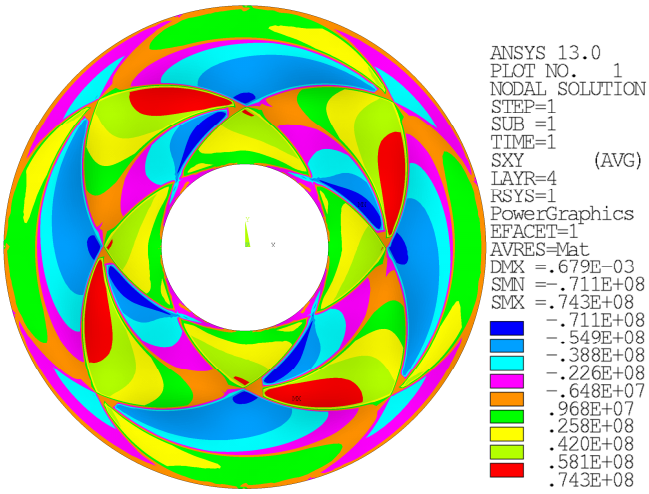

(ii) $\tau_{r\theta}$ (4-unit model)

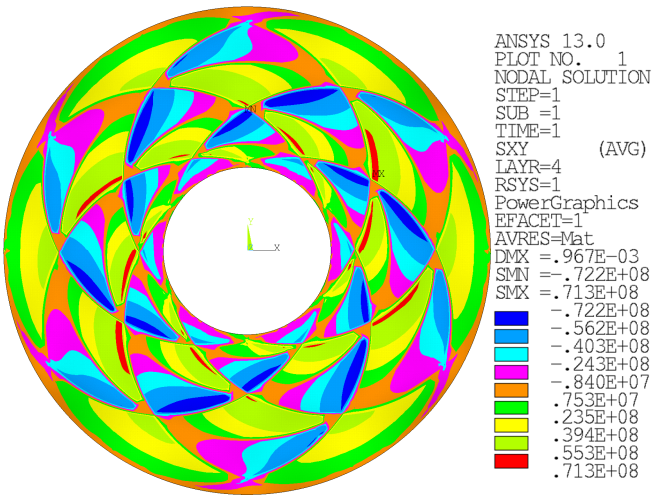

(iii) $\tau_{r\theta}$ (6-unit model)

Figure 3.16: Contour plots of $\tau_{r\theta}$ in models of 4-ply disk

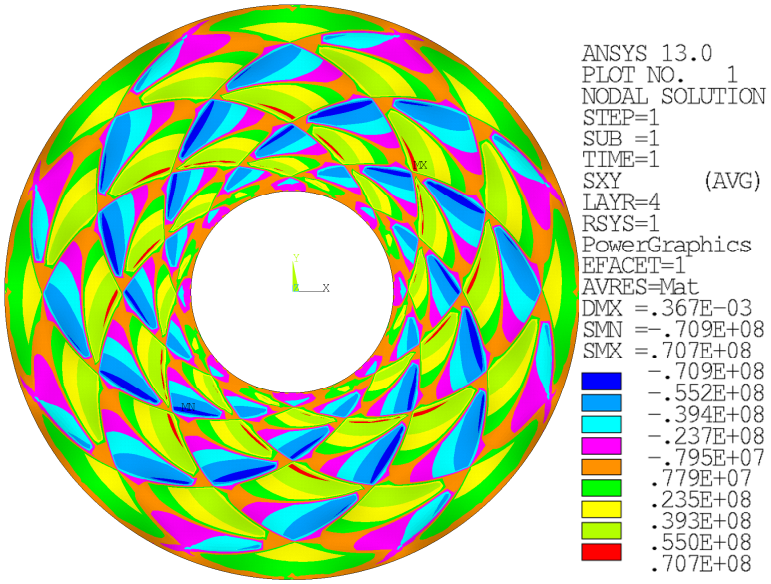

(iv) $\tau_{r\theta}$ (8-unit model)

Figure 3.16: Contour plots of $\tau_{r\theta}$ in models of 4-ply disk (*continued*)

Also, FE analyses of the mosaic-patterned models of the 8- and 14-ply disks illustrate the significant variations in stress values predicted for the various mosaic units. The contour plots of σ_r, σ_θ and $\tau_{r\theta}$ determined for the 8-unit model of both the 8- and 14-ply disks are shown in Figure 3.17 in which the stresses obtained are clearly distinguishable from those estimated using the conventional modelling technique. Considerable fluctuations in the predicted values of different stresses calculated using the mosaic-patterned models not only clearly indicate the effect of the mosaic pattern on stress distributions but also emphasise the necessity of incorporating manufacturing characteristics in the FE modelling and analysis of a filament-wound structure.

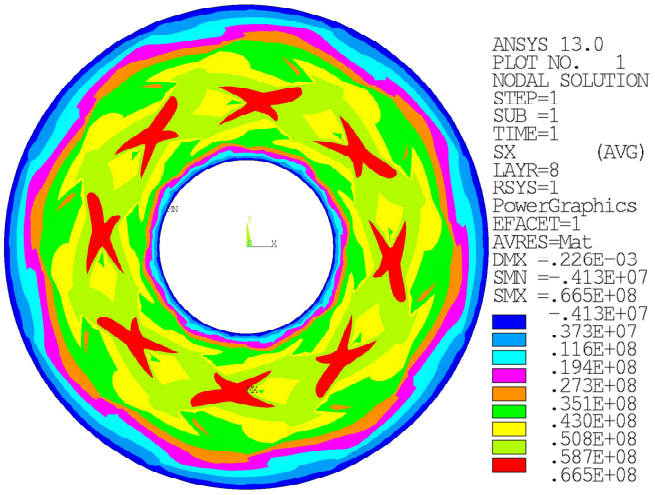

(i) σ_r (8-ply disk)

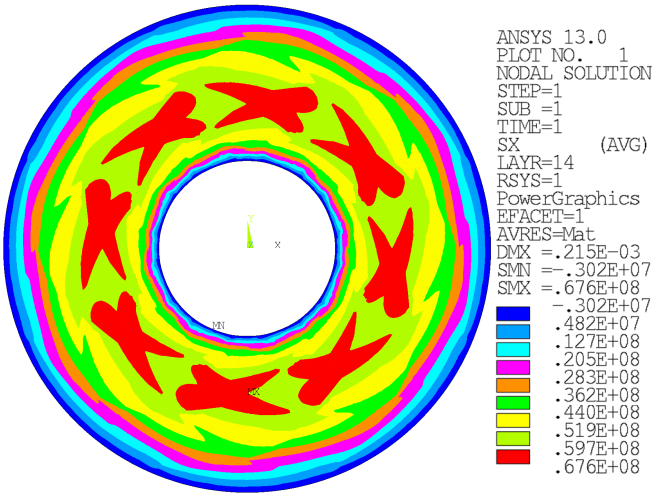

(ii) σ_r (14-ply disk)

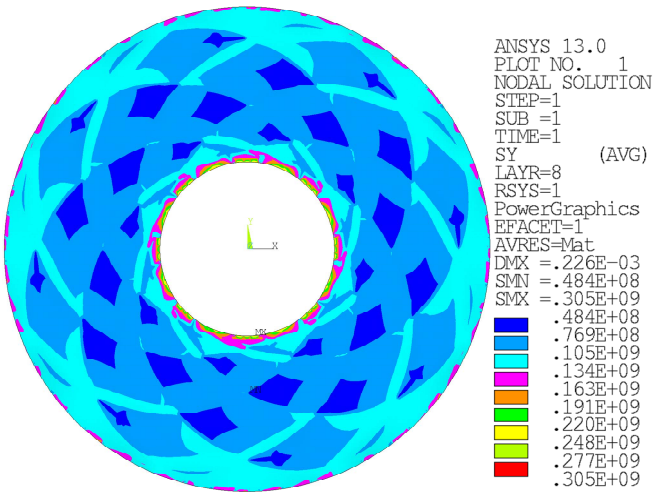

(iii) σ_θ (8-ply disk)

Figure 3.17: Contour plots of σ_r, σ_θ and $\tau_{r\theta}$ in 8-unit model

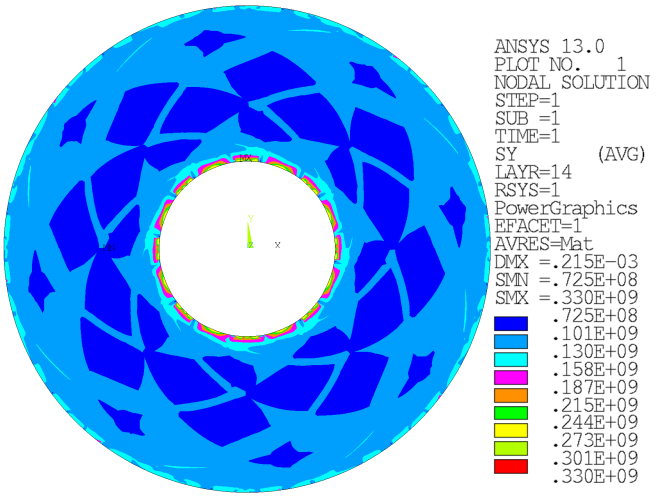

(iv) σ_θ (14-ply disk)

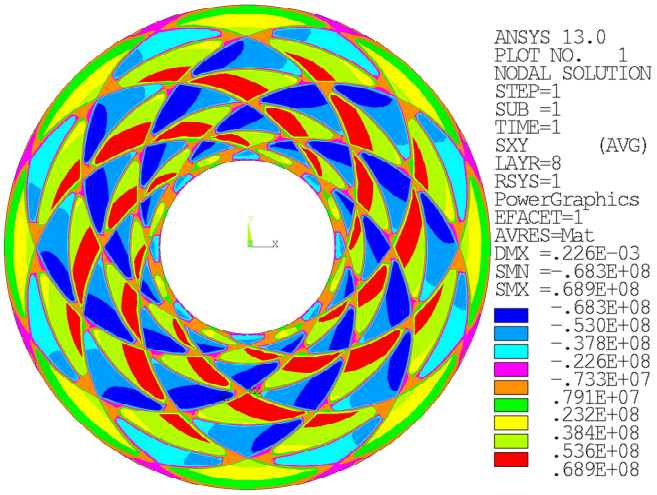

(v) $\tau_{r\theta}$ (8-ply disk)

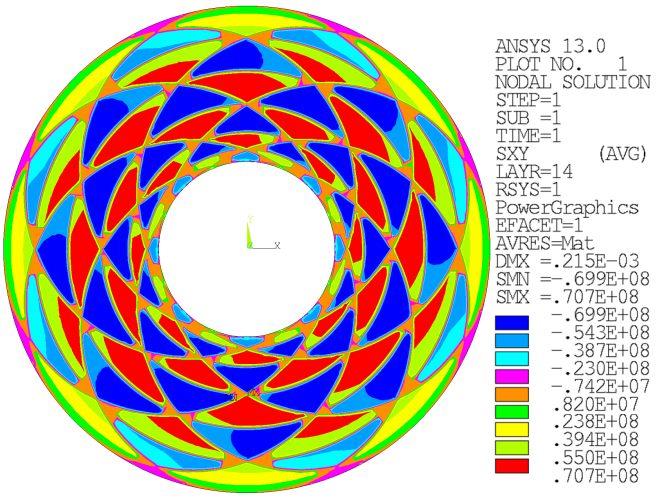

(vi) $\tau_{r\theta}$ (14-ply disk)

Figure 3.17: Contour plots of σ_r, σ_θ and $\tau_{r\theta}$ in 8-unit model (*continued*)

Stress distributions around the circumference of the filament-wound flywheel disk ($0^0 \leq \theta \leq 180^0$) are plotted with stress values calculated at a radial distance of 0.23885 m for each FE model and the two mosaic units of different sizes arranged circumferentially in alternating fashion at the radial location denoted 'Zone A' and 'Zone B'.

As can be seen in Figure 3.18, the circumferential distributions of both the radial (σ_r) and tangential (σ_θ) stresses predicted by the conventional and three mosaic-patterned FE models (with 4, 6 and 8 units) of the filament-wound 4-ply disk demonstrate that their values are substantially different, with those of the mosaic-patterned configurations maintaining noticeably different levels of values at different locations within a mosaic unit. The patterns of variations in the values of σ_r and σ_θ and their levels are greatly influenced by the numbers as well as locations of mosaic units around the disk's circumference.

As can be observed in Figure 3.18, both the radial and tangential stresses obtained from the mosaic-patterned models follow various repeating patterns and their magnitudes also fluctuate within a range of minimum and maximum values depending on the numbers of mosaic units whereas the conventional technique predicts almost constant values of both σ_r and σ_θ. The maximum deviations in values obtained from the 4-unit model (Figure 3.18(i-ii)) reach 65% for σ_r and 67% for σ_θ of those from the conventional model. Also, the 8-unit model yields deviations in values that reach maxima of 54% for σ_r and 69% for σ_θ, respectively, as shown in Figure 3.18(v-vi).

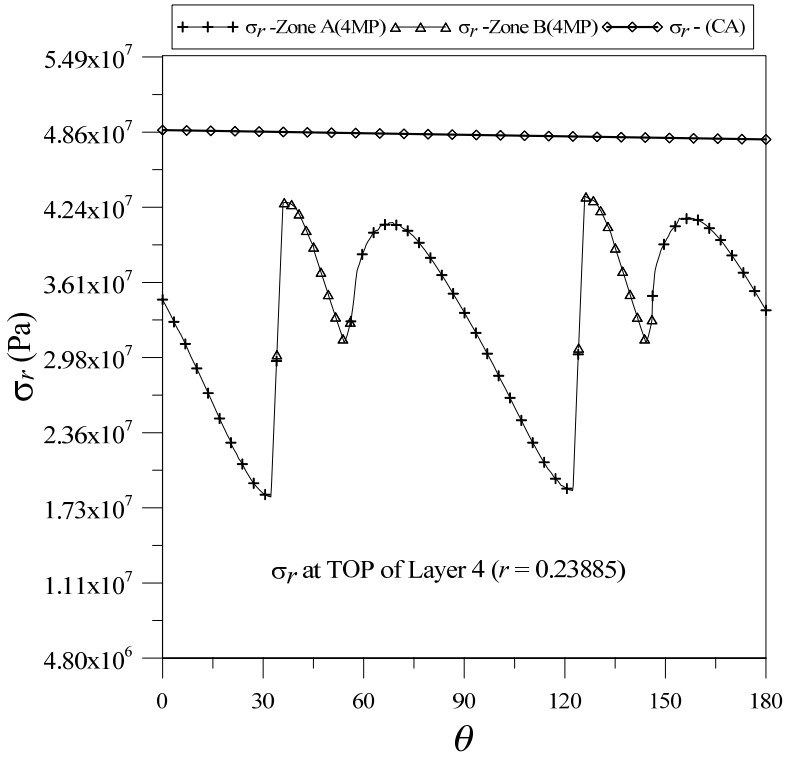

(i) σ_r (4-unit model)

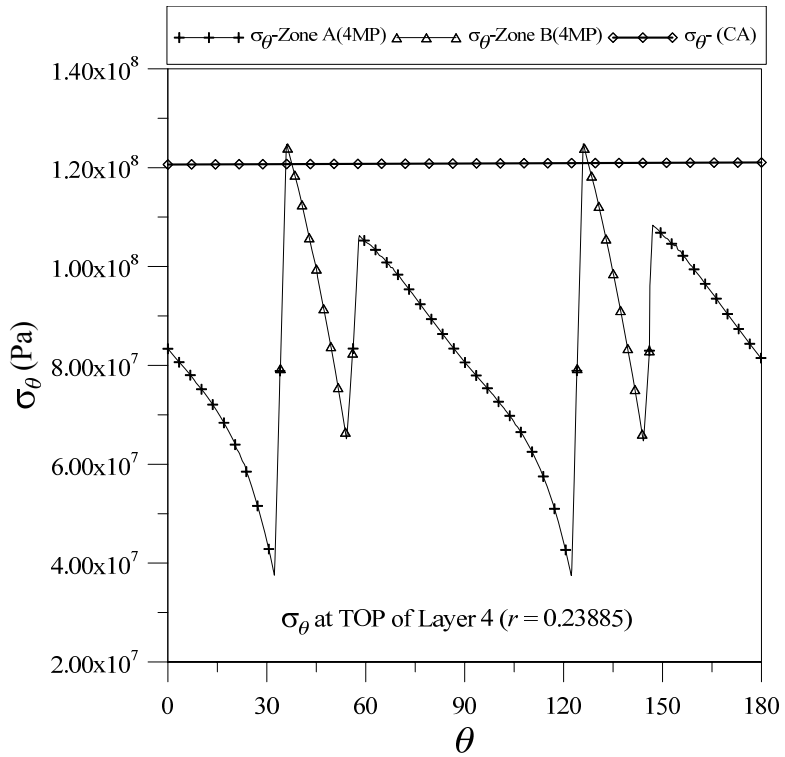

(ii) σ_θ (4-unit model)

Figure 3.18: Circumferential distributions of σ_r and σ_θ in 4-ply disk

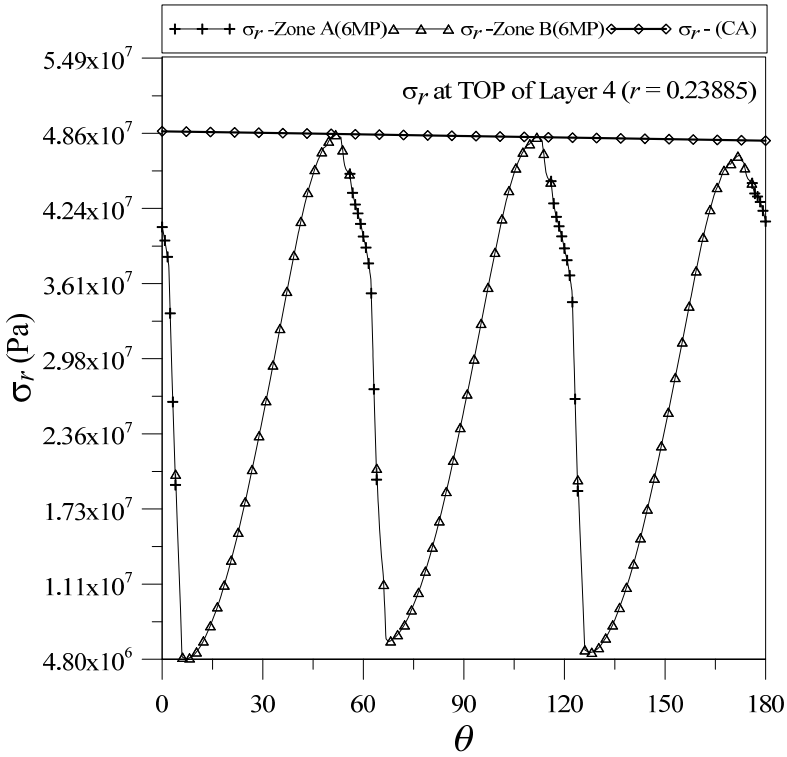

(iii) σ_r (6-unit model)

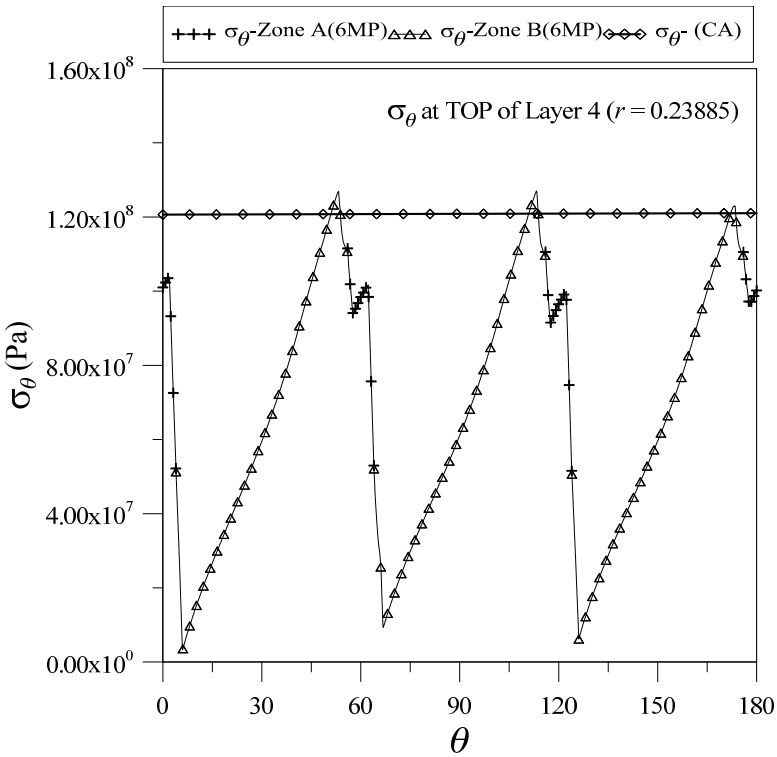

(iv) σ_θ (6-unit model)

Figure 3.18: Circumferential distributions of σ_r and σ_θ in 4-ply disk (*continued*)

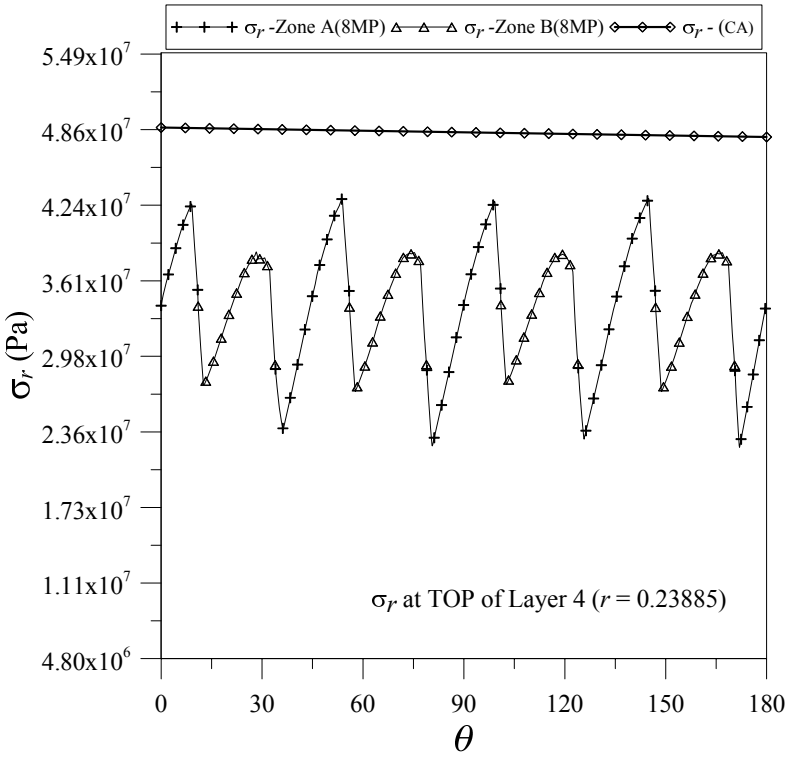

(v) σ_r (8-unit model)

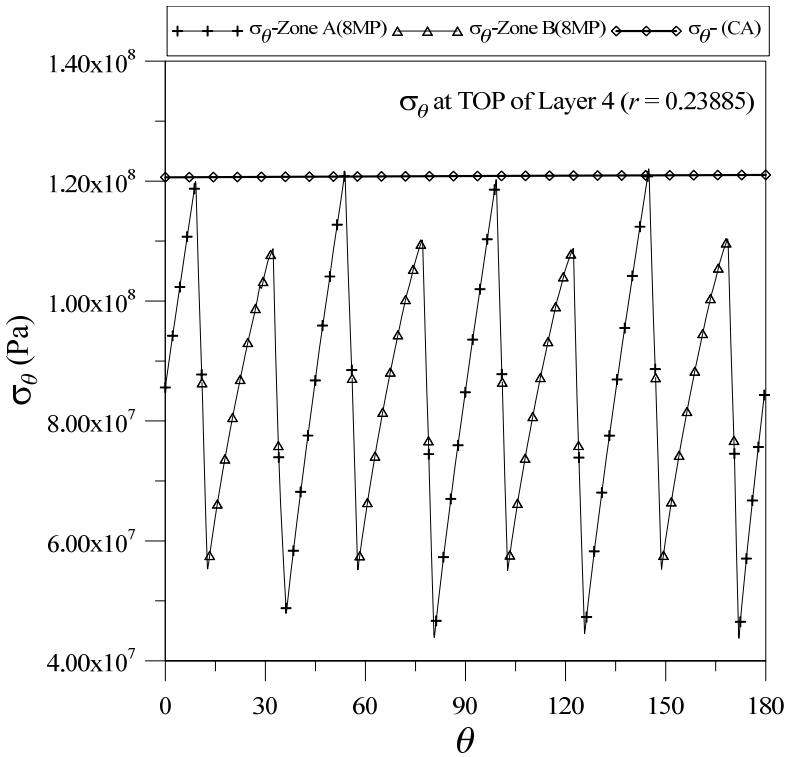

(vi) σ_θ (8-unit model)

Figure 3.18: Circumferential distributions of σ_r and σ_θ in 4-ply disk (*continued*)

Also, the circumferential distributions of the stresses along the fibres (σ_1) and across the fibres (σ_2) obtained from the FEA of the filament-wound disk's models with mosaic-patterned configurations reflect the effect of the structural characteristics in various layers. As can be observed in Figure 3.19, a conventional FEA technique predicts constant values of both σ_1 and σ_2 at the top layer of the 8-ply disk whereas their distributions determined using models with different numbers of mosaic units clearly vary within mosaic units at various locations. The maximum values of these stresses change slightly depending on the numbers of mosaic units incorporated in the filament-wound flywheel disk's FE models; for instance, the maximum values of σ_1 and σ_2 obtained are, respectively, 155 MPa and 13 MPa for the 4-unit, 154 MPa and 15 MPa for the 6-unit and 151 MPa and 12 MPa for the 8-unit models whereas the conventional technique calculates them to be 159 MPa and 10 MPa, respectively, and constant over all the selected circumferential locations. The values of both σ_1 and σ_2 predicted using the mosaic-patterned models of the 8-ply disk offer different levels of variation than those obtained from the conventional analysis, with the estimated maxima found to be 52% for σ_1 and 42% for σ_2 for the 6-unit model (Figure 3.19(iii-iv)).

The effect of an increasing number of mosaic units on the magnitudes of the stresses can be observed from a comparison of the stress distributions obtained from the conventional and mosaic-patterned 4-, 6- and 8-unit models. As can be seen in Figure 3.20, although the magnitudes of σ_1 and σ_2 determined using the 4-ply disk decrease with increasing numbers of mosaic units around its circumference, those obtained from the mosaic-patterned models still differ from those determined using the conventional technique.

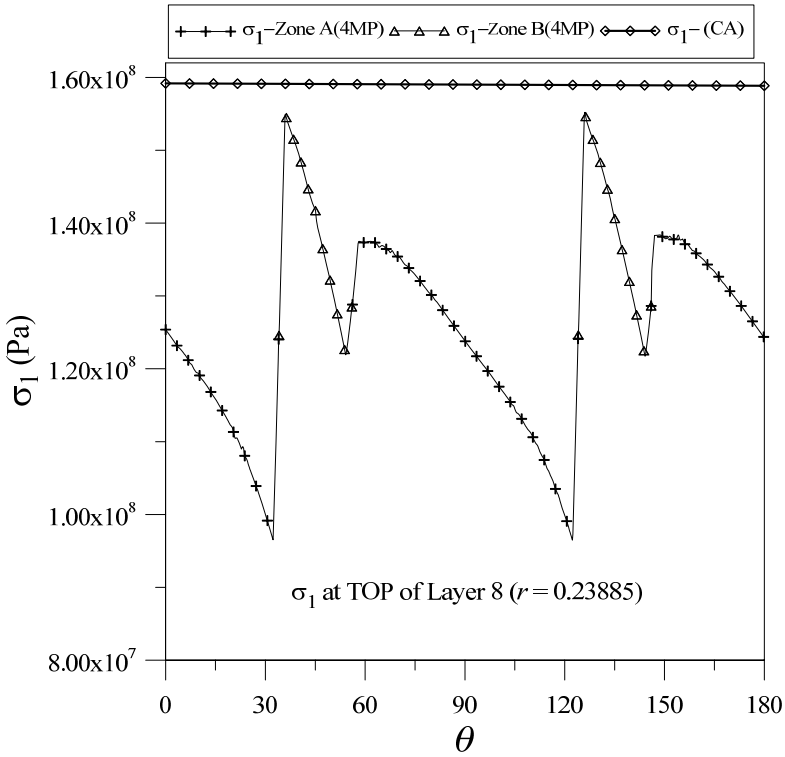

(i) σ_1 (4-unit model)

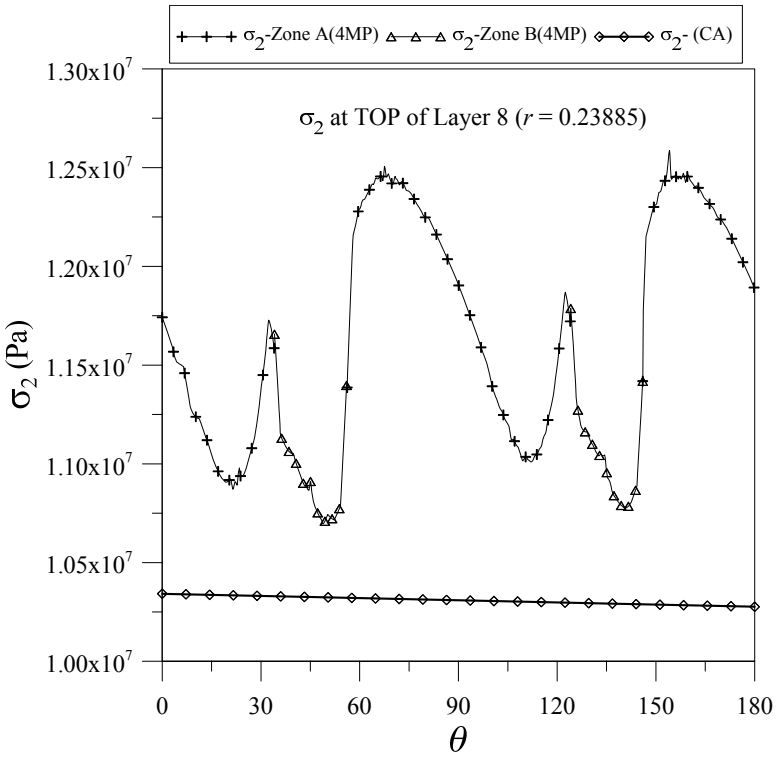

(ii) σ_2 (4-unit model)

Figure 3.19: Circumferential distributions of σ_1 and σ_2 in 8-ply disk

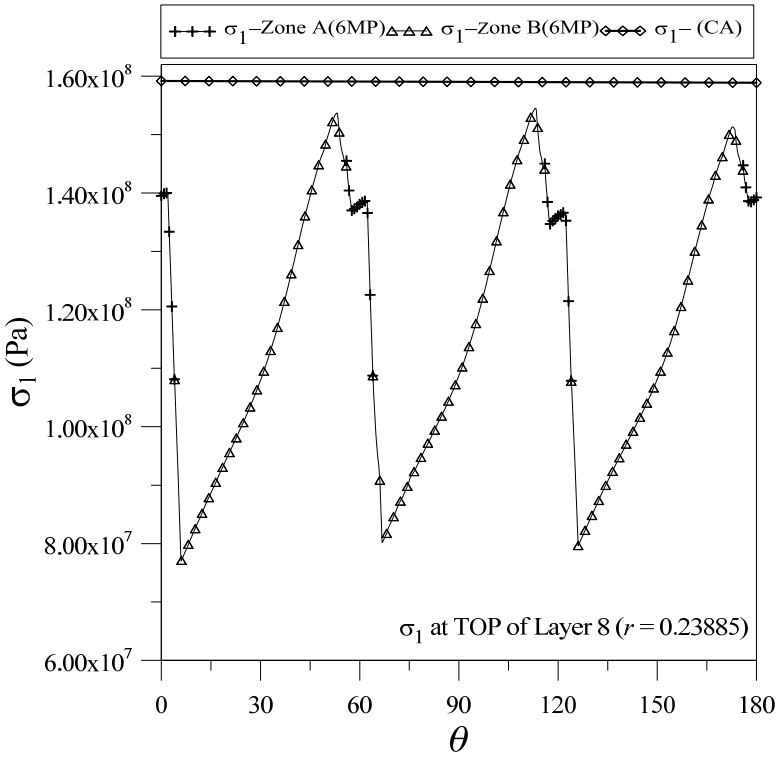

(iii) σ_1 (6-unit model)

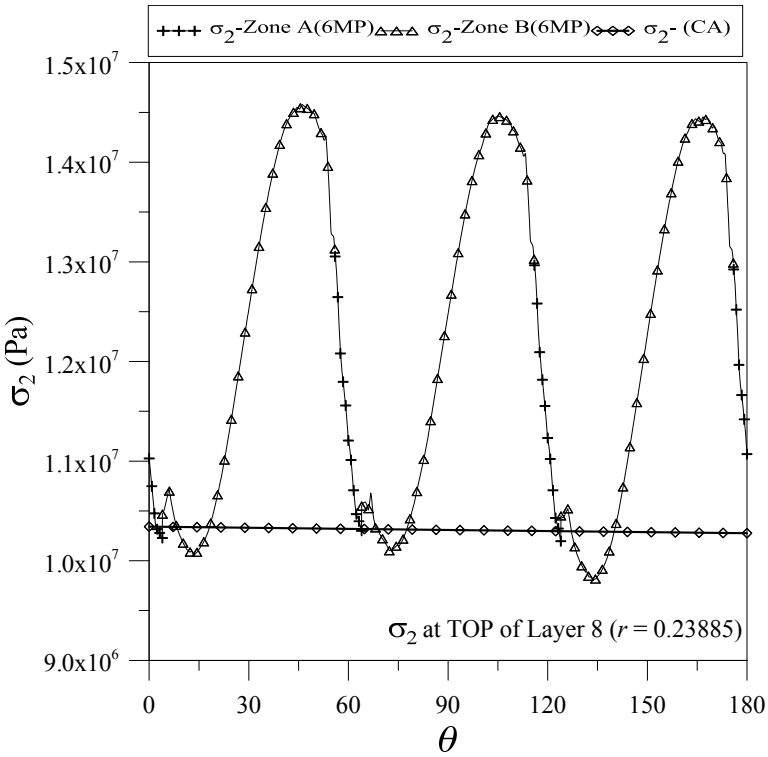

(iv) σ_2 (6-unit model)

Figure 3.19: Circumferential distributions of σ_1 and σ_2 in 8-ply disk (*continued*)

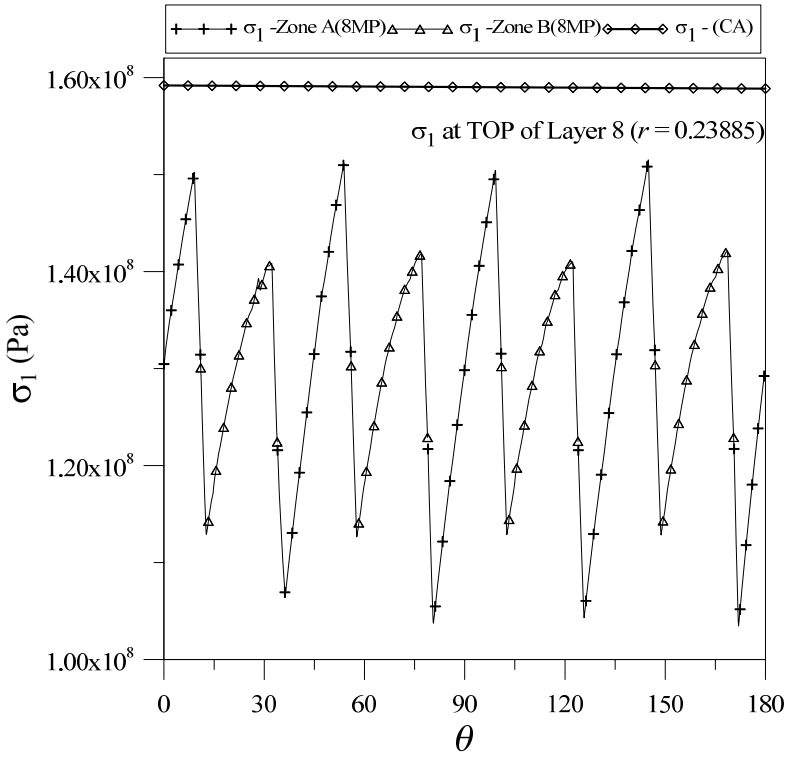

(v) σ_1 (8-unit model)

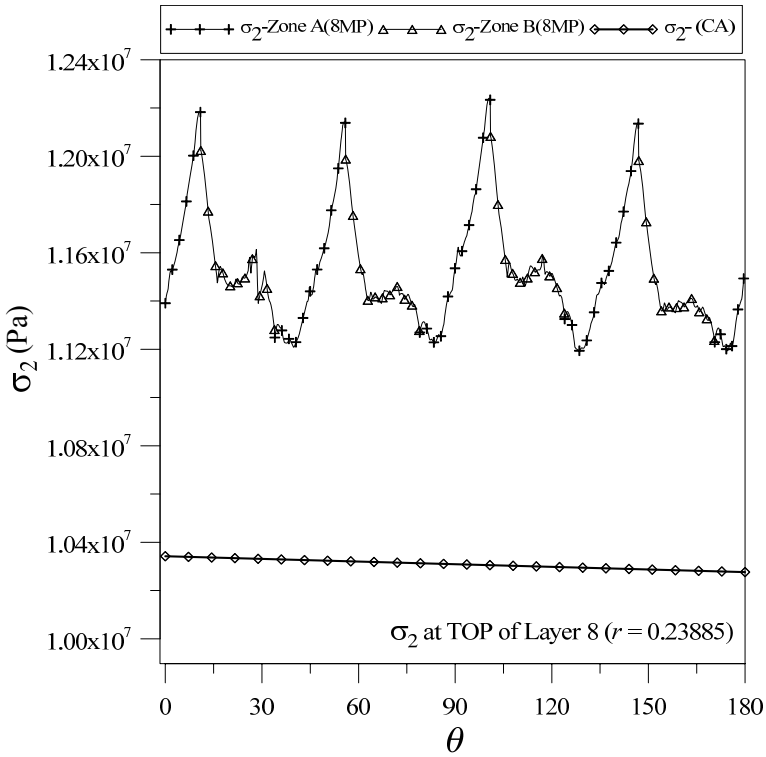

(vi) σ_2 (8-unit model)

Figure 3.19: Circumferential distributions of σ_1 and σ_2 in 8-ply disk (*continued*)

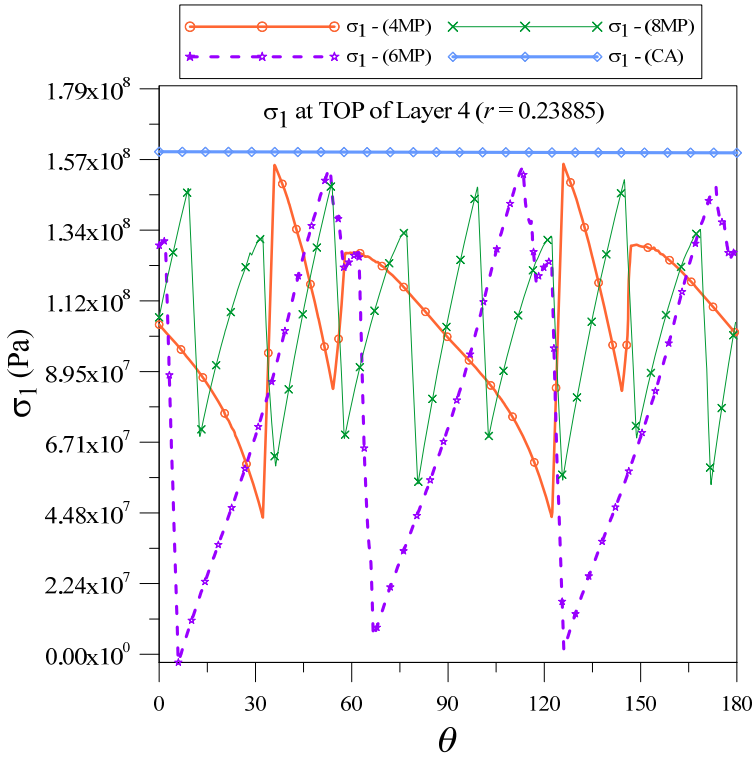

(i) σ_1(conventional and mosaic-patterned models)

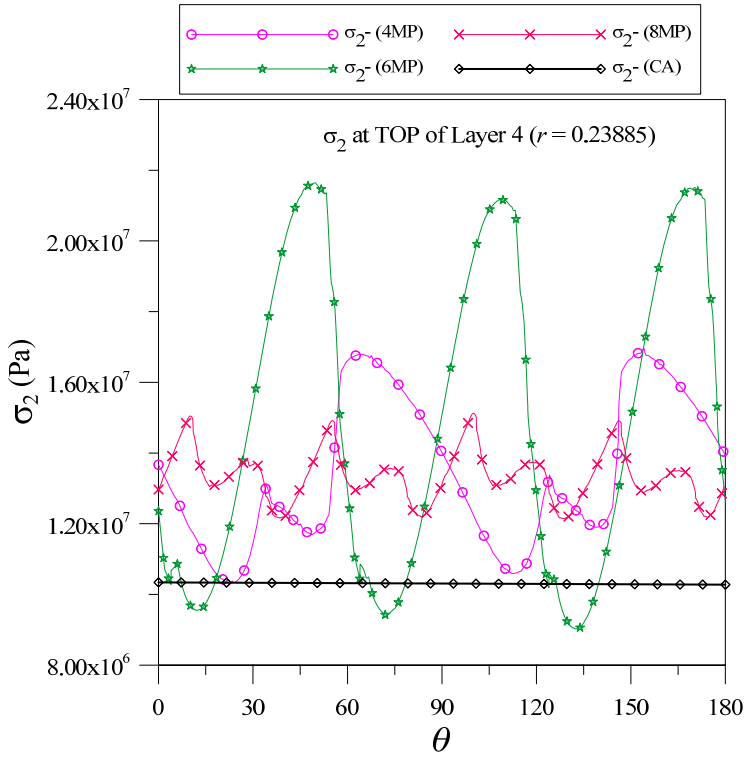

(ii) σ_2(conventional and mosaic-patterned models)

Figure 3.20: Effect of increasing number of mosaic units on circumferential stress distributions of (i) σ_1 and (ii) σ_2 in 4-ply disk

Also, variations in the different stresses along a radial cross-section orientated at 45^0 counter-clockwise from the $+x$ axes of the FE models (Figure 2.6) of the filament-wound disk are demonstrated. The first mosaic-patterned unit located in this cross-section and connected to the inner radius of the model is denoted 'Zone 1' and consecutive units numbered sequentially.

Although distributions of the tangential stress (σ_θ) along the selected radial cross-section in each conventional model of the 4-, 8- and 14-ply disks are quite dissimilar compared with those calculated using the mosaic-patterned models (Figure 3.21), those of σ_2 follow trends which are similar. The variations in stress values determined using the mosaic-patterned 4-, 8- and 14-ply disks are different from those produced by the conventional model. As can be observed in Figure 3.21(i-ii), the maximum magnitude variations of σ_θ and σ_2 obtained from the 4-ply disk reach 58% and 55%, respectively, of those from the conventional solution technique but gradually diminish with increments in the total numbers of plies, i.e., the thickness of the filament-wound disk considered. As can be observed from the radial distributions of σ_θ in the 8-ply disk shown in Figure 3.21(iii and v), the values of this stress determined using mosaic-patterned models gradually approach those obtained from the conventional technique and are closer for the 14-ply disk. Also, a similar trend is observed in the radial distributions of σ_2 shown in Figure 3.21(iv and vi) which implies that the effect of a mosaic-patterned configuration on radial stress distributions in a filament-wound flywheel disk diminishes gradually with increasing numbers of plies.

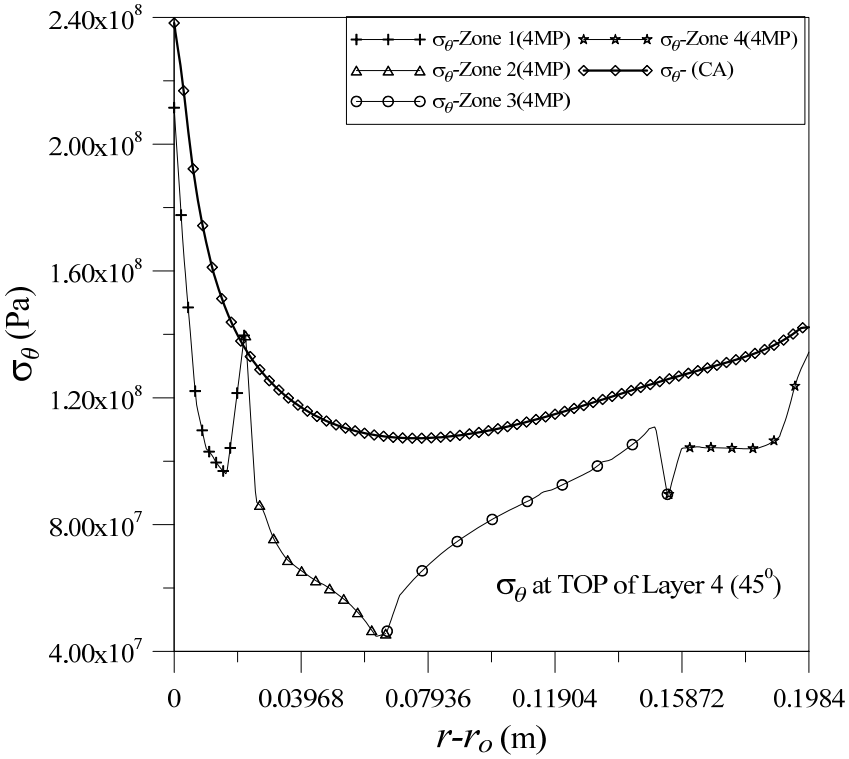

(i) σ_θ (4-ply disk)

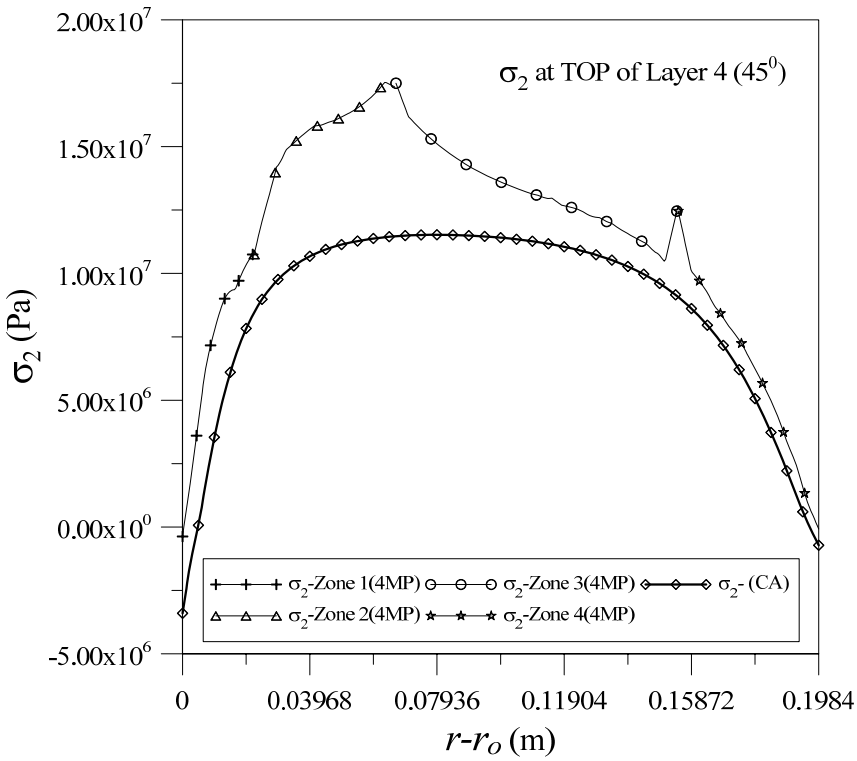

(ii) σ_2 (4-ply disk)

Figure 3.21: Radial distributions of σ_θ and σ_2 in 4-unit model

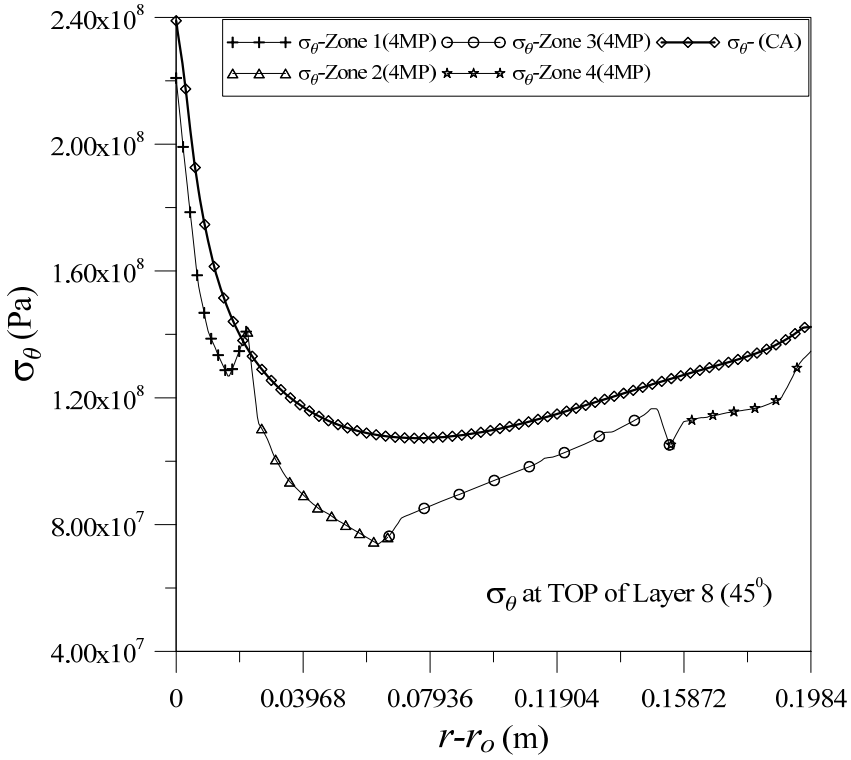

(iii) σ_θ (8-ply disk)

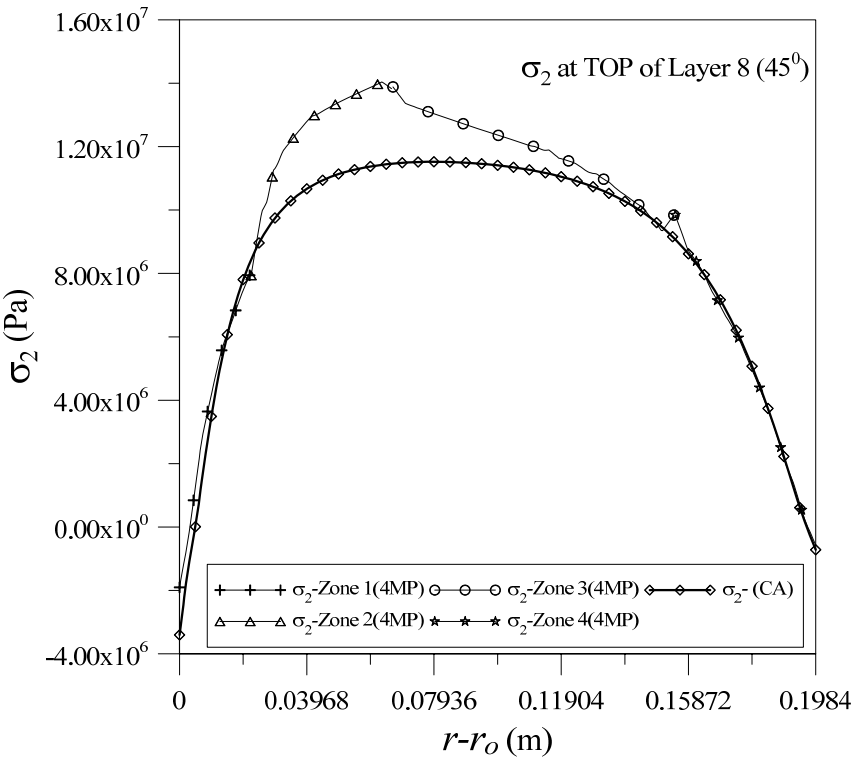

(iv) σ_2 (8-ply disk)

Figure 3.21: Radial distributions of σ_θ and σ_2 in 4-unit model (*continued*)

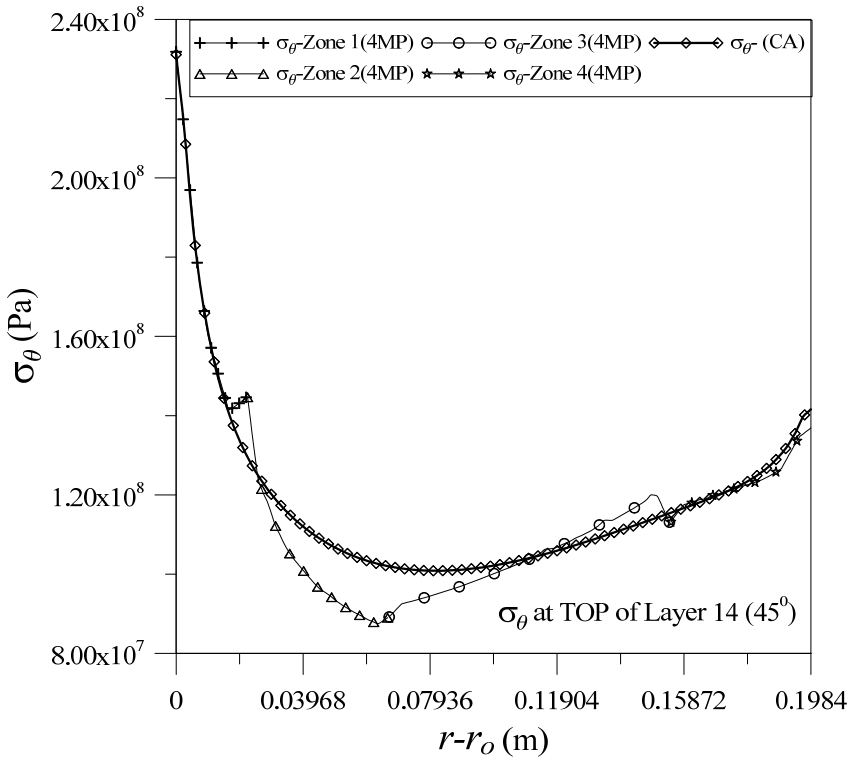

(v) σ_θ (14-ply disk)

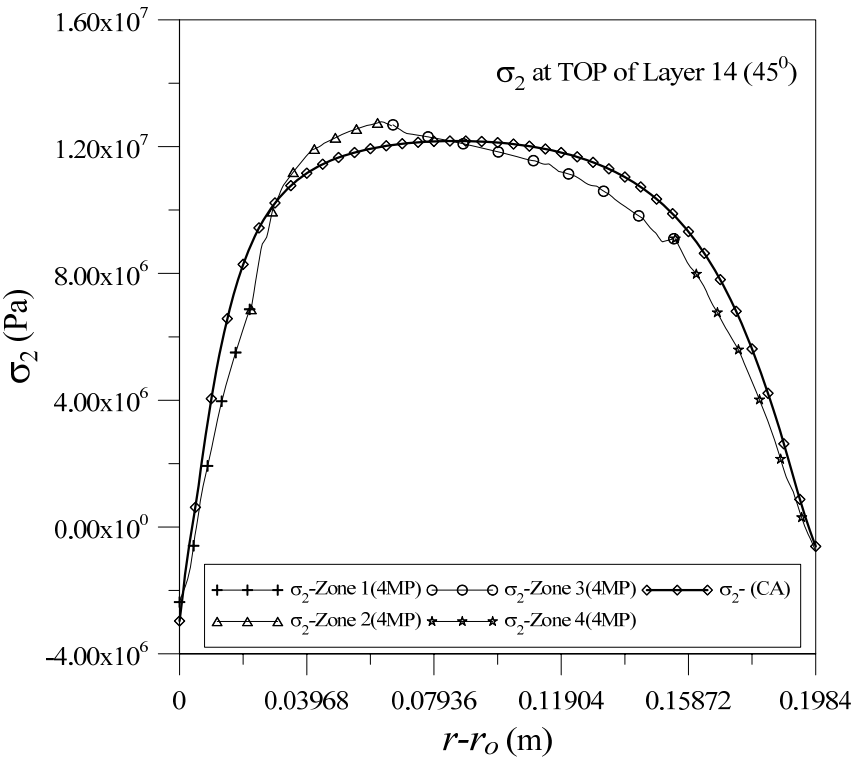

(vi) σ_2 (14-ply disk)

Figure 3.21: Radial distributions of σ_θ and σ_2 in 4-unit model (*continued*)

The maximum levels of the different stresses are considerably influenced by the incorporation of a mosaic-patterned configuration, to corroborate which, the maximum values of the stress across the fibres (σ_1) and circumferential stress (σ_θ) obtained from the mosaic-patterned and conventional models are compared, as shown in Figure 3.22, from which it follows that their FEAs produce diverse maximum values of these stresses based on both their different numbers of plies and mosaic units around the disk's circumference. For the 4-, 8- and 14-ply disks, each with 4, 6 and 8 mosaic units around its circumference, their maximum values of σ_1 and σ_θ are substantially different from those obtained from the conventional FEA; for instance, the maximum value of $\sigma_1$at the top of layer 3 in the 4-ply disk is determined to be 239 MPa from the conventional model but up to 357 MPa from the 8-unit mosaic-patterned model (Figure 3.22(i)). Similarly, the 8- and 14-ply disks with 8 mosaic units produce 27% and 17% higher values of σ_1 at the top of layer 7 and 13, respectively, than the conventional technique. Furthermore, the maximum values of the tangential stress (σ_θ) obtained from the mosaic-patterned models are observed to be higher than those calculated using the conventional model (Figure 3.22(ii)) (i.e., for the 4-ply disk, σ_θ= 328 MPa (4 units), 326 MPa (6 units) and 325 MPa (8 units) at the top of layer 3 and, for the conventional model, σ_θ= 236 MPa). In addition, the maximum values of σ_r and $\tau_{r\theta}$ obtained from the mosaic-patterned models are higher than those determined by the conventional FEA (i.e., for the 8-ply disk, σ_r = 103 MPa (4 units), 102 MPa (6 and 8 units) at the top of layer 7 and, for the conventional model, σ_r = 71 MPa). Both the conventional and mosaic-patterned models provide close values of σ_2 and τ_{12} in different plies (i.e., for the 14-ply disk, σ_2= 12 MPa (4, 6 and 8 units) at the top of layer 13 and, for the conventional model, σ_2= 11 MPa).

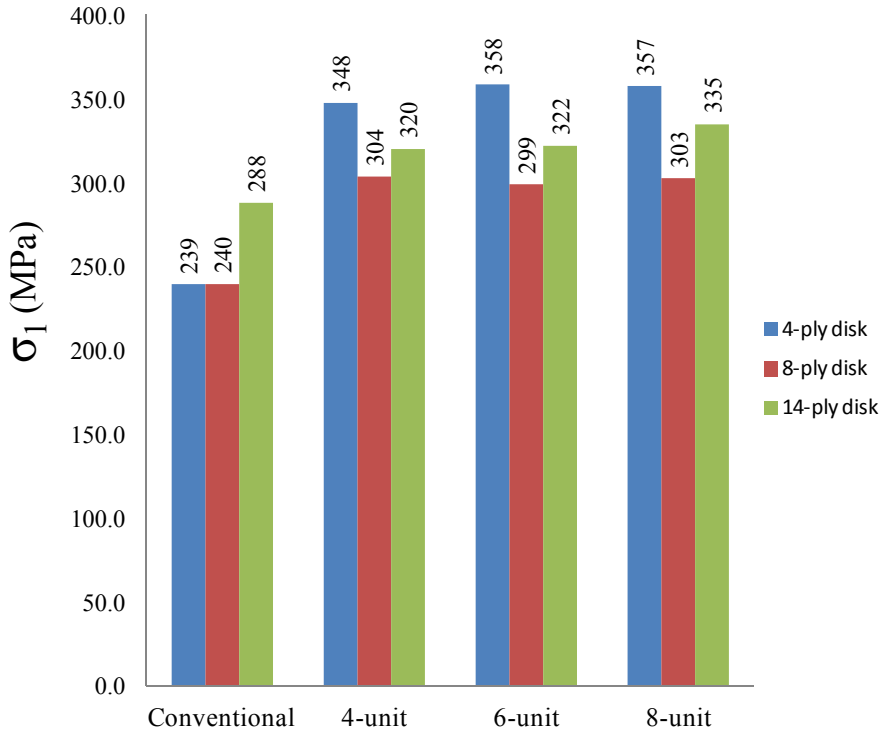

(i) σ_1 (conventinal and mosaic-patterned models)

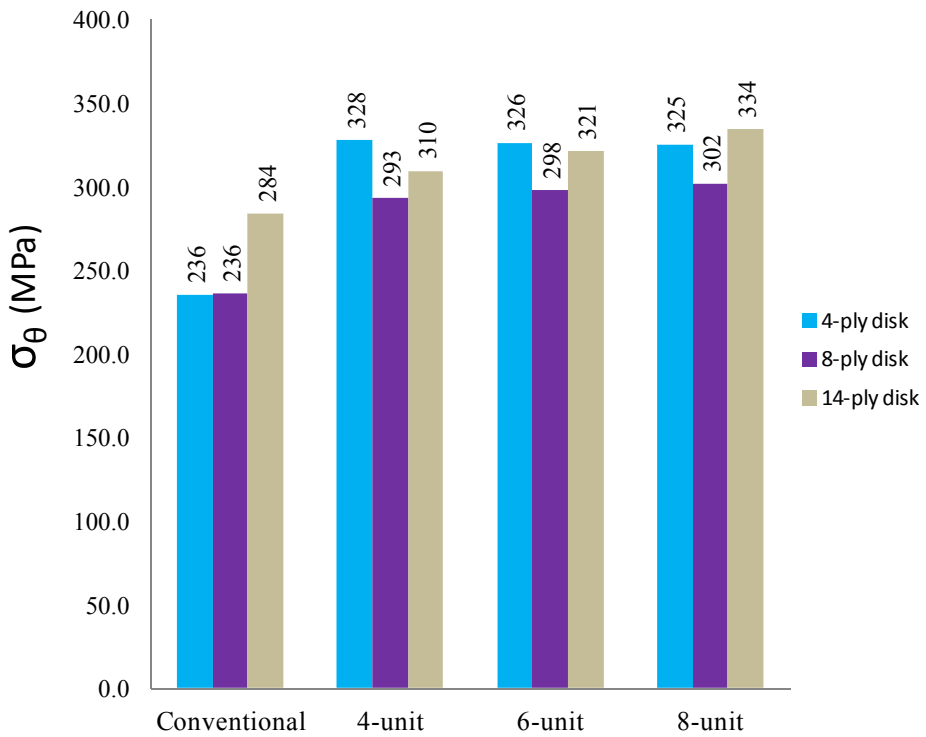

(ii) σ_θ (conventinal and mosaic-patterned models)

Figure 3.22: Comparisons of maximum values of (i) σ_1 and (ii) σ_θ at tops of layer 3 (4-ply disk), layer 7 (8-ply disk) and layer 13 (14-ply disk) in models

3.3.3 Increased thickness and effect of mosaic-patterned architecture

Distributions of the stresses and comparisons of their maximum values provide an indication that, in some cases, the levels of stresses in a spinning filament-wound composite flywheel disk can be underestimated to a certain extent by a general stress analysis based on the conventional mechanics of laminated structures that does not take into account the filament-winding mosaic pattern of $\pm\phi$ angle-ply layers which is most pronounced for filament-wound structures with relatively low thicknesses [6]. Multi-layered laminated shells with a large number of angle-ply layers experience the effect of the mosaic pattern to a lesser degree, with their stretching-twisting and bending-shear coupling coefficients calculated as [2]

$$C_{mn} = -\frac{1}{2}A_{mn}h\delta \tag{3.5}$$

where h is the laminate thickness, δ the ply thickness and A_{mn} the stiffness coefficients of the materials. If the thickness of a single ply (δ) is small compared with the overall thickness of a laminate composed of large numbers of $\pm\phi$ angle-ply layers, the effect of the filament-winding mosaic pattern is not very pronounced [6]. Radial distributions of the stresses from the 14-ply disk's mosaic-patterned model (8 units) illustrate the diminishing effect of the filament-winding mosaic pattern on the stress states in its different plies. As can be seen in Figure 3.23, both the conventional and mosaic-patterned models produce very close values of both σ_θ and σ_2 which is also true for the radial distributions of other stresses. Circumferential distributions of the stresses obtained from the mosaic-patterned models of the 14-ply disk maintain various levels of difference with respect to the stress magnitudes calculated using the conventional FEA technique, as can be observed in Figure 3.24 in which the distributions of both σ_θ and σ_2 follow dissimilar trends and the values at different points of the selected circumferential location maintain 4% to 15% differences.

Therefore, the effect of the filament-winding mosaic-patterned configuration will be gradually diminished with increasing thicknesses of a filament-wound shell.

The effect of the filament-winding mosaic pattern is also dependent on the positioning of the angle-ply layers in a filament-wound laminate. If curved triangular units with the same structure are placed on top of each other at the time of winding, the effect of the mosaic pattern could propagate through the overall thickness of a filament-wound laminate and transmit to the whole filament-wound shell whereas stacking triangular mosaic units with the opposite structure ($[\pm\phi]$ and $[\mp\phi]$) results in a symmetric laminate and, although the stretching-twisting and bending-shear coupling effects balance each other, additional inter-laminar stresses are induced [6]. Therefore, a filament-winding process requires special adjustments to maintain regular structures of laminated composite materials across the thickness of a filament-wound shell or the positions of consecutive filament-wound $\pm\phi$ angle-ply layers will be shifted arbitrarily and produce some uncertainty for the modelling and estimation of stress states in the structure as the effect of the mosaic pattern cannot be overlooked.

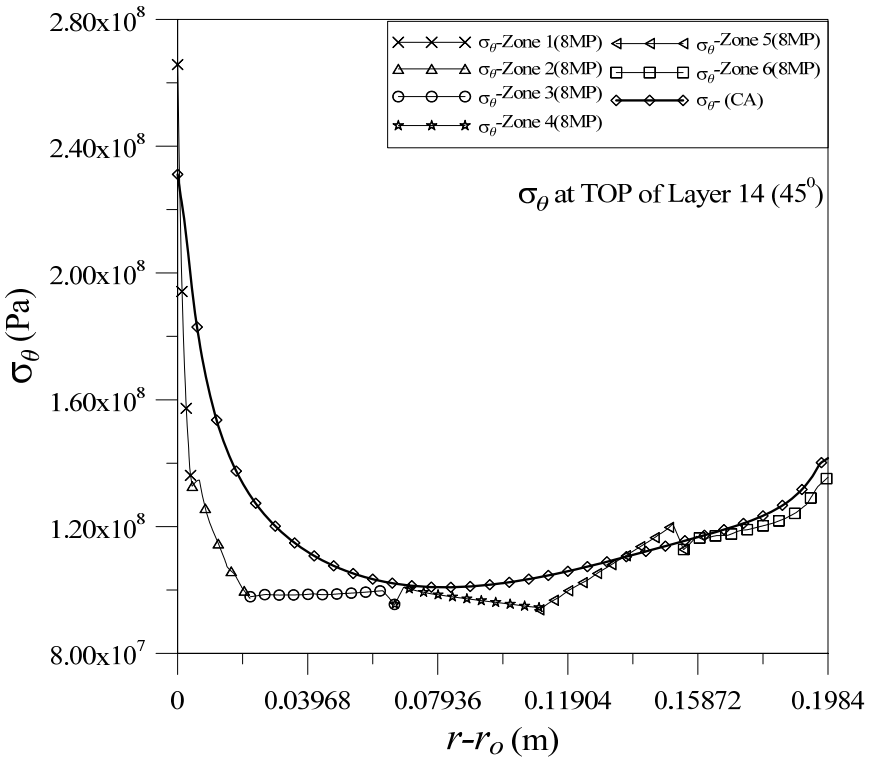

(i) σ_θ (8-unit model)

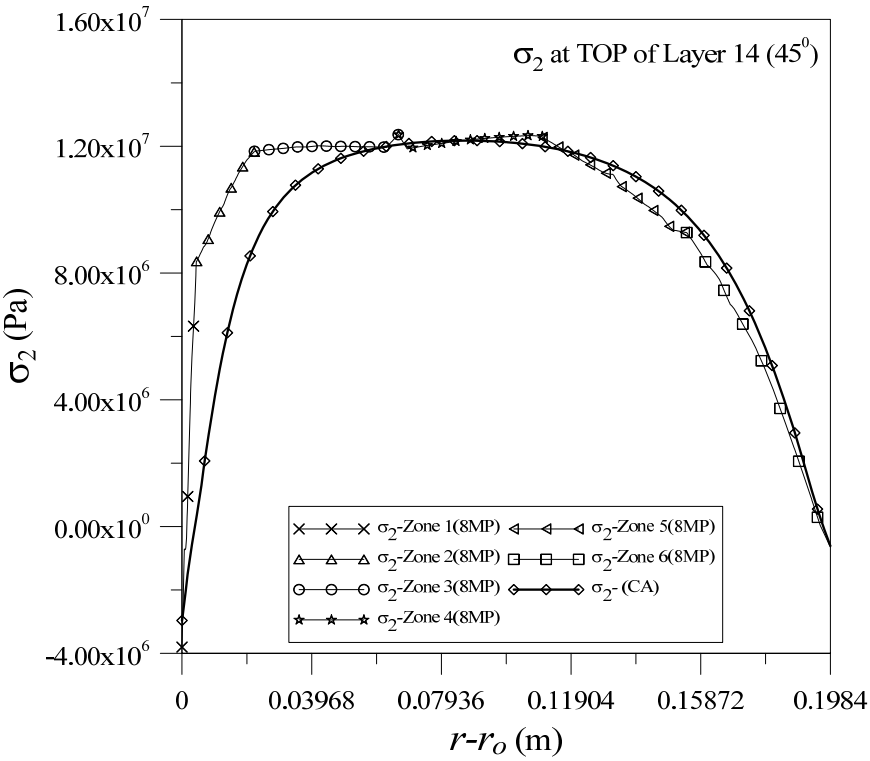

(ii) σ_2 (8-unit model)

Figure 3.23: Radial distributions of (i) σ_θ and (ii) σ_2 in 14-ply disk

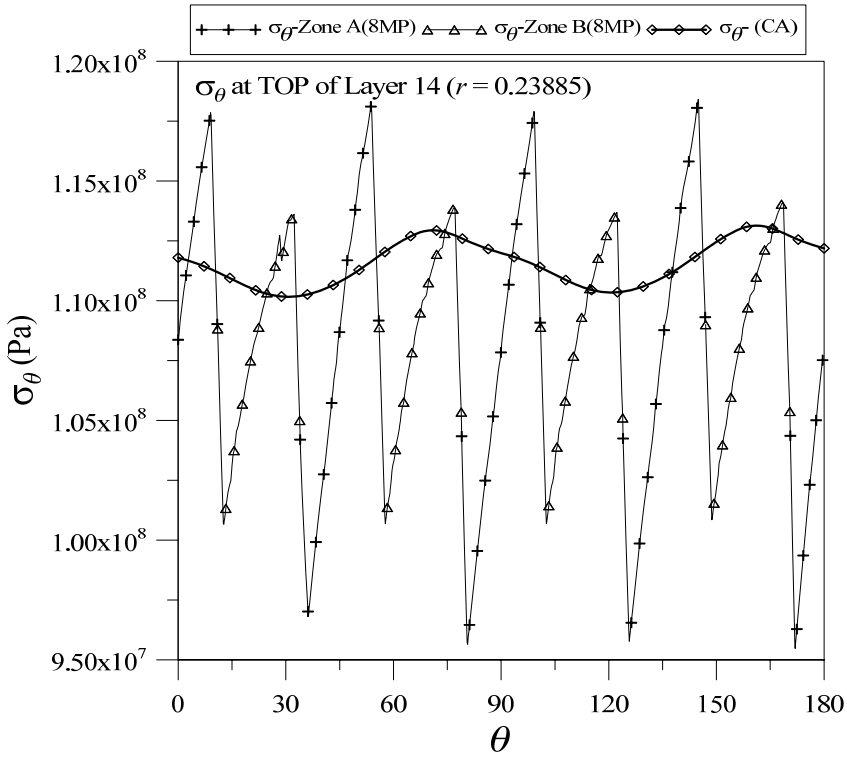

(i) σ_θ (8-unit model)

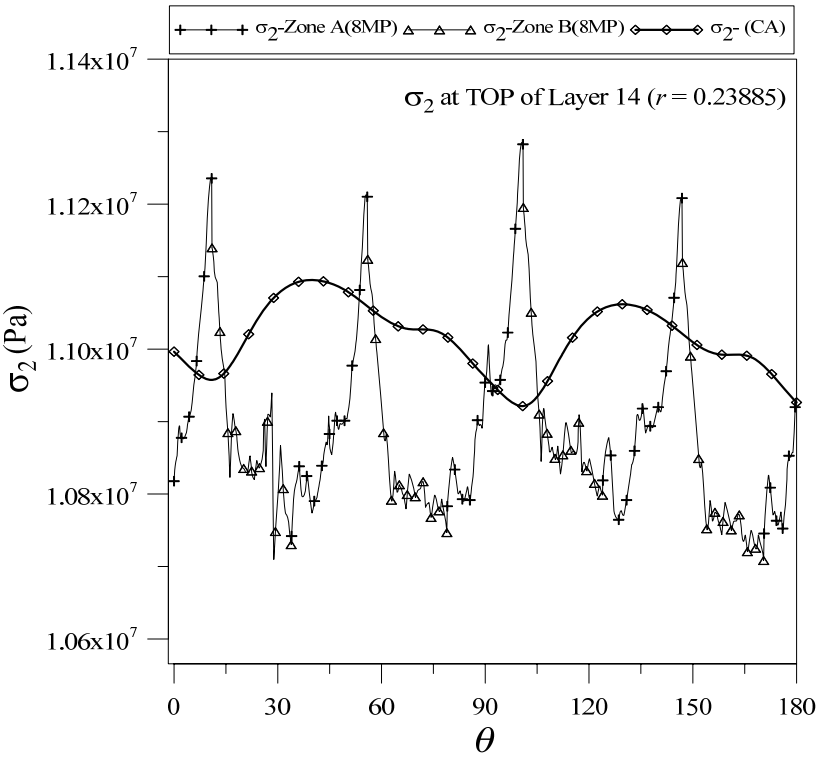

(ii) σ_2 (8-unit model)

Figure 3.24: Circumferential distributions of (i) σ_θ and (ii) σ_2 in 14-ply disk

3.4 Chapter summary

FE analyses of a filament-wound composite flywheel disk considering both a constant thickness and actual thickness variations generated during the filament-winding process are presented in this chapter to demonstrate the effect of the mosaic pattern created during this process on stress distributions and, effectively, the strength of the disk. It is demonstrated that variations in the stresses calculated in different layers of the spinning composite disk obtained from FE analyses of mosaic-patterned models with different levels of thickness differ substantially from those determined by a conventional analysis of a laminated shell; for instance, the maximum value of the hoop stress predicted by the 4-ply disk with 4 mosaic units around its circumference is 48% higher than that obtained from the conventional model. The levels of variation in stress values predicted by both the conventional and mosaic-patterned models fluctuate substantially among different mosaic units located at different positions on the filament-wound flywheel disk. This implies that the mechanical behaviour of the disk is sensitive to the mosaic-patterned configuration and stress distributions are affected by the number of mosaic units around the circumference and along the radius as well as the disk's thickness. As is observed, the 4-unit model of the 4-ply disk predicts an approximately 5% higher value of the maximum tangential stress than the 8-unit model. Similarly, it can be noted from the circumferential distributions that the 4- and 8-unit models of the 4-ply disk determine the maximum deviations of the stress values to be 65% and 54% for the radial stress and 67% and 69% for the hoop stress, respectively, of those obtained from the conventional model. Again, the maximum levels of difference in the stress values from the 6-unit model of the 8-ply disk are found to be 52% and 42% for the stresses along and across the fibres, respectively. With increments in the level of thickness, the effect of the mosaic pattern on the stress states gradually diminishes; for example, circumferential distributions of both the hoop stress and stress across the

fibres maintain 4% to 15% differences in values compared with those obtained from the conventional model. However, it can be stated that the levels of maximum stresses in a filament-wound disk with low levels of thickness could be underestimated by a conventional FEA technique. The results obtained clearly show the sensitivity of the mechanical behaviour of a spinning filament-wound composite flywheel disk and the effect of the mosaic pattern on its stress distributions in different plies. It also demonstrates the necessity of incorporating actual thickness variations induced in a filament-wound spinning disk in FE modelling and analysis as the disk's actual stress distributions could remain undetermined if both its mosaic pattern and actual level of thickness are disregarded.

It should be noted that, apart from the stress distributions having different characteristics due to the various mosaic-patterned configurations, the stresses' minima and maxima are located at different locations on the disk from those obtained from the conventional technique. This indicates that the results obtained from a conventional modelling technique may predict inaccurate results if actual manufacturing effects are not incorporated in the model of a filament-wound composite structure. The methodology proposed in this work will be useful in designing filament-wound composite structures and determining their mechanical responses under various loadings and boundary conditions.

Chapter 4

Finite Element Analysis of Variable-stiffness Laminates

4.1 Overview

As a composite material allows a laminate's stiffness and strength to be controlled, design flexibility is realised; for instance, to produce stiffness variations in a laminate, its fibre paths, composition, thickness and fibre volume fraction can be varied, with such a composite laminate termed a variable-stiffness (VS) laminate. Modern automated fibre-placement machines can precisely steer fibre tows and build composite laminates which have different elastic properties at different points. Allowing the fibres to follow curvilinear paths within the plane of a laminate offers an advanced tailoring option for modifying the load paths within the laminate to obtain suitable stress distributions and improve performances under various loadings. Compared with conventional straight-fibre laminates, VS laminates may exhibit advantageous properties in terms of buckling and first-ply failure resistance for a wide range of structural components. Therefore, many researchers have focused on analysing such laminates with spatially varying fibre paths which requires employing appropriate techniques to assess their actual responses under given loads. To achieve this, a finite element analysis (FEA) method could be utilised to analyse VS laminates and determine appropriate design parameters, such as fibre orientation angle, number of plies, thickness and stacking sequence. However, as some limitations of conventional approaches could make incorporating all these variables into FE modelling

using any FEA package a challenging task, there is a need to devise a methodology capable of overcoming them. As discussed in Chapter 2, a filament-wound composite flywheel disk characterised by not only curvilinear fibre trajectories but also a special mosaic-patterned configuration requires a special technique to accomplish appropriate FE modelling to take into account actual variations in the fibre angles due to varying trajectories and the in-built filament-wound mosaic pattern. As can be seen, performing this modelling using the FEA package ANSYS is a time-intensive process which involves accurate meshing and the handling of individual elements to define accurate fibre orientation angles in order to maintain the curvilinear fibre paths. Therefore, it is desirable to develop a simpler modelling approach, with a view to which a filament-wound flywheel disk is treated as a plate reinforced with different types of spatially varying fibre trajectories. Then, an attempt is made to model these rudimentary curvilinear fibre paths more accurately than can be achieved using a conventional technique. For simplicity, a rectangular composite plate is considered and FE analyses carried out based on the proposed method. The results obtained from comparative analyses considering different types of variations in fibre paths within the panel are presented in this chapter.

4.2 Effects of varying fibre paths

Composite materials offer a range of properties superior to those of traditional materials and allow the precise design and tailoring of materials to meet the demands of a particular application. As the steering of fibres creates variations in angles and generates stiffness variations in laminates, the fibre paths created have different fibre orientation angles at different points on a VS plate. For changing fibre paths, fibre orientation angles are varied in different ways. Steering the fibres in a composite laminate along the load path of a structure offers improvement in stiffness and strength; for example, steering of fibres using load path trajectories during the manufacturing of a composite joint increases both its initial

and ultimate failure strengths [72]. Also, the bearing strength of a bolted joint in a composite laminate is enhanced by steering the fibres to follow both the tensile and compressive principal stress trajectories around the hole [73] while an improvement in buckling performance is also achieved through the VS concept [7, 17, 31]. Numerical studies demonstrate the improvement in bending stiffness of simply supported rectangular plates with varying fibre orientation angles over that with constant fibre orientation angles [35]. Laminates tailored with constant fibre angles do not show the maximum possible strength to non-uniformly distributed in-plane stress [74]; for instance, holes and notches create non-uniform stresses. Therefore, fibres should be steered along load paths in order to enable a laminate to withstand the highest loads and handle stress concentration. Directing fibre paths according to the load path trajectories for stress variations under given loads facilitates the strengthening of laminates by diverting loads from the most sensitive regions of composite structures.

4.3 Tailoring of laminates with spatially varying fibre paths

An advanced composite material is characterised by a higher specific stiffness (stiffness/density) and specific strength (strength/density) than those of other engineering materials. Because of these properties, composite materials are used extensively in advanced engineering applications in various fields, such as the aeronautical and space industries, and automotive and military sectors. Traditionally, composite laminates have been tailored by exploiting their design variables, namely the fibre volume fraction, fibre orientation in each individual lamina, number of laminas and stacking sequence of all the plies bonded together, with fibre orientation angles within each ply generally assumed to be constant at all points in the plane of the laminate. The usual design of a laminate limits the potential of composite materials because any combination of these design variables with constant values produces unvarying laminate properties. However, they can be configured

in different ways to obtain laminates suitable for particular applications under different loadings.

Recent manufacturing technologies, such as computer-controlled filament-winding and tape-laying machines, and automated fibre and tow placements, make it possible to precisely steer the fibre tows and build composite laminates, the elastic properties of which vary at different points. For a flat panel, as steering the fibres along its axes results in variations of its fibre orientation angles from one location to another, it exhibits VS properties. Sometimes, the fibre orientation angles of some composite structures are automatically varied through manufacturing processes; for example, as the trajectories of the fibre paths automatically change during the manufacturing of a filament-wound pressure vessel, VS is inherently produced. Of the different techniques for tailoring a composite laminate, as the most flexible is to vary the fibre orientations at different locations throughout each lamina, VS laminates need to be manufactured with a high degree of precision. Therefore, correct fibre orientation angles should be maintained during both the laying of fibres and curing. With the help of a computer-controlled automated advanced fibre-placement machine, VS laminates can be produced according to the required configurations.

4.3.1 Varying fibre paths in flat panels

Various techniques for modelling and predicting the responses of VS laminates under different loadings have been attempted. In almost every case, the fibre orientation is spatially varied within a ply to improve the stiffness and, thereby, the structural performance of a laminate. Considering the practical limitations of processing techniques, the simple formulation for defining varying fibre paths using a minimum number of parameters devised by Gurdal and Olmedo [17, 32-33] allows the fibre orientation angle to

vary continuously throughout a composite panel in order to change the response of a fibre-reinforced laminate.

A linear variation of the fibre orientation angle along only one of the coordinates is considered in the formulation, with the angle of the reference fibre path assumed to be T_0 at the geometrical centre (x_0, y_0) of the panel and varying linearly to reach a value of T_1 at a specified distance (d), as illustrated in Figure 4.1, where d is regarded as the characteristic dimension of the composite panel to be designed. For a rectangular laminate, d is generally half the panel width in the direction along which the fibre orientation angle varies. The notation for the reference curvilinear fibre path defined using T_o and T_1 for a linear variation of the fibre orientation angle is abbreviated as $< T_0, T_1 >$.

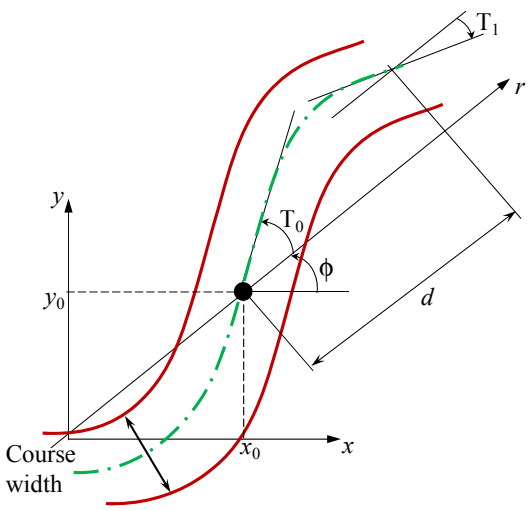

Figure 4.1: Reference fibre path with linear variation of angle

During the manufacturing process, an advanced fibre-placement machine follows the course of the reference fibre path when placing a band of tows with other fibre tows placed parallel to the reference course to cover the whole ply. To obtain a more general definition of the fibre path, the axis of variation of the fibre orientation is rotated by an angle (ϕ) from the x axis (Figure 4.1), with the new axis obtained after the rotation denoted by r and the reference fibre path assumed to be antisymmetric about the origin of variation of the angle.

To obtain the linear variation of the fibre orientation angle (θ) along the r axis, θ is defined in terms of ϕ, T_0, T_1 and r by the following piece-wise continuous functions [25].

$$\theta(r) = \begin{cases} \phi + (T_0 - T_1)\dfrac{r}{d} + T_0, & -d \le r < 0 \\ \phi + (T_1 - T_0)\dfrac{r}{d} + T_0, & 0 < r \le d \end{cases} \tag{4.1}$$

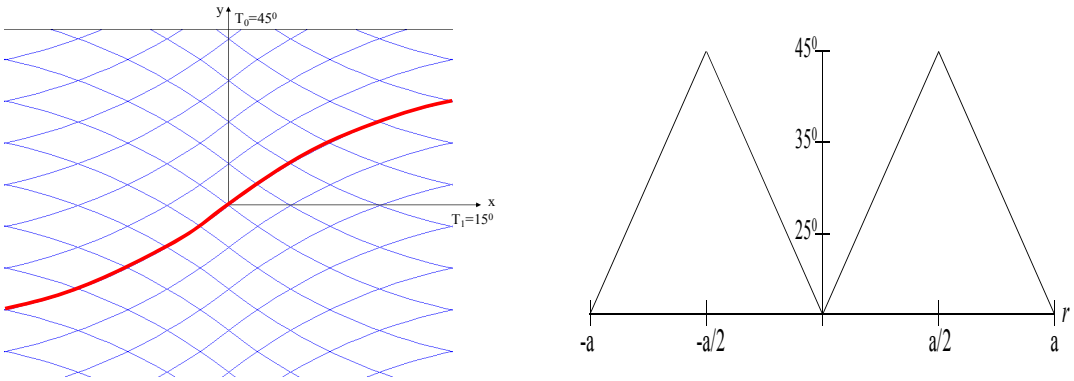

(i) fibre paths

(ii) linear saw-toothed pattern of variations of fibre orientation angle

Figure 4.2: Variable-stiffness panel configuration ($T_0 = 45^0, T_1 = 15^0, \phi = 0^0$)

As the fibre orientation angle from Eq. (4.1) repeats with a period of $2d$ so that $\theta(r)$ becomes periodic and continuous, the variation of the fibre orientation angle follows a linear saw-toothed pattern with limits of T_0 and T_1 [25, 28-29], and an example of a rectangular panel lamination with a linear combination of fibre orientation angles of $T_0 = 45^0$ at the mid-length and $T_1 = 15^0$ at the end of the laminate is presented in Figure 4.2(i) in which the reference fibre path is represented by a bold solid line, the other fibre paths defined through shifting the reference path along the y axis and two adjacent layers with equal and opposite fibre orientations considered for the laminate. For a moderate variation of the fibre angle, the fibre paths are parallel to one another and the linear variation of the angle maintains a saw-toothed pattern with limits of 45^0 and 15^0, as shown in Figure 4.2(ii), with the addition of ϕ to the fibre path defined by $< 45^0, 15^0 >$ rotating the axis along which the fibre orientation varies. It should be mentioned that, although the

fibre orientation angle can be varied in different ways, linear variation is the simplest method.

4.3.2 Circular arc variation

A different type of variation of the fibre orientation angle based on a circular arc instead of linear variation can be formulated using the same three parameters (T_0, T_1 and d) to define a constant-curvature reference fibre path [18, 75]. A schematic of a circular variation of the fibre orientation angle is illustrated in Figure 4.3.

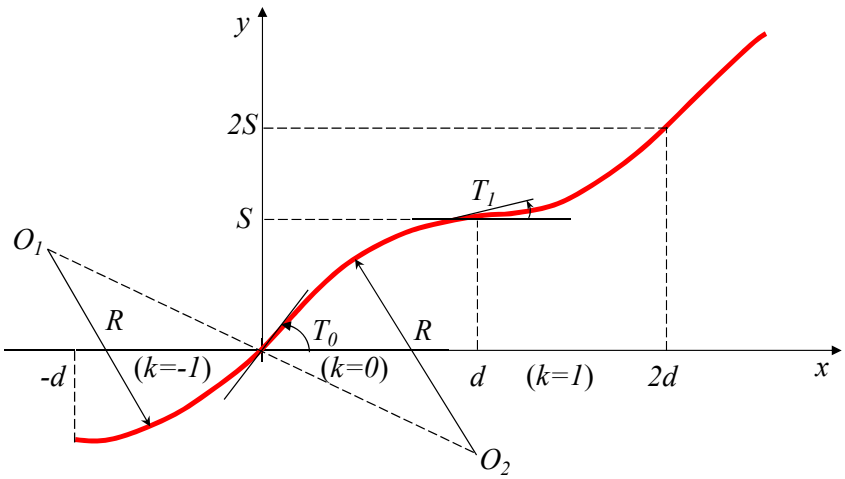

Figure 4.3: Reference fibre path with constant curvature based on circular arc

This technique of defining a reference fibre path based on a circular arc variation has the advantage of producing courses of constant curvature that correspond to the manufacturing constraints of a fibre-placement machine. The first parameter (T_0) represents the fibre orientation angle at the origin of the coordinate system and the second (T_1) the fibre orientation angle at a certain distance (d) from the origin. Each segment of the reference fibre path represents the constant curvature arc with a radius (R) equivalent to the reciprocal of the curvature which can be determined geometrically using the parameters (T_0, T_1 and d) as [75]

$$\kappa(x) = \frac{1}{R} = \frac{(-1)^k(\sin T_1 - \sin T_0)}{d}, \quad k = \text{floor}\left[\frac{x}{d}\right] \tag{4.2}$$

where the *floor* function truncates the real number to the nearest integer that is less than or equal to it.

It should be noted that the curvature is a signed quantity for determining on which side of the arc the centre of curvature is located and the centre of each arc can be calculated as

$$(x_c, y_c) = \begin{pmatrix} (kd - R\sin T_0, kS + R\cos T_0), & k \text{ even} \\ (kd - R\sin T_1, kS + R\cos T_1), & k \text{ odd} \end{pmatrix}$$
$$k = \text{floor}\left[\frac{x}{d}\right], \quad S = d\frac{\cos T_1 - \cos T_0}{\sin T_0 - \sin T_1} \tag{4.3}$$

where S represents the span of one arc in the y direction.

The relationship of the fibre orientation angle is determined as

$$\sin\theta(x) = \begin{Bmatrix} \sin T_0 + (\sin T_1 - \sin T_0)\left(\frac{x}{d} - k\right), & k \text{ even} \\ \sin T_1 + (\sin T_0 - \sin T_1)\left(\frac{x}{d} - k\right), & k \text{ odd} \end{Bmatrix}, \quad k = \text{floor}\left[\frac{x}{d}\right] \tag{4.4}$$

The ordinate of each point on the fibre path following the circular arc can be expressed as a function of the constant curvature and fibre orientation angle at that particular point as

$$y(\kappa, \theta) = \begin{Bmatrix} kS - \frac{1}{\kappa}(\cos\theta - \cos T_0), k \text{ even} \\ kS - \frac{1}{\kappa}(\cos\theta - \cos T_1), k \text{ odd} \end{Bmatrix} \tag{4.5}$$

4.3.3 Representation of multi-parameter fibre orientation angle

The linear and circular arc variations of the fibre orientation angle presented in the previous sections generate curves that represent limited classes of fibre orientation variations considering their manufacturability with the help of available fabrication techniques, with their fibre paths resulting in a relatively narrow design space. As this requires continuous design variables for treating variations of the fibre orientation angles at every point of the layer without any restrictions, it generates some issues with fibre

continuity and manufacturability [7, 18, 76-77]. To overcome the limitations of the previously mentioned variations of the fibre orientation angles, a new approach in which variations are defined based on Lobatto-Legendre polynomials has been introduced [18-19].

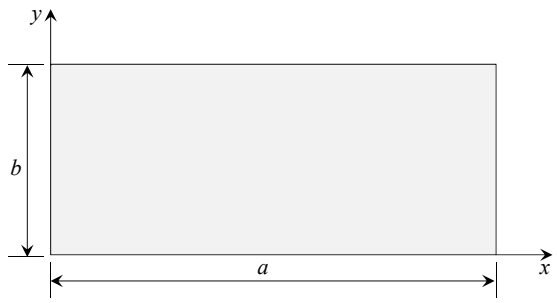

Figure 4.4: Rectangular domain with coordinate system

For the rectangular domain shown in Figure 4.4, the normalised coordinates can be defined as

$$\xi = \frac{2x - a}{a}, \quad \eta = \frac{2y - b}{b}; \ -1 \leq \xi, \eta \leq 1 \tag{4.6}$$

The fibre orientation angle in the $\xi - \eta$ plane is defined as

$$\theta(\xi, \eta) = \sum_{i=0}^{m-1} \sum_{j=0}^{n-1} T_{ij} L_i(\xi)\, L_j(\eta) \tag{4.7}$$

where m and n are the numbers of basis functions used in the ξ and η directions, respectively, T_{ij} the unknown coefficients (called the Lobatto coefficients) and L_i the Lobatto polynomials defined as

$$L_i(\xi) = \int_{-1}^{\xi} P_{i-1}(\mu) d\mu\,, \ \ i \geq 2; \quad L_0(\xi) = 1, L_1(\xi) = \xi \tag{4.8}$$

Eq. (4.8) can be written in a recursive form as

$$L_i(\xi) = \frac{1}{i}\big(\xi P_{i-1}(\xi) - P_{i-2}(\xi)\big)\ , \qquad i \geq 2 \tag{4.9}$$

where P_i are the Legendre polynomials given by

$$P_i(\xi) = \frac{[(2i-1)\xi P_{i-1}(\xi) - (i-1)P_{i-2}(\xi)]}{i} \quad , \quad i \geq 2 \tag{4.10}$$

where $P_0(\xi) = 1$ and $P_1(\xi) = \xi$.

As, to visualise the variation of the fibre orientation angle given by Eq. (4.7), it is considered that this angle varies along one axis (i.e., ξ) and can be defined as

$$\theta(\xi) = \sum_{i=0}^{m-1} T_i L_i(\xi) \tag{4.11}$$

Considering three, four and five coefficients, the fibre orientation angles become, respectively

$$\theta(\xi) = T_0 + T_1\xi + \frac{1}{2}T_2(\xi^2 - 1)$$
$$\theta(\xi) = T_0 + T_1\xi + \frac{1}{2}T_2(\xi^2 - 1) + \frac{1}{2}T_3\xi(\xi^2 - 1)$$
$$\theta(\xi) = T_0 + T_1\xi + \frac{1}{2}T_2(\xi^2 - 1) + \frac{1}{2}T_3\xi(\xi^2 - 1) + \frac{1}{8}T_4(5\xi^4 - 6\xi^2 + 1)$$

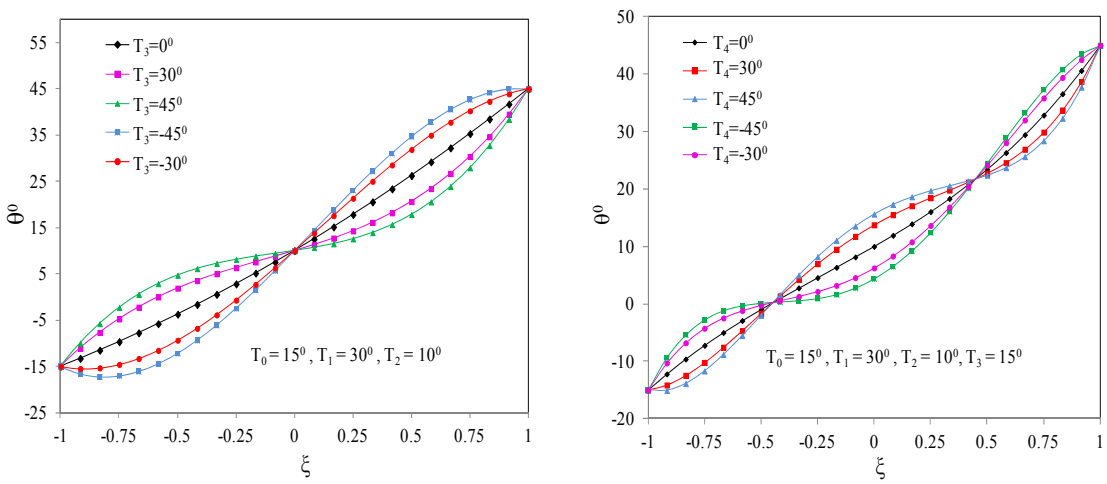

(i) four coefficients (ii) five coefficients

Figure 4.5: Distributions of fibre angle with different number of coefficients

It can be noted that a variation of the fibre orientation angle ($\theta(\xi)$) becomes linear if only the first two coefficients are considered and represents the two-parameter linear fibre angle variation given in Eq. (4.1). The distributions of the fibre angles illustrated in Figure

4.5 demonstrate variations of θ based on considering four and five Lobatto coefficients for different values of T_3 and T_4. It is clear that there is a greater capability to represent variations of the fibre orientation angles along one axis by increasing the number of Lobatto coefficients but, as greater flexibility will be achieved by varying the fibre orientation angles along both axes of the 2D domain, composite laminates can be built using the directional properties of the fibres to meet certain requirements.

4.3.4 Variable fibre orientations in conical and cylindrical shells

The material properties of conical and cylindrical composite shells can be tailored to improve performances under different loadings through varying the fibre orientations in terms of their circumferential positions. VS in conical and cylindrical shells can be obtained through two types of variations of the fibre orientation angle: an axial angle variation for both general conical shells and cylinders; and a circumferential angle variation for cylindrical shells [78-80].

4.3.5 Fibre paths in VS flat panels

As the fibres must follow specific paths to obtain their expected orientation variations based on the geometric surfaces of composite structures, to attain manufacturability, a reference fibre path should be defined in terms of a suitable coordinate system for the particular geometry [75]; for example, the Cartesian coordinate system for rectangular composite panels and the polar coordinate system for a rectangular plate with a circular hole. Similarly, axial and circumferential coordinates are used to model cylindrical shells and polar coordinates for conical shells. Therefore, the geometry of a composite structure dictates the configuration of its reference fibre path for steering fibre tows during the manufacturing process. In order to define this path for an automated fibre-placement machine, a 3D surface of the expected structure needs to be transformed to two coordinates

and the tow courses defined by these two coordinates converted again to 3D space for the structure under construction using mathematical or numerical transformations [75]. A reference fibre path defined for a specific geometry cannot conform to arbitrary surfaces.

For a linear variation of the fibre orientation angle in a flat composite panel, the fibre orientation is assumed to be symmetric with respect to the axis perpendicular to the axis along which the fibre orientation is made to vary. Therefore, a fibre path that passes through the geometrical centre of the considered laminate is a smooth antisymmetric function of the coordinate along which the fibre angle varies linearly. The reference fibre path can be derived using the following technique. As the fibre orientation angle differs at each point along the described reference fibre path on the rectangular laminated composite panel in Figure 4.1, the slope of the reference fibre path is

$$\frac{dy}{dr} = \tan\,[\theta(r)] \tag{4.12}$$

Using this relationship, we can establish the path equation for a particular fibre orientation if the start and end angles of the fibre, the angle of rotation of the axis along which the variation occurs and some boundary conditions are provided. Therefore, the reference fibre path with a linear variation of the angle is defined as

$$y = \int \tan[\theta(r)]\ dr \tag{4.13}$$

For the fibre orientation angle (θ) defined in Eq. (4.1), the equation of the reference fibre path which covers the whole panel shown in Figure 4.2(i) is obtained by integrating Eq. (4.13) as

$$y = \frac{d}{(T_1 - T_0)} \ln\left[\cos\left(\phi + T_0 - (T_1 - T_0).\frac{r}{d}\right)\right] + C_1, \quad -d \leq r < 0$$
$$y = -\frac{d}{(T_1 - T_0)} \ln\left[\cos\left(\phi + T_0 + (T_1 - T_0).\frac{r}{d}\right)\right] + C_2, \quad 0 < r \leq d \tag{4.14}$$

The integration constants (C_1 and C_2) can be obtained from the boundary condition, which states that, at the origin of the panel (x_0, y_0), the value of r is zero, as

$$C_1 = y_0 - \frac{d}{(T_1 - T_0)} \ln[\cos(\phi + T_0)]$$
$$C_2 = y_0 + \frac{d}{(T_1 - T_0)} \ln[\cos(\phi + T_0)] \tag{4.15}$$

Therefore, a reference fibre path that passes through the origin of the panel along the r axis is defined as

$$y = y_0 + \frac{d}{(T_1 - T_0)}\left[\ln\left[\cos\left(\phi + T_0 - (T_1 - T_0).\frac{r}{d}\right)\right] - \ln[\cos(\phi + T_0)]\right] \quad -d \leq r < 0$$
$$y = y_0 + \frac{d}{(T_1 - T_0)}\left[-\ln\left[\cos\left(\phi + T_0 + (T_1 - T_0).\frac{r}{d}\right)\right] + \ln[\cos(\phi + T_0)]\right] \quad 0 < r \leq d \tag{4.16}$$

A panel lamination is presented in Figure 4.2(i) with $\phi = 0^0$, $T_0 = 45^0$ and $T_1 = 15^0$ for the origin at its mid-length. It should be noted that a panel with $T_0 = T_1$ is actually one with straight fibres and constant stiffness along its length.

4.4 Advanced automated fibre-placement techniques

Advanced fibre placement is a fully automated manufacturing process for composite laminates in which a tow-placement machine precisely accommodates fibre tows on a working surface of the advanced composite part to be manufactured. Its capability to control the speed, feed and tension in each individual tow makes it possible to steer the fibres over complex contours, a process which can maintain a true fibre orientation on a specific surface to allow fibres to be laid down only where required. Therefore, to obtain the desired stiffness variation through varying the fibre orientation, appropriate

manufacturing and design approaches should be followed provided the physical operating limits of the automated fibre-placement machine are incorporated into the component design. These are critical factors for maintaining an efficient manufacturing process and also ensuring that the manufactured component meets the requirements of a particular application [81]. Offline programming is employed to implement a specific fibre path design and its feasibility checked through simulations [25] whereas the automated tow-placement technique greatly improves the repeatability of the process with increased speed.

In order to manufacture the desired composite part while maintaining predefined fibre paths, individual prepreg fibre tows are fed through a fibre delivery system into the tow-placement head, which can accommodate up to 32 tows [25], compacted and then placed on the working surface as a single fibre band. During this fibre-placement process, the head can cut any of the tows or restart which can control the width of the fibre band, changing which facilitates elimination of the gaps or overlaps between adjacent courses. A tow-placement head offers seven degrees of freedom (DOFs) – three position and three orientation axes, and one axis to rotate the mandrel – and the different motions it describes make it possible to align the tows in any direction. The compaction roller attached to the tow-placement head presses the tows onto the working surface and removes trapped air which eliminates the need for vacuum debulking [25]. Compacting using low-tension positioning of the tows allows the fibres to be placed on concave surfaces, with controlled heat used to enhance tackiness while laminating the tows onto the layup surface.

Some composite structures manufactured by the automated fibre-placement technique and used in the aerospace industry are inlet ducts, contoured fuselage panels, full fuselage barrel sections, contoured fairings, nacelle skins, payload shrouds/adapters and structural shafts (straight and contoured) [81].

4.5 Theory of VS laminates

Structures made of composite materials are often designed and manufactured as plates or shells with laminations of successive layers. The most widely used theory of plates/shells, the first-order shear deformation theory (FSDT) which takes into account the effect of transverse shear deformation, is used to model and analyse VS composite laminates.

4.5.1 Plate element formulation

For the four-nodal rectangular element shown in Figure 4.6, the DOFs chosen for each node are u^0, v^0, w^0, θ_x and θ_y, where u^0, v^0 and w^0 are the displacements of a point on the mid-plane along the x, y and z axes, respectively, and θ_x and θ_y the independent rotations of the normal to mid-plane about the x and y axes, respectively. As deformation components comprise membrane (mid-plane), bending and transverse shear parts, strain-displacement relationships can be written in terms of nodal displacements as

$$\begin{bmatrix} \varepsilon_{xx} \\ \varepsilon_{yy} \\ \gamma_{xy} \end{bmatrix} = (\mathrm{B_m} - z.\mathrm{B_b})\boldsymbol{U}$$
$$\begin{bmatrix} \gamma_{zx} \\ \gamma_{yz} \end{bmatrix} = \mathrm{B_s}\boldsymbol{U} \tag{4.17}$$
$$\boldsymbol{U} = \begin{bmatrix} w^0 & \theta_x & \theta_y & u^0 & v^0 \end{bmatrix}^T$$

where $\mathrm{B_m}$, $\mathrm{B_b}$ and $\mathrm{B_s}$ are the strain matrices for the membrane, bending and transverse shear parts, respectively, and $\boldsymbol{U}$ the displacement vector.

As the strain matrices should be determined from the derivatives of the displacements and are dependent on the natural coordinates (ξ and η) (Figure 4.6), the Cartesian coordinate system is transformed into the natural coordinate system for each element the matrix of which is calculated individually.

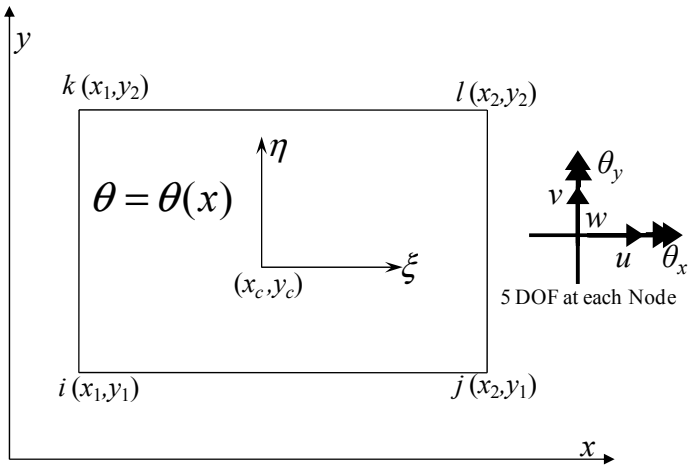

Figure 4.6: Four-nodal quadrilateral element

The shape functions for a four-nodal quadrilateral element are dependent on the natural coordinates as

$$N_m = \frac{1}{4}(1+\xi_m\xi)(1+\eta_m\eta) \quad m = 1,2,3,4$$
$$\xi_m = \pm 1 \ \& \ \eta = \pm 1 \tag{4.18}$$

Using the shape functions, nodal displacements and rotations ($u^0, v^0, w^0, \theta_x, \theta_y$) can be expressed as

$$u^0 = \sum_{i=1}^{4} u_i^0 N_i \quad v^0 = \sum_{i=1}^{4} v_i^0 N_i \quad w^0 = \sum_{i=1}^{4} w_i^0 N_i$$
$$\theta_x = \sum_{i=1}^{4} \theta_{x_i} N_i \quad \theta_y = \sum_{i=1}^{4} \theta_{y_i} N_i \tag{4.19}$$

The strain matrices are determined from the derivatives of the nodal displacements and rotations and, for the four-nodal plate element, are

$$B_m = [B_m^1 \quad B_m^2 \quad B_m^3 \quad B_m^4]$$

$$B_b = [B_b^1 \quad B_b^2 \quad B_b^3 \quad B_b^4]$$

$$B_s = [B_s^1 \quad B_s^2 \quad B_s^3 \quad B_s^4]$$

where

$$B_m^i = \begin{bmatrix} 0 & 0 & 0 & \frac{\partial N_i}{\partial x} & 0 \\ 0 & 0 & 0 & 0 & \frac{\partial N_i}{\partial y} \\ 0 & 0 & 0 & \frac{\partial N_i}{\partial y} & \frac{\partial N_i}{\partial x} \end{bmatrix} \quad (i = 1,2,3,4)$$

$$B_b^i = \begin{bmatrix} 0 & 0 & -\frac{\partial N_i}{\partial x} & 0 & 0 \\ 0 & \frac{\partial N_i}{\partial y} & 0 & 0 & 0 \\ 0 & \frac{\partial N_i}{\partial x} & -\frac{\partial N_i}{\partial y} & 0 & 0 \end{bmatrix} \quad (i = 1,2,3,4) \tag{4.20}$$

$$B_s^i = \begin{bmatrix} \frac{\partial N_i}{\partial x} & 0 & N_i & 0 & 0 \\ \frac{\partial N_i}{\partial y} & -N_i & 0 & 0 & 0 \end{bmatrix} \quad (i = 1,2,3,4)$$

The derivatives of the shape functions are determined using the Jacobean matrix (J) as

$$\begin{bmatrix} \frac{\partial}{\partial x} \\ \frac{\partial}{\partial y} \end{bmatrix} = [\mathrm{J}]^{-1} \begin{bmatrix} \frac{\partial}{\partial \xi} \\ \frac{\partial}{\partial \eta} \end{bmatrix} \tag{4.21}$$

4.5.2 Stiffness matrix of element

The stiffness matrix of a plate element is determined using the potential energy approach in which the total potential energy (**Π**) is the sum of the strain energy (***H***) and potential energy of the external loads (***E***), with the strain energy

$$\boldsymbol{H} = \frac{1}{2}\int_{\mathrm{v}} (\varepsilon^T \sigma + \gamma^T \tau)\, dV \tag{4.22}$$

For a VS composite laminates, the strain energy in terms of the mid-plane strain and curvature is given by

$$\boldsymbol{H} = \frac{1}{2}\boldsymbol{U}^{\mathrm{T}}[\mathrm{R_{mb}}]\boldsymbol{U} + \frac{1}{2}\boldsymbol{U}^{\mathrm{T}}[\mathrm{R_s}]\boldsymbol{U} \tag{4.23}$$

where

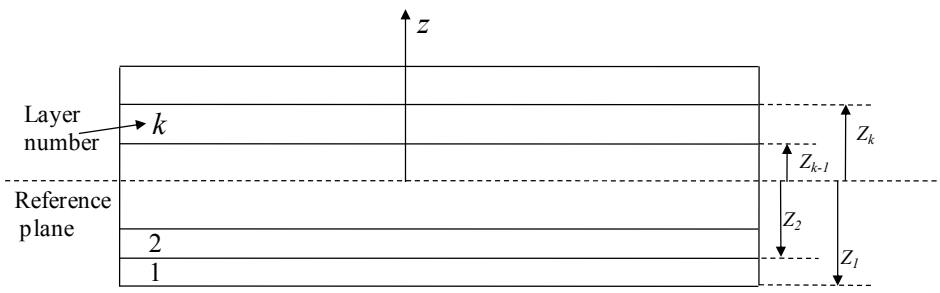

Figure 4.7: Laminate and its reference plane

$$\mathrm{R_{mb}} = \int_{\mathrm{A}} \int_{\mathrm{z_k}}^{\mathrm{z_{k+1}}} [B_m{}^T \bar{Q}^k B_m - z\, B_m{}^T \bar{Q}^k B_b - z\, B_b{}^T \bar{Q}^k B_m + z^2 B_b{}^T \bar{Q}^k B_b] dz\, dA$$

And

$$\mathrm{R_s} = \int_{\mathrm{A}} \int_{\mathrm{z_k}}^{\mathrm{z_{k+1}}} [B_s{}^T \bar{Q}_s{}^k B_s] dz\, dA$$

where $\bar{Q}^k$ and $\bar{Q}_s^k$ are the stiffnesses of the *k*th layer (Figure 4.7). For a VS laminate, these terms are functions of the panel coordinates and must remain part of the integral.

The potential energy of the external loads is given by

$$\boldsymbol{E} = -\boldsymbol{U}^{\mathbf{T}} \int_{\mathrm{V}} [N]^{\mathrm{T}} [\boldsymbol{W}] dV - \boldsymbol{U}^{\mathbf{T}} [\boldsymbol{P}] - \boldsymbol{U}^{\mathbf{T}} \int_{\mathrm{S}} [N]^{\mathrm{T}} [\boldsymbol{T_S}] dS \tag{4.24}$$

where $\boldsymbol{W}$ is the body force, $\boldsymbol{P}$ the concentrated load and $\boldsymbol{T_s}$ the surface traction, and the total potential energy is

$$\boldsymbol{\Pi} = \boldsymbol{H} + \boldsymbol{E}$$

The nodal displacement vector ($\boldsymbol{U}$) corresponding to the minimum of function ($\boldsymbol{\Pi}$) is determined by the condition

$$\left[\frac{\partial \boldsymbol{\Pi}}{\partial \boldsymbol{q}}\right] = \mathbf{0}$$

Therefore, the element stiffness matrix can be written as a combination of the membrane ($\mathbf{K}^{\mathrm{e}}_{mm}$), membrane-bending ($\mathbf{K}^{\mathrm{e}}_{mb}$), bending-membrane ($\mathbf{K}^{\mathrm{e}}_{bm}$), bending ($\mathbf{K}^{\mathrm{e}}_{bb}$) and shear stiffness ($\mathbf{K}^{\mathrm{e}}_{ss}$) matrices as

$$\mathbf{K}^{\mathrm{e}} = \mathbf{K}^{\mathrm{e}}{}_{mm} - \mathbf{K}^{\mathrm{e}}{}_{mb} - \mathbf{K}^{\mathrm{e}}{}_{bm} + \mathbf{K}^{\mathrm{e}}{}_{bb} + \mathbf{K}^{\mathrm{e}}{}_{ss} \tag{4.25}$$

where

$$
\begin{aligned}
\mathbf{K}^{\mathrm{e}}{}_{mm} &= \sum_{k=1}^{nl} \int_{\mathrm{A}} {B_m}^T \bar{Q}^k \, B_m (z_{k+1} - z_k) dA \\
&= \int \int B_m^T(x,y) [\sum_{k=1}^{nl} \bar{Q}^k(x,y)(z_{k+1} - z_k)] \, B_m(x,y) \;\; dx \, dy \\
&= \det \mathrm{J} \int_{-1}^{1} \int_{-1}^{1} B_m^T(\xi,\eta) \left[\sum_{k=1}^{nl} \bar{Q}^k(\xi,\eta) \;\; \{z_{k+1} - z_k\} \right] B_m(\xi,\eta) \;\; d\xi \, d\eta \\
&= \det \mathrm{J} \int_{-1}^{1} \int_{-1}^{1} B_m^T(\xi,\eta) \; [A(\xi,\eta)] B_m(\xi,\eta) \;\; d\xi \, d\eta \\
&= \det \mathrm{J} \sum_{j=1}^{2} \sum_{i=1}^{2} B_m^T(\xi_i,\eta_j) \; \left[A(\xi_i,\eta_j)\right] B_m(\xi_i,\eta_j) \, W_i W_j
\end{aligned}
$$

where nl is the number of laminae in the laminate (Figure 4.7), W_i and W_j are the weights of Gaussian quadrature and $\det \mathrm{J}$ the Jacobian determinant. Although a standard 2×2 Gaussian integration scheme is found to be sufficient for calculating the stiffness matrix using Eq. (4.25), the shear stiffness matrix is calculated on the basis of a 1×1 integration scheme for which $W_i = W_j = 2.0$.

Similarly, the other stiffness matrices are

$$
\begin{aligned}
\mathbf{K}^{\mathrm{e}}{}_{mb} &= \sum_{k=1}^{nl} \int_{\mathrm{A}} {B_m}^T \bar{Q}^k \, B_b \frac{1}{2} ({z_{k+1}}^2 - {z_k}^2) dA \\
&= \det \mathrm{J} \sum_{j=1}^{2} \sum_{i=1}^{2} B_m^T(\xi_i,\eta_j) \; \left[B(\xi_i,\eta_j)\right] B_b(\xi_i,\eta_j) \, W_i W_j
\end{aligned}
$$

$$
\begin{aligned}
\mathbf{K}^{\mathrm{e}}{}_{bm} &= \sum_{k=1}^{nl} \int_{\mathrm{A}} {B_b}^T \bar{Q}^k \, B_m \frac{1}{2} ({z_{k+1}}^2 - {z_k}^2) dA \\
&= \det \mathrm{J} \sum_{j=1}^{2} \sum_{i=1}^{2} B_b^T(\xi_i,\eta_j) \; \left[B(\xi_i,\eta_j)\right] B_m(\xi_i,\eta_j) \, W_i W_j
\end{aligned}
$$

$$
\begin{aligned}
\mathbf{K}^{\mathrm{e}}{}_{bb} &= \sum_{k=1}^{nl} \int_{\mathrm{A}} {B_b}^T \bar{Q}^k \, B_b \frac{1}{3} ({z_{k+1}}^3 - {z_k}^3) dA \\
&= \det \mathrm{J} \sum_{j=1}^{2} \sum_{i=1}^{2} B_b^T(\xi_i,\eta_j) \; \left[D(\xi_i,\eta_j)\right] B_b(\xi_i,\eta_j) \, W_i W_j
\end{aligned}
$$

$$
\mathbf{K}^{\mathrm{e}}{}_{ss} = \sum_{k=1}^{nl} \int_{\mathrm{A}} {B_s}^T \bar{Q}_s^k \, B_s (z_{k+1} - z_k) dA
$$

$$= \det \mathrm{J} \sum_{j=1}^{1} \sum_{i=1}^{1} B_s^T(\xi_i, \eta_j) \left[C\left(\xi_i, \eta_j\right)\right] B_s(\xi_i, \eta_j)\, W_i W_j$$

4.6 Modelling of laminates with spatially varying fibre paths

As the application of composite materials to different engineering components has spurred a major effort to perform analyses to accurately determine their responses under various types of loadings, an efficient tool for the accurate modelling of VS laminates is required. To serve this purpose, a FE method has become an important and frequently indispensable part of engineering analysis and design. However, in the available commercial FE packages, a constant fibre angle needs to be used in each element to approximate varying fibre paths which limits exploiting the capability of a FE method as the actual stiffness variations due to changing fibre paths is not reflected in the modelling of laminates with steered fibre paths.

4.6.1 Conventional FEA of VS laminates

Although many researchers have tried to determine an analytical solution for VS laminates, the most frequently used technique is the FE method as it is easy to consider all the variables in a FE model for predicting responses. Hyer and Lee [7-8] used curvilinear fibre paths to create a VS laminate and analysed a plate with a hole in its centre through FE discretisation but assumed that the fibre orientation within each element was constant. Earlier, Tatting and Gurdal [9] developed a FE solver that could translate an existing FE model into one defined using tow-steered definitions. In it, each element must be assigned a unique stacking sequence according to the location of its centroid, a process which requires an excessive amount of pre-processing time. As they assumed a constant fibre angle within each element, they ignored the actual local stiffness variations within the element's domain.

Discontinuous fibre orientation angles among elements such as those shown in Figure 4.8 have also been used by researchers to model varying fibre courses [10-13].

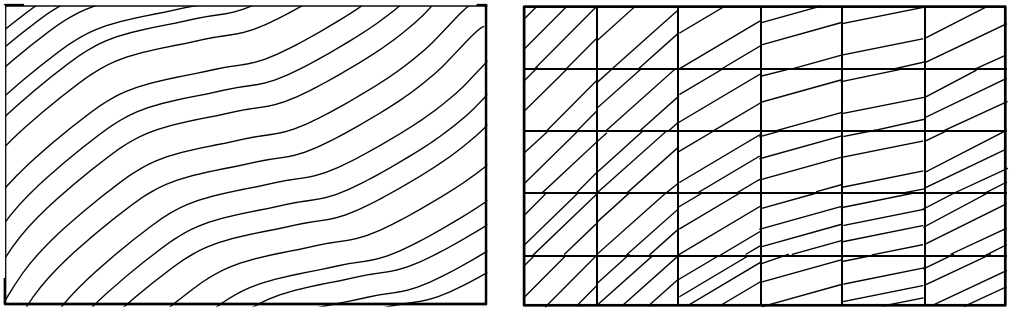

(i) layer with varying fibre paths (ii) approximations of fibre paths

Figure 4.8: Modelling of varying fibre paths considering straight fibre course within elements

For the FE modelling of a VS laminate composite plate, Blom et al. [82] used a fully integrated S4 shell element and Ahmad et al. [18-20] and Lopes[15] shell element (S4R) with reduced integration from the commercial FEA package Abaqus. The local stacking sequence at the centre of each element was determined and manually inserted in the shell section property card which led to not only an excessive pre-processing time but also discrete variations of the fibre angles, with the maximum fibre angle difference between each two neighbouring elements 6^0 [15-16]. Therefore, stiffness variations due to varying fibre paths in an element were ignored. Thus, discretisation of fibre paths employing a constant fibre orientation in each element results in inadequate approximations of continuously varying fibre paths in the modelling of stiffness panels. Eventually, the stress values are highly discrete among the FEs which necessitates a modified approach to improve the accuracy of stress analyses of VS composite plates. As can be observed in Figure 4.9, as considering a constant angle in each element (denoted by small rectangular area) produces considerable discontinuity of the fibre angle (θ) from one element to another, the linear variation defined in Eq. (4.1) is not properly reflected. Therefore, the

actual stiffness variation is substantially affected in FE modelling. As can be seen in Figure 4.10, the normalised effective x-directional modulus (E_x/E_1) that represents the local stiffness of a laminated panel with varying fibre paths is not appropriately reflected in different elements, noting that E_1 is the modulus of a panel with straight fibres.

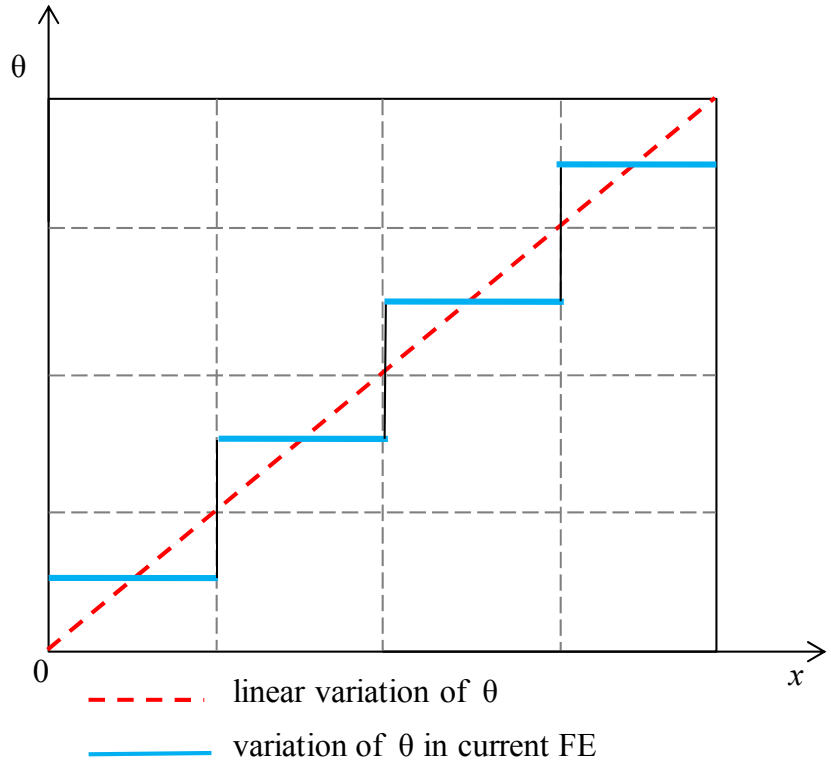

Figure 4.9: Variation of fibre orientation angle in different elements

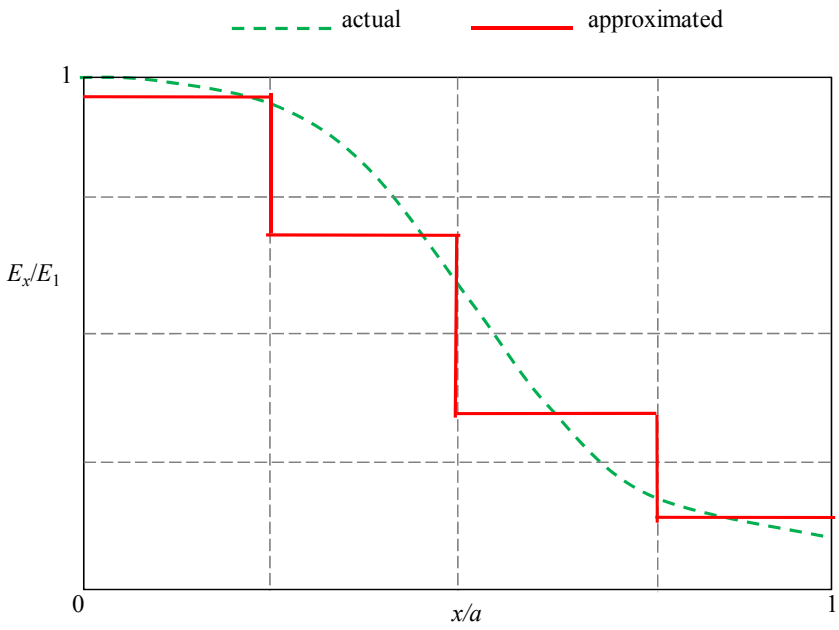

Figure 4.10: Variation of effective axial modulus due to approximations of varying fibre paths

4.7 Modified approach for modelling VS laminates

To minimise the discontinuity in the fibre orientation angles among different elements, a modified approach for calculating the global stiffness matrix of an element for the FE modelling and analysis of a moderately thick, rectangular composite plate with spatially varying fibre paths is adopted. A four-nodal isoparametric rectangular FE that considers four different angles at four Gaussian points (A, B, C and D) based on the definition of continuously varying fibre paths that produce VS panels is chosen (Figure 4.11) and termed a VS element (VSE) which is based on the FSDT.

Different numerical studies are performed to demonstrate the accuracy and efficiency of the VSE and, before conducting a FEA of VS laminates using it, convergence studies of composite laminates with constant fibre paths are undertaken.

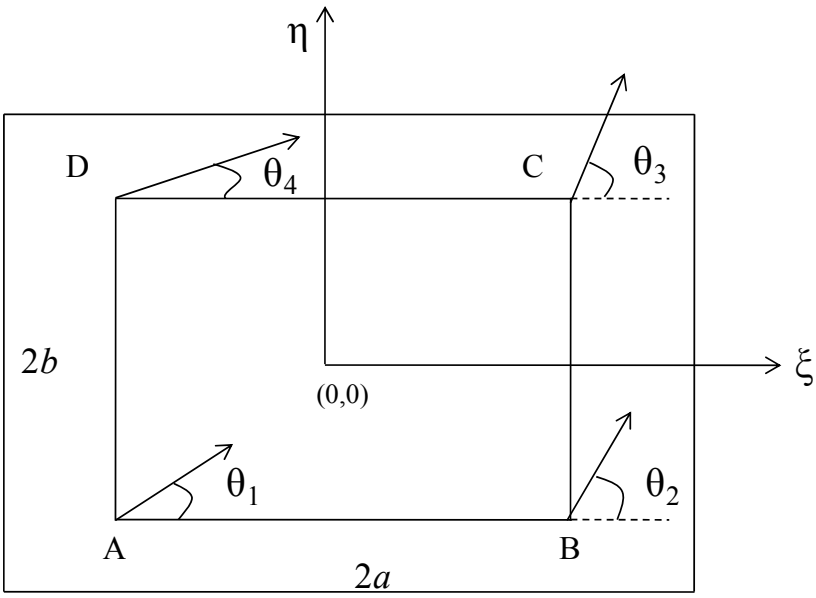

Figure 4.11: Four-nodal isoparametric plate element

4.7.1 Convergence study of VSE

To test the convergence of the proposed technique, the VSE is used for two different problems from published works associated with composite laminates with constant fibre orientations.

Firstly, the VSE is used to predict the central deflection of a simply supported thin, square cross-ply $(0/90)_s$ composite plate 400 mm long and 4 mm high under a uniformly distributed load, the material properties of which are given in Table 4.1, and the result compared with the exact solution [68, 83] and FE solution from ANSYS.

The exact central deflection is given in the form of a double Fourier series as

$$w(x^0, y^0) = \frac{16q}{\pi^6} \sum_{m=1,3,5\ldots}^{\infty} \sum_{n=1,3,5\ldots}^{\infty} \frac{\sin\frac{m\pi}{2}\sin\frac{n\pi}{2}}{mn[D_{11}\left(\frac{m}{l}\right)^4 + 2(D_{12}+2D_{66})\left(\frac{m}{l}\right)^2\left(\frac{n}{l}\right)^2 + D_{22}\left(\frac{n}{l}\right)^4]} \tag{4.26}$$

where l is the length of the square plate and D the bending stiffness of the laminate.

Table 4.1: Material properties of cross-ply composite plate

Material properties	Geometric properties	Loading
E_1 = 140.5 GPa	Length = 0.4 m	250 N/m^2
E_2 = 10.0 GPa	Height = 0.004 m	(uniformly distributed)
G_{12} = 5 GPa		
$G_{13} = G_{23}$ = 3.5 GPa		
ν_{12} = 0.30		

Using $m = n = 13$, the central displacement is calculated from the rapidly convergent series in Eq. (4.26) and the central deflection (w) obtained from different methods are shown in Table 4.2.

Table 4.2: Central deflection of cross-ply composite plate

w (m)	Fourier series	ANSYS (12×12)	VSE (12×12)
	1.0956×10^{-4}	1.09924×10^{-4}	1.09536×10^{-4}

Secondly, an example of numerical analysis ('VM82') is chosen from the verification manual in ANSYS in which the central deflection of the square simply supported orthotropic plate [84] shown in Figure 4.12 is calculated using the VSE and the results compared with those obtained from other techniques to check convergence. The geometric properties used for this analysis are given in Table 4.3 and the convergence of the central deflections obtained from different techniques shown in Figure 4.13. It can be seen that the maximum central deflection converges to both the analytical solution and solution obtained using ANSYS with increases in the numbers of elements, and that even a very coarse mesh of only four elements yields sufficiently accurate results.

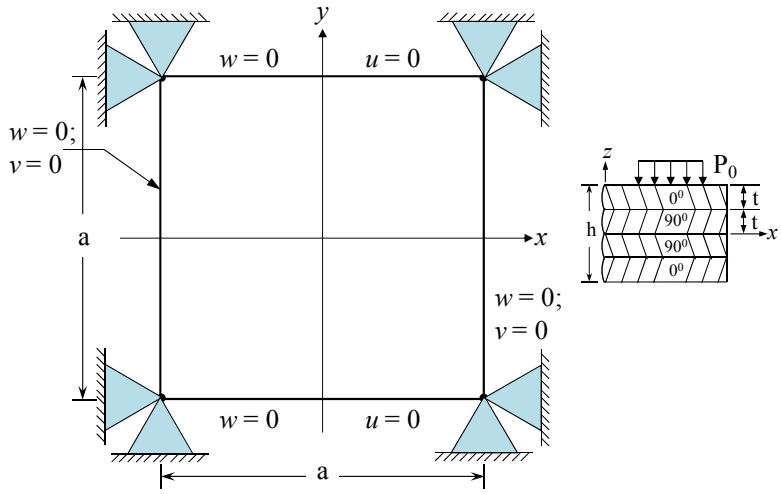

Figure 4.12: Simply supported laminated plate

Table 4.3: Properties of laminated composite plate (VM82.dat)

Material properties	Geometric properties	Loading (P_o)
E_1 = 25 MPa	a = 0.4 m	1 N/m^2
E_2 = 1 MPa	h = 0.1 m	(uniformly distributed)
$G_{12} = G_{13}$ = 0.5 MPa	t = 0.025 m	
G_{23} = 0.2 MPa		
ν_{12} = 0.25		

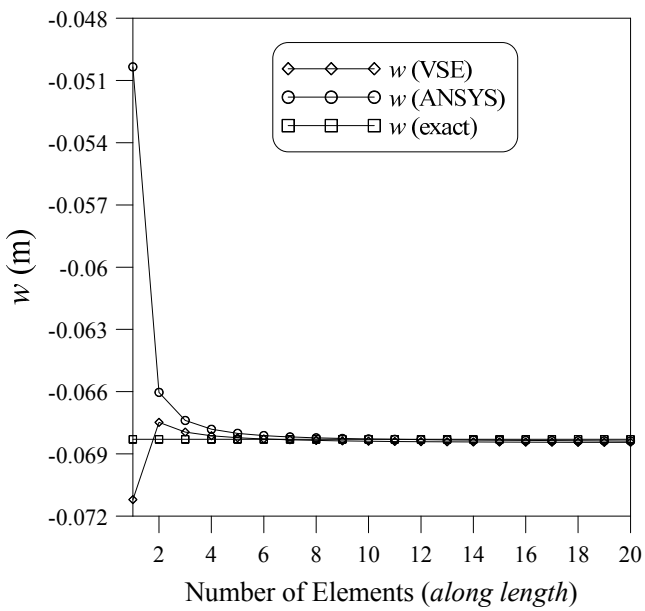

Figure 4.13: Convergences of central deflection of orthotropic plate

4.8 Analysis of composite plate with constant fibre angle

To validate the efficiency of the VSE developed for the study of composite panels with both constant and varying fibre paths, an initial FEA is carried out for a composite plate reinforced with straight fibres. The symmetric balanced composite plate shown in Figure 4.14 is analysed to confirm that the VSE accurately predicts the response of the composite plate under applied tension.

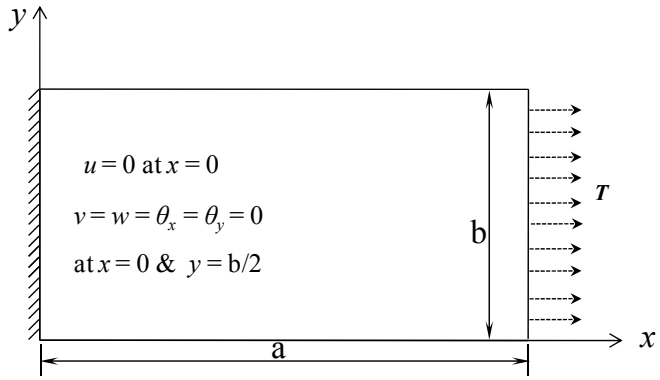

Figure 4.14: Laminated composite plate

The symmetric balanced laminate with a constant fibre orientation $(-60/60)_s$ is analysed using both the VSE and ANSYS for the boundary conditions shown in Figure 4.14. It has four graphite-epoxy layers of a uniform thickness (t), its material properties are given in Table 4.4 and it is loaded with a uniform tension of T at $x = a$. A mesh size of 20×10 is considered for analyses in both the VSE and ANSYS and, for that in ANSYS, the SHELL181 element is used.

Table 4.4: Properties of symmetric balanced laminated composite plate

Material properties	Geometric properties	Loading
E_1 = 180.99 GPa	a = 0.50 m	T = 500 N
E_2 = 10.3 GPa	b = 0.25 m	(uniform tension)
$G_{12} = G_{13}$ = 7.17 GPa	t = 1.27×10^{-3} m	
G_{23} = 3.0 GPa		
ν_{12} = 0.28		

4.8.1 Numerical results

The displacement patterns of the plate under tension are compared with both the VSE and ANSYS predictions as are the stress and strain distributions through the thickness, and the stress resultant. Also, the stress distributions across the mid-length and at the edge of the plate are evaluated.

The nodal displacements (both *u* and *v*) are calculated at three different positions (Figure 4.14) along the *y* axis (at y = 0, b/2 and b) and compared in Figures 4.15 and 4.16 in which it can be clearly observed that the VSE predicts them exactly as ANSYS does and, for laminates with straight fibres, the *u* and *v* displacements are linear with respect to *x* and *y*, respectively.

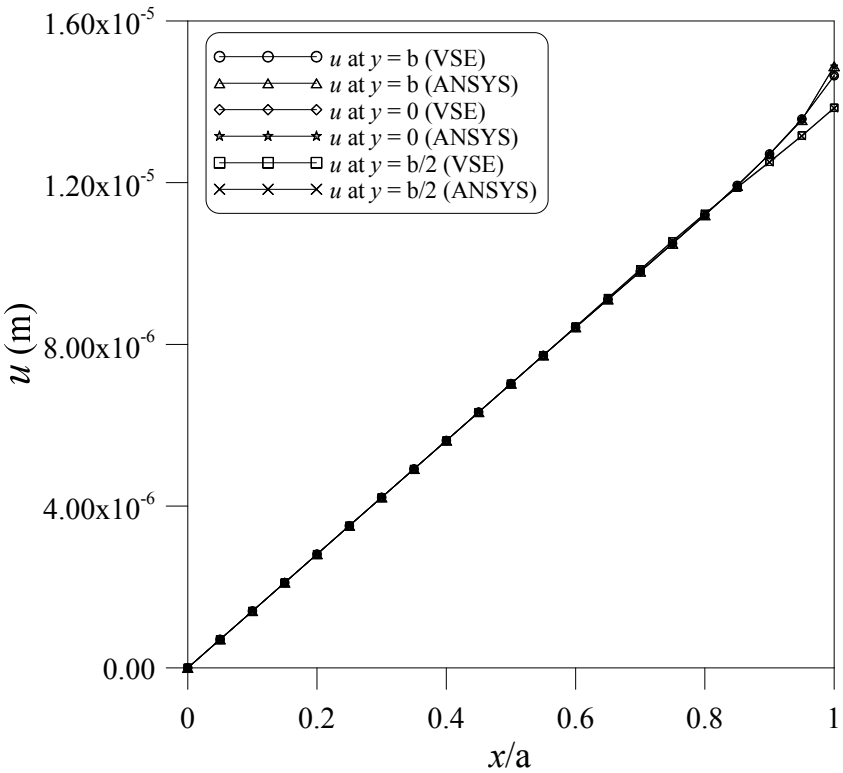

Figure 4.15: *u* displacements at different positions along the *y* axis

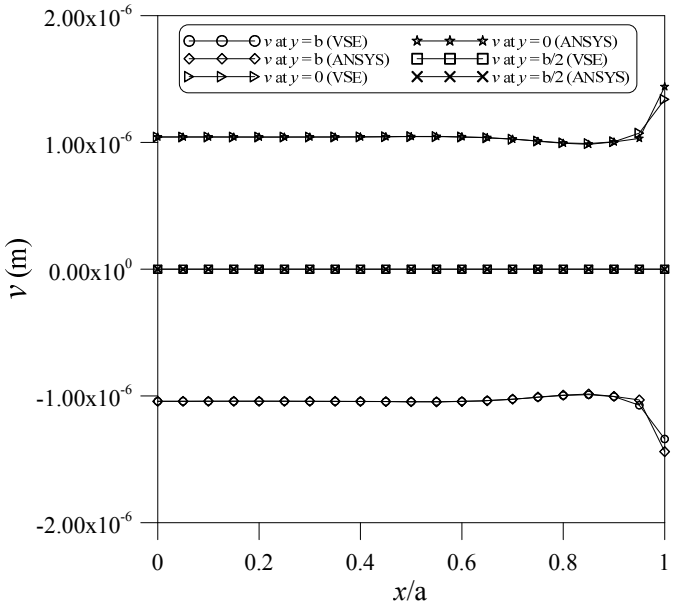

Figure 4.16: v displacements at different positions along the y axis

The through-thickness distributions of the stresses (σ_{xx} and σ_{xy}) are evaluated at the centre of the plate and compared with the predicted results from the VSE and ANSYS. No difference is visible between the results for σ_{xx} calculated using both techniques (Figure 4.17) or for the in-plane shear stress (σ_{xy}) (Figure 4.18).

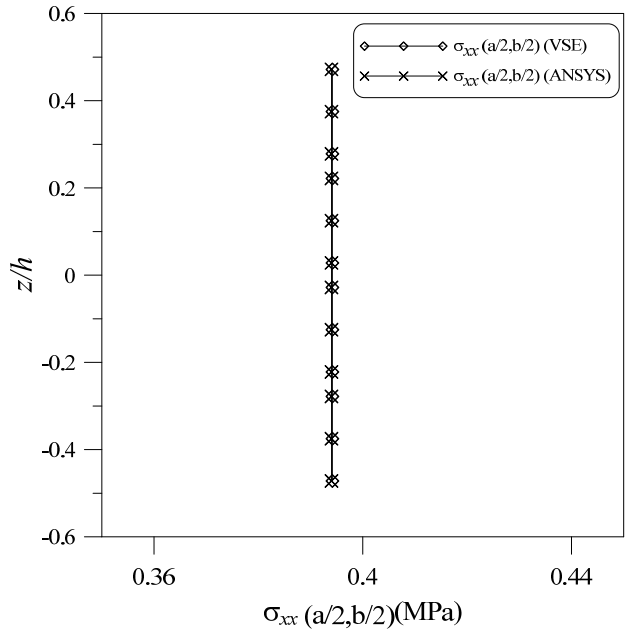

Figure 4.17: Through-thickness distributions of axial stress ($\sigma_{xx}(\frac{a}{2},\frac{b}{2},z)$)

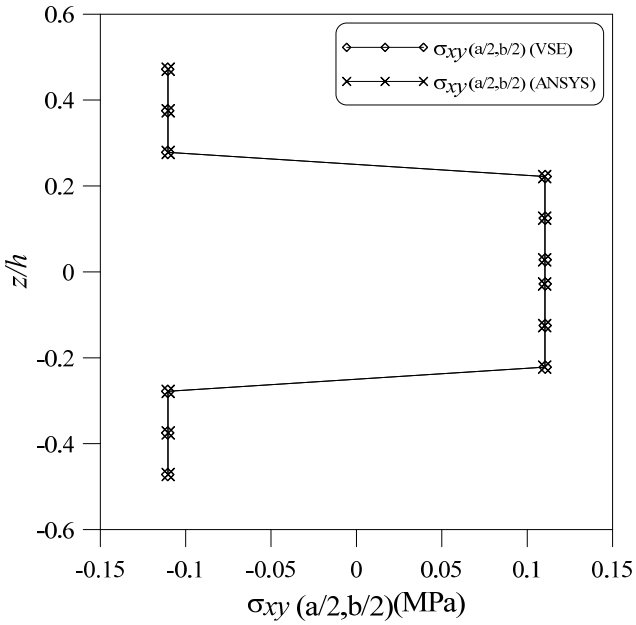

Figure 4.18: Through-thickness distributions of in-plane shear stress ($\sigma_{xy}(\frac{a}{2},\frac{b}{2},z)$)

The through-thickness distributions of the strain (ε_{xx}) determined at the centre of the plate (Figure 4.19) also confirm that the VSE accurately calculates the strain values of the laminates with a constant fibre orientation angle and match the ANSYS-predicted results.

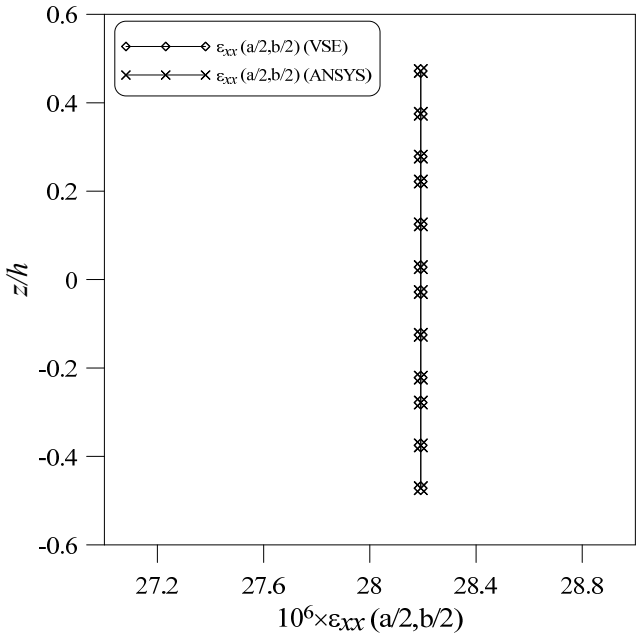

Figure 4.19: Through-thickness distributions of in-plane axial strain ($\varepsilon_{xx}(\frac{a}{2},\frac{b}{2},z)$)

For the symmetric balanced composite plate with a constant fibre orientation, its axial (N_x), transverse (N_y) and shear (N_{xy}) stress resultants are calculated at three different positions along the y axis (at y = 0, b/2 and b), with those from the VSE and ANSYS having similar patterns, as shown in Figures 4.20, 4.21 and 4.22, thereby clearly demonstrating the capability of the VSE to predict stress resultant values for the FEA of a composite plate under any loading condition.

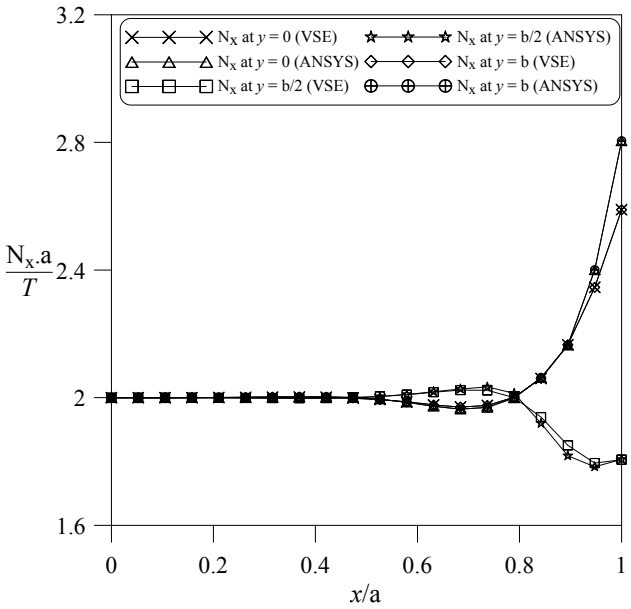

Figure 4.20: Axial stress resultants as function of x and y

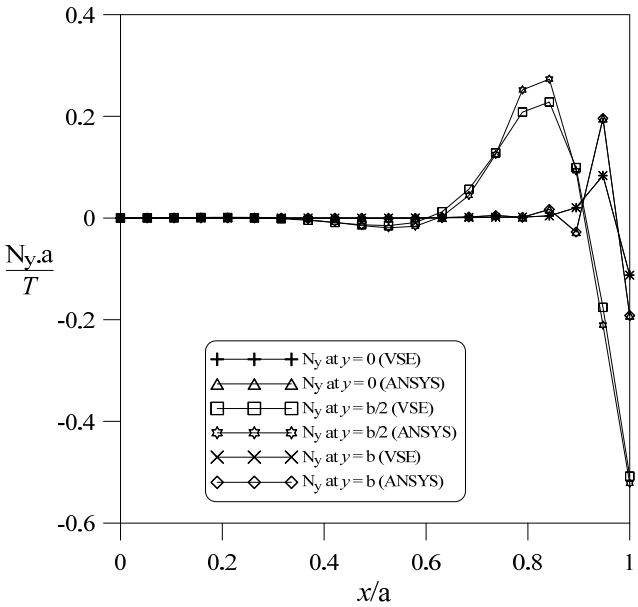

Figure 4.21: Transverse stress resultants as function of x and y

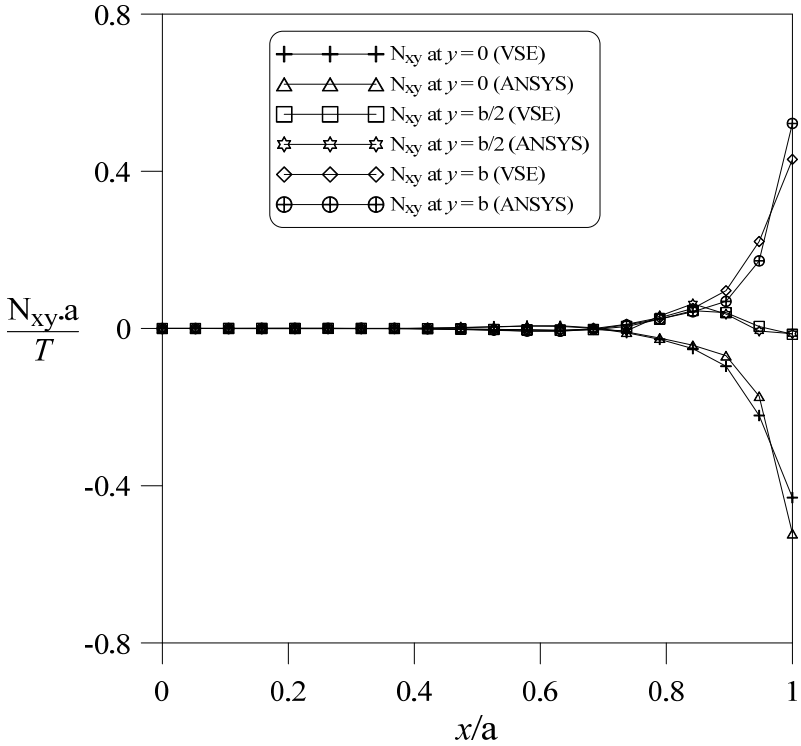

Figure 4.22: Shear stress resultants as function of x and y

4.9 Analysis of panels with spatially varying fibre paths

A symmetric balanced laminate with linearly varying fibre orientations is analysed using both the VSE and ANSYS for the case illustrated in Figure 4.23 in which the transverse edge of the panel is traction free. As, because of the two-fold symmetry of the problem, only one-quarter of the panel is modelled, the boundary conditions at $x = 0$ and $y = 0$ represent the symmetry conditions. The panel is loaded by a uniform end-shortening (u_o), applied at $x = \mathrm{a}/2$, the laminate has four graphite-epoxy layers each with a thickness t of 0.127 mm, the panel is square ($\mathrm{a} = \mathrm{b} = 254$ mm) and the material properties used for the analysis are given in Table 4.5. The panel has linear variation of the fibre orientation angle and the meshing is performed considering 18 elements along both its length and width.

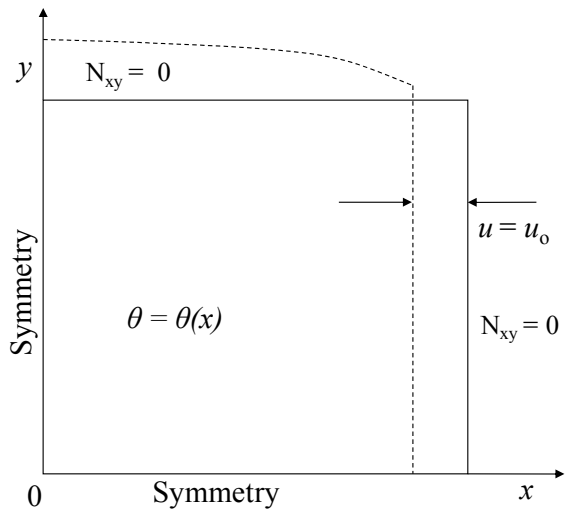

Figure 4.23: Boundary conditions for quarter of laminated composite plate

Table 4.5: Properties of laminated composite plate

Material properties	Geometric properties	Loading
E_1 = 180.99 GPa E_2 = 10.3 GPa $G_{12} = G_{13}$ = 7.17 GPa G_{23} = 3.0 GPa ν_{12} = 0.28	a = 0.254 m b = 0.254 m t = 1.27×10^{-4} m	uniform end shortening

A linear variation of the fibre orientation angle along the *x* axis is obtained using the definition of the fibre angle according to the following relationship.

$$\theta(x) = \begin{cases} T_0 - \dfrac{2(T_1 - T_0)}{\mathrm{a}}.\ x_l & -{}^{\mathrm{a}}/_{2} \le x_l \le 0 \\ T_0 + \dfrac{2(T_1 - T_0)}{\mathrm{a}}.\ x_r & 0 \le x_r \le {}^{\mathrm{a}}/_{2} \end{cases} \tag{4.27}$$

The fibre angle starts from T_0 at the middle of the panel and reaches a value of T_1 at the end of the panel, with the angles (T_o and T_1) chosen to range between 0^0 and 45^0, as shown in Figure 4.24.

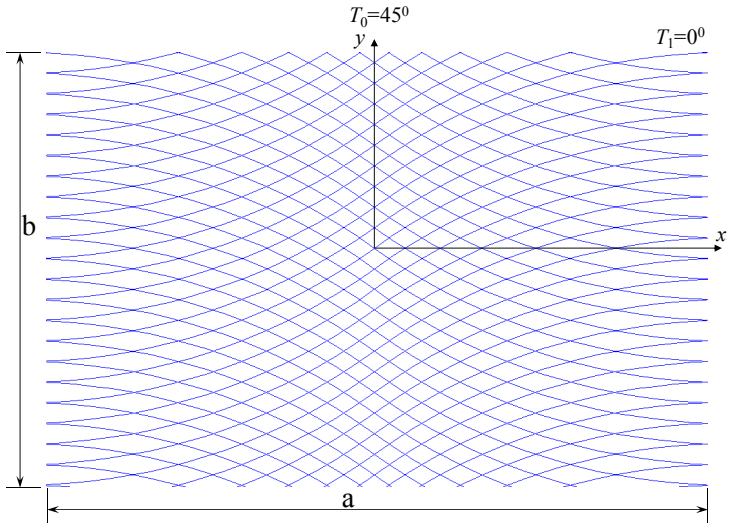

Figure 4.24: Variable-stiffness configuration ($\pm\theta$ layers shown)

4.9.1 Numerical results

The elastic response of the VS panel is analysed using both the VSE and ANSYS with various results obtained. The normalised axial and transverse stress resultants are plotted as functions of x for two values of y/b and compared with the analytical solutions of Gurdal and Olmedo [17] and Senocak and Tanriover [27] (Figures 4.25 and 4.26, respectively), and their calculated values change with respect to both x and y. As can be observed in Figure 4.25, the almost constant value of N_x at $y = 0$ obtained from the analytical solution of Gurdal and Olmedo [17] differs considerably from those obtained from other solutions, being about 33% higher. As the value of y approaches the free edge at $y = \mathrm{b}/2$, the analytical solutions overestimate the value of N_x, with that from Gurdal and Olmedo [17] about 66% higher and that from Senocak and Tanriover [27] 16% higher than those from the VSE and ANSYS.

For considerable angle variations, even though the panel is loaded uniaxially, the value of the transverse stress resultant N_y may become substantial as it is not zero in the interior of the panel. The calculated transverse stress resultant is illustrated in Figure 4.26 as a function of x for $y = 0$ and $y = \mathrm{b}/2$ and its values predicted by ANSYS and the VSE vary

from the analytical solution of Gurdal and Olmedo [17] but are negligibly different from those of Senocak and Tanriover [27].

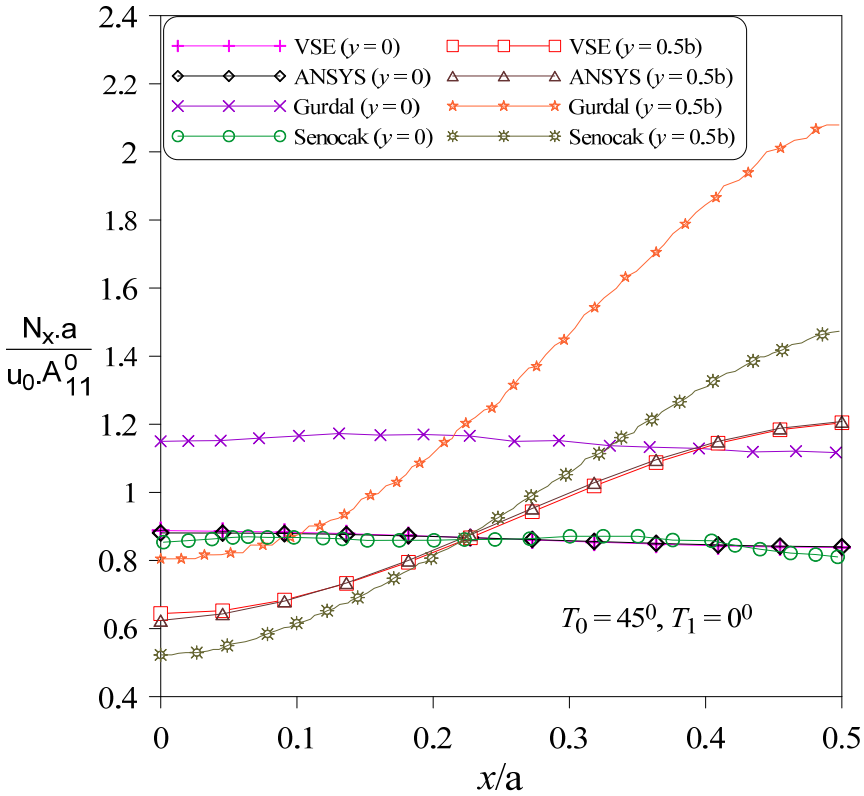

Figure 4.25: Axial stress resultants as function of x and y

The variations of N_x as a function of the y coordinate are shown in Figure 4.27 for the panel with $T_0 = 45^0$ and two different values of T_1. As, because of the continuously changing fibre paths, the expansion of the panel due to the Poisson effect is not uniform under the compressive load, shear strains are induced which produce the shear stress resultant N_{xy}. However, as the boundary conditions require that N_{xy} be zero at the panel edges and the planes of symmetry, large gradients develop from the middle of the quarter plate to these areas. For $T_1 = 45^0$, the gradient effect does not appear as the laminate has a straight fibre format but as the difference between T_0 and T_1 increases, the gradient in N_x close to the transverse edge becomes more pronounced. As can be seen in the figure, the

results predicted by ANSYS and the VSE differ considerably from those calculated by the analytical solution of Gurdal and Olmedo [17] but are exactly the same as each other.

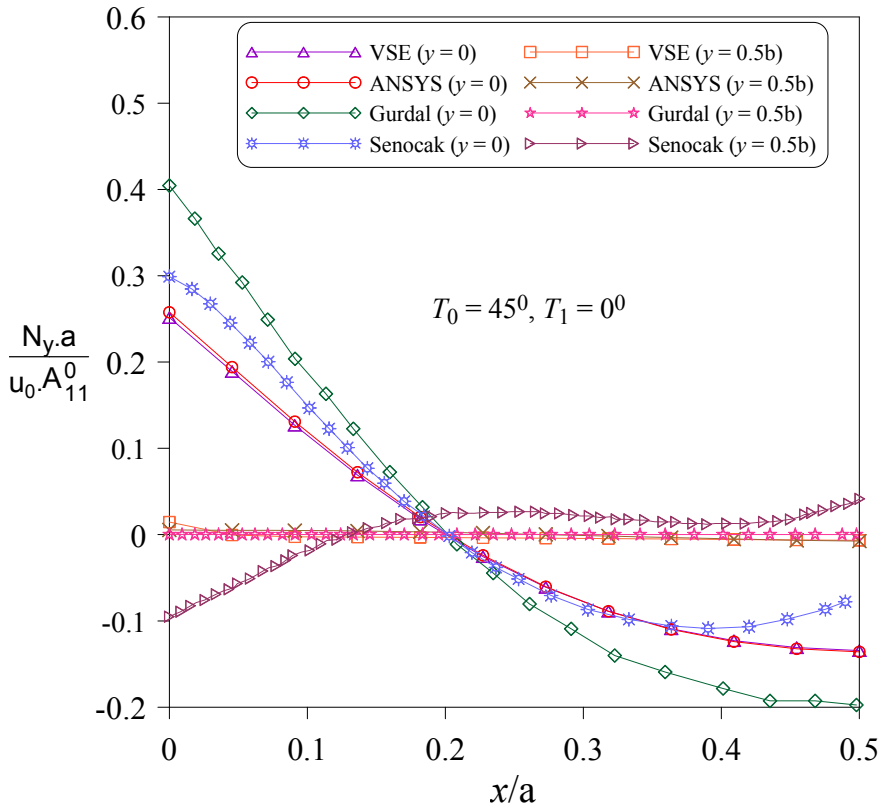

Figure 4.26: Transverse stress resultants as function of x and y

The analyses of laminates with linearly varying fibre orientation angles indicate that the VSE with the modified approach predicts various results with a negligible amount of difference from those obtained by ANSYS considering the same number of elements for meshing. Therefore, the influence of the mesh size on the predicted results should be investigated in order to confirm the efficiency of the modified approach.

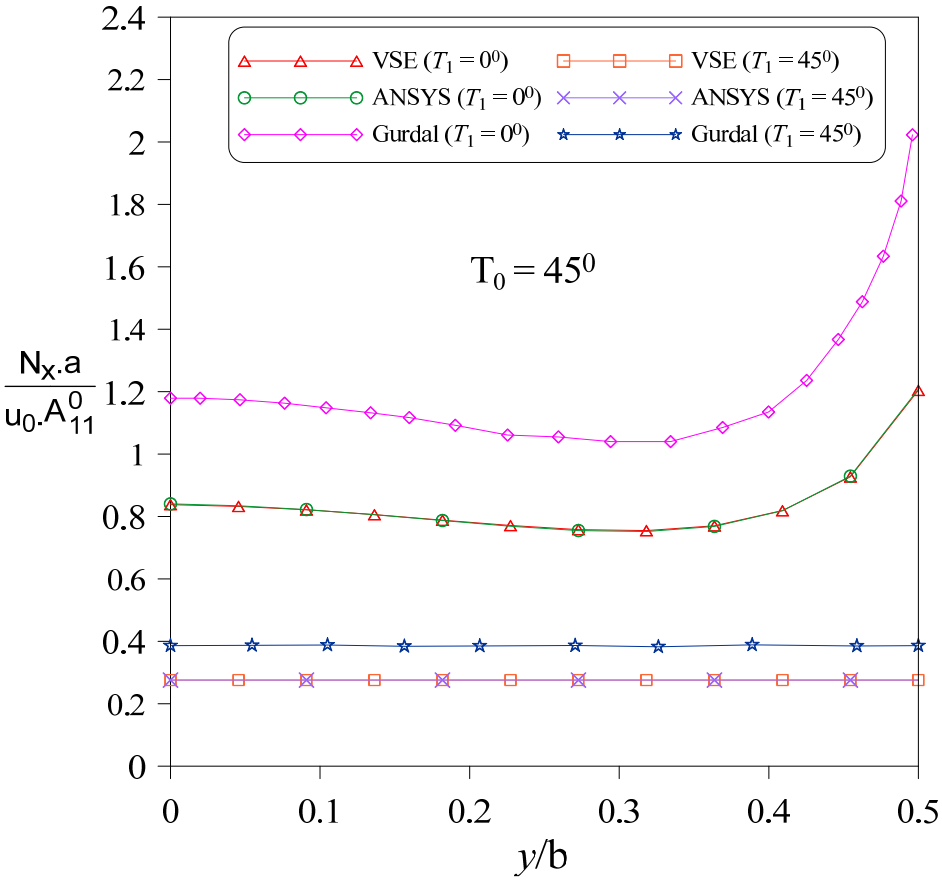

Figure 4.27: Axial stress resultants at x = a/2

4.9.2 Influence of mesh size in analysis of VS laminate

The same problem of the composite plate from Gurdal and Olmedo [17] presented in Section 4.9 is solved using different mesh sizes to check convergences of the results for the axial stress resultants from both the VSE and ANSYS.

The axial stress resultant (N_x) is calculated at two different positions of y (0 and b/2) using six different mesh sizes. As can be seen in Figures 4.28 and 4.29, the increased mesh size does not significantly affect the axial stress resultant values calculated using ANSYS and the VSE as they are almost the same.

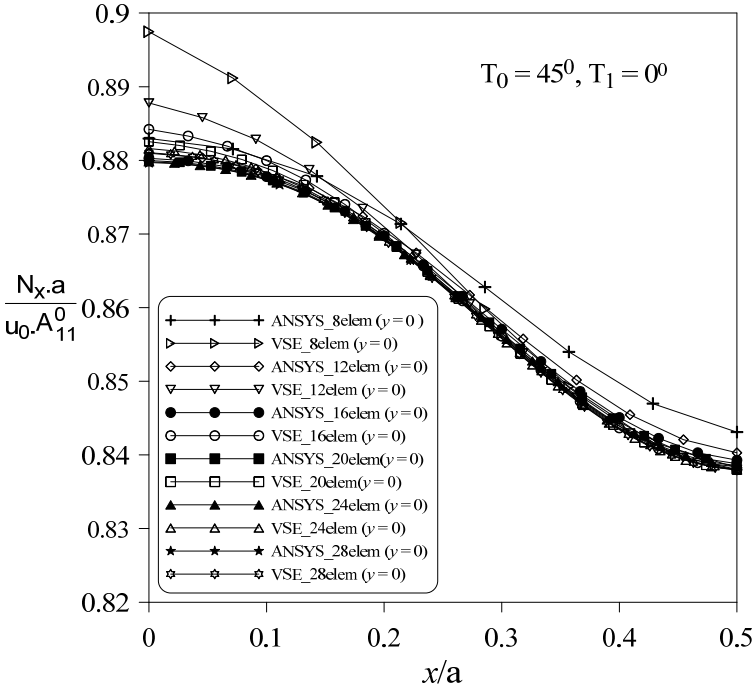

Figure 4.28: Axial stress resultant at y = 0 for different mesh sizes

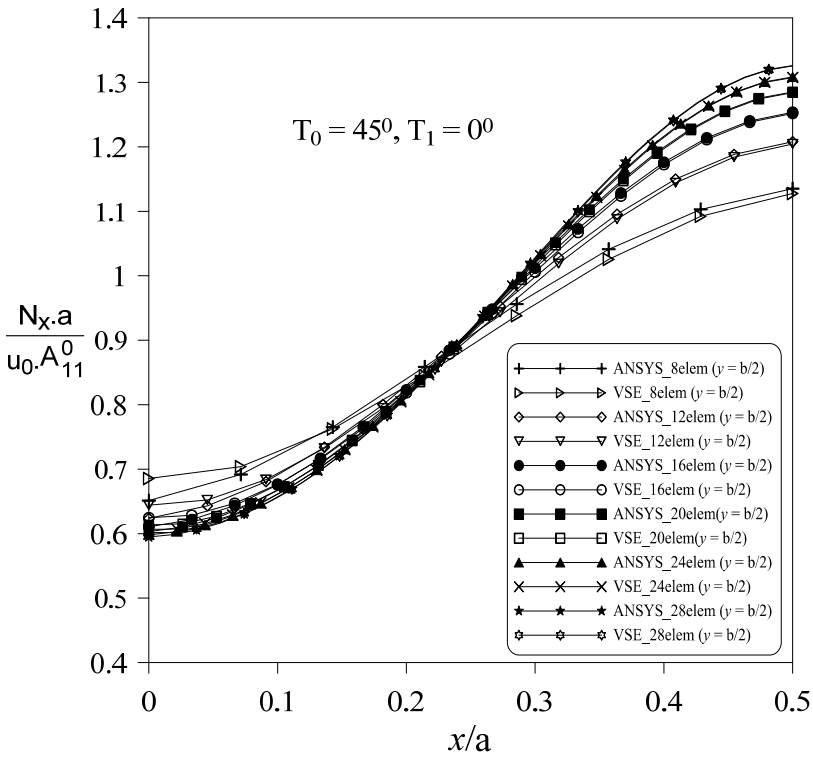

Figure 4.29: Axial stress resultant at y = b/2 for different mesh sizes

4.9.3 Results for large angle variation

Also, the problem of the composite plate of Gurdal and Olmedo [17] is solved for a larger angle variation for the case shown in Figure 4.23. The fibre orientation angle at the centre of the plate (T_0) is considered to be 0^0 and that at the edge (T_1) 90^0. A comparison of the stress (σ_{xx}) and axial stress resultant (N_x) values obtained from the VSE and ANSYS is carried out to check their differences. To represent the angle variation, a constant angle in each element is given as the input to ANSYS but, for the VSE, four different angles are chosen at four Gaussian points in an element. However, the stress and axial stress resultant plots in Figures 4.30 and 4.31, respectively, indicate that the differences between the calculated values are significantly small. This demonstrates that ANSYS predicts the responses correctly despite considering a constant angle in each element because discretising the varying fibre path using a large number of elements results in a negligible discontinuity of the angle between two consecutive elements.

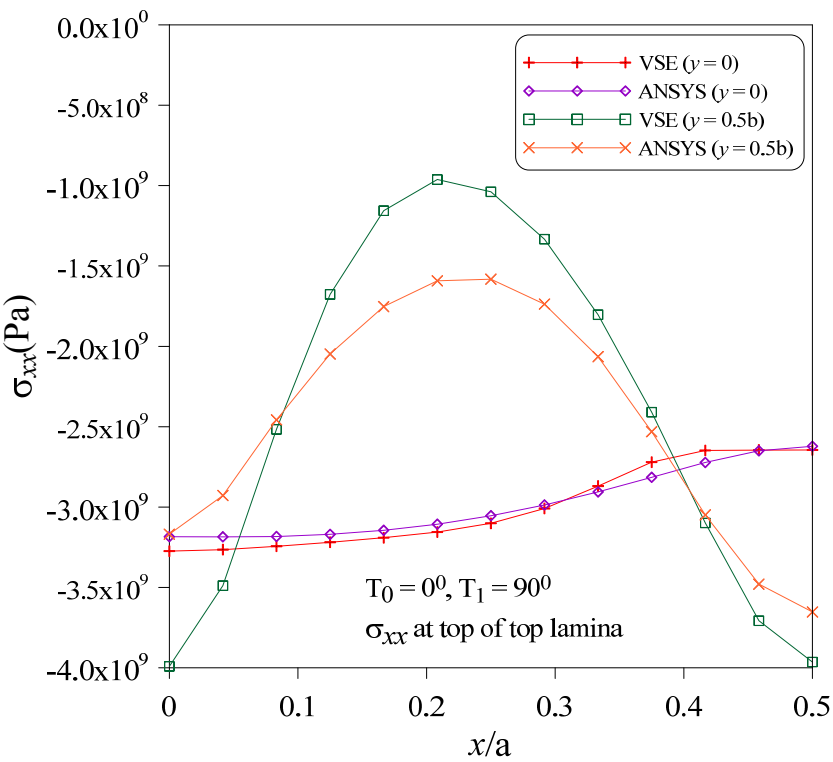

Figure 4.30: Axial stresses at top of top lamina (along the *x* axis)

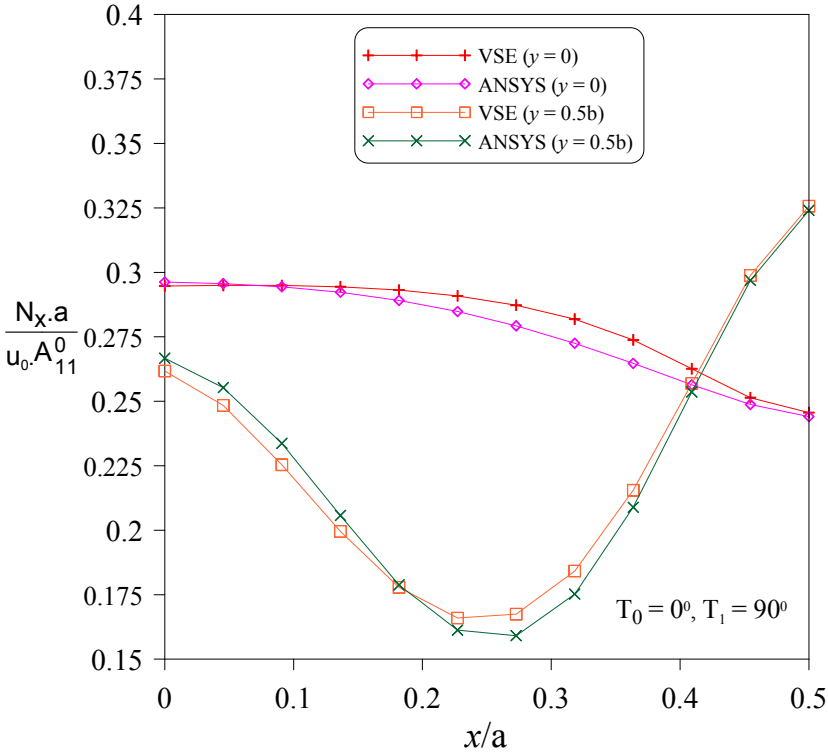

Figure 4.31: Axial stress resultants as function of x and y

4.10 Analysis of composite plate with $< 60^0, 0^0 >$ fibre path

The symmetric balanced laminate with four graphite-epoxy layers shown in Figure 4.14 is also analysed for linearly varying fibre orientations using both the VSE and ANSYS under the same boundary conditions, with both coarse (20×10) and refined (40×20) FE meshes considered and the material properties chosen from Table 4.4. The linear variation of the fibre orientation along the x axis from Eq. (4.27), with the angles (T_0 and T_1) varying between 60^0 and 0^0, respectively, is chosen.

An analysis of the VS symmetric balanced composite plate is performed to compare the responses predicted by the VSE for the VS composite plate under applied tension with the results obtained from ANSYS. A tension of 500 N is applied at one edge of the plate and the SHELL181 element is used in ANSYS.

4.10.1 Numerical results

The displacement patterns of the VS plate under tension predicted by the VSE and ANSYS are compared as are the through-thickness stress and strain distributions.

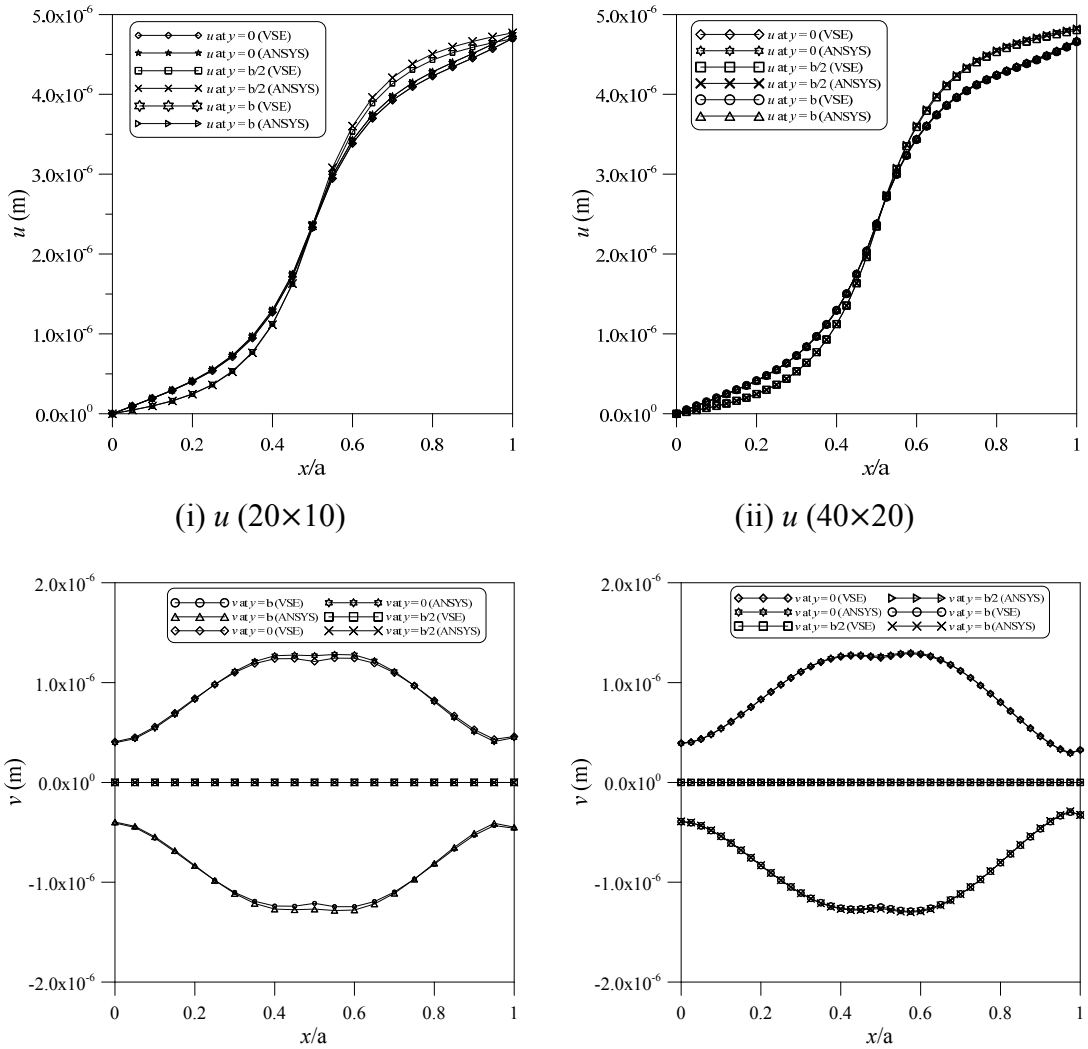

(i) u (20×10) (ii) u (40×20)

(iii) v (20×10) (iv) v (40×20)

Figure 4.32: u and v displacements at different positions along length of plate

Because of the change in stiffness, loading a VS panel with a prescribed tension at the edge will yield a different elastic response from that obtained using a straight fibre configuration. Therefore, the displacement fields are different from those for laminates with constant fibre orientation angles; that is, the u and v displacements are not linear with respect to x and y, respectively. In Figure 4.32, variations of the nodal displacements, with

u and v as functions of x when y = 0, b/2 and b, are shown. It can be clearly seen that ANSYS predicts the u and v displacement values exactly as VSE does. For different mesh sizes, both the u and v displacement curves from the VSE and ANSYS merge completely which supports the contention that larger mesh sizes can help to more accurately approximate varying fibre paths.

Two stresses (σ_{xx} and σ_{yy}) calculated through the thickness are evaluated at the centre of the plate and compared to determine the difference between the predicted results from the VSE and ANSYS. For σ_{xx}, those from ANSYS differ from those calculated using the VSE, with that for the 20×10 mesh size about 37% higher (Figure 4.33) and that for the higher mesh size (40×20) 16% higher from the VSE. Also, the values of σ_{yy} predicted by ANSYS are about 76% higher for the 20×10 and 47% higher for the 40×20 meshes than those predicted by the VSE (Figure 4.34).

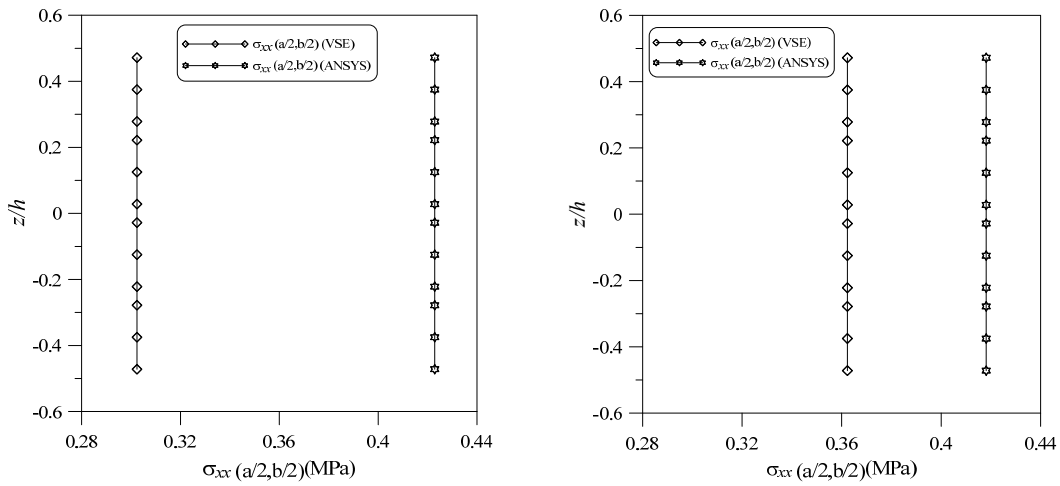

(i) $\sigma_{xx}(\frac{a}{2},\frac{b}{2},z)$ (20×10) (ii) $\sigma_{xx}(\frac{a}{2},\frac{b}{2},z)$ (40×20)

Figure 4.33: Through-thickness distributions of axial stress ($\sigma_{xx}(\frac{a}{2},\frac{b}{2},z)$)

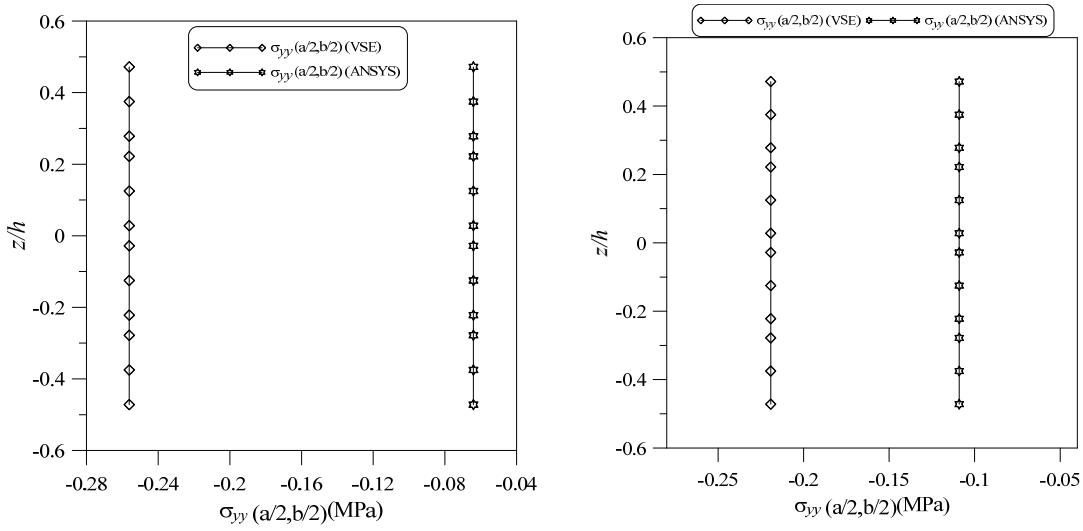

(i) $\sigma_{yy}(\frac{a}{2},\frac{b}{2},z)$ (20×10) (ii) $\sigma_{yy}(\frac{a}{2},\frac{b}{2},z)$ (40×20)

Figure 4.34: Through-thickness distributions of transverse stress ($\sigma_{yy}(\frac{a}{2},\frac{b}{2},z)$)

4.11 Influence of mesh size in analysis of VS laminate

In order to check the convergence rates while performing analyses using the VSE and ANSYS of the VS composite laminate shown in Figure 4.14 with $< 60^0, 0^0 >$ fibre trajectories, both the *u* displacements and in-plane axial stresses (σ_{xx}) are determined for different mesh sizes from 4×2 to 40×20. The results demonstrate different responses from the VSE and ANSYS. The *u* displacement is calculated for the node located at point (a, b) and σ_{xx} at point ($\frac{a}{2}$, $\frac{b}{2}$).

The convergences of the *u* displacement obtained from the VSE and ANSYS are quite different, as shown in Figure 4.35. Starting from a relatively low value, the VSE-predicted values suddenly ascend and remain almost constant. On the other hand, the ANSYS-predicted results gradually decrease from a higher value and approach a constant value. However, ANSYS tends to overestimate the value of *u* at the panel's corner point.

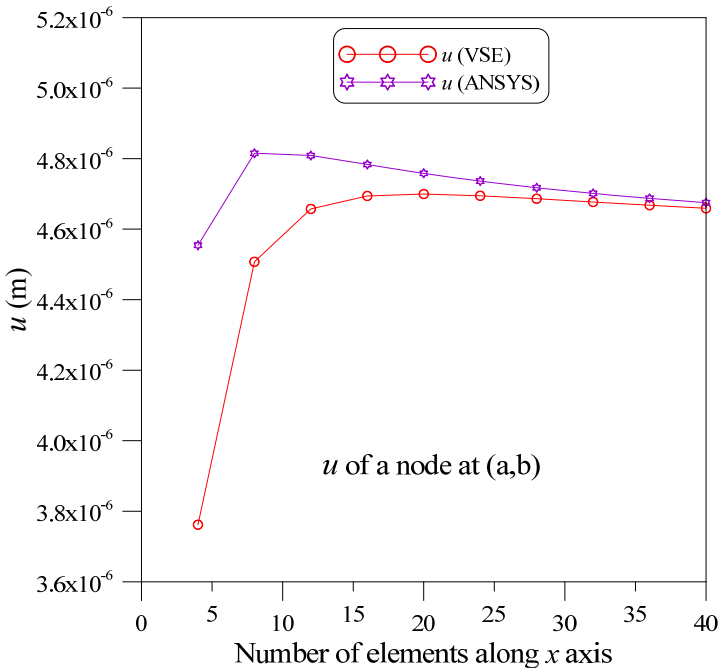

Figure 4.35: Convergences of u displacement with increasing numbers of elements

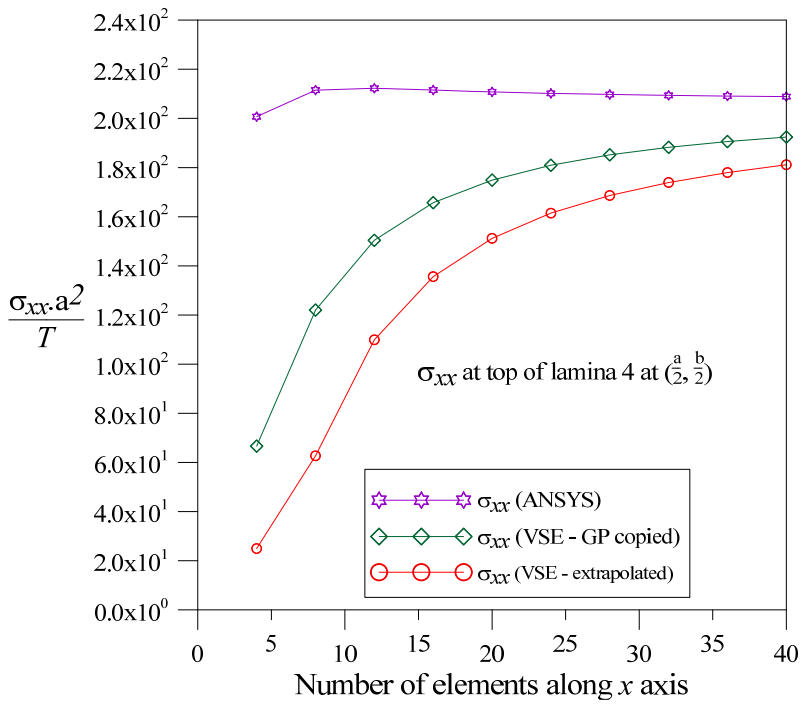

Figure 4.36: Convergences of σ_{xx} with increasing numbers of elements

The convergence of the in-plane axial stress obtained from the VSE differs significantly from that determined using ANSYS. It can be seen in Figure 4.36 that the ANSYS-

predicted values for σ_{xx} remain constant for all mesh sizes from 8×4. For the VSE, the nodal values for σ_{xx} are directly copied and extrapolated from the Gaussian points (GP) to compare their results and, in both cases, gradually rise to become steady. However, for higher mesh sizes, considerable differences can be observed between the predicted values for σ_{xx} from both techniques.

4.12 Effect of discretisation on stiffness

From all the previous analyses of the composite plate with linearly varying fibre orientation angles (Sections 4.9 and 4.10), it can be clearly observed that there is no significant difference between the VSE-predicted and ANSYS-calculated responses for a VS laminate. Although, in ANSYS, a constant fibre orientation angle is assigned in each element, the effect of stiffness variations among different elements is not significantly pronounced. As can be seen from Eq. (4.25), the stiffness of an element is largely dependent on the extensional stiffness matrix A where no bending is considered. Due to the varying fibre orientation angle, matrix A should also have changing values at different points in the laminate. Therefore, to determine the reason for the negligible differences among the predicted results, different terms of A for a composite laminate are plotted to observe the influence of variations of the fibre orientation angles at different Gaussian points in an element. In ANSYS, the average value of the fibre angle determined for the linear variation is assigned to each element. In contrast, four different angles are considered at four Gaussian points in the modified four-nodal isoparametric element, VSE. It can be observed in Figures 4.37 to 4.40 that various terms of A ($A_{16} = 0$ for this case) converge to a fixed value when the difference among the fibre orientation angles at the Gaussian points in an element tends to be zero. This indicates that the FEA package ANSYS almost accurately predicts the response of a composite plate with linearly varying fibre orientations and a larger mesh size, and is the reason for responses obtained from both the

VSE and ANSYS being similar for composite laminates with linear variations of their fibre orientation angles.

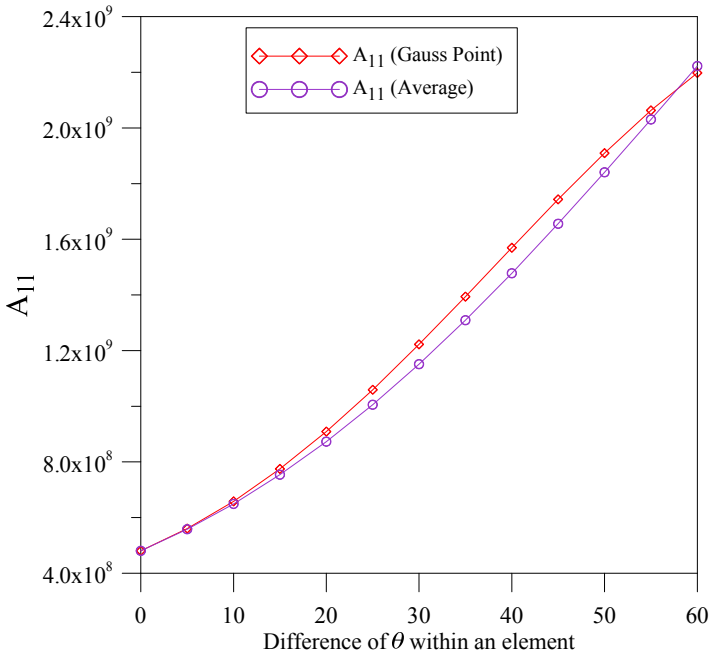

Figure 4.37 Changes in values of A_{11} with decreasing angle difference

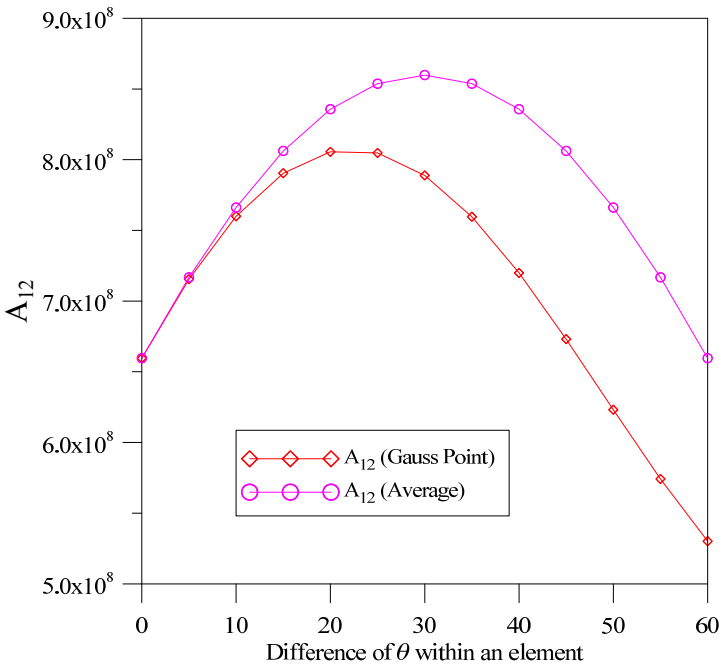

Figure 4.38 Changes in values of A_{12} with decreasing angle difference

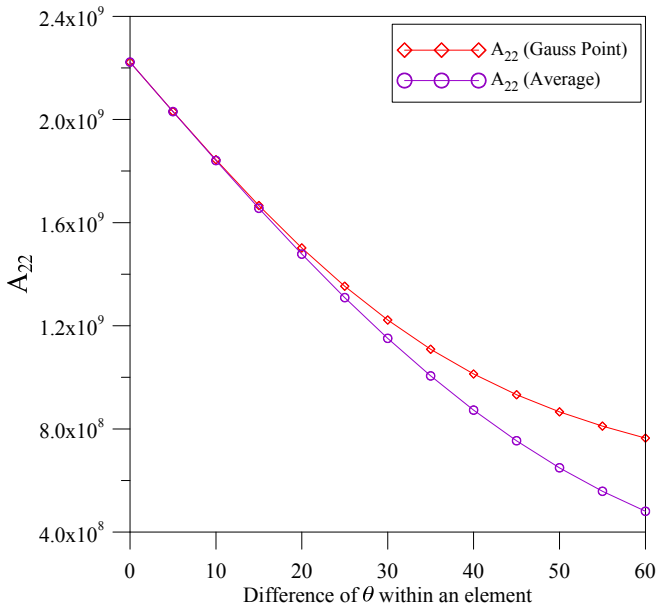

Figure 4.39: Changes in values of A_{22} with decreasing angle difference

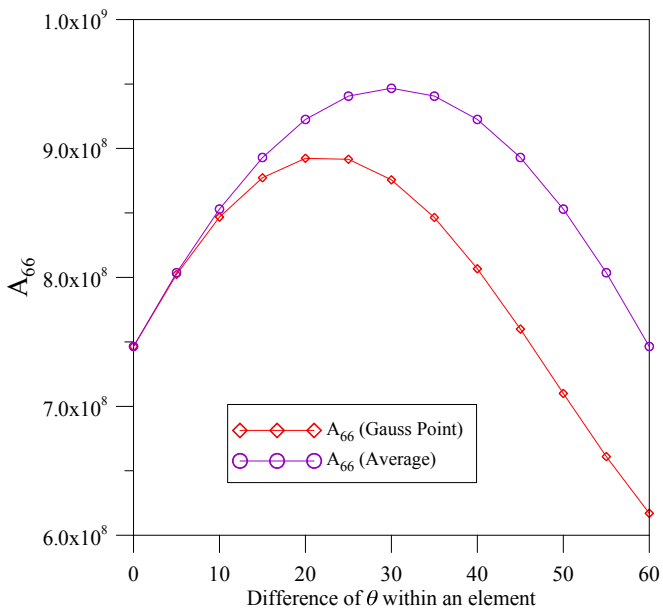

Figure 4.40: Changes in values of A_{66} with decreasing angle difference

4.13 Analysis of composite plate with nonlinear variation of fibre angle

The symmetric balanced laminate shown in Figure 4.14 which is composed of four graphite-epoxy layers is also analysed with nonlinear variation of fibre orientation angle using both the VSE and ANSYS, and the same boundary conditions used for the analysis presented in Section 4.8. A laminate with such a nonlinearly varying fibre orientation is

also termed a 'VS laminate' and its material properties used for this analysis are chosen from Table 4.4.

The sinusoidal fibre path along the x axis shown in Figure 4.41 is used in this analysis and defined as

$$y = \chi \sin\left(\frac{2\pi x}{\lambda}\right) \tag{4.28}$$

The corresponding fibre orientation angle is

$$\theta = \tan^{-1}\left(\frac{2\pi\chi}{\lambda}\cos\left(\frac{2\pi x}{\lambda}\right)\right) \tag{4.29}$$

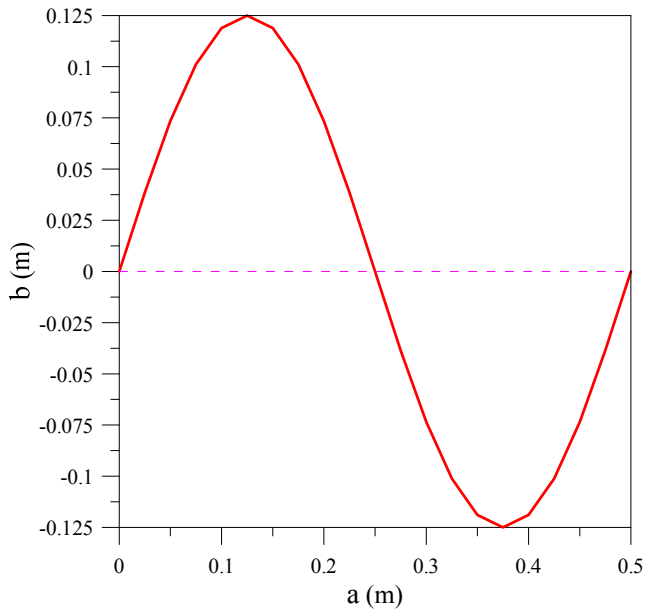

Figure 4.41: Sinusoidal fibre path

The elastic response of the VS panel is analysed using both the VSE and ANSYS in order to compare the VSE-predicted response for a composite plate with nonlinear variations of its fibre angles and the response determined using ANSYS under a tension of 500 N applied at one edge of the plate. The same mesh size of 40×20 is considered in both the VSE and ANSYS analyses, and the SHELL181 element is used for ANSYS.

4.13.1 Numerical results

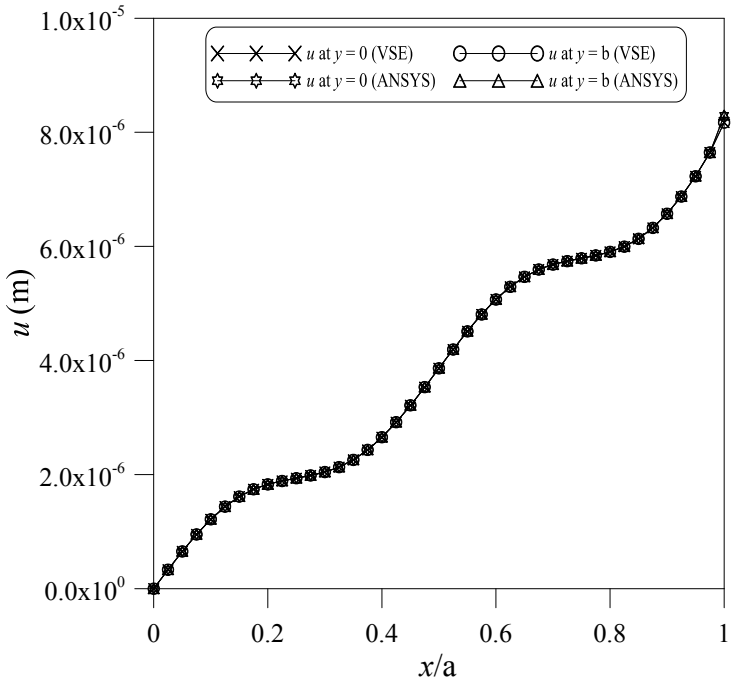

Figure 4.42: *u* displacements at different positions

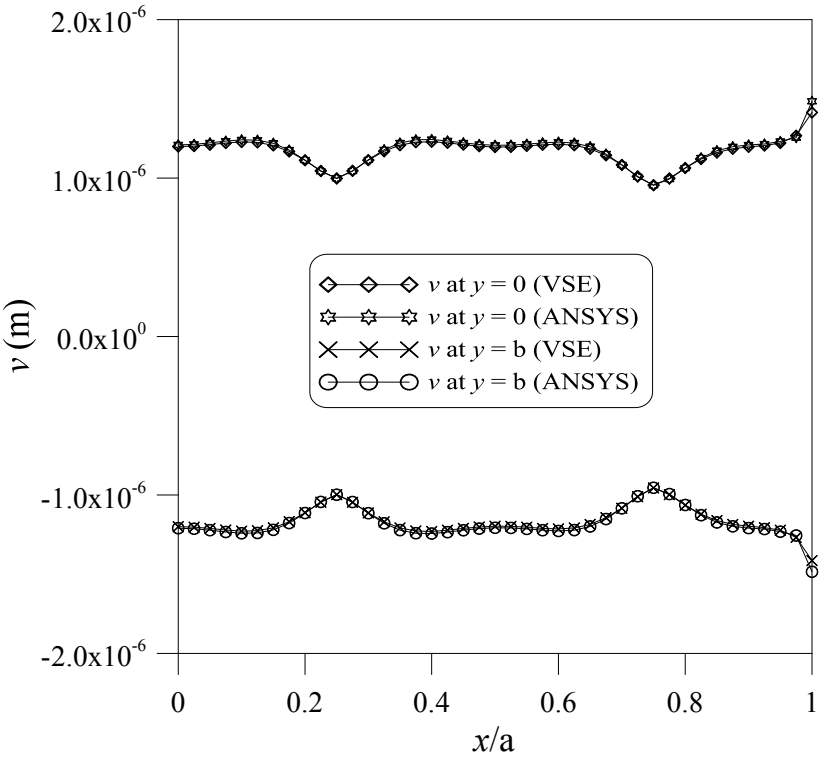

Figure 4.43: *v* displacements at different positions

The change in stiffness due to nonlinear variations of the fibre orientation angles yields a different elastic response from that obtained for linear variations. The displacement fields of the VS plate are not linear with respect to x and y and differ from those for laminates with linear variations of the fibre angles. Comparisons of the u and v displacements calculated at y = 0 and b and predicted by the VSE and ANSYS (Figures 4.42 and 4.43, respectively) clearly indicate that, even for nonlinear variations of the fibre angles, assigning a constant angle in each element does not influence the predicted displacement results.

The stresses are evaluated through the thickness at the centre of the plate and compared to check whether the results predicted by the VSE and ANSYS differ for nonlinear variations of the fibre orientation angles and, as can be seen in Figure 4.44, for σ_{xx} there is a negligible difference. The values of the transverse stress (σ_{yy}) and in-plane shear stress (σ_{xy}) obtained from the VSE are also very close to those determined using ANSYS, as illustrated in Figures 4.45 and 4.46, respectively. Therefore, the stress values can be determined accurately using larger mesh sizes despite choosing a constant angle in an element.

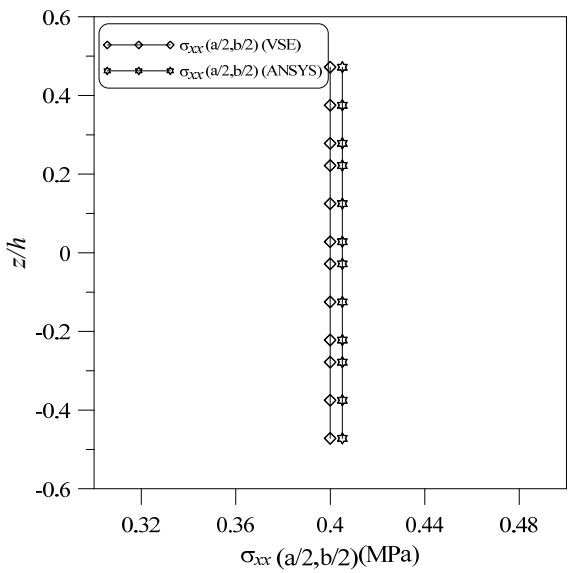

Figure 4.44: Through-thickness distributions of axial stress ($\sigma_{xx}(\frac{a}{2},\frac{b}{2},z)$)

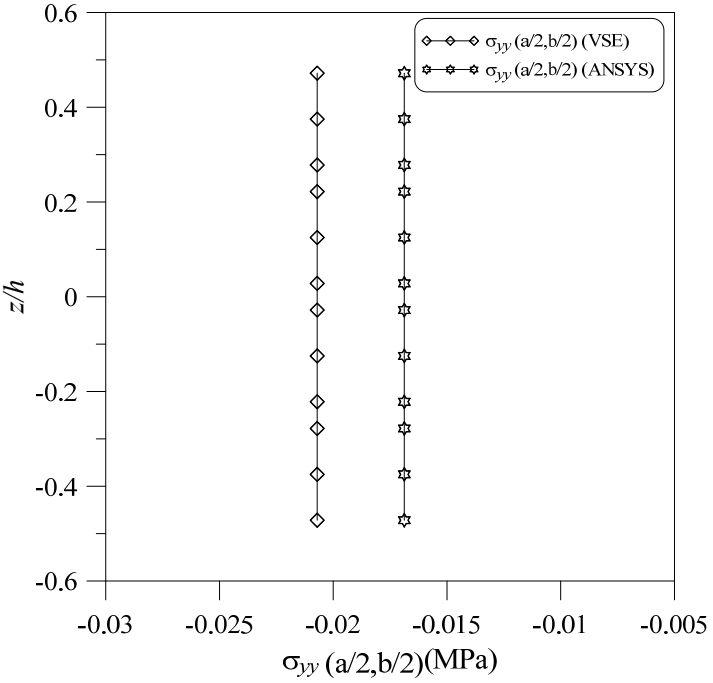

Figure 4.45: Through-thickness distributions of transverse stress ($\sigma_{yy}(\frac{a}{2},\frac{b}{2},z)$)

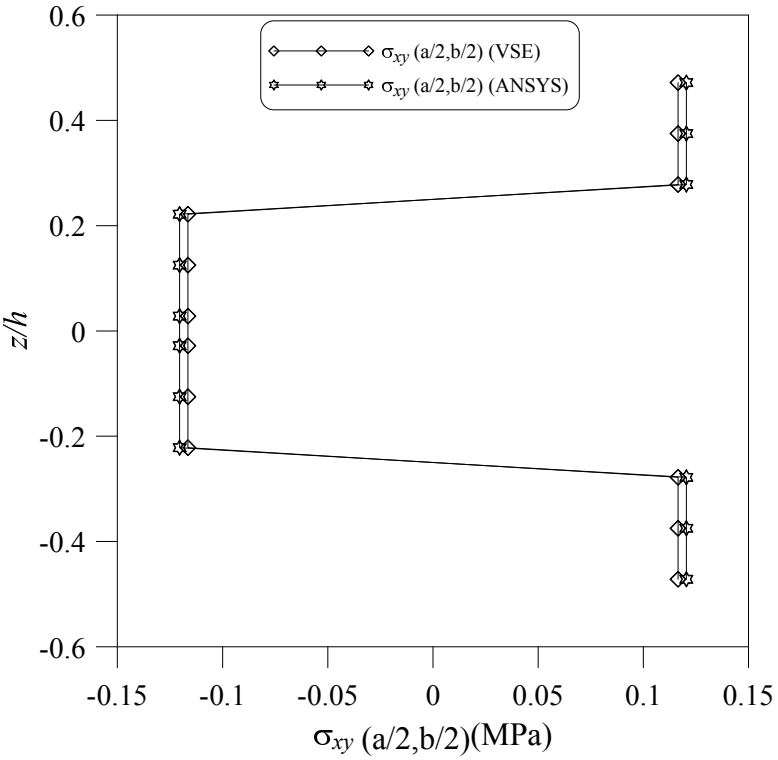

Figure 4.46: Through-thickness distributions of in-plane shear stress ($\sigma_{xy}(\frac{a}{2},\frac{b}{2},z)$)

4.13.2 Influence of mesh size for nonlinear variation of fibre angle

In order to check the convergence rate while performing the analysis of a VS composite laminate with nonlinearly varying fibre orientations, its *u* displacement and axial and transverse stress and stress resultants are determined for different mesh sizes from 4×2 to 40×20. The results demonstrate the influence of the mesh size on predictions of the composite plate's responses calculated using both the VSE and ANSYS. The *u* displacement is calculated for the node located at point (a, b) and the axial and transverse stresses at point $(\frac{a}{2}, \frac{b}{2})$, with both the axial and transverse stress resultants calculated for the element located at (a, b).

The *u* displacements from the VSE and ANSYS converge in a similar fashion to reach steady values, as shown in Figure 4.47. From the lower value for the 4×2 mesh, the predicted values suddenly ascend for the 8×4 mesh and then gradually increase and remain at almost constant values for the larger mesh sizes, with the difference between those calculated using the ANSYS and VSE negligible. This convergence phenomenon for nonlinearly varying fibre orientations is comparable to that shown in Figure 4.35 for a composite plate with linearly varying fibre orientations.

On the other hand, as shown in Figure 4.48, the *v* displacements from the VSE and ANSYS converge in different ways as the values predicted by ANSYS increase from a lower value for the 8×2 mesh and gradually approach a constant value whereas those predicted by the VSE gradually decrease and finally reach an almost constant value.

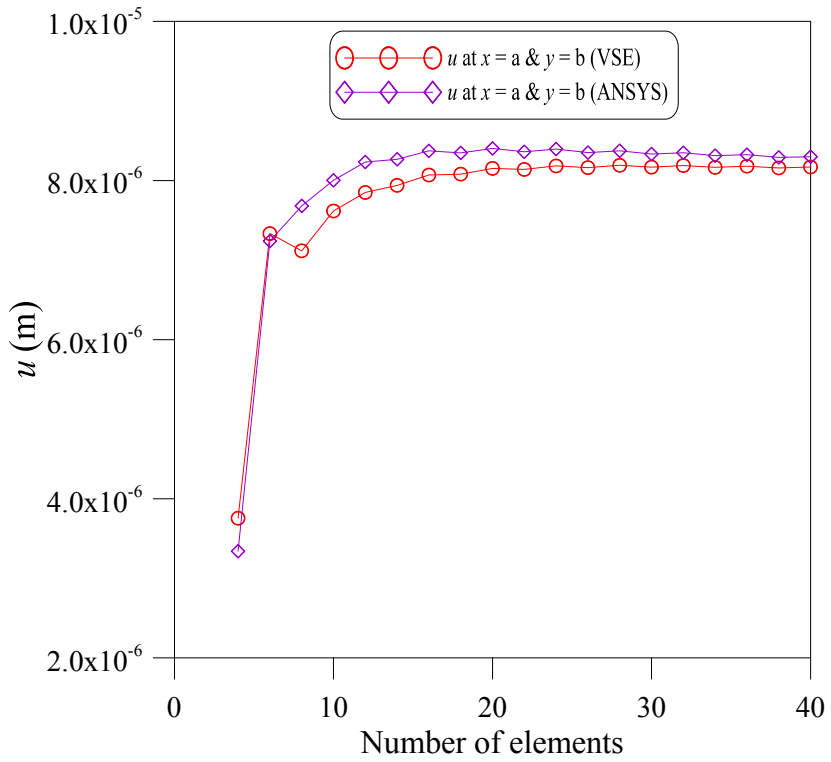

Figure 4.47: Convergences of u with increasing numbers of elements

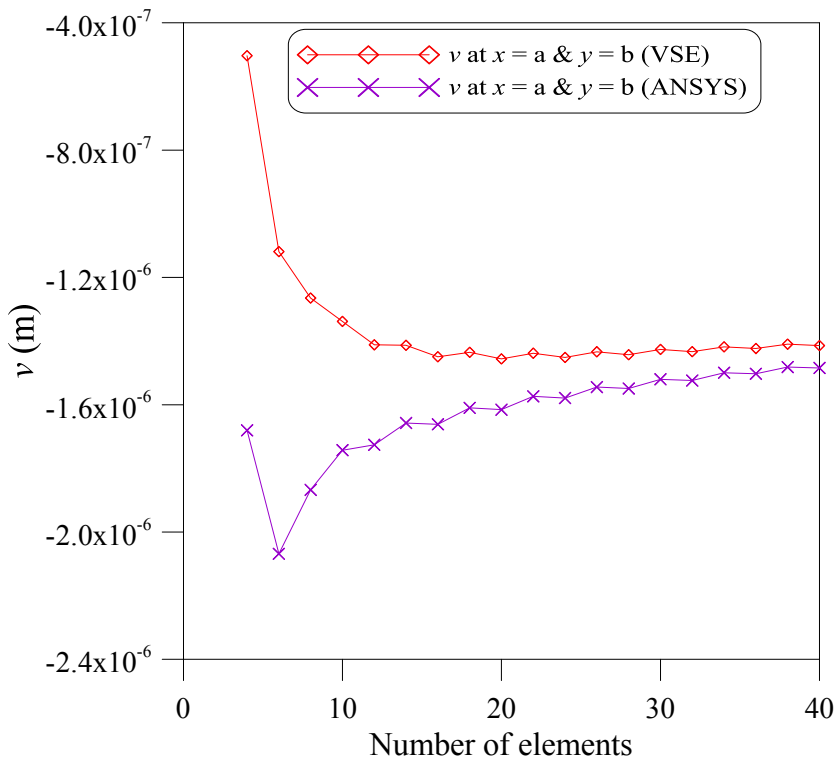

Figure 4.48: Convergences of v with increasing numbers of elements

The convergences of the axial stress resultant (N_x) calculated for the element located at (a, b) of the composite plate (Figure 4.49) clearly indicate that the axial stress values predicted by both the ANSYS and VSE start from the same point for the 4×2 mesh and then continue to rise but with a considerable difference observed between them. The gradually increasing trend of N_x in both cases indicates that this difference would be larger for higher mesh sizes.

Also, the convergences of the transverse stress resultant (N_y) calculated using the VSE for the element located at (a, b) of the composite plate with nonlinear variations of its fibre angles differ noticeably from that determined by ANSYS, with both N_y having negative values (Figure 4.50). Although, for the given boundary conditions, the value of N_y should be zero at $y = b$, those predicted by ANSYS are lower than zero while those predicted by the VSE are much closer to zero.

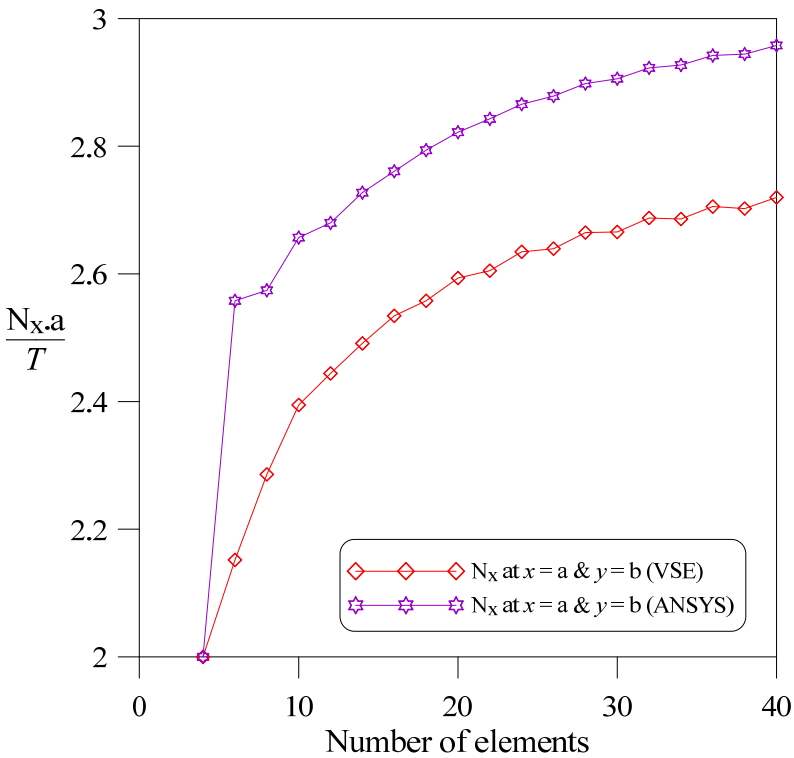

Figure 4.49 Convergences of N_x with increasing numbers of elements

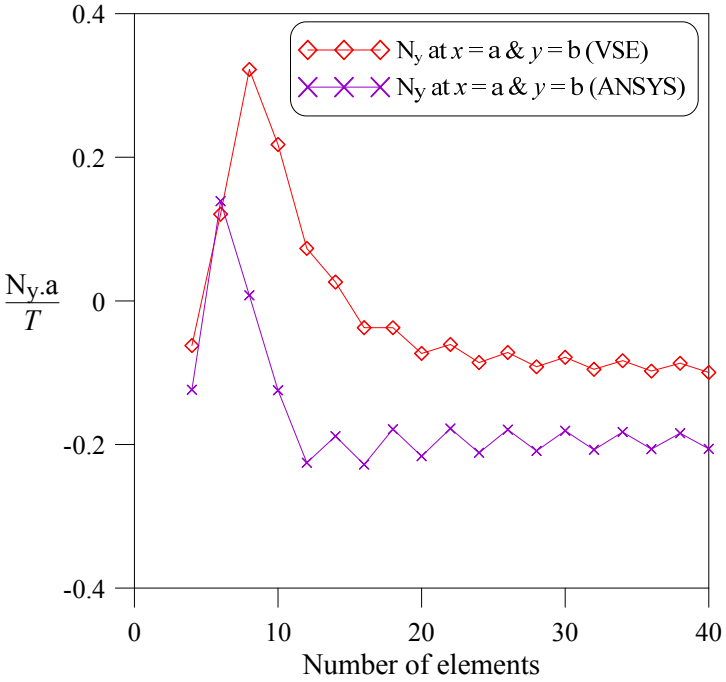

Figure 4.50 Convergences of N_y with increasing numbers of elements

4.13.2.1 Influence of increased load

To check the effect of the applied load on the convergence rates for the *u* and *v* displacements, the composite plate with nonlinearly varying fibre orientations is analysed under an increased load of 10,000 N. In comparison with the convergences of the *u* displacements for a lower load of 500 N (Figure 4.47), the *u* values calculated for the same composite plate with nonlinear variations of its fibre angles and under an increased load follow a similar trend (Figure 4.51), with a slight difference found between those predicted by the two techniques.

Also, the convergences of the *v* displacement (Figure 4.52) follow a similar trend to those shown in Figure 4.48 for a lower loading, with both ANSYS and the VSE predicting small negative values close to zero. However, under the given boundary conditions, the *v* displacement should be zero.

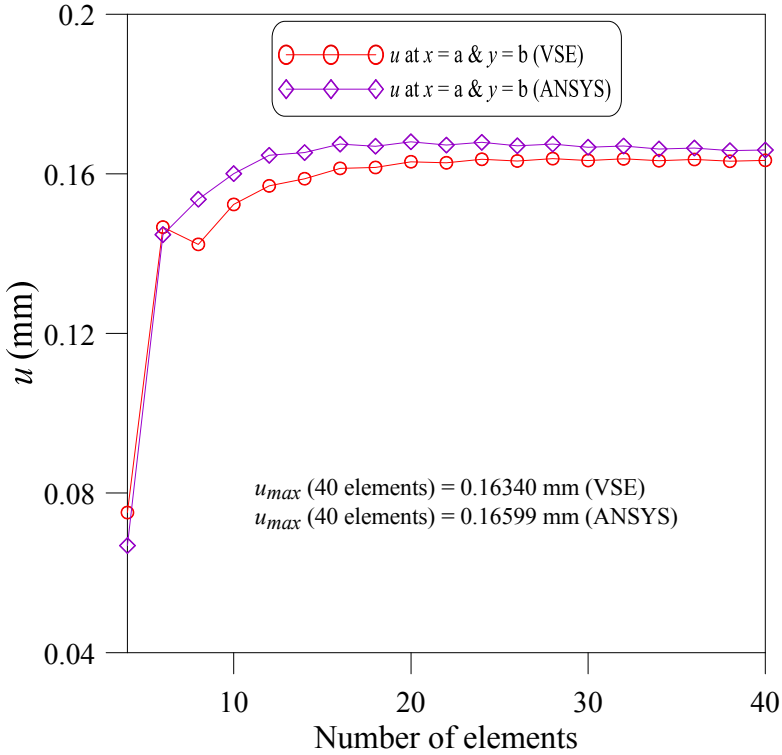

Figure 4.51 Convergences of *u* displacement with increasing numbers of elements

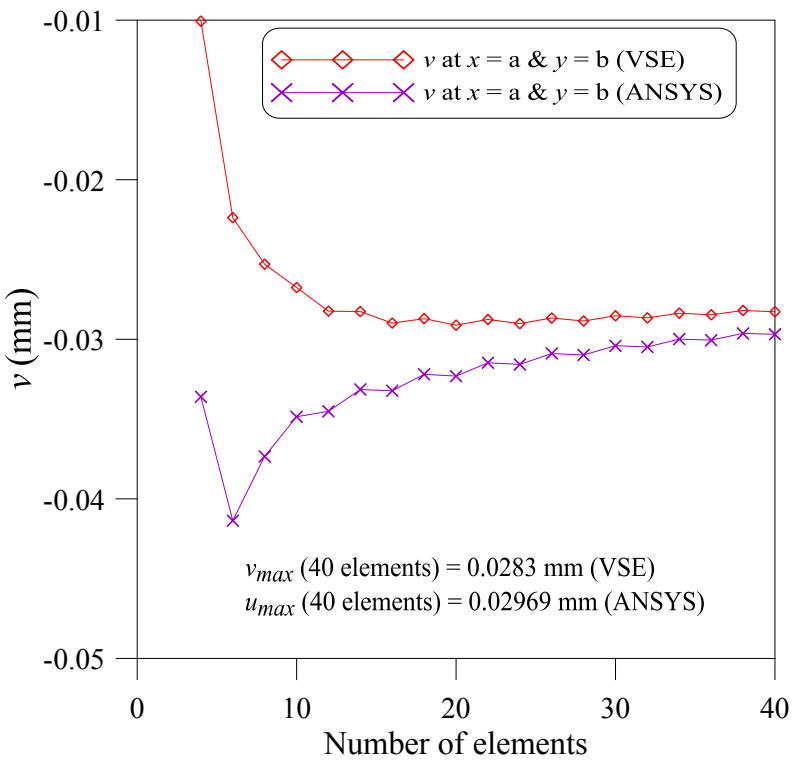

Figure 4.52 Convergences of *v* displacement with increasing numbers of elements

4.14 Chapter summary

The objective of the work presented in this chapter is to describe how the varying fibre paths of VS laminates should be adequately modelled, and present a modified scheme for incorporating changing fibre angles in each FE. Analyses of simple problems for composite panels with various types of fibre angle variations are performed and comparisons with available analytical solutions made.

Different analyses are conducted to determine the responses of a composite plate with varying fibre orientations using both a VSE formulation and the commercial package ANSYS. It follows from the results obtained from the preliminary analyses of a VS composite plate that varying fibre paths for a simple composite plate can be reasonably accurately approximated using ANSYS by discretising the path with a sufficiently fine mesh. However, defining the desired fibre paths and assigning corresponding fibre orientation angles as section properties for the analysis of a composite laminate with spatially varying fibre paths using ANSYS is a rather cumbersome task which involves a substantial amount of work and time. From this perspective, the VSE-based approach developed in this work, which considers four different angles at four Gaussian points implemented for a four-nodal isoparametric element which, apparently, hinders a closer representation of the fibre path in an element, can provide an attractive alternative. However, it is shown that this approach could model stiffness variations more accurately in cases of composite structures with complex fibre paths.

From all the analyses performed, we can conclude that developing a new FE to obtain accurate solutions for VS composite laminates in a most convenient way is quite practical and provides a good indication of the applicability of a FE technique for analysing VS laminates. Because of the unavailability of a suitable theory for determining stresses in a composite structure with various types of fibre paths, the search for a more effective

analysis technique should continue. The procedures for analysing VS laminates considered in this work should be of value in the proper evaluation of any proposed laminate with predefined varying fibre paths and in the general search for more effective analyses of such composite structures.

Despite the attractiveness of the proposed approach, its application to the modelling and analysis of a filament-wound flywheel disk is hampered by the limitations of existing FEA packages. In particular, as most do not support the function of assigning different fibre orientation angles at Gaussian points in a FE, implementing the VSE-based methodology requires a special generation of meshes for such a disk. To achieve this, a suitable FE mesh generator capable of accurately representing the geometry of the disk model and then meshing by controlling the sizes and shapes of the elements should be developed. However, this would be a time-consuming and complex task which is beyond the scope of the current study.

It can be stated conclusively that the results obtained from the analyses of a simple VS rectangular plate provide some insights into the effect of fibre orientation variations and, thereby, the necessity of accurately modelling the fibre paths of such structures. They also indicate that the proposed approach would allow for a wide range of complex VS configurations to be quickly and efficiently modelled through the integration of steered-ply definitions and, therefore, less computational time would be required for detailed analyses of VS laminates under general loading and boundary conditions. This approach has the potential to contribute greatly towards the advancement of tow-steered concepts for the elastic tailoring of composite laminates.

Chapter 5

Design Considerations for Filament-wound Composite Flywheel Disk

5.1 Overview

Although advanced fibre-placement machines allow the steering of fibre tows and, thereby, increase structural design flexibility, this capability is not fully exploited in various engineering applications which, in most cases, take advantage of only the accuracy and convenience of an automated process. Because of developments of fibres with high strengths and moduli, research into flywheels is surging and, predominantly, that into developing a flywheel energy storage (FES) system is a rapidly evolving field due to its commercial viability for a wide range of applications. A composite flywheel system fabricated with newly developed fibres is very compact and lightweight, and offers the same energy storage capacity as a heavier metallic one. Therefore, the performance of a filament-wound flywheel disk should be assessed in terms of different design parameters to provide information regarding its energy storage capability and robustness for different applications. In this chapter, parametric and comparative analyses of a spinning filament-wound composite flywheel disk are conducted based on the results obtained from numerical analyses of the disk, including with a mosaic-patterned configuration and different performance-controlling factors. Also, various design aspects are assessed in terms of the dimensions and energy storage capacity of the disk.

This study focuses on various parameters involved in designing a filament-wound flywheel disk; for instance, its limit angular speed, limit regimes of braking, rotational stability and energy storage capability are investigated with emphasis on determining the effects of its geometric and material parameters. Firstly, fields in which flywheels have been applied are explored and, based on the specifications and requirements for practical cases, various comparative analyses are performed for the chosen filament-wound flywheel disk.

5.2 Applications of composite flywheels

The concept of flywheel energy storage (FES) started a long time ago. During the 1960s and 1970s, NASA-sponsored programs suggested applying a FES system as the possible primary source for space missions, as was also proposed for electric vehicles and stationary power back-up [85-86] and, in following years, composite rotors were fabricated and tested in a laboratory by US Flywheel Systems (USFS) and other organisations [87-88]. Tests of the USFS-designed flywheel showed a power density of 11.9 kWh/kg at its design speed of 110,000 rpm and efficiency of 93% [89]. The University of Texas in Austin manufactured a composite flywheel that achieved a rotational speed of 48,000 rpm with 90,000 charging/discharging cycles without any loss of functionality [90]. A composite flywheel-based FES system is particularly suitable for applications that involve a large number of charging/discharging cycles, such as the International Space Station (ISS), Low Earth Orbits (LEOs), Hybrid Electric Vehicles (HEVs) for pulse-power transfer and improving the overall efficiency, controlling Power Quality (PQ); and resolving many other issues [85].

At present, composite flywheels are being developed as alternatives to expensive chemical batteries and promise improved performances and increased service lives in different NASA and military applications, such as spacecraft, launch vehicles, aircraft

power systems, uninterruptible power supplies and planetary outposts and rovers [41, 91]. Advanced composite materials are being considered as materials of choice for energy applications because of achievable higher energy and power densities [92]. A composite flywheel offers a better energy-density storage capability per unit mass than that of a battery which has slow loading and unloading cycles due to its chemical process and short life [45]. An optimal composite flywheel can attain a much higher rotational speed than a metallic one which compensates for the low mass of its rotor without compromising its kinetic energy storage capacity [1]. In general, a structure's mass can be reduced by 20% to 30% through the replacement of its metal alloys by composite materials [2]. A flywheel facilitates the recovery of a vehicle's kinetic energy lost as heat during braking which it can store and release in automotive vehicles in fractions of a second [93].

One prominent application of a composite flywheel is storing the energy generated by photovoltaic cells in satellites passing through half an orbit with greater reliability and lower weight [94]. Two fields that have been mentioned [95] for the application of a composite flywheel are the orbiting ISS and advanced locomotives. The ISS relies on only electricity for all its functions; for example, powering its lights, its life support systems and computers as well as scientifically important experiments [96], with rechargeable nickel-hydrogen batteries powered by photovoltaic cells using sunlight providing power for it when it enters the Earth's shadow during each orbit. The ISS's orbit takes 90 minutes, with 60 minutes in sunlight when power is collected by solar arrays and stored in batteries, and 30 minutes in shadow when batteries supply all the power required for different functions. Unfortunately, electrochemical batteries can charge and discharge only a limited number of times with a high depth of discharging [97] while a chemical battery has only a five-year lifetime. Electrochemical batteries are considered critical for the overall mass of a spacecraft [98] but replacing worn-out ones is very expensive. Considering these factors, a

FES system would be an efficient option as a flywheel-based battery has a lower weight and at least a 15-year lifetime under the same conditions. NASA could save tens of millions of dollars a year in equipment and energy costs by using flywheel batteries which could be used in satellites, space stations.. They could also be used in other terrestrial applications to provide backup power for hospitals and serve as a power bridge to fill the gap between power outages and generator start-ups in manufacturing plants. It is estimated by NASA that more than US$ 200 million can be saved if space station batteries are replaced by a FES system [90]. Flywheel batteries in satellites and space stations use two composite flywheels to augment chemical nickel-hydrogen batteries and each NASA flywheel unit is able to store more than 15 MJ and deliver a peak power of 4.1 kW [86], an efficiency which may make placing satellites in a Low Earth Orbit economically feasible [96] whereby They could fly closer to Earth from geostationary orbit and be used for communications without lag times. As researchers have determined that flywheels can be discharged at a higher percentage than electrochemical batteries under the same conditions, 80 percent more energy can be recovered from them. This increase in available stored energy, called the depth of discharging, combined with a flywheel having less weight, more charging/discharging cycles with less wear/tear and a longer life span, offers several advantages. Recent advances in both the materials used in manufacturing flywheels and their control techniques, such as better magnetic bearings, have enabled flywheels to spin at higher speeds and, thus, their total amounts of stored kinetic energy have begun to surpass, on a mass basis, those of electrochemical batteries. Magnetic bearings can suspend a flywheel rotor in a vacuum and enable it to attain a rotational speed of as high as 60,000 rpm [96].

Besides being applied in a space station, a composite flywheel is also used in a hybrid-powered locomotive to not only supplement its turbine during acceleration but also store its

braking energy, called regenerative braking, which is used for acceleration at the locomotive's starting time to improve efficiency. The University of Texas at Austin tested the performance of a FES system mounted in a hybrid electric bus and found that it could accelerate the fully loaded bus to 100 km/h, store about 7.2 MJ of energy and provide a peak power capability of 150 kW, while a specific energy of more than 120 kJ/kg and specific power of 2.5 kW/kg of its rotating mass were achieved [99].

A flywheel can play important roles in preventing blackouts and regulating the functioning of not well-meshed networks in electricity distribution [100]. Also, a FES system can be used to maintain power quality in other sectors as it meets short-term, random fluctuations in demand and avoids the need for frequency regulation [85], and can provide 'ride through' for momentary power outages and harmonic distortions, and eliminate voltage sags and surges. Companies in both Europe and the United States have developed systems for storing surplus electricity generated during off-peak hours to meet high demand during the day [101]; for example, a FES system has been installed by Piller GmbH (Germany) in the combined heat and power station of an AMD semiconductor fabrication facility in Dresden, Germany, and its multiple-flywheel storage subsystem can supply or absorb 5 MW for 5 s while the plant has an overall power rating of 30 MW [85]. A plastic product manufacturer has installed 17 flywheels delivered by Active Power (Austin, Texas) with a combined power rating of 4.75 MW for power conditioning and protection against outages [99], and a 10 MWh commercial FES system has been developed by the New Energy Development Organisation (NEDO) to level loads at electricity substations [102]. Also, a 250 kVA flywheel-based uninterrupted power supply (UPS) has performed well in protecting loads from sags and momentary power outages [103]. Flywheels are of utmost interest for the localised storage of electricity generated by wind turbines and photovoltaic cells because of their variable and intermittent outputs. A

flywheel-based storage unit can remove the need for downstream power electronics to track fluctuations and, thereby, improve overall efficiency [104-105].

Also, a FES system has the potential to replace existing steam catapults used to launch aircraft from carriers [106] as it is considered to be a better energy storage choice due to its low weight and volume, high tolerance to charging/discharging cycles and fewer maintenance requirements. An electromagnetic aircraft launching system (EMALS) consists of four major subsystems, an energy storage subsystem, a power-conditioning subsystem, a launch engine and a control system. The advanced flywheel rotor in each module of EMALS operates at a maximum rotational speed of 7,018 rpm and stores 126 MJ of energy which provides a specific energy of 47.6 kJ/kg [106]. Therefore, a flywheel-based EMALS technology can be regarded as having good potential for future aircraft carriers.

Various systems used for effective energy storage and their specific energies are listed in Table 5.1 [44, 107] which shows that a composite flywheel system is capable of generating a much higher specific energy than other systems.

Table 5.1: Specific energies of various systems used for energy storage

Storage type	System	Specific energy (Wh/kg)
Magnetic fields	Superconducting coil	1 – 2
Elastic deformations	Steel spring	0.09
	Natural rubber band	8.8
Electrochemical reactions	Lead-acid battery	17.9
	Nickel-cadmium battery	30.6
Kinetic energies	Maraging steel flywheel	55.5
	4340 steel flywheel	33.3
	Composite flywheel	213.8[1]

[1]using longitudinal strength of Kevlar without any shape factor

In recent years, there has been increasing interest in developing FES devices for industrial applications [108], such as UPS and transport systems, as this technology

provides superior attributes compared with other energy storage alternatives, such as electrochemical batteries [90], includes faster charging/discharging capabilities, has longer durability and an increased energy density. In particular, the enhancement of high-strength materials, such as fibre-reinforced polymer composites (FRPC), and advances in power electronics and loss-reduction approaches, such as magnetic bearings, have improved the performance of a FES system [108].

The flywheel-based UPS technology is an emerging option for storing energy kinetically rather than chemically. As opposed to dozens of 100-pound containers of lead plates submerged in sulphuric acid, its magnetically-levitated flywheel rotor stores energy more efficiently and effectively, regenerates power when necessary and eliminates issues related to mechanical bearings, such as friction, cooling requirements, energy wastage and high maintenance costs.

The combined energy and attitude control system (CEACS) used in spacecraft for attitude control and energy storage consists of a high-speed composite flywheel rotor, magnetic bearings, a motor/generator and control electronics [97], and has been reported to be a prospective option for energy storage in small satellites. The requirements of different types of small satellites (i.e., nanosatellite, microsatellite and enhanced microsatellite) for peak power vary from 7 to 98 W while the energy storage capacity of a flywheel used in the CEACS should be between 4.2 and 60 Wh and inertia within the range of 1.3×10^{-3} to 15.5×10^{-3} kgm^2. A flywheel is considered to be ideal for this purpose because of its high efficiency, long life cycle, wide range of operating temperatures, high power and energy densities, and lack of charging/discharging frequencies.

An advanced FES system can supply a specific energy of more than 200 Wh/kg [44] whereas 100 Wh/kg is obtained from a common FES system while an electrochemical battery-based system has specific energies of only around 30 Wh/kg with a lead-acid

battery and 100 Wh/kg with a lithium-ion battery. Although a FES system costs about eight times more per unit amount of stored energy than a lead-acid battery system, this is offset by its significant longer life span and practically unlimited number of charging/discharging cycles which exceed those of an electrochemical battery [90, 109]. A FES system provides a stored energy recovery efficiency of up to 95% whereas that of a typical battery, such as a lead-acid, is only 70%. Also, it has less environmental impact due to its lack of harmful chemicals.

As some applications require a high peak-power output for a very short period of time, the total amount of energy they need is small; for example, an energy storage system is/has been used in a hybrid electric vehicle to enhance the power of its internal combustion engine not only for rapid acceleration but also to recover energy during regenerative braking [110]. Another example is the application of an energy storage system for the maintenance of power quality in different fields, such as data centres, semiconductor production, paper production, etc., where an outage lasting for even less than 1 second can cause hours of downtime and production loss [90].

A FES system can be categorised into two groups – low- and high-speed. The former operates in a range of rotational speeds of up to 6,000 rpm and its flywheel is usually made of steel and mechanical bearings with a magnetic support to increase bearings' service life as the rotor is heavy. On the other hand, a high-speed FES system operates at from 10,000 to 100,000 rpm, with its flywheel made of composites, its mass moment of inertia, weight and dimensions relatively lower, and its rotor supported by magnetic bearings which results in negligible losses [111]. As it has been estimated that over 80% of utility power problems last for less than 1 second [90, 110], an energy storage system capable of supplying power for only a few seconds can greatly reduce the frequency and ensuing damage caused by power quality problems.

A recent study [112] showed that a flywheel made of advanced composite materials can be useful in converting an aircraft's high kinetic energy on landing, which is usually dissipated at its wheel brakes as heat, to useful electrical energy that can be stored in a battery. It was found that applying such a system, with a conservative estimate of five landings per day, to the Boeing 777 aircraft family in active service today results in total energy savings comparable to the amount of electricity generated from a 4.6 MW coal-fired power plant.

In general, the total amount of stored energy in a FES system is determined by the size, weight and maximum possible rotational speed within the strength limit of the flywheel's rotor. Considering different fields for the application of a FES system and their various requirements, the key factors for a flywheel technology should be determined accurately and the flywheel's rotor manufactured accordingly.

The minimum requirement for a FES system is an efficient rotor shape to take full advantage of its materials' strengths, minimise its losses, ensure its reliable operation over a long lifetime, attain a high efficiency in power conversion and minimise damage in the case of its/the rotor's failure [113]. Four constraints must be taken into consideration for the various types of flywheels used in a number of applications: (i) the strength of the flywheel's materials, (ii) the loading conditions, (iii) the shape and size of the flywheel's rotor and (iv) the maximum rotational speed of the rotor [89].

5.3 Design considerations including mosaic-patterned effect

A FES system consists of a rotor, motor/generator, magnetic bearings, touchdown bearings, vacuum housing and power conversion system [114-115]. The magnetic bearings provide a very low frictional loss by supporting the flywheel's rotor and, as the rotor needs to maintain a high rotational speed during its operation, its proper design using materials with high mechanical strengths for stability is an important step in developing a FES

system. Although current research studies deal with optimum designs and stress analyses of flywheel rotors [1], these must be preceded by determining accurate geometric parameters for a flywheel rotor for a particular application.

Typically, although a flywheel's hoop strength can be increased by improving the strength of its reinforcing fibres, it is difficult to attain improved radial strength, i.e., strength along the transverse directions of the fibres. Therefore, as the radial stress due to rotation is critical in terms of its performance [116], a flywheel should be designed in a way that minimises the radial stress developed to prevent failure of the fibres in the transverse directions. The results obtained from stress analyses of a filament-wound flywheel disk with a mosaic-patterned configuration indicate that the levels of different stresses can be underestimated by a general stress analysis based on the conventional mechanics of laminated structures which does not take into account the effect of the mosaic pattern of $\pm\phi$ angle-ply layers. Therefore, to design a filament-wound flywheel disk that fulfils the requirements for a particular application, manufacturing effects produced during the filament-winding process should be included to determine its actual strength under various loadings.

5.4 Fabrication of filament-wound composite flywheel disk

Standard technologies for fabricating filament-wound structures are based on the fact that the form of a mandrel corresponds to that of the final product. Fixing both the structure and form itself is undertaken at the heat treatment stage, after which the final stiffness and strength characteristics that depend on the reinforcement are achieved for the desired structure [117]. A filament-winding process is realised through fulfilling a number of conditions, such as maintaining the continuity and regularity of winding, stability of the winding trajectory and adjacency of the fibres to the surface of a mandrel. Although these restrictions may not be completely or even partially satisfied due to the form of a particular

structure or the law of required reinforcement, introducing a transformation stage during the process makes it possible in some cases to not only remove the existing restrictions but also obtain a non-standard structure that may possess unique characteristics. A transformation technology involves selecting a pre-form and a winding which subsequently creates the desired form. When the final shape and law of required reinforcement of a filament-wound flywheel disk are given, the shape of the pre-form made by geodesic winding needs to be determined, a method for calculating which is demonstrated by Mitkevich et al. [117] for various dimensions of both the inner and outer radii. In the first stage, the filament-wound disk is fabricated by winding fibres onto an inflated elastic mandrel similar to that shown in Figure 5.1. Then, after a shell of revolution with the appropriate filament-winding pattern is fabricated, the pressure is continuously reduced and the shell compressed in the axial direction between two plates and, as a result, transformed into a flat disk, after which the resin in the composite material is cured. The transformation stages and resultant disk are illustrated in Figure 5.2 [2, 117-118]. Therefore, the finished filament-wound flywheel disk has an annular band of smooth, continuously turning fibre trajectories tangent to both its outer and inner peripheries.

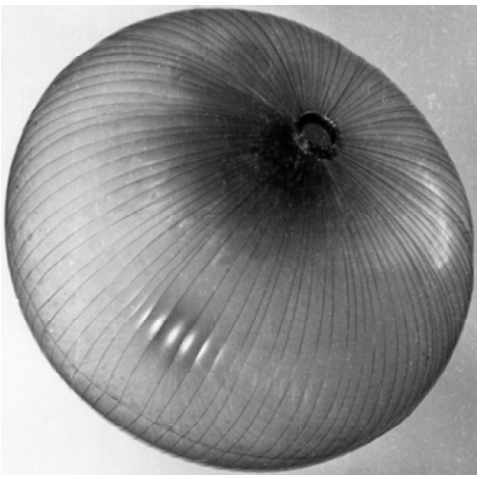

Figure 5.1: Inflated elastic mandrel reinforced along meridians [2]

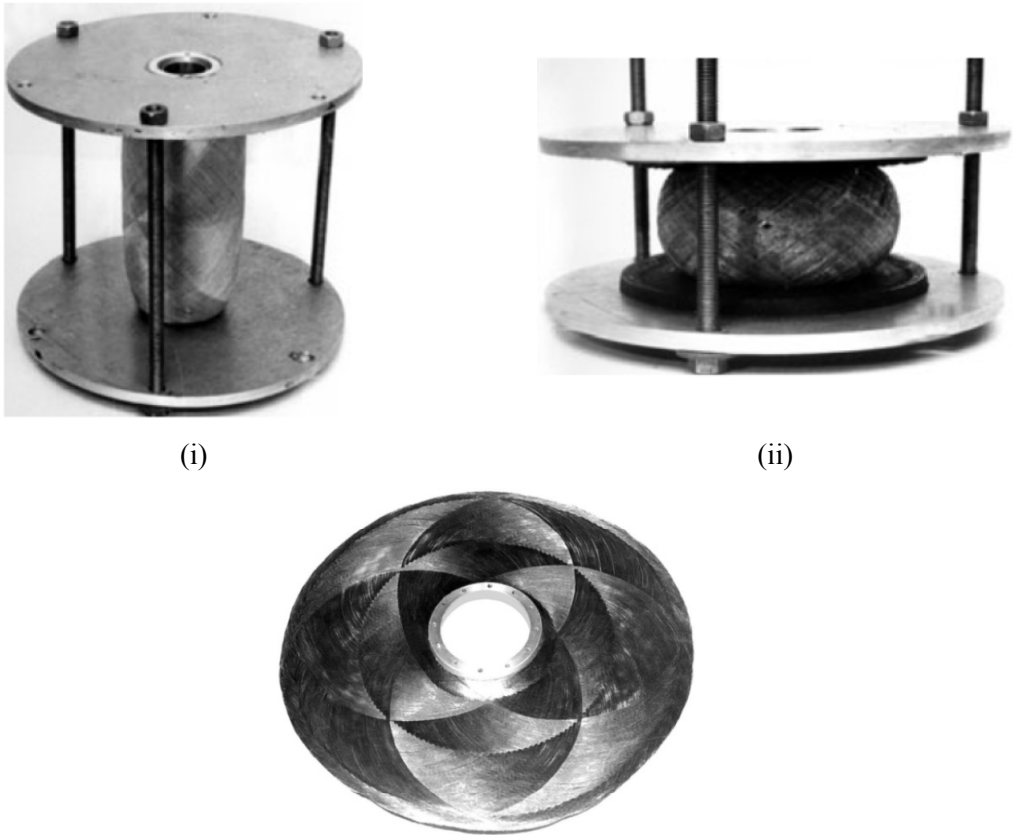

Figure 5.2: Transformation stages of shell pre-form to filament-wound flywheel disk: (i) initial shell preform, (ii) intermediate deformation stage and (iii) resultant filament-wound flywheel disk

5.5 Processes for designing flywheel rotor

Over the years, flywheel rotors have been designed for different types of applications, as discussed in Section 5.2 and, for a composite rotor design, many approaches have been employed, with one very popular design a filament-wound rim fabricated using advanced composite materials [119] which can consist of either one or multiple rings, with a single-rim design either a flat disk or cylinder. Both designs comprise a single thick ring attached to a metal hub using an interference fit that eliminates high radial tensile stress in the rim by developing a compressive radial stress up to a maximum possible operating speed.

For a design, trade-offs among the main objectives of a filament-wound composite flywheel disk need to be made [109]; for example, a heavy and expensive rotor can offer a large absolute energy value but, for a flywheel disk's given geometry, selecting the lightest fabricating materials can minimise its weight. Therefore, various aspects of a filament-wound flywheel disk should be considered for parametric and comparative analyses and, for any shape of a flywheel rotor, the following information should be taken into account when evaluating its performance [113]:

- the kinetic energy stored in it;
- the kinetic energy per unit of its mass; and
- its allowable stress limits.

5.5.1 Flywheel geometry

Flywheels for use as energy storage systems can be of different shapes and sizes. Various studies [113, 120-122] have reported a number of possible shapes, such as a constant stress disk, conical disk, constant thickness (pierced and unpierced) disk, a disk with a rim and a multi-ring hybrid flywheel.

In a single-rim design, a thin rim with a large radius can be employed to achieve high instantaneous power and a large energy storage capability [119]. However, as housing constraints may limit its radius, a single rim may not be able to supply the desired level of energy output. Therefore, it is necessary to study the dimensions of a designed flywheel rotor in order to determine how much energy can be obtained from it.

5.5.2 Material selection

As the main objective of using a flywheel in different applications is to store energy in the form of kinetic energy and retrieve it when required, the design of a flywheel should ensure the maximum possible energy storage capacity. However, this is limited by the

strengths of the materials used to manufacture it, with its maximum specific energy density (energy storage capacity per unit mass) (E_{sp}) related to the maximum tensile strengths (σ_{ult}) and densities (ρ) of its materials which can be expressed as [3, 85, 123]

$$E_{sp} = K\frac{\sigma_{ult}}{\rho} \tag{5.1}$$

where K is the shape factor which is a measure of a flywheel rotor's shape efficiency in a stress-limited case. The dependence of E_{sp} on the material properties demonstrates the importance of using materials with high tensile strengths as well as low densities. The theoretical specific energy capacity calculated using $K = 0.5$ for a flywheel made of different types of fibres is shown in Table 5.2 in which it can be clearly observed that a flywheel made of fibre-reinforced composites offers a higher specific energy storage capacity than a steel one. In addition, a composite flywheel provides safety in the case of the maximum allowable rotational speed being exceeded because its fibres undergo gradual delamination and disintegration from its outer circumference rather than exploding unpredictably [124].

Table 5.2: Physical parameters of commercial fibres [85]

Flywheel material	σ_{ult} (GPa)	ρ (kg/m^3)	E_{sp} (Wh/kg)
E-glass	3.5	2540	190
S-glass	4.8	2520	265
Kevlar	3.8	1450	370
Spectra 1000	3.0	970	430
T-700 graphite	7.0	1780	545
T-1000 graphite (projected)	10.0	-	780
Maraging steel	2.7	8000	47

As, for a composite structure, its fibres are the main contributors to its strength, they should be selected carefully based on their strength data for the fabrication of a flywheel rotor. Static strength data for the fibres and matrix materials used in fabricating a composite rotor documented in the literature [119, 125] are presented in Table 5.3 and these obtained from

different tests can be used as a guide when choosing the proper types of fibres for a filament-wound composite flywheel disk. Currently, a high-speed composite flywheel rotor developed for an energy storage system is fabricated with high-modulus fibres.

Table 5.3: Mechanical properties of fibres [119, 125]

Fibre type	σ_{ult} (MPa)	ρ (kg/m^3)	Elastic modulus (GPa)
T300	4210	1780	230
M40J	4400	1777	377
T1000G	6370	1800	294
T700 (carbon)	4830	1804	228
Kevlar 49	3620	1448	120
Kevlar 29	3620	1437	58
Twaron	3150	1437	80
Twaron HM	3150	1448	124
Technora	3040	1386	70
Spectra 900	2680	970	117
Spectra 1000	3120	970	173
Dyneema	2700	970	87
Zylon HM	5800	1560	269

5.5.3 Rotational speed

The amount of kinetic energy stored in a flywheel increases quadratically with its rotational speed (ω) and linearly with its mass moment of inertia (I). However, its maximum attainable angular speed is limited by the strength of its fabricating materials, as can be seen in Eq. (5.1). It should be noted that, for the purpose of a FES application, instead of a flywheel's total energy, the difference between its maximum and minimum energy storage capacities is preferred, that is, the energy that can be utilised by discharging each FES cell at the limits of its limit rotational velocities (ω_{max} and ω_{min}) and, therefore, the useful energy is less than the stored energy. The speed ratio (k) is defined as the ratio of the maximum to minimum speeds. In addition, the discharge efficiencies of a flywheel's motor/generator and power converter further limit the energy delivered to the load, with the energy extracted from a flywheel by a motor/generator

$$E_{\text{extracted}} = \frac{1}{2} I\left(\omega_{max}^2 - \omega_{min}^2\right) = \frac{1}{2} I \omega_{max}^2 \left[1 - \frac{1}{k^2}\right] \tag{5.2}$$

5.5.4 Loadings

For a successful rotor design, different types of loads need to be taken into account. Researchers have reported a variety of loading conditions and their effects on the performance of a flywheel rotor during its service life, with a number of studies of composite rotors performed over the last four decades [120, 126]. The main obstacle to achieving remarkable success in developing a composite flywheel rotor is the radial stress induced by thermal deformation and the rotational body force [116] which is considered to be critical for a composite flywheel that is not very thin as this stress develops inside its rotor [45]. The radial stress is typically 10 times less than the hoop stress and acts in the transverse direction in which the strength of the fibres is up to 30 times less than in the longitudinal direction. For a thick flywheel rotor, radial stress is responsible for failure whereas hoop stress is more detrimental for a thin rotor.

In a FES system, as the charging/discharging cycles become progressively shorter, the effect of angular acceleration becomes prominent and needs to be incorporated in an analysis procedure [63] as do the residual stresses due to cooling after a curing process and resin moisturisation throughout a rotor's life. Although hygro-thermal stresses are not present in a unidirectional flat composite laminate, non-negligible residual stresses up to 20% of the mechanical ones are induced in the closed circumferential geometry of a flywheel rotor [45].

5.5.5 Bearings

A composite flywheel offers high efficiency, a long life cycle, a wide range of operating temperatures, freedom from the depth-of-discharge effect and high power and energy densities on the basis of both mass and volume [85, 99, 127]. To serve the purposes of a

variety of applications, a flywheel rotor must be precisely positioned and accurately controlled while the vibration of a high-speed rotor must be attenuated for stability [128-130]. To achieve these goals, mechanical bearings are replaced by active magnetic bearings (AMB) that can accommodate very high rotational speeds with minimum vibration. Recently developed high-temperature superconducting magnetic bearings offer very low frictional coefficients, in the order of 10^{-6} or even less, that result in lower loss and higher precision in attitude control for space applications.

5.6 Schemes for maximising energy storage capacity of flywheel

Different optimal schemes are used to maximise the energy storage capacity of a flywheel according to different aspects of its application, such as energy per unit mass (EPM), energy per unit volume (EPV), energy per unit cost (EPC) and energy per unit mass and cost together (EPMC) [63]. Based on these, a flywheel should be designed to meet the specific requirements of different applications; for example, a FES system to be used in satellites must provide maximum energy with minimum mass, for a mobile, uninterrupted power supply, it should provide maximum energy per unit volume and, for a stationary electric power supply, the key goal is to maximise the energy output per unit cost while, similarly, maximisation of the energy output per unit mass and cost together is required for electric vehicles [63].

A performance criterion that is useful for analysing a flywheel disk is the energy density (α) which, for a flat disk, may be determined from

$$\alpha = \frac{\omega^2}{14400}\left(\frac{R^4 - r_o^4}{R^2 - r_o^2}\right) \qquad [\frac{\mathrm{Wh}}{\mathrm{kg}}] \tag{5.3}$$

where ω is the angular velocity at failure, R the outer radius, r_o the inner radius and α a measure of the total amount of energy that can be stored in the disk per unit mass.

The energy density of a flywheel can also be expressed in terms of the strengths of the materials used as [3, 85, 123]

$$\alpha = K\frac{\sigma_{ult}}{\rho}$$

This indicates that the energy density of a flywheel is directly proportional to the ratio of the ultimate tensile strengths of the fibres to their densities. The design constant (K), which depends on the stress distributions and, therefore, the flywheel design itself, relates to how effectively the strengths of the fibres are being utilised in a fabricated flywheel disk. It is desirable to maintain the maximum possible value of K to increase the amount of energy stored per unit mass in a flywheel's rotor and it is reported that K has a value approaching 0.5 for a thin rim and, for a disk with a larger radius, 0.31. Another criterion used in flywheel design is the amount of energy stored per unit volume of the disk which is called the volumetric energy density (ψ) and can be determined for a flat disk by

$$\psi = \rho\left(1 - \left(\frac{r_o}{R}\right)^2\right)\alpha \ [\frac{\mathrm{Wh}}{\mathrm{m}^3}]$$

The energy density (α) is maximised to efficiently utilise the strengths of the fibres used in a filament-winding process and, similarly, the volumetric energy density (ψ) is maximised to utilise the space for a flywheel's rotor. For the purpose of saving space, the ratio of the inner to outer radii of a flywheel disk can be taken as a controlling variable to maximise ψ.

For a flywheel with a known geometry, i.e., r_o, R and h are given, maximising its energy density can be accomplished by increasing its rotational speed up to a level at which failure of its materials occurs. Therefore, a failure criterion should be employed to estimate the start of failure of a spinning flywheel disk's materials, with the three most often used the maximum stress failure, maximum strain failure and Tsai-Wu failure criteria.

As, besides its geometry, the performance of a flywheel disk also depends on its maximum rotational speed (ω) which is dictated by its stress distributions due to its rotational load, a failure criterion must be implemented to determine it. As, during the operation of a flywheel, its fibres may experience both compressive and tensile loads, the failure criterion chosen should take into consideration the difference between the compressive and tensile strengths of the laminates. Therefore, the Tsai-Wu failure criterion is a better option for optimisation as it is expressed in the form of a single continuous function and, according to it, a lamina in plane stress is considered to have failed if the following condition is fulfilled [131]

$$H_1\sigma_1 + H_2\sigma_2 + H_6\tau_{12} + H_{11}\sigma_1^2 + H_{22}\sigma_2^2 + H_{66}\tau_{12}^2 + 2H_{12}\sigma_1\sigma_2 = 1 \tag{5.4}$$

The components of this equation are defined as

$$H_1 = \frac{1}{(\sigma_1^T)_{ult}} - \frac{1}{(\sigma_1^C)_{ult}}$$

$$H_{11} = \frac{1}{(\sigma_1^T)_{ult}\,(\sigma_1^C)_{ult}}$$

$$H_2 = \frac{1}{(\sigma_2^T)_{ult}} - \frac{1}{(\sigma_2^C)_{ult}}$$

$$H_{22} = \frac{1}{(\sigma_2^T)_{ult}\,(\sigma_2^C)_{ult}}$$

$$H_6 = 0$$

$$H_{66} = \frac{1}{(\tau_{12})_{ult}^2}$$

Although the value of component H_{12} should be found experimentally, it can be determined empirically by [131]

$$H_{12} = -\frac{1}{2}\sqrt{\frac{1}{(\sigma_1^T)_{ult}(\sigma_1^C)_{ult}(\sigma_2^T)_{ult}(\sigma_2^C)_{ult}}}$$

Timoshenko and Goodier [132] showed that the stresses in a rotating disk are proportional to the density (ρ) of its material and square of its rotational speed (ω) and, using this fact, defined the set of stress functions

$$x_{11} = \frac{\sigma_1}{\rho\omega^2}$$

$$x_{22} = \frac{\sigma_2}{\rho\omega^2}$$

$$x_{12} = \frac{\tau_{12}}{\rho\omega^2}$$

Using these functions, we obtain

$$\rho^2\omega^4(H_{11}x_{11}^2 + H_{22}x_{22}^2 + H_{66}x_{12}^2 + 2H_{12}x_{11}x_{22}) + \rho\omega^2(H_1x_{11} + H_2x_{22}) - 1 = 0$$

which is a quadratic equation from which the value of ω^2 can be determined by (taking only a positive value)

$$\omega^2 = \frac{-b + \sqrt{b^2 + 4a}}{2a} \tag{5.5}$$

where the constants are

$$a = \rho^2(H_{11}x_{11}^2 + H_{22}x_{22}^2 + H_{66}x_{12}^2 + 2H_{12}x_{11}x_{22})$$

$$b = H_1x_{11} + H_2x_{22}$$

The maximum allowable rotational speed of a flywheel disk considering the strengths and stresses of its plies for ensuring that it will not fail, which occurs when the first ply starts to fail, is determined from the minimum values of this quadratic equation's roots.

In this study, the possible failure of a filament-wound disk at different rotational speeds is evaluated at the top and bottom (or middle) of each ply at each of the in-plane integration points. The FEA package ANSYS is utilised to calculate the values of the Tsai-Wu failure criterion, which verifies the strength conditions, for the disk's three designs composed of 4, 8 and 14 plies, each of which is associated with three types of mosaic-patterned configurations. The maximum possible rotational speeds calculated are presented in Table

5.4 in which it can be observed that they vary considerably depending on not only the number of mosaic units incorporated in each FE model but also the model's thickness, i.e., total number of plies, which indicates that estimations of these speeds require consideration of manufacturing effects, such as mosaic patterns.

Table 5.4: Maximum values of allowable rotational speeds

Number of mosaic units	ω (rpm)		
	4-ply disk	8-ply disk	14-ply disk
4	17500	22000	24000
6	14000	19000	22000
8	15000	20000	23000

5.7 Performance parameters for filament-wound flywheel disk

The stresses in the principal coordinate of a ply are functions of the fibre orientation angles which, for a filament-wound disk, are defined as (based on a monotropic model)

$$\phi = \sin^{-1}\left[\frac{R}{r}\sqrt{1-\frac{\lambda}{2}\left(1-\frac{r^4}{R^4}\right)}\right] \tag{5.6}$$

and vary between -90^0 and $+90^0$ [2, 4].

The thickness of the flywheel disk is varied according to the following equation

$$h(r) = \frac{kw_o\delta}{2\pi r\cos\phi} \qquad r_o < r < R \tag{5.7}$$

where

$$\cos\phi = \frac{1}{\sqrt{2}\,r}\mathcal{Z} \tag{5.8}$$

in which

$$\mathcal{Z} = \sqrt{\frac{2(r^2-r_o^2)(R^2-r^2)}{R^2+r_o^2}}$$

It follows from this equation that r must satisfy the condition $r_o < r < R$.

If the filament-wound spinning disk is assumed to be of uniform strength then, as per a monotropic model, $\sigma_1 = (\sigma_1)_{ult}$, where $(\sigma_1)_{ult}$ is the ultimate stress for a unidirectional composite under tension along its fibres, under which condition, the ultimate angular velocity ($\bar{\omega}$) is calculated by

$$\bar{\omega}^2 = \frac{2(\sigma_1)_{ult}}{\rho R^2\left[1+\left(\frac{r_o}{R}\right)^2\right]} \tag{5.9}$$

The linear circumferential velocity at the outer circumference of the spinning disk ($r = R$) using Eq. (5.9) and $\bar{v}_R = R\bar{\omega}$ is

$$\bar{v}_R = \sqrt{\frac{2(\sigma_1)_{ult}}{\rho\left[1+\left(\frac{r_o}{R}\right)^2\right]}} \tag{5.10}$$

The volume of the flywheel disk is

$$V = \int_a^b dV = 2\pi\int_a^b rh(r)\,dr \quad r_o < a, b < R \tag{5.11}$$

after integrating Eq. (5.11), we obtain

$$V = \left[-\frac{Rkw_o\delta}{\sqrt{2\lambda}}\tan^{-1}\left(\frac{\sqrt{\frac{\lambda}{R^2}}(R^2-\lambda r^2)}{\lambda\mathcal{Z}}\right)\right]_a^b \tag{5.12}$$

The mass moment of inertia of the flywheel disk is

$$I = \int_a^b r^2\,dm = \rho\int_a^b r^2\,dV = 2\pi\rho\int_a^b r^3h(r)\,dr \tag{5.13}$$

integrating Eq. (5.13) gives

$$I = \left[-\frac{1}{\sqrt{2}}\frac{R^3\rho kw_o\delta\left(\mathcal{Z}\sqrt{\frac{\lambda}{R^2}}+\tan^{-1}\left(\frac{\sqrt{\frac{\lambda}{R^2}}(R^2-\lambda r^2)}{\lambda\mathcal{Z}}\right)\right)}{\lambda\sqrt{\lambda}}\right]_a^b \tag{5.14}$$

The energy storage capacity of the flywheel disk is calculated by

$$E = \frac{1}{2} I \omega^2 \tag{5.15}$$

The maximum kinetic energy that can be stored in the flywheel disk is

$$E_{max} = \pi \bar{\omega}^2 \rho \int_a^b h(r) r^3 dr \tag{5.16}$$

integrating Eq. (5.16) gives

$$E_{max} = \left[-\frac{1}{2\sqrt{2}} \frac{\bar{\omega}^2 R^3 \rho k w_o \delta \left(\mathcal{Z} \sqrt{\frac{\lambda}{R^2}} + \tan^{-1} \left(\frac{\sqrt{\frac{\lambda}{R^2}} (R^2 - \lambda r^2)}{\lambda \mathcal{Z}} \right) \right)}{\lambda \sqrt{\lambda}} \right]_a^b \tag{5.17}$$

The mass of the composite disk considering a uniform density is

$$M = 2\pi \rho \int_a^b h(r) r dr \tag{5.18}$$

after integrating Eq. (5.18), we obtain

$$M = \left[-\frac{R \rho k w_o \delta}{\sqrt{2\lambda}} \tan^{-1} \left(\frac{\sqrt{\frac{\lambda}{R^2}} (R^2 - \lambda r^2)}{\lambda \mathcal{Z}} \right) \right]_a^b \tag{5.19}$$

The specific energy storage (energy per unit mass) capacity of the filament-wound flywheel disk can be determined from Eqs. (5.17) and (5.19).

It can be noted from Eqs. (5.7) to (5.19) that the different performance parameters depend on several variables that can be controlled to achieve the desired level of energy storage capacity, that is, the numbers of fibrous tapes passing through the circumference (k), and the tape width (w_o), tape thickness (δ), inner radius (r_o), outer radius (R) and material density (ρ). However, for a particular material selected based on its strength for fabricating the disk, all these variables except R and r_o can be assumed to be constant. The outer radius (R) should be properly adjusted for applications in which the volume of the

flywheel needs to be constrained to a particular given value. Similarly, for an application in which a restriction on the shaft diameter needs to be maintained, the inner radius (r_o) should be properly adjusted to obtain the required performance. Therefore, the performance-controlling parameters of the disk are assessed by changing its dimensions (r_o and R) to obtain their appropriate values.

A flywheel's high rotational speeds cause stress states which are dependent on its material properties, geometry and rotational speed while its stored kinetic energy is dependent on its mass moment of inertia and rotational speed. Different parameters of the filament-wound flywheel disk are analysed to explore their influence on the energy storage capacity and performance of the disk without it failing during operation. To achieve reliable performance, its specific energy storage capacity should be assessed on the basis of the maximum allowable stress states developed in it for the given materials.

5.8 Assessment of performance parameters for flywheel disk

For a filament-wound composite flywheel disk with $r_o = 0.1016$ m and $R = 0.3$ m, and made of IM6-Epoxy with $\rho = 1600$ kg/m^3 and $(\sigma_1)_{ult} = 3.5 \times 10^3$ MPa, its maximum attainable angular velocity determined using Eq. (5.9) is 63,061 rpm (6603.73 rad/s). It follows from Eq. (5.9) that the maximum rotational speed depends on the strength and density of the material used to fabricate it and its dimensions. The dependence of its maximum possible angular and peripheral speeds ($\bar{\omega}$ and $\bar{v}_R$, respectively) on a disk's dimensions is assessed while keeping the inner radius fixed but varying the outer radius (Figure 5.3). For the selected material, both $\bar{\omega}$ and $\bar{v}_R$ depend on the values of r_o and R as, with increasing values of R, the limit peripheral velocity increases while $\bar{\omega}$ gradually decreases and, for $r/r_o < 2$ (where r is used as a variable for denoting changing parameters), $\bar{v}_R$ suddenly plummets which indicates that, for any application, the value of this ratio should be greater than 2.

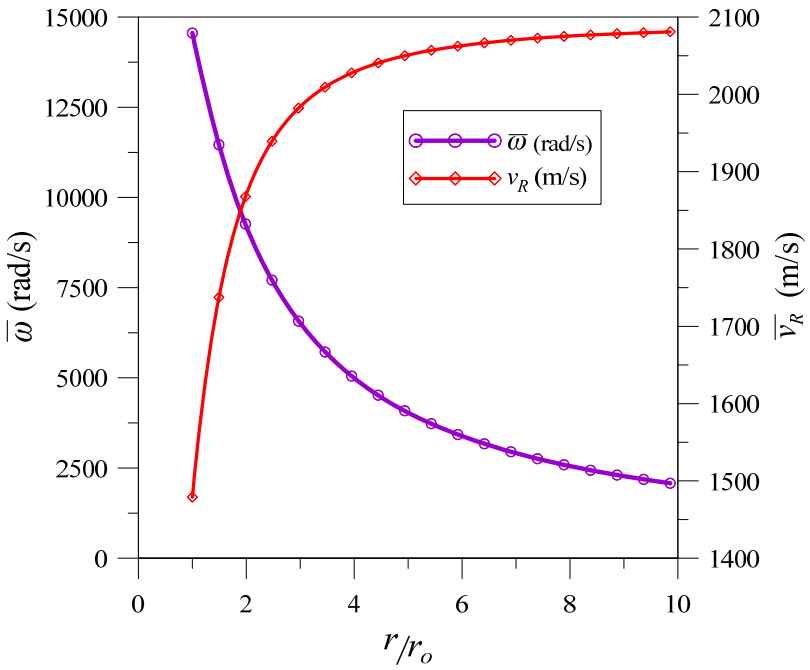

Figure 5.3: Variations in $\bar{\omega}$ and $\bar{v}_R$ with respect to changing R (with constant r_o)

From Eq. (5.10), the maximum values of the linear circumferential velocity ($\bar{v}_R$) of a particular flywheel disk vary depending on the selection of the proper material and its strength and density with those for the chosen disk fabricated with different fibres shown in Figure 5.4.

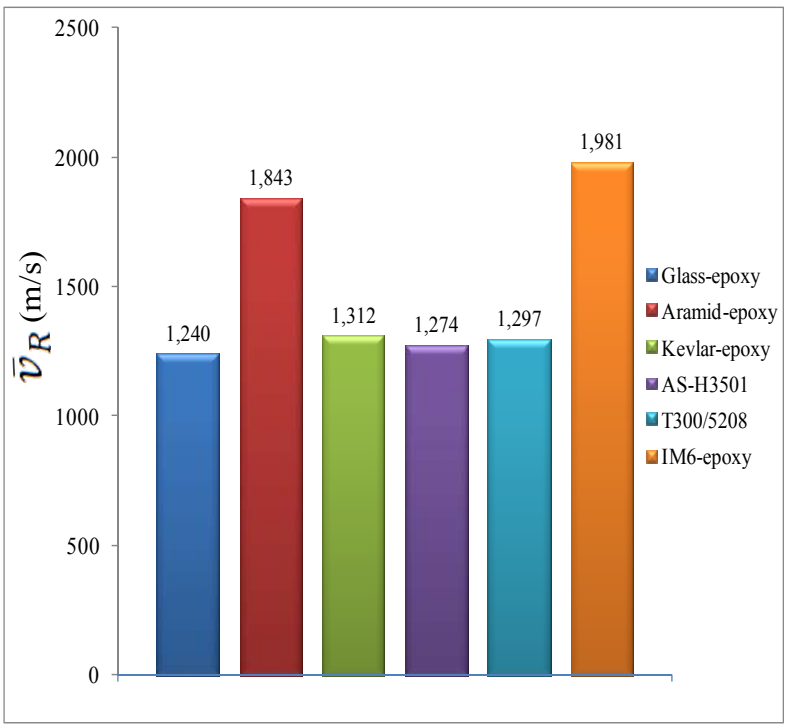

Figure 5.4: Maximum values of circumferential velocity for filament-wound disk

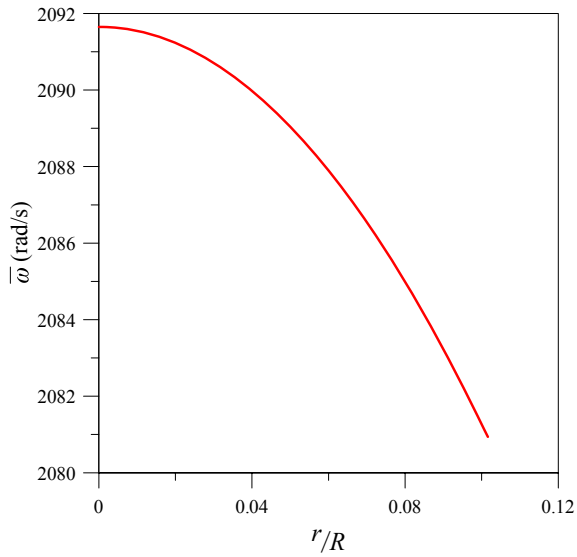

Figure 5.5: Variations in $\overline{\omega}$ with respect to changing r_o (with constant R)

Again, if the outer radius (R) is kept constant and the inner radius (r_o) varied, the results obtained show small changes in the maximum angular speed of the filament-wound disk, as illustrated in Figure 5.5, from which it follows that the maximum value of the ultimate angular speed corresponds to $r_o = 0$, i.e., to a disk without a central opening. Furthermore, it can be observed that relatively small central openings have practically no effect on $\overline{\omega}$; for example, for $r_o/R = 0.10$, the value of $\overline{\omega}$ calculated from Eq. (5.9) is only 0.5% less than its ultimate value.

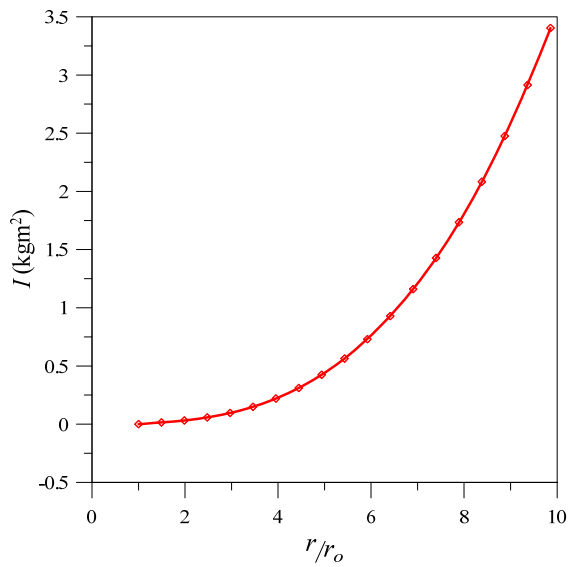

Figure 5.6: Variations in mass moment of inertia with respect to varying R (with constant r_o)

As, according to Eq. (5.15), the energy storage capacity of a flywheel is proportional to its mass moment of inertia (I), a flywheel with a high value of I is expected to offer better energy storage capacity than one with a low I. Variations in I according to Eq. (5.14) with respect to a varying outer radius (R) and fixed inner radius (r_o) are illustrated in Figure 5.6 in which it is observed that a larger magnitude of r/r_o leads to a higher mass moment of inertia. However, this may cause higher stresses and require a reduction in the rotational speed to within a safe limit which will result in lowering the specific energy of the flywheel. On the other hand, as a very small r/r_o ratio results in a lower mass moment of inertia, the specific energy storage of the disk decreases. Therefore, it is important to determine an optimal value of r/r_o which obtains values of both I and $\bar{\omega}$ capable of achieving the maximum possible specific energy from the flywheel disk. It follows from Figure 5.7 that, for $r/r_o < 6.2$, I decreases while $\bar{\omega}$ increases whereas both I and $\bar{\omega}$ follow opposite trends for $r/r_o > 6.2$. Therefore, the dimensions (r_o and R) of a filament-wound flywheel disk should be carefully determined by assessing both the mass moment of inertia and corresponding attainable angular speed for a particular r/r_o ratio anticipated to yield optimal conditions.

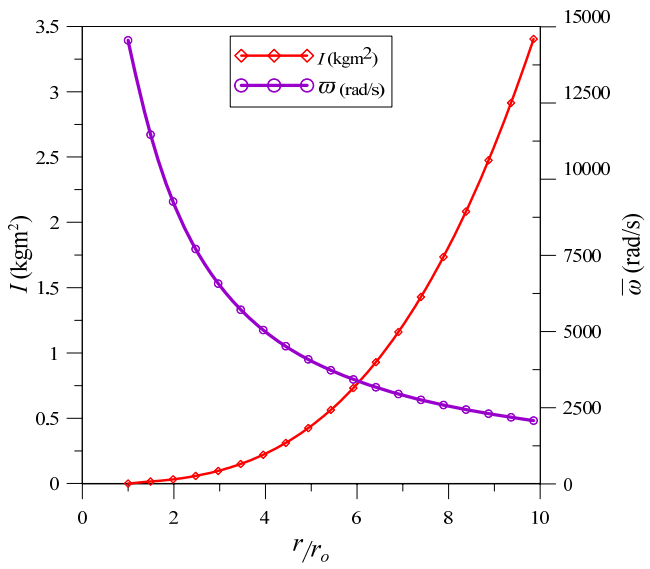

Figure 5.7: Variations in I and $\bar{\omega}$ with respect to variations in outer radius R (with constant r_o)

Variations in r_o with a fixed R (r/R ratio) have a negligible effect on the mass moment of inertia of the filament-wound flywheel disk, as can be seen in Figure 5.8.

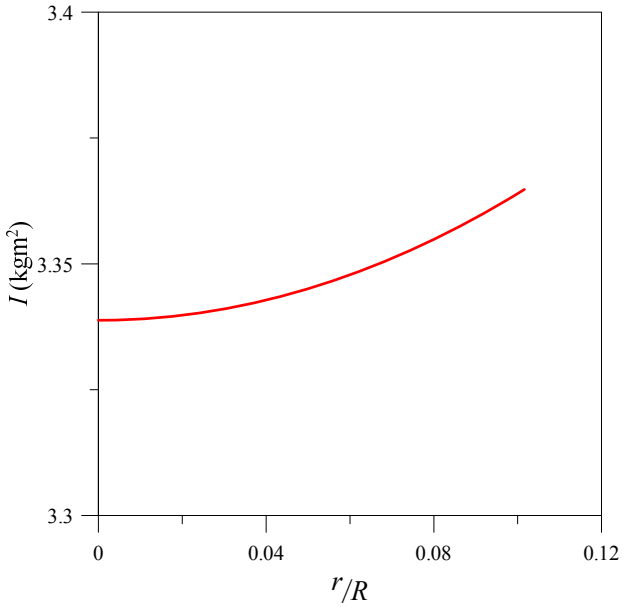

Figure 5.8: Influence of variations in r_o on mass moment of inertia (with constant R)

The influence of r/r_o on the total mass of the filament-wound disk is shown in Figure 5.9 in which a larger r/r_o ratio results in an increased mass. However, varying r_o while keeping R constant does not have a significant effect and the total mass can also be controlled by using different thickness levels which depend mainly on the total number of fibrous tapes passing through the disk's circumference (k), as can be seen in Eq. (5.7). Minimising a flywheel rotor's mass is an important aspect that is particularly significant for mobile applications.

Variations in the maximum energy storage (E_{max}) of the filament-wound flywheel disk according to Eq. (5.17) is demonstrated with respect to the r/r_o ratio in Figure 5.10 which shows that E_{max} follows a gradually increasing trend with increments in the r/r_o ratio. However, a change in the inner radius (r_o) has a negligible effect on the maximum kinetic energy storage capacity of the disk.

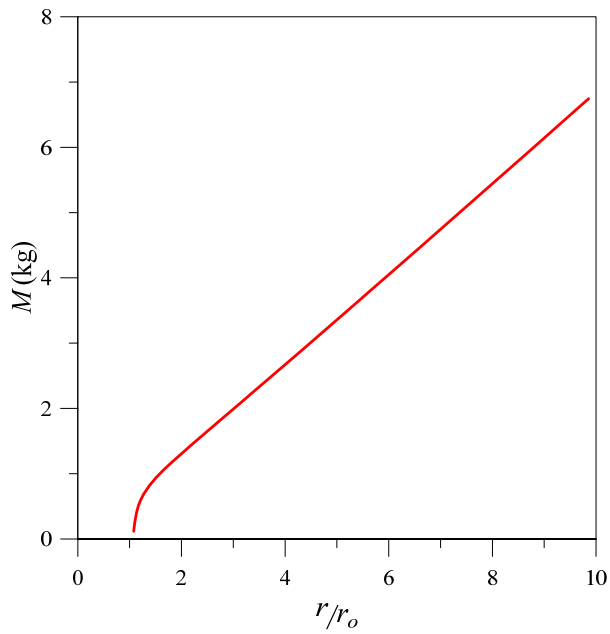

Figure 5.9: Influence of r/r_o ratio on total mass of filament-wound disk

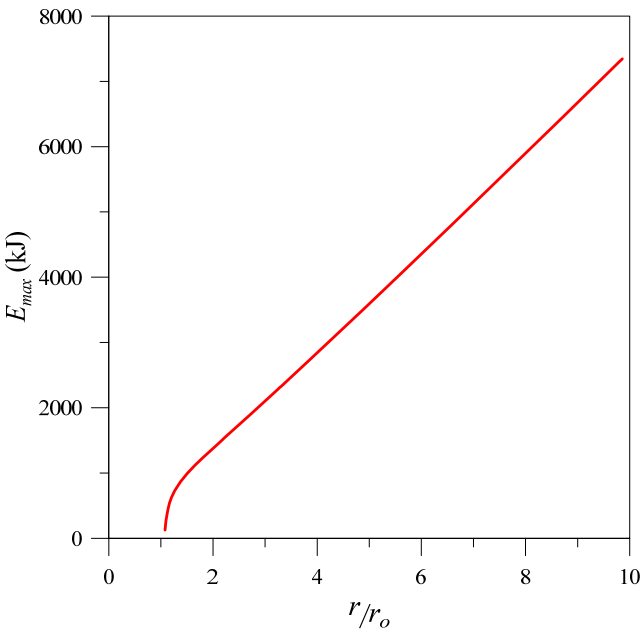

Figure 5.10: Influence of r/r_o ratio on maximum energy storage of flywheel disk

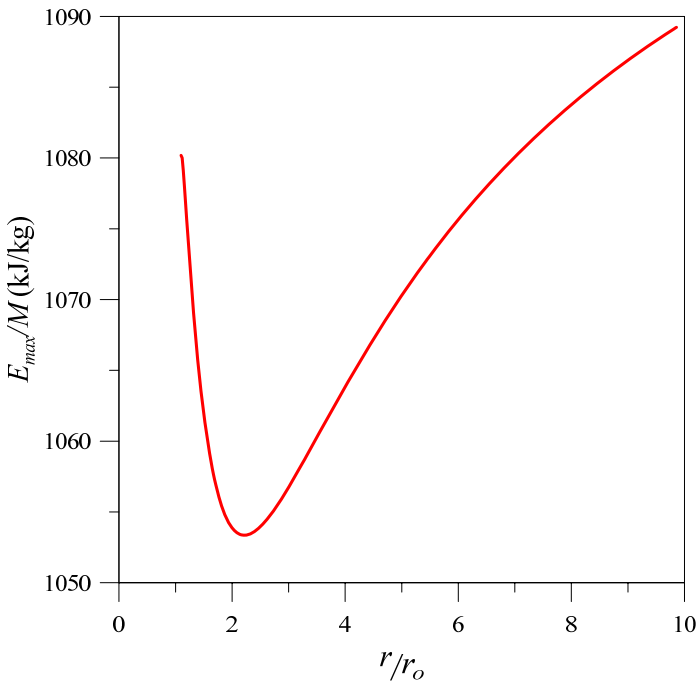

Figure 5.11: Influence of r/r_o ratio on specific energy density of flywheel disk

In order to obtain a design of a flywheel rotor which meets both requirements, i.e., high energy storage capacity and low mass, it is intuitive to maximise the ratio of its energy storage to its mass (E_{max}/M) which is also known as its specific energy density (energy storage capacity). Variations in the specific energy density of the considered filament-wound flywheel disk with respect to its geometric parameters, i.e., R and r_o, are illustrated in Figures 5.11 and 5.12, respectively. As, for $r/r_o < 2.2$, the disk becomes too thin, loses robustness and has a higher tendency to buckle, and $r/r_o = 1$ is impractical because R equals r_o, a filament-wound disk should be designed considering $r/r_o > 2.2$. As can be observed in Figure 5.11, the specific energy capacity of the disk increases gradually with higher values of the r/r_o ratio but its mass also increases, as shown in Figure 5.9. Therefore, depending on the requirements of a particular application, a proper geometry (r_o and R) of the disk as well as other parameters that determine its thickness should be chosen.

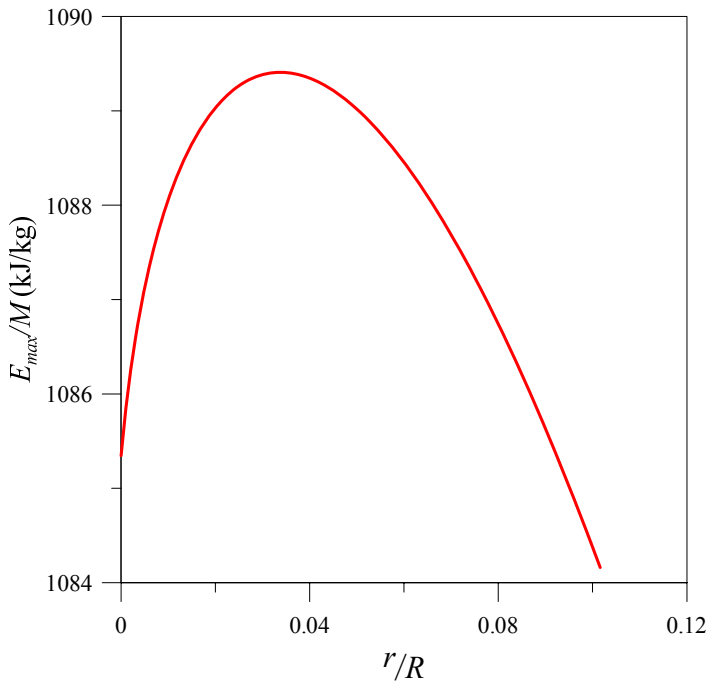

Figure 5.12: Influence of r/R ratio on specific energy density of flywheel disk

Again, to determine the size of a shaft, the energy output per unit mass from the flywheel disk should be assessed by varying r_o while keeping R constant. As can be seen in Figure 5.12, lower values of the r/R ratio yield higher specific energies but $r/R = 0$ is not a viable option for practical applications as the disk does not have a central hole. The effect of varying r_o on the specific energy capacity of the flywheel disk is not very significant as the specify energy values do not differ greatly from the maximum possible ones.

For the filament-wound flywheel disk considered, variations in its volumetric energy density with respect to changing values of its outer radius (R) are presented in Figure 5.13 which shows that, for increasing values of $r/r_o > 2.2$, the volumetric energy density continues to rise.

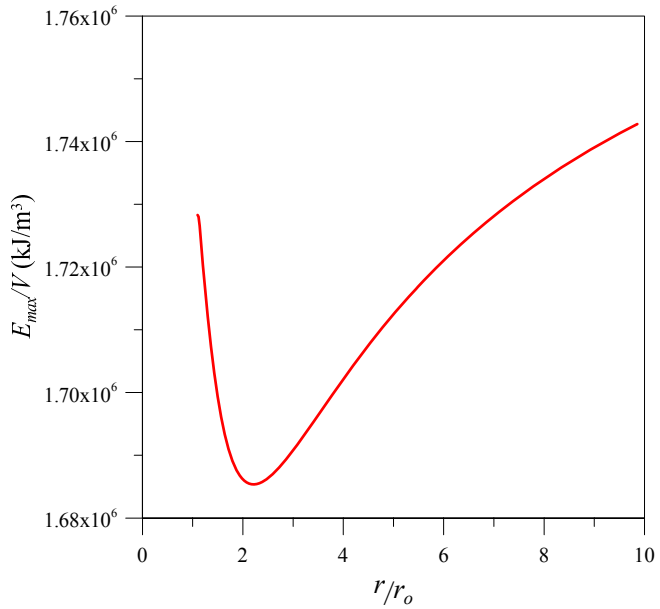

Figure 5.13: Volumetric energy densities of filament-wound flywheel disk with variations in outer radius R (with constant r_o)

5.9 Benchmark design

Thielman and Fabien [37] used an optimal control approach for the design of a stacked-ply composite flywheel using Toray T300 fibre. A benchmark design with disk dimensions of $R = 0.127$ m and $r_o = 0.01905$ m and a stacked-ply arrangement with only tangential ($\phi = 90^0$) and radial plies ($\phi = 0^0$) was determined although an optimised flywheel disk should have different radial reinforcement plies, as shown in Figure 1.5 (Chapter 1). The performances (energy densities) of both these benchmark and optimised designs with the material properties listed in Table 5.5 were calculated.

The filament-wound flywheel disk selected is analysed using the same dimensions and material properties but different reinforcement plies with the fibre trajectories in accordance with Eq. (5.6). A comparison of the energy densities obtained from these three types of flywheel disks indicates that the filament-wound flywheel disk achieves energy density increases of approximately 22% and 8% of those of the benchmark and optimised designs, respectively, as illustrated in Figure 5.14.

Table 5.5: Material properties used in benchmark design

	T300/Epoxy
E_1 (GPa)	142.61
E_2 (MPa)	61.402
G_{12} (MPa)	23.3328
ρ (kg/m^3)	1760
ν_{12}	0.25
$(\sigma_1^T)_{ult}$ (MPa)	2190
$(\sigma_1^C)_{ult}$ (MPa)	2190
$(\sigma_2^T)_{ult}$ (MPa)	2.41
$(\sigma_2^C)_{ult}$ (MPa)	7.23
$(\tau_{12})_{ult}$ (MPa)	2.52

It can be noted that the filament-wound flywheel disk achieves an energy density close to 173 Wh/kg which is five times higher than that of a typical automobile lead-acid battery of 30 – 40 Wh/kg.

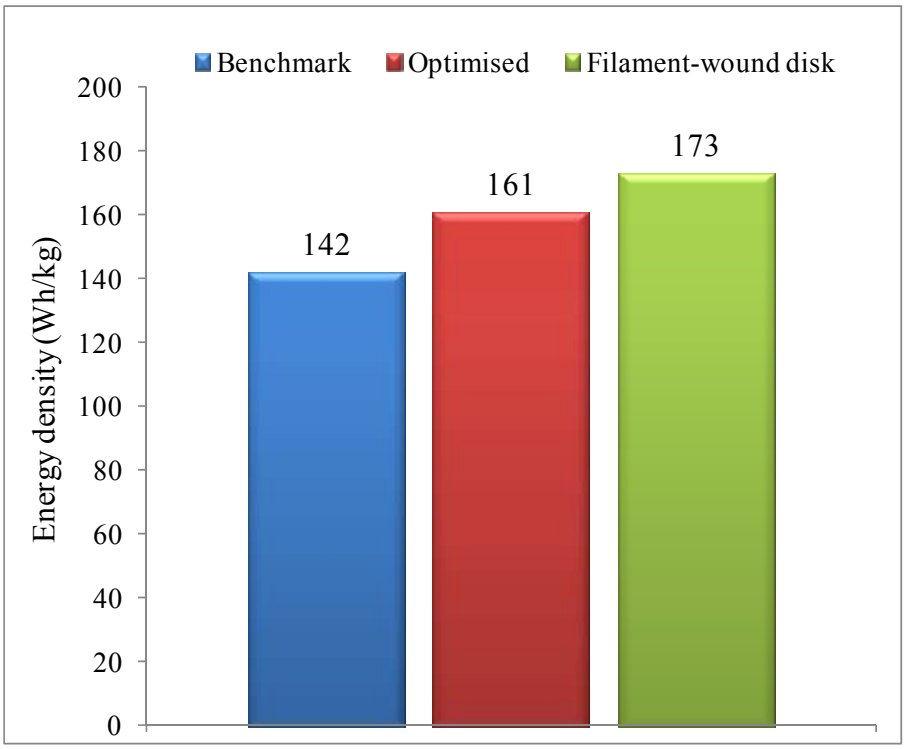

Figure 5.14: Comparison of performances of three types of flywheel disks

5.10 Rotational stability of filament-wound disk

The natural frequencies and mode shapes of a structure provide vital information for understanding its behaviour under general excitation [133] and, in the case of excitation in one of its natural frequencies, a structure faces a catastrophic effect and fails. As, to evaluate the serviceability of a filament-wound flywheel disk with a particular specific energy capacity, its dynamic properties – resonant frequencies, critical rotational speed, etc. - could be decisive factors [134], it is important to determine its natural frequencies and corresponding modes as designers need to control its natural frequencies in order to avoid vibrational resonance. For the filament-wound composite flywheel disk considered, its natural frequencies depend not only on its dimensions and material properties but also its fibre orientation angles [135]. Therefore, a filament-wound disk considering different numbers of plies is analysed using a FEA technique to illustrate how its natural frequencies and mode shapes change according to different numbers of plies and the mosaic-patterned configuration generated during the filament-winding process. Also, the natural frequencies of conventional models of it are calculated.

The natural frequencies of the filament-wound disk with changing thicknesses and consisting of 4, 8 and 14 plies are calculated by the Block Lanczos method in ANSYS. In-plane rigid body motions in the radial and circumferential directions and out-of-plane rigid body motion in the axial direction are prevented by applying displacement and rotational boundary conditions at both the inner and outer radii. The data used for this modal analysis of the disk are presented in Tables 2.1 and 2.2 (Chapter 2).

The natural frequencies considering 10 modes are presented in Table 5.6 in which it can be observed that, under given conditions, those obtained for the 14-ply disk differ considerably from those calculated for the 4- and 8-ply disks and increase significantly as the number of plies, i.e., thickness increases. Furthermore, the fundamental frequencies of a

conventional model of the disk are higher than those of a mosaic-patterned model; for example, the first mode's natural frequency obtained from a conventional model of the 4-ply disk is approximately 10% higher than that calculated for the mosaic-patterned model with the same number of plies.

Table 5.6: Natural frequencies of 4-, 8- and 14-ply disks

Mode	Natural frequencies (Hz)					
	Mosaic patterned models			Conventional models		
	4-ply disk	8-ply disk	14-ply disk	4-ply disk	8-ply disk	14-ply disk
1	77.98	138.26	204.71	85.509	144.11	212.07
2	80.98	138.29	204.73	85.539	145.02	214.24
3	81.00	138.97	212.81	86.905	150.53	220.7
4	86.44	145.86	215.25	87.349	154.31	232.17
5	151.90	247.78	355.97	154.83	255.53	365.99
6	165.57	273.39	395.76	170.94	283.85	408.23
7	165.63	273.57	396.09	171.00	286.31	411.98
8	186.31	303.76	438.74	194.74	321.31	458.35
9	203.14	338.81	482.24	204.45	340.98	492.37
10	216.79	359.55	515.37	217.7	362.44	526.74

The first three mode shapes (first, second and third) of the 4-ply mosaic-patterned model of the disk under the considered boundary conditions are illustrated in Figure 5.15 in which it can be observed that they are affected by the variable stiffness of the filament-wound flywheel disk. Furthermore, the numbers of mosaic units around the circumference of the disk influence its mode shapes. As variations in the fibre orientation angles due to spatially varying fibre paths result in changes in the natural frequencies of vibration, this offers a great degree of design flexibility to adjust the natural frequencies and mode shapes in order to avoid vibrational resonance.

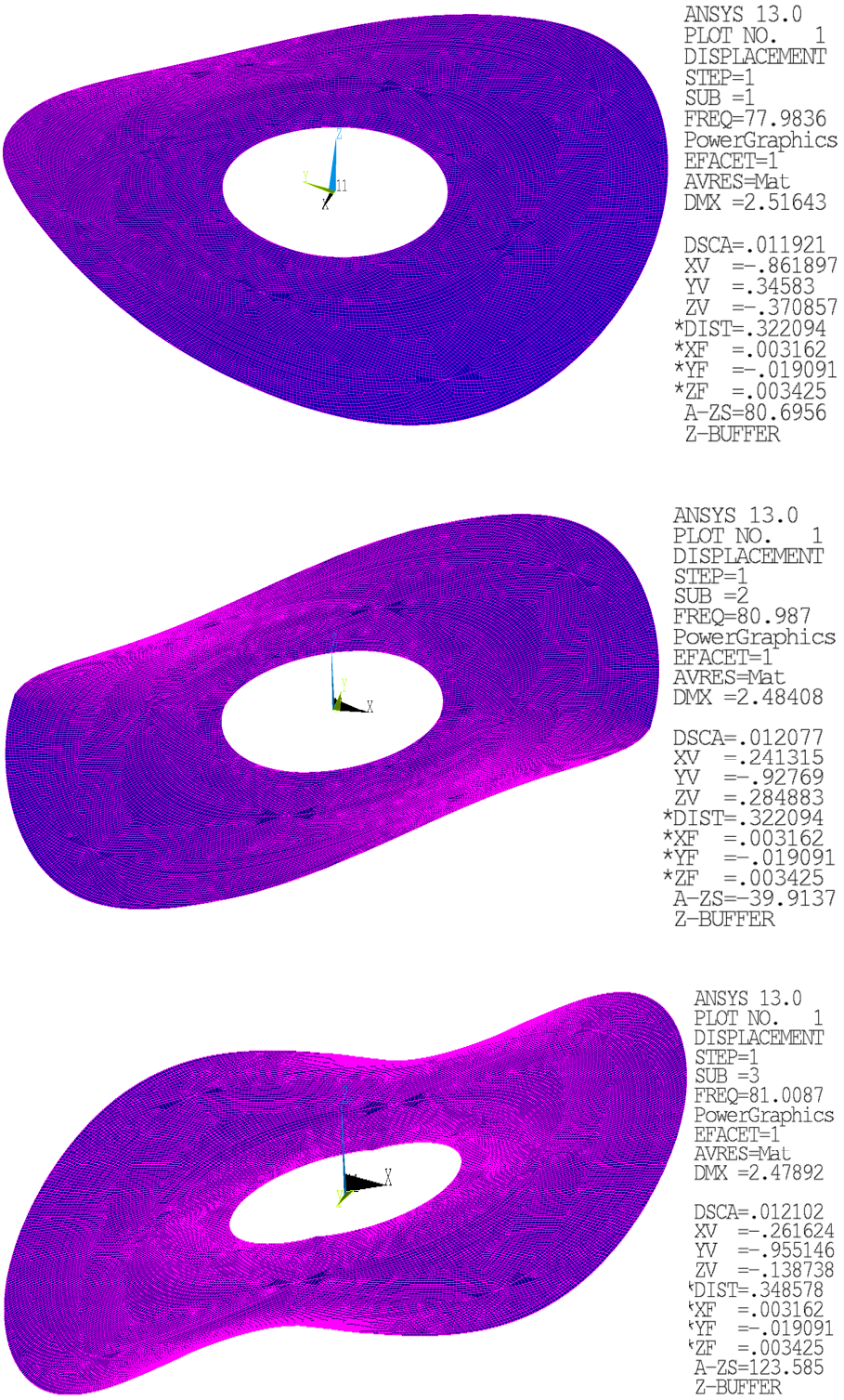

Figure 5.15: First, second and third mode shapes of 4-ply mosaic-patterned model of filament-wound composite flywheel disk

5.11 Limit regimes of braking for filament-wound flywheel disk

It has been reported that, for the generation of short-term impulses of very high power, a set of small identical flywheels is more effective than one large flywheel with an equivalent mass [58]. In most cases, the energy output of a FES system is realised in the form of an electrical impulse of pre-arranged power, the duration of which depends on the amount of energy stored in the flywheel. As the power of a spinning flywheel is proportional to its angular speed, braking rate (angular acceleration) and polar moment of inertia, higher angular acceleration at a given angular speed supplies higher output power from a FES system. As, theoretically, maximum power and maximum stored energy are dependent on the strength of the flywheel and its connection to a shaft, calculating these values in each particular case requires knowledge of the stress states in the flywheel and the strengths of the materials used. A general technique is used to estimate the possibility of achieving a given power impulse ($\dot{W} = \dot{W}(t)$) from a filament-wound composite flywheel-based energy storage system whereby a combination of the current power and energy limits of the flywheel is determined in an invariant form based on calculations of its limit stress states under the actions of centrifugal and inertial forces.

5.11.1 Limit regimes of acceleration-braking

The limit rotational speed of a filament-wound composite flywheel disk can be determined based on the maximum stress failure criterion

$$\frac{\left(\sigma_1(r)\right)_{max}}{(\sigma_1)_{ult}} = 1 \qquad \text{or} \qquad \frac{\left(\sigma_2(r)\right)_{max}}{(\sigma_2)_{ult}} = 1 \tag{5.20}$$

where $\sigma_1$and σ_2 are the stresses along and across fibres, respectively, and $(\sigma_1)_{ult}$ and $(\sigma_2)_{ult}$ their corresponding strengths.

The stresses (σ_1 and σ_2) can be expressed in non-dimensional form, i.e., $\bar{\sigma}_1$ and $\bar{\sigma}_2$, as

$$\bar{\sigma}_1(\delta) = \frac{\sigma_1(\delta)}{\rho\omega^2 R^2}$$
$$\bar{\sigma}_2(\delta) = \frac{\sigma_2(\delta)}{\rho\omega^2 R^2} \tag{5.21}$$

where R is the outer radius (characteristic dimension), ω the angular speed, ρ is density and $\delta = \frac{r}{R}$ the non-dimensional radius.

The limit peripheral speed (v_{max}) can be obtained by substituting Eq. (5.21) into Eq. (5.20) and its maximum value should be invariant with respect to similar changes in the flywheel dimensions, with $v_{max} = \omega_{max}R$ equal to

$$\sqrt{\left(\frac{(\sigma_1)_{ult}}{\rho\left(\bar{\sigma}_1(\delta)\right)_{max}}\right)} \quad \text{Or} \quad \sqrt{\left(\frac{(\sigma_2)_{ult}}{\rho\left(\bar{\sigma}_2(\delta)\right)_{max}}\right)} \tag{5.22}$$

where ω_{max} is the limit angular speed of the filament-wound flywheel that rotates at a constant angular speed ($\dot{\omega} = 0$).

The limit regime of the acceleration (braking) of the flywheel disk can be determined based on a failure criterion which considers the interaction between σ_2 and the shear stress (τ_{12}) [58, 136-137] and can be expressed as

$$\frac{\tau_{12}}{(\tau_{12})_{ult}} + \frac{\sigma_2}{(\sigma_2)_{ult}} = 1 \tag{5.23}$$

As the non-dimensional stress ($\bar{\tau}_{12}$) and non-dimensional time ($\bar{t}$) from which the angular acceleration ($\dot{\omega}$) are considered to be uniform throughout the flywheel as

$$\bar{\tau}_{12}(\delta) = \frac{\tau_{12}(\delta)}{\rho\dot{\omega}R^2}$$
$$\bar{t} = t\omega_{max} \tag{5.24}$$

the angular speed and acceleration can be defined as

$$\omega = \frac{d\theta}{dt} = \frac{d\theta}{d\bar{t}/\omega_{max}} = \bar{\omega}\omega_{max}$$
$$\dot{\omega} = \frac{d\omega}{dt} = \frac{d\bar{\omega}.\omega_{max}}{d\bar{t}/\omega_{max}} = \dot{\bar{\omega}}\omega_{max}^2 \tag{5.25}$$

Now, the strength-failure condition can be written as

$$\frac{\dot{\bar{\omega}}.\bar{\tau}_{12}(\delta)}{(\tau_{12})_{ult}} + \frac{\bar{\omega}^2.\bar{\sigma}_2(\delta)}{(\sigma_2)_{ult}} \leq \frac{1}{\rho.v_{max}^2} \tag{5.26}$$

As, from Eq. (5.26), $\dot{\bar{\omega}}$ and $\bar{\omega}$ must be invariants because $\bar{\sigma}_2(\delta)$, $\bar{\tau}_{12}(\delta)$ and v_{max} are invariants, for given $\dot{\bar{\omega}}$ and $\bar{\omega}$, susceptibility to failure will be equal for similar disks and does not depend on the characteristic dimensions.

The current mass energy storage capacity can be written as

$$W^M = \frac{\omega^2 R^2 \bar{I}}{2} = \bar{\omega}^2 \frac{\omega_{max}^2 R^2 \bar{I}}{2} = \bar{\omega}^2 (W^M)_{max} \tag{5.27}$$

where $\bar{I} = I/(R^2 M)$ is the non-dimensional polar moment of inertia of the flywheel with a total mass of M, and it is observed that $(W^M)_{max}$ is also an invariant.

The current mass specific power is expressed as

$$\dot{W}^M = \omega\dot{\omega}R^2\bar{I} \tag{5.28}$$

multiplying both sides of Eq. (5.28) by R and using Eq. (5.25), we obtain

$$R\dot{W}^M = \bar{\omega}\dot{\bar{\omega}}\omega_{max}^3 R^3 \bar{I} = 2\bar{\omega}\dot{\bar{\omega}}v_{max}(W^M)_{max} \tag{5.29}$$

As can be deduced from Eq. (5.29), as all the quantities on the right-hand side are invariants, $R\dot{W}^M$ is also an invariant which means that $R\dot{W}^M$ will be the same for disks with different R and given $\bar{\omega}$ and $\dot{\bar{\omega}}$. Therefore, as the coordinate sets in the phase plane $((\bar{\omega}, \dot{\bar{\omega}})$, $(\bar{\omega}R, \dot{\bar{\omega}}R^2)$ and $(W^M, R\dot{W}^M))$ are not dependent on the absolute dimensions of the filament-wound flywheel disk, the limit regimes of acceleration-braking corresponding to Eq. (5.23) can be used to characterise a flywheel disk regardless of its absolute dimensions

and those obtained using Eqs. (5.23) and (5.26) in the $(\bar{\omega}, \dot{\bar{\omega}})$ coordinate set can be expressed as

$$\dot{\bar{\omega}} + A(\delta)\bar{\omega}^2 = B(\delta) \qquad 0 \leq \bar{\omega} \leq 1 \tag{5.30}$$

where

$$A(\delta) = \frac{\bar{\sigma}_2(\delta)(\tau_{12})_{ult}}{\bar{\tau}_{12}(\delta)(\sigma_2)_{ult}}, \quad B(\delta) = \frac{(\tau_{12})_{ult}}{\rho v_{max}^2}\frac{1}{\bar{\tau}_{12}(\delta)}$$

The maximum allowable value of $\dot{\bar{\omega}}$ for a given $\bar{\omega}$ can be determined using Eq. (5.30) and is defined as the minimum of all $\dot{\bar{\omega}}$ calculated for δ ranging between $\alpha = r_o/R$ and 1, where r_o is the inner radius of the filament-wound flywheel disk, with the position of the most stressed point possibly changing with the $\dot{\bar{\omega}}/\bar{\omega}$ ratio.

5.11.1.1 Numerical example

To assess the limit regimes of acceleration-braking, a filament-wound flywheel disk with an inner solid aluminium hub and the material properties given in Table 5.7, which has a relative radius of the Al hub of 0.3387, a normalised total mass (divided by hR^2, where h is the thickness of the flywheel disk) of 4.45×10^3 kg/m^3, a normalised total energy capacity (divided by hR^2) of 3.96×10^8 J/m^3, a mass energy storage capacity of 8.91×10^4 J/kg (24.74 Wh/kg) and a maximum peripheral speed of 878.39 m/s, is considered.

Distributions of normalised σ_2 (divided by ω^2R^2) and τ_{12} (divided by $\dot{\omega}R^2$) are shown in Figures 5.16 and 5.17, respectively with, for a constant rotational speed, the most stressed point located at δ = 0.5489. The dangerous stress state due to braking is estimated according to the failure criterion given in Eq. (5.23) and, in this case, the most stressed point is displaced from δ = 0.5489 to lower values of δ, as illustrated by the relationship (Figure 5.18) between the calculated values (satisfying Eq. (5.30)) of the allowable normalised acceleration ($\dot{\bar{\omega}}$) and δ for different values of the normalised angular speed ($\bar{\omega}$). For $\bar{\omega} < 0.95$, the most stressed point shifts to the close of the inner radius of the disk (δ =

0.356) while the limit acceleration ($\dot{\bar{\omega}}_f$) for a given rotational speed corresponds to the absolute minimum values of $\dot{\bar{\omega}}$ and the value of the corresponding angular speed is denoted by $\bar{\omega}_f$, with the values of $\dot{\bar{\omega}}_f$ and $\bar{\omega}_f$ plotted in Figure 5.19. As can be observed, the knee in the $\dot{\bar{\omega}}_f$ vs $\bar{\omega}_f$ curve is caused by the transfer of the most stressed point.

Using the data for the limit combination of $\dot{\bar{\omega}}_f$ and $\bar{\omega}_f$ presented in Figure 5.19, a relationship between other invariants can be determined, such as the current limit values of both the normalised mass energy storage capacity ($\bar{W}_f^M$) and normalised mass power multiplied by R ($R\dot{\bar{W}}_f^M$) which can be calculated by

$$\begin{aligned} \bar{W}_f^M &= W_f^M / W_{max}^M = \bar{\omega}_f^2 \\ R\dot{\bar{W}}_f^M &= R\dot{W}_f^M / W_{max}^M = 2\bar{\omega}_f \dot{\bar{\omega}}_f v_{max} \end{aligned} \tag{5.31}$$

The relationship between $R\dot{\bar{W}}_f^M$ and $\bar{W}_f^M$ is illustrated in Figure 5.20.

Table 5.7: Material properties of filament-wound flywheel disk

Material	ρ (kg/m^3)	$(\sigma_1)_{ult}$ (MPa)	$(\sigma_2)_{ult}$ (MPa)	$(\tau_{12})_{ult}$ (MPa)
IM6/Epoxy	1600	3500	56	98
Aluminium	2770	207	207	-

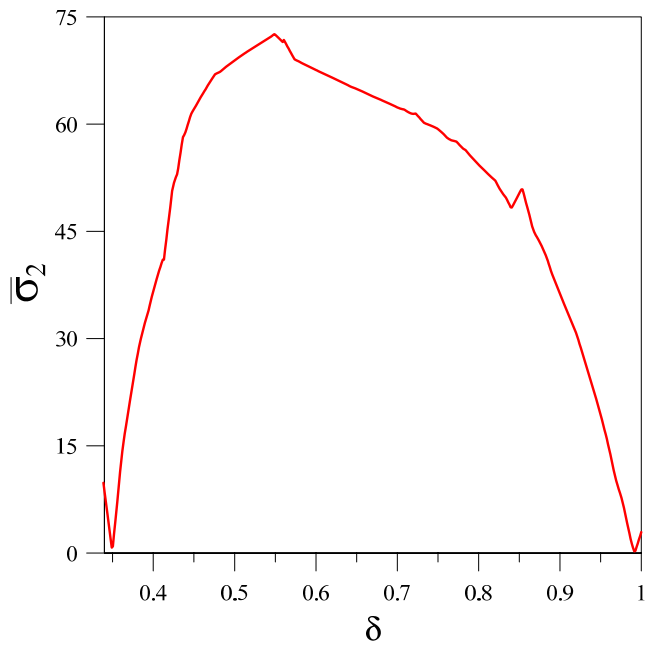

Figure 5.16: Distribution of normalised stress across fibre ($\bar{\sigma}_2 = \sigma_2/\omega^2 R^2$) along radius of disk

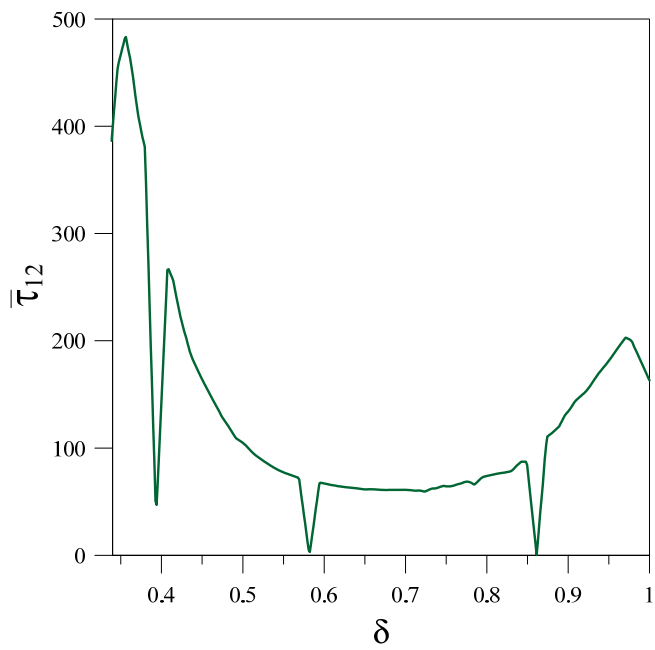

Figure 5.17: Distribution of normalised shear stress ($\bar{\tau}_{12} = \tau_{12}/\dot{\omega} R^2$) along radius of disk

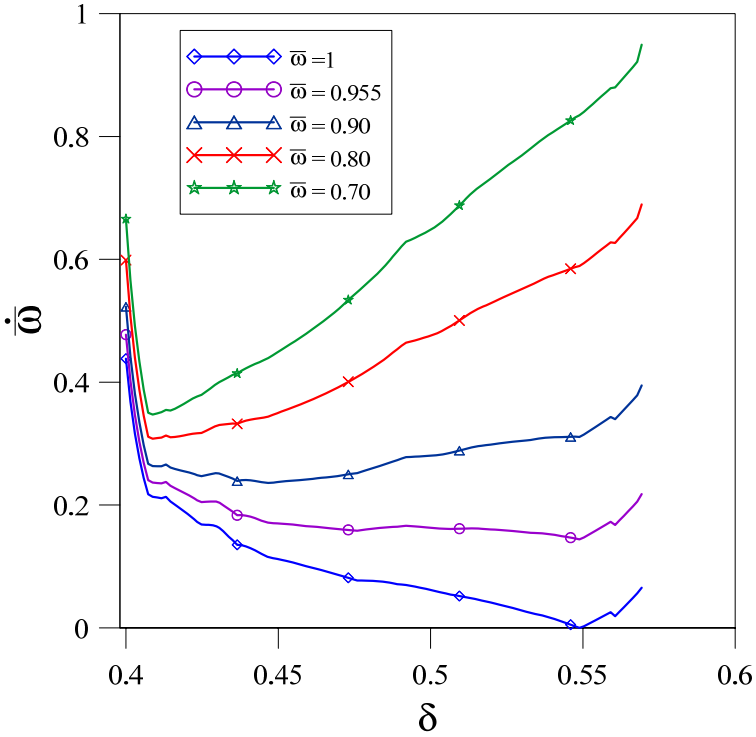

Figure 5.18: Values of maximum allowable $\dot{\overline{\omega}}$ for various values of $\overline{\omega}$

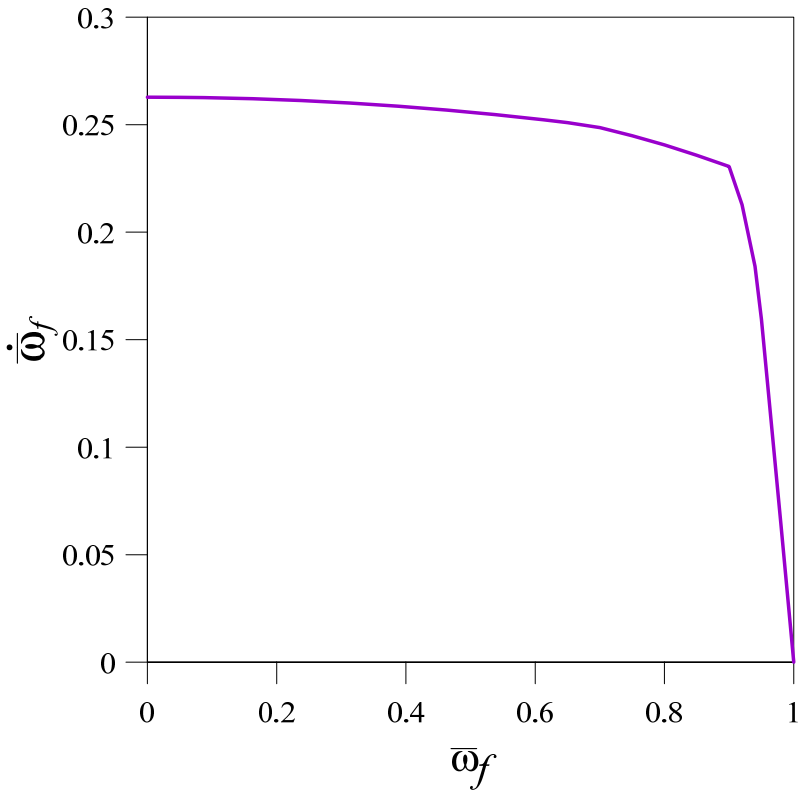

Figure 5.19: Limit normalised acceleration ($\dot{\overline{\omega}}_f$) vs. normalised angular speed ($\overline{\omega}_f$) for whole range of rotational speeds

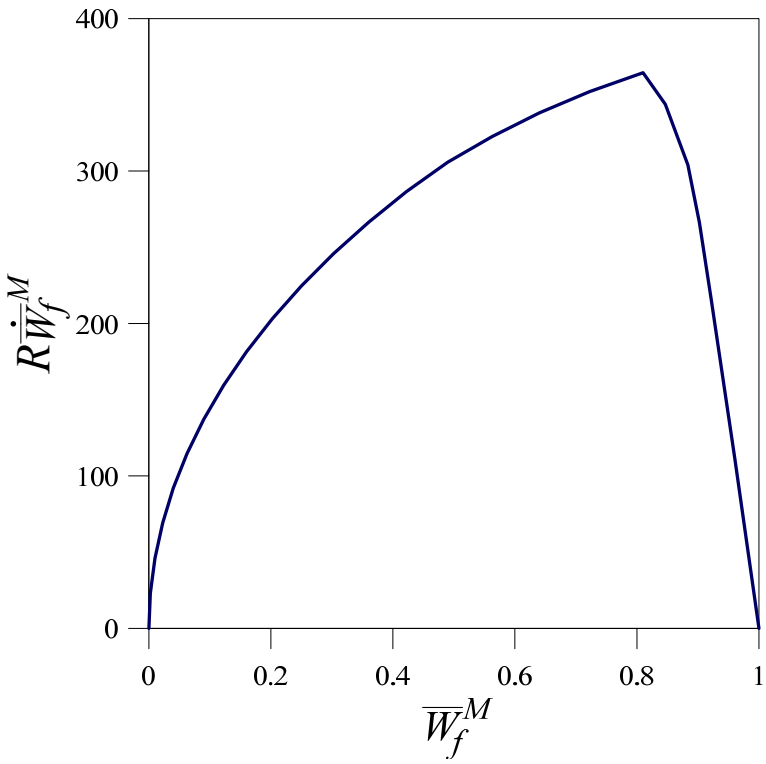

Figure 5.20: Relationship between limit values of invariant characteristics of power ($R\dot{\overline{W}}_f^M$) and current values of energy ($\overline{W}_f^M$)

5.11.1.2 Minimum full braking time

The maximum stressed point does not change its location in the filament-wound flywheel disk due to braking for $0 \leq \overline{\omega}_f \leq 0.95$ (δ = 0.356) but shifts to δ = 0.5489 as soon as $\overline{\omega}_f$ falls in the range of $0.95 \leq \overline{\omega}_f \leq 1$. Taking this into consideration, an analytical solution to the limit regimes of braking (acceleration) ($\overline{\omega}_f = \overline{\omega}_f(\overline{t})$) can be obtained by assuming the coefficients $A(\delta)$ and $B(\delta)$ from Eq. (5.30) to be constants. In this case, the solution to Eq. (5.30) is [58]

$$\overline{\omega}_f(\overline{t}) = \frac{\overline{\omega}_{f_0}\sqrt{AB} + B\tanh\left[\sqrt{AB}(\overline{t} - \overline{t}_0)\right]}{\sqrt{AB} + A\overline{\omega}_{f_0}\tanh\left[\sqrt{AB}(\overline{t} - \overline{t}_0)\right]} \tag{5.32}$$

where $\overline{t}_0$ and $\overline{\omega}_{f_0}$ are the initial conditions.

For $0 \leq \overline{\omega}_f \leq 0.95$, the values of $A(\delta)$ and $B(\delta)$ calculated for δ = 0.356 (the location of the most stressed point) are equal to 0.028076 and 0.262804, respectively. Choosing the

initial conditions as $\bar{t}_0 = 0$ and $\bar{\omega}_f = 0$, the root of Eq. (5.32) for $\bar{\omega}_f = 0.95$ is found to be $\bar{t} = 3.74$. These values are the initial conditions for the second part of the problem, where $0.95 \leq \bar{\omega}_f \leq 1$ and $A(\delta) = B(\delta) = 1.636284$, with the relationship of $\bar{\omega}_f$ vs $\bar{t}$ presented in Figure 5.21. The minimum full time of fastest braking (acceleration) for $0 \leq \bar{\omega}_f \leq 1$ has to comply with the requirement that the failure criterion in Eq. (5.23) is satisfied for all values of $\bar{\omega}_f$ which is achieved by choosing a corresponding maximum possible value of acceleration ($\dot{\bar{\omega}}_f$). If these conditions are satisfied, the minimum full braking time ($\bar{t}_f$) can be determined as the root of Eq. (5.32) for $\bar{\omega}_f = 1$. In the present case, $\bar{t}_f = 9.40$, and it should be noted that the reduced time ($\bar{t}$) is equal to the real time (t) multiplied by ω_{max} for the given R, as shown in Eq. (5.24).

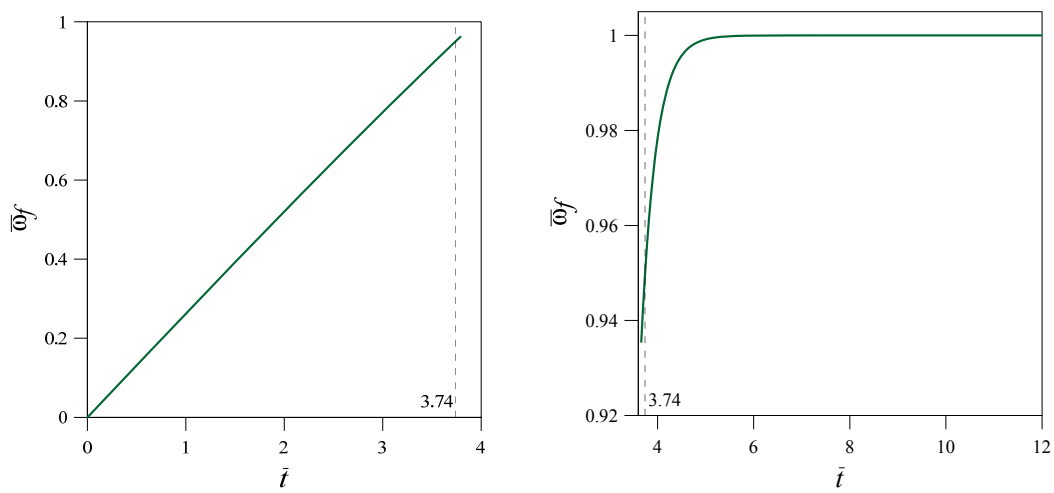

(i) (ii)

Figure 5.21: Normalised angular speeds ($\bar{\omega}_f$) vs. normalised times ($\bar{t}$) during fastest possible braking (acceleration) for (i) first and (ii) second parts of solution to Eq. (5.32)

For $R = 0.3$ m, $\omega_{max} = v_{max}/R = 2928$ rad/s, with the real time of the fastest possible braking equal to 0.00321 s, a very small value due to the low specific mass and small size of the flywheel disk as fast braking regimes are few and far between. Using special impact generators helps to approximate these regimes in a FES system [58] but their dynamic

effects should also be taken into account in a case of fast braking. For a FES system, the curves described in this section should be employed to characterise the flywheel independently of its dimensions and evaluate its capacity to produce the necessary power. Any braking regime can be realised without the flywheel failing if it does not fall outside the region determined by the corresponding limit curve.

5.11.2 Comparative analysis of capabilities of one large flywheel and set of small flywheels

Now, we compare the capabilities of one larger flywheel and a set of similar but smaller flywheels in terms of realising an impulse of given power. For an increase in the size (R_o) of a flywheel k times (i.e., $R_k = kR_o$), its mass increases k^3 times (i.e., $M_k/M_o = k^3$), with the limit of energy storage for the small flywheel $W_{0_{max}} = M_o(W_0^M)_{max}$ and that for the large one $W_{k_{max}} = M_k(W_k^M)_{max}$. Therefore, the ratio of the limit of energy storage is $W_{k_{max}}/W_{0_{max}} = k^3$ and, again,

$$R_o\left(\dot{W}_0^M\right)_{max} = \frac{R_o\dot{W}_{0_{max}}}{M_o}, \quad R_k\left(\dot{W}_k^M\right)_{max} = \frac{R_k\dot{W}_{k_{max}}}{M_k} \tag{5.33}$$

As the left-hand side of each part of Eq. (5.33) is an invariant, $\frac{R_o\dot{W}_{0_{max}}}{M_o} = \frac{R_k\dot{W}_{k_{max}}}{M_k}$. Thus, the ratio of the limit powers is

$$\frac{\dot{W}_{k_{max}}}{\dot{W}_{0_{max}}} = \frac{M_k}{M_o}\frac{R_o}{R_k} = k^2 \tag{5.34}$$

Consequently, the limit power for the large flywheel is k^2 times (but not k^3) higher than that for a small flywheel and, if k is a natural number, the limit power for a set of k^3 flywheels is k^3 times greater than that for one flywheel. Therefore, the ratio of the limit power for a set of k^3 flywheels to that for one large flywheel of an equal mass is

$$\frac{\dot{W}_{set_{max}}}{\dot{W}_{k_{max}}} = \frac{k^3 \dot{W}_{0_{max}}}{k^2 \dot{W}_{0_{max}}} = k \tag{5.35}$$

Therefore, if $k = 2$, the limit power for a set of $k^3 = 8$ flywheels is twice as high as that for one large flywheel of an equal mass.

Let us consider a numerical example for the filament-wound flywheel disk. Eight flywheels, each with an outer radius of 0.3 m and axial thickness of 5.6×10^{-3} m, and one large flywheel with an outer radius of 0.6 m and axial thickness of 1.12×10^{-2} m have equal total masses and maximum energy storage capacities of 7.80×10^{3} kJ (2.167 kWh) but different limit powers, as can be seen in Figure 5.22. It is indicated that, in the limit braking regime, the same amount of total energy can be extracted faster from the set of small flywheels than the one large flywheel of an equivalent mass.

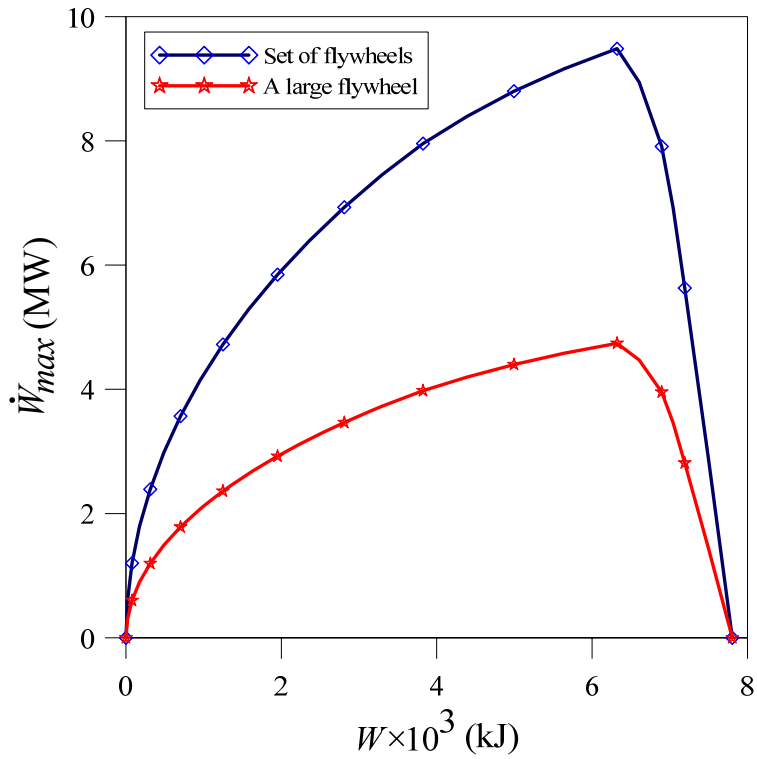

Figure 5.22: Possible limit combinations of current values of power ($\dot{W}_{max}$) and energy (W) for set of eight flywheels and one large flywheel of equal mass

For converting low values of power into an impulse, the set of flywheels and one equivalent-mass flywheel show negligible differences [58]. However, for a short impulse of very high power, there is a considerably significant difference; for instance, a power of 4.74 MW to 9.48 MW can only be achieved using the set of eight flywheels (Figure 5.22). Therefore, although the necessary power can be obtained by either a set of flywheels or one large flywheel for low power values, the energy realised in the impulse using a set of flywheels might be significantly greater than that using one flywheel of an equal mass and the energy stored in a FES system will be properly utilised; for example, the maximum possible operating times for a power impulse of a constant power equal to 4.74 MW are 1.33 s for the one large flywheel and 0.26 s for the set of flywheels. Therefore, using a set of small flywheels will be more effective for a system generating an impact impulse but this type of short-term loading must be accompanied by adequate calculations of the stress states in the flywheel, including dynamic effects.

5.12 Efficiency

The specific energy and volumetric energy density of a FES system are important factors in space applications [89]. Although the former can be related to the ultimate strength of a flywheel rotor's material as, for its speed-limited operating mode, this is not applicable, its shape is determined on the basis of its polar moment of inertia. For a composite flywheel rotor, its maximum stress levels depend not only on its shape but also its fabrication process, loading conditions, failure modes and other factors. Although an isotropic metal rotor provides twice the shape factor that can be obtained from a composite rotor, the theoretical energy density of a composite flywheel rotor is about five times higher than that of a metallic one due to the greater specific strength of a composite material [89].

A flywheel's energy density can be defined as the ratio of its stored kinetic energy to its volume and is also related to the ultimate strength of its rotor's material as

$$\frac{E}{v} = K\sigma_{ult} \tag{5.36}$$

where v is the volume of a flywheel. This equation is also applicable for a composite flywheel rotor if its average density is used. A composite flywheel rotor in which all fibres take the load can have up to a five-fold advantage in terms of volumetric energy density over that of a metallic one [89], with the volumetric energy densities of the filament-wound composite flywheel disk illustrated in Figure 5.13.

The energy density of a FES system can be categorised as [123]

- low: ≤ 10 Wh/kg (36 kJ/kg);
- medium: 10 to 25 Wh/kg (36 to 90 kJ/kg); or
- high: ≥ 25 Wh/kg (90 kJ/kg).

5.13 Chapter summary

In this chapter, various design aspects of a filament-wound flywheel disk with a variable thickness are assessed in terms of its dimensions and energy storage capacity. Firstly, several design parameters are identified based on the requirements of a FES system for several real applications. Then, the process for designing a filament-wound composite flywheel rotor is discussed in terms of its geometry, material selection, angular speed, types of loadings and mounting to a shaft. Based on schemes for maximising its energy storage capacity, performance-controlling parameters are calculated and assessed to determine their effects. It is shown that the maximum allowable rotational speed calculated based on the Tsai-Wu failure criterion varies considerably depending on the mosaic-patterned configuration, with the maximum changes in allowable rotational speeds for 4, 6 or 8 mosaic units 17%, 10% and 5% for 4-, 8- and 14-ply disks, respectively. The energy storage capacity of this disk is compared with that of an example of an optimised flywheel design using a different fibre pattern and a benchmark flywheel design. The results indicate

that that of the filament-wound flywheel disk with fibre trajectories as per a monotropic model is approximately 22% and 8% higher than those of the benchmark and optimised designs, respectively. Also, the fundamental frequencies of the disk with different numbers of plies are checked and it is shown that the natural frequencies calculated based on conventional models of the filament-wound flywheel disk are approximately 1% to 10% higher than those of the mosaic-patterned models. Finally, limit regimes of the braking-acceleration of the filament-wound flywheel disk are determined utilising a failure criterion, with the results obtained showing that a set of small flywheels outperforms one large flywheel with an equivalent mass when short-term impulses of very high power are required. Furthermore, the limit power of a set of flywheels is twice that of one large flywheel of equal mass. The findings obtained from the parametric and comparative analyses of the filament-wound flywheel disk clearly indicate that this type of disk would be an appropriate option for generating impulses of high power for short periods.

Chapter 6

Conclusions

6.1 Research summary

A FE modelling and analysis technique is well suited as a general method owing to its ease of use, capability to evaluate the responses of complex structures under various types of loadings and applicability to a wide range of problems. Although existing FE packages offer great flexibility to include details of the problem considered for analysis, some characteristics still need to be incorporated to determine their effects on the responses of structures. The filament-winding mosaic-patterned configuration is one such manufacturing effect that needs to be taken into account when performing a stress analysis of a filament-wound flywheel disk.

The research reported in this thesis is focused on developing a methodology for modelling a filament-wound flywheel disk which includes manufacturing effects and then performing stress analyses based on the developed models. The strategy of such modelling involves partitioning the whole disk into multiple areas that represent mosaic-patterned units to include the anisotropy of the antisymmetric angle-ply structures of the units and then combining finite elements into the respective alternating groups.

Stress analyses of the filament-wound flywheel disk based on the developed models, including a mosaic-patterned architecture demonstrate the changes in stress levels in different layers and the extent of the influence of ply interlacing. Comparing the results from the proposed and conventional technique clearly indicates that the stress levels in a

thin filament-wound flywheel disk could be underestimated if structural analysis is carried out using the conventional mechanics of laminated structures.

The results calculated for the mosaic-patterned models of the filament-wound disk with varying fibre trajectories signify not only the necessity of including manufacturing effects but also ensuring accurate approximations of predefined varying fibre trajectories for the modelling and analysis of variable-stiffness composite laminates. If stiffness variation due to changes in fibre paths is not properly reflected in FE models, the entire analysis process might produce erroneous results. Therefore, an approach for the FE modelling and analysis of such variable-stiffness laminates in which continuously varying fibre angles are taken into account is proposed.

In the design of the filament-wound composite flywheel disk, the primary goal is to maximise the energy output with minimum possible mass under given operational conditions. Based on the requirements of different applications of flywheels, various design aspects of this filament-wound flywheel disk are identified and then assessed in terms of dimensions and energy storage capacity. Parametric and comparative analyses are carried out considering different performance-controlling factors.

The results obtained using the modelling and analysis strategy developed are promising and demonstrate the potential of the proposed approaches for improving the analysis procedure and obtaining more accurate assessments of the responses of filament-wound structures under various loading conditions.

6.2 Conclusions

The findings reported in the thesis can be summarised as follows.

1. The methodology developed for modelling a filament-wound flywheel disk, including a mosaic-patterned configuration and actual thickness variation, proves to be useful for modelling and analysing filament-wound structures as

it incorporates the special manufacturing effects of the filament-winding process. It would act as a framework for designers to model and analyse filament-wound structures and, thereby, exploit the directional properties of composite materials in various advanced engineering applications.

2. Variations in the calculated stresses in different layers of the spinning composite disk obtained from stress analyses of the mosaic-patterned models with different levels of thickness differ substantially from those determined by a conventional analysis of laminated shells. The levels of variation in the stress values predicted by both the conventional and mosaic-patterned models fluctuate substantially among different mosaic units located at various positions over the filament-wound flywheel disk; for instance, the maximum stress value along the fibres at the top of layer 3 in the 4-ply disk is determined to be approximately 50% higher for the 8-unit mosaic-patterned model than that obtained from the conventional model. Similarly, the maximum stress levels along the fibres are, respectively, 27% and 17% higher when calculated at the tops of layer 7 of the 8-ply and layer 13 of the 14-ply disk models with 8 mosaic units around their circumferences.

3. The mechanical behaviour of the disk is sensitive to the mosaic-patterned configuration and its stress distributions are affected by the number of mosaic units around its circumference and along its radius as well as its thickness. With increments in thickness, the effect of the mosaic pattern on the stress state gradually diminishes; for example, the circumferential distributions of both the hoop stress and stress across the fibres maintain 4% to 15% differences in values compared with those obtained from the conventional model. However, it is shown that the maximum stress levels in the filament-

wound disks with low levels of thickness could be underestimated by a conventional FEA technique.

4. The findings from stress analyses of mosaic-patterned models of the disk also demonstrate the necessity of incorporating a mosaic-patterned configuration, as well as the actual thickness variation induced in a filament-wound spinning disk, in FE modelling and analysis as actual stress distributions could remain undetermined if these characteristics are disregarded.
5. It should be noted that, apart from the different characteristics of stress distributions due to various mosaic-patterned configurations, the stress minima and maxima are found at different locations on the disk than those obtained from the conventional technique. This indicates that results obtained from conventional modelling techniques may be erroneous if the actual manufacturing effects are not incorporated in models of filament-wound composite structures.
6. Comparisons of the performances of the filament-wound flywheel disk, being an optimal composite structure, a benchmark design and an optimised design taken from published work show the improved energy density of the disk with spatially oriented fibre trajectories.
7. Based on the free vibration analysis, it is demonstrated that the natural frequencies obtained from the conventional modelling approach could be very different from those predicted using actual mosaic-patterned models.
8. A comparative analysis clearly demonstrates that the capability of a set of small identical filament-wound flywheel disks to realise a short-term impulse of very high power is more efficient than that of one large flywheel with an equivalent mass.

9. The factors responsible for stiffness variation should be carefully assessed and included for the modelling and analysis of variable-stiffness laminates. As the steering of fibres while fabricating laminates offers different benefits, a FEA needs to be performed accurately to obtain reasonable results that would help in utilising such a concept in advanced engineering applications.

6.3 Recommendations for future work

It follows from the results presented that, for practical applications of not only filament-wound disks but also other complicated composite structures with intricate designs and manufacturing characteristics, using adequate modelling and analysis procedures is as important as improving the performance and efficiency of these structures for increasing number of applications in multi-disciplinary fields. Therefore, it is logical to extend the present research work to other areas to obtain benefits from the developed methodology.

The filament-wound flywheel disk could be analysed considering other types of loadings, such as temperature, residual stress generated from curing and angular acceleration, which would provide detailed information about its performance. It would be advantageous to perform a failure analysis to evaluate the initiation of delamination during its operation taking into account the mosaic pattern of a composite structure.

A finite element could be formulated to incorporate varying fibre trajectories and, thereby, more accurately determine stiffness variation in composite structures. This would assist in carrying out more efficient modelling and analysis of variable-stiffness laminates which would enable us to comprehend their responses under different loading conditions. Thus an accurate control of the steering of fibres along load paths would be possible.

To identify the changes in fibre paths during the phase of transforming a shell of revolution to a flat disk when fabricating a filament-wound flywheel disk could be simulated with the help of an advanced FE technique. This would help to control the

process parameters in order to obtain the desired stiffness variation through maintaining appropriate fibre paths in the final product.

To assess a filament-wound flywheel disk's mechanical responses under rotational and other loadings, various types of fibre paths rather than one based on a monotropic material model could be investigated which would provide the option to further enhance and more accurately control the performance of the flywheel.

References

[1] M. A. Arslan, "Flywheel geometry design for improved energy storage using finite element analysis," *Materials and Design,* vol. 29, pp. 514-518, 2008.

[2] V. V. Vasiliev and E. V. Morozov, *Advanced mechanics of composite materials*,2nd ed.: Elsevier, 2007.

[3] S. C. Thielman, "Design and optimisation of a material property distribution in a composite flywheel," Doctor of Philosophy in Mechanical Engineering, University of Washington, 1997.

[4] A. C. Kyser, "The uniform-stress spinning filamentary disk," Contractor Report, NASA CR-106, 1964.

[5] E. V. Morozov, M. Hoarau, and K. E. Morozov, "Filament-winding patterns and stress analysis of thin-walled composite cylinders," in *Proceedings of Fiber Society 2003 Symposium*, Loughborough University, Loughborough, UK, 2003.

[6] E. V. Morozov, "The effect of filament-winding mosaic patterns on the strength of thin-walled composite shells," *Composite Structures* vol. 76, pp. 123-129, 2006.

[7] M. W. Hyer and H. H. Lee, "The use of curvilinear fibre format to improve buckling resistance of composite plates with central circular holes," *Composite Structures,* vol. 18, pp. 239-261, 1991.

[8] M. W. Hyer and R. F. Charette, "Use of curvilinear fibre format in composite structure design," *AIAA Journal,* vol. 29, pp. 1011-1015, 1991.

[9] B. F. Tatting and Z. Gurdal, "Automated Finite Element Analysis of Elastically-Tailored Plates," Contractor Report, NASA/CR-2003-212679, 2003.

[10] C. K. Wu and Z. Gurdal, "Variable stiffness panel structural analyses with material nonlinearity and correlation with tests," in *Proceedings of the 47th AIAA/ASME/ASCE/AHS/ASC Structures, Structural Dynamics and Materials Conference*, Newport, Rhode Island 2006, pp. 1-19.

[11] K. C. Wu, Z. Gurdal, and J. J. H. Starnes, "Structural response of compression-loaded, tow-placed, variable stiffness composite panels," in *Proceedings of the 43rd AIAA/ASME/ASCE/AHS/ASC Structures, Structural Dynamics and Materials Conference*, Denver, Colorado, 2002, pp. 1-22.

[12] L. Parnas, S. Oral, and U. Ceyhan, "Optimum design of composite structures with curved fiber courses," *Composites Science and Technology* vol. 63, pp. 1071–1082, 2003.

[13] P. T. Langley, "Finite element modelling of tow-placed variable-stiffness composite laminates," Master of Science, Engineering Mechanics, Virginia Polytechnic Institute and State University, 1999.

[14] A. W. Blom, C. S. Lopes, P. J. Kromwijk, Z. Gurdal, and P. P. Camanho, "A theoretical model to study the influence of tow-drop areas on the stiffness and strength of variable-stiffness laminates," *Journal of Composite Materials,* vol. 43, pp. 403-425, 2009.

[15] C. S. Lopes, "Damage and failure of non-conventional composite laminates," Doctor of Philosophy, Mechanics, Aerospace Structures & Materials, Delft University of Technology, 2009.

[16] C. Lopes, P. P. Camanho, and Z. Gurdal, "Tailoring of strength of steered-fibre composite panels with cutouts," in *Proceedings of the 51st AIAA/ASME/ASCE/AHS/ASC Structures, Structural Dynamics and Materials Conference*, Orlando, Florida, 2010, pp. 1-8.

[17] Z. Gurdal and R. Olmedo, "In-plane response of laminates with spatially varying fiber orientations: variable stiffness concept," *AIAA Journal,* vol. 31, pp. 751-758, 1993.

[18] A. A. Ahmad, "Design tailoring of panels for pressure pillowing using tow-placed steered fibres," Doctor of Philosophy, Aerospace Engineering, Delft University of Technology (TU Delft), 2008.

[19] A. A. Ahmad, M. M. Abdalla, and Z. Gurdal, "Design tailoring for pressure pillowing using tow-placed steered fibres," *Journal of Aircraft,* vol. 45, pp. 630-640, 2008.

[20] A. A. ahmad, M. M. Abdalla, and Z. Gurdal, "Optimal design of tow-placed fuselage panels for maximum strength with buckling considerations," *Journal of Aircraft,* vol. 47, pp. 775-782, 2010.

[21] H. Akhavan, P. Ribeiro, and M. F. S. F. D. Moura, "Large deflection and stresses in variable stiffness composite laminates with curvilinear fibres," *International Journal of Mechanical Science,* vol. 73, pp. 14-26, 2013.

[22] C. S. Sousa, P. P. Camanho, and A. Suleman, "Analysis of multistable variable stiffness composite plates," *Composite Structures,* vol. 98, pp. 34-46, 2013.

[23] J. Díaz, C. Fagiano, M. M. Abdalla, Z. Gurdal, and S. Hernández, "A study of interlaminar stresses in variable stiffness plates," *Composite Structures,* vol. 94, pp. 1192-1199, 2011.

[24] A. Khani, S. T. IJsselmuiden, M. M. Abdalla, and Z. Gurdal, "Design of variable stiffness panels for maximum strength using lamination parameters," *Composites Part B: Engineering,* vol. 42, pp. 546-552, 2011.

[25] C. S. Lopes, Z. Gurdal, and P. P. Camanho, "Variable-stiffness composite panels: buckling and first-ply failure improvements over straight-fibre laminates," *Computers and Structures,* vol. 86, pp. 897-907, 2008.

[26] Z. Gurdal, B. F. Tatting, and C. K. Wu, "Variable stiffness composite panels: effects of stiffness variation on the in-plane and buckling response," *Composites Part A: Applied Science and Manufacturing,* vol. 39, pp. 911-922, 2008.

[27] E. Senocak and H. Tanriover, "Analysis of composite plates with variable stiffness using Galerkin Method," *Aeronautical Journal,* vol. 111, pp. 247-255, 2007.

[28] C. Waldhart, "Analysis of tow placed, variable stiffness laminates," Master of Science in Engineering Mechanics, M.S Thesis Virginia Polytechnic Institute and State University, Virginia, 1996.

[29] B. F. Tatting and Z. Gurdal, "Design and manufacture of elastically tailored tow placed plates," Contractor Report, NASA/CR-2002-211919, 2002.

[30] C. K. Wu and Z. Gurdal, "Thermal testing of tow-placed, variable stiffness panels," in *Proceedings of the 42nd AIAA/ASME/ASCE/AHS/ASC Structures, Structural Dynamics and Materials Conference & Exhibit*, Seattle, Washington, 2001, pp. 1-21.

[31] A. F. Marting and A. W. Leissa, "Application of the Ritz method to plane elasticity problems for composite sheets with variable fibre spacing," *International Journal of Numerical Methods in Engineering,* vol. 28, pp. 1813-1825, 1989.

[32] R. Olmedo and Z. Gurdal, "Buckling response of laminates with spatially varying fibre orientations," presented at the 34th AIAA/ASME/ASCE/AHS/ASC Structures, Structural Dynamics and Materials Conference, La Jolla, CA, 1993.

[33] Z. Gurdal and R. Olmedo, "Composite laminates with spatially varying fiber orientations:"variable stiffness panel concept"," in *Proceedings of the 33rd AIAA/ASME/ASCE/AHS/ASC Structures, Structural Dynamics and Materials Conference*, Dallas, TX, 1992, pp. 798-808.

[34] S. Setoodeh, M. M. Abdalla, Z. Gurdal, and B. Tatting, "Design of variable-stiffness composite laminates for maximum in-plane stiffness using lamination parameters " in *Proceedings of the 46th AIAA/ASME/ASCE/AHS/ASC Structures, Structural Dynamics and Materials Conference* Austin, Texas, 2005, pp. 1-9.

[35] A. Muc and A. Ulatowska, "Design of plates with curved fibre format," *Composite Structures,* vol. 92, pp. 1728-1733, Jun 2010.

[36] S. T. IJsselmuiden, M. M. Abdalla, S. Setoodeh, and Z. Gurdal, "Design of variable stiffness panels for maximum buckling load using lamination parameters," presented at the 49th AIAA/ASME/ASCE/AHS/ASC Structures, Structural Dynamics, and Materials Conference Schaumburg, IL, 2008

[37] S. Thielman and B. C. Fabien, "An optimal control approach to the design of stacked-ply composite flywheels," *Engineering Computations,* vol. 17, pp. 541-555, 2000.

[38] Y. V. Bokov, V. V. Vasil'ev, and G. G. Portnov, "Optimum shapes and paths of reinforcement in rotating composite shells," *Mechanics of Composite Materials,* vol. 17, pp. 572-579, 1982.

[39] L. N. Seleznev and G. G. Portnov, "Chord winding of composite-tape disks," *Mechanics of Composite Materials,* vol. 13, pp. 832-835, 1977.

[40] G. J. Nie, Z. Zhong, and R. C. Batra, "Material tailoring for orthotropic elastic rotating disks," *Composites Science and Technology,* vol. 71, pp. 406-414, 2011.

[41] A. Abdul-Aziz, G. Baaklini, and J. Trudell, "Structural analysis of composite flywheels: an integrated NDE and FEM approach," Technical memorandum, NASA/TM-2001-210461, 2001.

[42] M. Krack, M. Secanell, and P. Mertiny, "Cost optimisation of hybrid composite flywheel rotors for energy storage," *Structural and Multidisciplinary Optimization,* vol. 41, pp. 779-795, 2010.

[43] A. C. Arvin and C. E. Bakis, "Optimal design of press-fitted filament wound composite flywheel rotors," *Composite Structures,* vol. 72, pp. 47-57, 2006.

[44] S. M. Arnold, A. F. Saleeb, and N. R. Al-Zoubi, "Deformation and life analysis of composite flywheel disk systems," *Composites: Part B,* vol. 33, pp. 433-459, 2002.

[45] J. L. Pérez-Aparicio and L. Ripoll, "Exact, integrated and complete solutions for composite flywheels," *Composite Structures,* vol. 93, pp. 1404-1415, 2011.

[46] F. Abdel-Hady, G. Baaklini, Y. Gowayed, R. Creighton, D. Lee, and J. Trudell, "Manufacture and NDE of multi-direction composite flywheel rims," *Journal of Reinforced Plastics and Composites,* vol. 24, pp. 413-421, 2005.

[47] R. J. Hayes, J. P. Kajs, R. C. Thompson, and J. H. Beno, "Design and testing of a flywheel battery for a transit bus," *SAE Transactions - Part 2,* vol. 108, pp. 2199-2209, 1998.

[48] S. K. Ha, S. J. Kim, S. U. Nasir, and S. C. Han, "Design optimisation and fabrication of a hybrid composite flywheel rotor," *Composite Structures,* vol. 94, pp. 3290-3299, 2012.

[49] J. E. Shigley and C. Mischke, *Mechanical Engineering Design*,5th ed.: McGraw-Hill, 1989.

[50] B. C. Fabien, "The influence of failure criteria on the design optimisation of stacked-ply composite flywheels," *Structural and Multidisciplinary Optimization,* vol. 33, pp. 507-517, 2007.

[51] P. J. J. v. Rensburg, "Energy storage in composite flywheel rotors," Master of Science in Engineering, Department of Mechanical and Mechatronic Engineering, Stellenbosch University, 2011.

[52] N. N. Alexandrova and P. M. M. V. Real, "Preliminary design of a composite material flywheel," *Materials Science Forum,* vol. 623, pp. 21-35, 2009.

[53] S. K. Ha, H.-M. Jeong, and Y.-S. Cho, "Optimum design of thick-walled composite rings for an energy storage system," *Journal of Composite Materials,* vol. 32, pp. 851-873, 1998.

[54] R. Zheng-yi, L. Jing-na, L. Qing-fen, and L. Ke-fei, "Finite element analysis of composite flywheel with two-layer pre-stressed rotor structure," *Key Engineering Materials,* vol. 488-489, pp. 134-137, 2012.

[55] J. T. Tzeng, R. Emerson, and P. Moy, "Composite flywheels for energy storage," *Composites Science and Technology,* vol. 66, pp. 2520-2527, 2006.

[56] C. P. R. Hoppel, J. F. Newill, J. T. Tzeng, L. W. Burton, J. M. Bender, B. P. Burns, and W. H. Drysdale, "Ordnance applications of polymer-matrix composite materials," presented at the 30th International SAMPE Technical Conference, Paris, 1998.

[57] S. R. Holm, "Modelling and optimisation of a permanent-magnet machine in a flywheel," Doctor of Philosophy, Information Technology and Systems, Technical University of Delft, The Netherlands, 2003.

[58] G. Portnov, I. Cruz, R. P. Fiffe, and F. Arias, "Limit regimes of braking of disc-type composite flywheels made by filament winding," *Mechanics of Composite Materials,* vol. 40, pp. 37-44, 2004.

[59] J. D. Herbst, S. M. Manifold, B. T. Murphy, J. H. Price, R. C. Thompson, W. A. Walls, A. Alexander, and K. Twigg, "Design, fabrication, and testing of 10 MJ composite flywheel energy storage rotors," in *Proceedings of the SAE Conference* 1998, pp. 235-244.

[60] J. C. Thesken, C. L. Bowman, S. M. Arnold, and R. C. Thompson, "Time-temperature dependent response of filament wound composites for flywheel rotors," Technical memorandum, NASA TM-2004-212102, 2004.

[61] N. D. Ebrahimi, "Optimum design of flywheels," *Computers and Structures,* vol. 29, pp. 681-686, 1988.

[62] S. Adali, V. E. Verijenko, and B. Chevallereau, "Design optimisation of composite rotating disks under multiple loads," in *Proceedings of the 7th AIAA/USAF/NASA/ISSMO Symposium on Multidisciplinary Analysis and Optimization*, St Louis, Missouri, USA, 1998, pp. 890-896.

[63] S. Wen and S. Jiang, "Optimum design of hybrid composite multi-ring flywheel rotor based on displacement method," *Composites Science and Technology,* vol. 72, pp. 982-988, 2012.

[64] D. W. Jensen and S. P. Pai, "Theoretical sensitivity of composite cylinders in compression to filament-winding pattern," in *Proceedings of the 9th International Conference on Composite Materials (ICCM-9)*, Madrid, Spain, 1993, pp. 447-454.

[65] H. H. Mian and H. Rahman, "Influence of mosaic patterns on the structural integrity of filament wound composite pressure vessels," *International Journal of Structural Integrity,* vol. 2, pp. 345-356, 2011.

[66] A. C. Kyser, "Uniform-stress spinning filamentary disk," *AIAA Journal,* vol. 3, pp. 1313-1316, 1965.

[67] Waterloo Maple Inc., "Maple 13," 13 ed: Maplesoft, 2009.

[68] J.-M. Berthelot, *Composite materials - mechanical behavior and structural analysis*: Springer, 1999.

[69] "ANSYS academic research," version 12.0.1 ed, 2009.

[70] R. G. Budynas, *Advanced strength and applied stress analysis*: McGraw-Hill Book Company, 1977.

[71] S. Timoshenko, *Strength of materials : part II - advanced theory and problems*,3rd ed.: D. Van Nostrand Company, 1958.

[72] R. Li, D. Kelly, A. Crosky, H. Schoen, and L. Smollich, "Improving the efficiency of fibre steered composite joints using load path trajectories," *Journal of Composite Materials* vol. 40, pp. 1645-1658, 2006.

[73] R. Li, D. Kelly, and A. Crosky, "Strength improvement by fibre steering around a pin loaded hole " *Composite Structures* vol. 57, pp. 377-383, 2002.

[74] A. Muc and A. Ulatowska, "Local fibre reinforcement of holes in composite multilayered plates," *Composite structures,* vol. DOI: 10.1016/j.compstruct.2011.11.017, 2011.

[75] Z. Gurdal and B. F. Tatting, "Tow placement technology and fabrication issues for laminated composite structures," in *Proceedings of the 46th AIAA/ASME/ASCE/AHS/ASC Structures, Structural Dynamics & Materials Conference*, Austin, Texas, 2005, pp. 1-18.

[76] M. W. Hyer and R. F. Charette, "The use of curvilinear fibre format in composite structure design," in *Proceedings of the 30th AIAA/ASME/ASCE/AHS/ASC Structures, Structural Dynamics and Materials Conference*, Mobile, AL, USA, 1989, pp. 2137-2145.

[77] S. Setoodeh, M. M. Abdalla, and Z. Gurdal, "Design of variable-stiffness laminates using lamination parameters," *Composites: Part B,* vol. 37, pp. 301-309, 27 december 2005 2006.

[78] A. W. Blom, B. F. Tatting, J. M. A. M. Hol, and Z. Gurdal, "Fiber path definitions for elastically tailored conical shells," *Composites Part B: Engineering* vol. 40, pp. 77-84, 2009.

[79] A. W. Blom, P. B. Stickler, and Z. Gurdal, "Optimisation of a composite cylinder under bending by tailoring stiffness properties in circumferential direction," *Composites Part B: Engineering,* vol. 41, pp. 157-165, 2010.

[80] A. W. Blom, "Structural performance of fibre placed, variable stiffness composite conical and cylindrical shells," Doctor of Philosophy, Aerospace Structures, Delft University of Technology, 2010.

[81] Handbook, *Military handbook: composite materials handbook, volume 3 - polymer matrix composites materials usage, design, and analysis* 3 ed. vol. 3: U.S. Department of Defense, 2002.

[82] A. W. Blom, C. S. Lopes, P. J. Kromwijk, Z. Gurdal, and P. P. Camanho, "A theoretical model to study the influence of tow-drop areas on the stiffness and strength of variable-stiffness laminates," *Journal of Composite Materials,* vol. 00, pp. 1-23, 2008.

[83] J. Argyris and L. Tenek, "A natural triangular layered element for bending analysis of isotropic, sandwich, laminated composite and hyhrid plates," *Computer Methods in Applied Mechanics and Engineering* vol. 109, pp. 197-218, 1993.

[84] J. N. Reddy, "Exact solutions of moderately thick laminated shells," *Journal of Engineering Mechanics,* vol. 110, pp. 794-809, 1984.

[85] H. Liu and J. Jiang, "Flywheel energy storage - an upswing technology for energy sustainability," *Energy and Buildings,* vol. 39, pp. 599-604, 2007.

[86] R. C. Wagner, D. R. Boyle, and K. Decker, "Commercialisation of flywheel energy storage technology on the international space station," in *Proceedings of the 37th Intersociety Energy Conversion Engineering Conference (IECEC)*, Washington, DC, United States, 2002, pp. 146-150.

[87] C. D. Hall, "High speed flywheels for integrated energy storage and attitude control " in *Proceedings of the 1997 American Control Conference* Albuquerque, New Mexico, USA, 1997, pp. 1894-1898.

[88] J. G. Bitterly, "Flywheel technology: past, present, and 21st century projections," *Aerospace and Electronic Systems Magazine, IEEE*, vol.13, no.8, pp. 13-16, August 1998.

[89] V. Babuska, S. M. Beatty, B. J. deBlonk, and J. L. Fausz, "A review of technology developments in flywheel attitude control and energy transmission systems," in *Proceedings of the 2004 IEEE Aerospace Conference*, Big Sky, MT, USA, 2004, pp. 2784-2800.

[90] R. Hebner, J. Beno, and A. Walls, "Flywheel batteries come around again," *IEEE Spectrum*, vol.39, no.4, pp. 46-51, April 2002.

[91] S. Ashley, "Flywheels put a new spin on electric vehicles," *Mechanical Engineering (ASME),* vol. 115, pp. 44-51, 1993.

[92] M. Olszewski, D. B. Eisenhaure, N. Beachley, and J. A. Kirk, "On the Fly or Under Pressure," *Mechanical Engineering (ASME),* vol. 110, pp. 50-58, 1988.

[93] C. M. Jefferson and M. Ackerman, "A flywheel variator energy storage system," *Energy Conversion and Management,* vol. 37, pp. 1481-1491, 1996.

[94] D. A. Christopher and R. Beach, "Flywheel technology development program for aerospace applications," *Aerospace and Electronic Systems Magazine, IEEE*, vol.13, no.6, pp. 9-14, June 1998.

[95] "Composite flywheels aid space station," *Reinforced Plastics*, vol.43, no.2, p. 6, February 1999.

[96] C. C. Snare, "*From child's toy to ISS: flywheels hold the power*," 2003, Available: http://spaceresearch.nasa.gov/general_info/flywheel.html

[97] R. Varatharajoo, "A combined energy and attitude control system for small satellites," *Acta Astronautica,* vol. 54, pp. 701-712, 2004.

[98] W. Robinson, J. Hanks, G. Gisler, L. Spina, and D. S. Ginter, "Spacecraft energy storage systems," in *Proceedings of the IEEE 1997 National Aerospace and Electronics Conference (NAECON)*, Dayton, OH, 1997, pp. 609-616.

[99] Z. Kohari and I. Vajda, "Losses of flywheel energy storages and joint operation with solar cells," *Journal of Materials Processing Technology,* vol. 161, pp. 62-65, 2005.

[100] Y. Suzuki, A. Koyanagi, M. Kobayashi, and R. Shimada, "Novel applications of the flywheel energy storage system," *Energy* vol. 30, pp. 2128-2143, 2005.

[101] D. R. Brown and W. D. Chvala, "Flywheel energy storage: an alternative to batteries for UPS systems," *Energy Engineering,* vol. 102, pp. 7-26, 2005.

[102] R. M. Dell and D. A. J. Rand, "Energy storage - a key technology for global energy sustainability," *Journal of Power Sources,* vol. 100, pp. 2-17, 2001.

[103] R. G. Lawrence, K. L. Craven, and G. D. Nichols, "Flywheel UPS," *Industry Applications Magazine, IEEE*, vol.9, no.3, pp. 44-50, May-June 2003.

[104] J. A. Carta, J. Gonzalez, and V. Subiela, "Operational analysis of an innovative wind powered reverse osmosis system installed in the Canary Islands," *Solar Energy,* vol. 75, pp. 153-168, 2003.

[105] T. Boutot, L. Chang, and D. M. Luke, "A low speed flywheel system for wind energy conversion," presented at the Canadian Conference on Electrical and Computer Engineering, Winipeg, Manitoba, 2002.

[106] D. W. Swett and J. G. Blanche, "Flywheel charging module for energy storage used in Electromagnetic Aircraft Launch System," *IEEE Transactions on Magnetics,* vol. 41, pp. 525-528, 2005.

[107] B. Kaftanoglu, R. Soylr, and S. Oral, "Mechanical energy storage using flywheels and design optimisation," *Energy storage systems,* pp. 619-648, 1989.

[108] M. Krack, M. Secanell, and P. Mertiny, "Cost optimisation of a hybrid composite flywheel rotor with a split-type hub using combined analytical/numerical models," *Structural and Multidisciplinary Optimization,* vol. 44, pp. 57-73, 2011.

[109] M. Krack, M. Secanell, and P. Mertiny, "Rotor design for high-speed flywheel energy storage systems," in *Energy Storage in the Emerging Era of Smart Grids*, R. Carbone, Ed., 2011, pp. 41-68.

[110] P. I.-P. Tsao, "An integrated flywheel energy storage system with a homopolar inductor motor/generator and high-frequency drive," Doctor of Philosophy, Engineering-Electrical Engineering and Computer Sciences, University of California, Berkeley, 2003.

[111] G. Portnov, I. Cruz, F. Arias, and R. P. Fiffe, "Flywheels for low-speed kinetic energy storage systems," CIEMAT, Madrid, Spain, Technical Report, Ref. No. 38115067, 2003.

[112] M. A. Conteh and E. C. Nsofor, "Flywheel energy recovery and storage system from aircraft brakes," presented at the 11th International Energy Conversion Engineering Conference, San Jose, CA, 2013.

[113] J. A. Kirk, "Flywheel energy storage - I: basic concepts," *International Journal of Mechanical Science,* vol. 19, pp. 223-231, 1977.

[114] B. H. Kenny, P. E. Kascak, R. Jansen, and T. Dever, "A flywheel energy storage system demonstration for space applications," in *Proceedings of the IEEE International Electric Machines and Drives Conference (IEMDC'03)* 2003, pp. 1314-1320.

[115] Y. Han, Z. Ren, and Y. Tong, "General design method of flywheel rotor for energy storage system," *Energy Procedia,* vol. 16, pp. 359-364, 2012.

[116] J. Koyanagi, "Durability of filament-wound composite flywheel rotors," *Mechanics Of Time-Dependent Materials,* vol. 16, pp. 71-83, 2012.

[117] A. B. Mitkevich, A. A. Kul'kov, and A. A. Berlin, "Transformation technologies in forming composite structures," *Mechanics of Composite Materials,* vol. 47, pp. 37-46, 2011.

[118] V. I. Smyslov, B. G. Mayorov, N. G. Moroz, and M. S. Rezaev, "Investigation of the possibility of creating structures from composite fibrous materials by the method of transformation of forms," Scientific and Technical Report, 1984.

[119] J. K. H. Ratner, J. B. Chang, and D. A. Christopher, "Composite flywheel rotor technology - a review," in *Composite Materials: Testing and Design*. vol. 14, C. E. Bakis, Ed.: ASTM International, 2003.

[120] B. Bolund, H. Bernhoff, and M. Leijon, "Flywheel energy and power storage systems," *Renewable and Sustainable Energy Reviews,* vol. 11, pp. 235-258, 2007.

[121] G. Genta, *Kinetic energy storage: theory and practice of advanced flywheel systems*: Butterworths, London,England, 1985.

[122] G. C. Chang and F. Hirschfeld, "For the latest in energy storage, try the flywheel," *Mechanical Engineering (ASME),* vol. 100, pp. 38-45, 1978.

[123] N. Meeker and B. Walker, "Flywheel technology for energy storage," Technical Report, 2010.

[124] K. Demachi, K. Miya, R. Takahata, H. Kameno, and H. Higasa, "Numerical evaluation of rotation speed degradation of superconducting magnetic bearing caused by the electromagnetic phenomena," *Physica C: Superconductivity,* vol. 378-381, pp. 858-863, 2002.

[125] K. Takahashi, S. Kitade, and H. Morita, "Development of high speed composite flywheel rotors for energy storage systems," *Advanced Composite Materials,* vol. 11, pp. 40-49, 2002.

[126] G. Genta, "On the design of thick rim composite material filament- wound flywheels," *Composites,* vol. 15, pp. 49-55, 1984.

[127] T. L. Wilson, "A high-temperature superconductor energy-momentum control system for small satellites," *IEEE Transactions on Applied Superconductivity,* vol. 13, pp. 2287-2290, 2003.

[128] E. J. Lee, "A micro HTS renewable energy/attitude control system for micro/nano satellites," *IEEE Transactions on Applied Superconductivity,* vol. 13, pp. 2263-2266, 2003.

[129] K. B. Ma, Y. Zhang, Y. Postrekhin, and W.-K. Chu, "HTS bearings for space applications: reaction wheel with low power consumption for minisatellites," *IEEE Transactions on Applied Superconductivity,* vol. 13, pp. 2275-2278, 2003.

[130] J. Tang, J. Fang, and W. Tong, "Superconducting magnetic bearings and active magnetic bearings in attitude control and energy storage flywheel for spacecraft," *IEEE Transactions on Applied Superconductivity,* vol. 22, p. 5702109, 2012.

[131] A. K. Kaw, *Mechanics of composite materials*,2nd ed.: CRC Press - Taylor and Francis Group, 2006.

[132] S. Timoshenko and J. N. Goodier, *Theory of elasticity*: McGraw-Hill, New York, 1970.

[133] C. W. d. Silva, *Vibration and shock handbook*: CRC Press, 2010.

[134] G. G. Portnov and I. N. Barinov, "Experimental study of the natural vibration frequencies and decrements of composite rim flywheels," *Mechanics of Composite Materials,* vol. 28, pp. 445-454, 1992.

[135] H. Akhavan and P. Ribeiro, "Natural modes of vibration of variable stiffness composite laminates with curvilinear fibers," *Composite Structures,* vol. 93, pp. 3040-3047, 2011.

[136] Y. N. Rabotnov, *Mechanics of deformable rigid bodies*: Nauka, Moscow, 1979.

[137] V. P. Nikolaev, V. D. Popov, and A. K. Sborovskii, *Strength and reliability of wound GFRP*: Mashinostroenie, Leningrad, 1983.